Investigations Towards Biofunctionalised and ^{99m}Tc Radiolabelled Gold Nanoparticles

Inaugural-Dissertation

zur

Erlangung des Doktorgrades

Doctor rerum naturalium

(Dr. rer. nat.)

der

Mathematisch-Naturwissenschaftlichen Fakultät

der Universität zu Köln

vorgelegt von

M. Sc. Annabelle Mattern

aus Gießen

Köln 2021

Gutachter:	Prof. Dr. Mathias S. Wickleder
	Prof. Dr. Holger Grüll
	Prof. Dr. Roger Alberto
Vorsitz:	Prof. Dr. Ines Neundorf
Beisitz:	Dr. Markus Zegke
Tag der mündlichen Prüfung:	25.10.2021

„Es ist nicht alles Gold, was glänzt. Aber es glänzt auch nicht alles, was Gold ist.“

- Christian Friedrich Hebbel -

Die Arbeiten zu dieser Dissertation wurden im Zeitraum von Januar 2018 bis Juli 2021 am *Institut für Anorganische Chemie der Universität zu Köln* im Arbeitskreis von *Prof. Dr. Mathias S. Wickleder*, sowie während eines zweimonatigen Forschungsaufenhaltes am *Department für Chemie der Universität Zürich*, durchgeführt.

Acknowledgements

First of all, I would like to thank my supervisor Prof. Dr. Mathias S. Wickleder for giving me the opportunity to continue working on this highly interesting research topic afters finishing my master's thesis in Giessen. Thank you for allowing me to work within in your research group in Cologne and to explore freely the scientific world. Over the years, you enabled me to attend numerous excursions, workshop events and international conferences, for which I am very grateful.

Furthermore, I would like to thank Prof. Dr. Ines Neundorf and Prof. Dr. Holger Grüll for their quick, friendly and supportive response to take over the chair of the Thesis defense committee and the second evaluation of this thesis, respectively.

A huge "merci" goes out to Prof. Dr. Roger Alberto (University of Zurich), not only for writing the further evaluation of this thesis. Moreover, you allowed me to carry out all the exciting ^{99m}Tc experiments independently in your laboratories and to perform exceptional, outstanding and unique research in Zurich.

I would like to express my particular gratitude to Prof. Dr. Martin Diener (Justus Liebig University Giessen) for being a cooperative, open minded and accurate collaboration partner over the last years. Thank you for being my second advisor during my PhD, who supported me with new impulses for the development of my research.

Furthermore, I would like to thank the other cooperation partners Prof. Dr. Moritz Bünemann (Philipps University Marburg) and Prof. Dr. Klaus Dieter Schlüter (Justus Liebig University Giessen). Particularly these interdisciplinary collaborations create new inspiration for approaches and make the project extremely fascinating, remarkable and multifaceted.

During my work I received the opportunity to be trained in many analytical methods. A huge thank you goes to Dr. Stefan Roitsch for teaching me how to take focused images of my NPs by TEM. Thank you also for performing the EDX measurements for this thesis. I would like to thank Prof. Dr. Berkessel and his assistant Sarwar Aziz for the introduction to ESI MS and HPLC in their research group. Additionally, I would like to thank Dr. Eva Krakor and Prof. Dr. Dr. (h.c.) Sanjay Mathur for the permission to use the *Zetasizer*. Many thanks goes to Dirk Pullem for performing all CHNS measurements.

I would like to thank the many dear colleagues and former colleagues in Cologne and in Giessen, who have supported me in various ways throughout the last years, both scientifically and personally: Dr. Natalia Arefyeva, Désirée Badea, Dr. Jörn Bruns, Tim Brückmann, Niko T. Flosbach, Dr. David van Gerven, Dr. Corinna Hegemann, Christopher James, Dr. Christian Logemann, Dr. Friederike Machka, Alisha Mertens, Dr. Vanessa Nahrstedt, Dr. Jan Peilstöcker, Dr. Bertold Rasche, Dr. Aida Raauf, Tobias Rennebaum, Lars Schneider, Jasmin Schönzart, Dr. Anne Schulze, Dr. Pascal Specht, Stefan Sutorius, Dr. Erik Strub, Dr. Alexander Weiz, Dr. Daniel Werner, Dr. Miriam Wern, Fabian Wojtalla.

Special thanks goes to my laboratory partner Laura Straub. Thank you for being a nanochemistry support within the circle of solid-state chemists around us. Cheers to us and our nanos, the many TEM sessions and our serenity during a Rosamunde Pilcher excursion. A deep thank you goes to Dr. Markus Zegke for showing me the world with your “thirst for knowledge”-glasses on, especially during lunch time walks when you “worship the sun”. Even when the motivation for this work faded a little, you re-lightened the fire for science in me so that great results followed.

A particular thank you goes out to Rebecca Claßen (Justus Liebig University) and Dr. Ervice Pouokam as well as the technical assistants of the Diener group for all the fruitful discussions and meetings throughout our collaboration over the past years.

A huge thank you goes to the Alberto group in Zurich for giving me such a friendly and warm welcome in the cold season. And for training my brain and me to handle another foreign language. Especially, I would like to thank Dr. Henrik Braband as the Re/Tc sub group leader for trusting me to do the “hot stuff” on my own and for giving me scientific input during, but also after my time in Zurich. Thank you, Raphael Lengacher for the experimental training in handling radioactive substances. “Es huere grosses merci” goes to Robin Bolliger for all his big and small help within the lab, at the university and especially as a phenomenal Swiss German teacher.

I would like to express my warmest thanks to my numerous students, who have actively supported this thesis through their diligent practical work in the laboratory and even realised a part of it. These include, among others: Sebastian Habermann, Katharina Lauchner, Nahal Rouzbeh, Sven Saniternik, Patrick Scholz and Gina Wycich.

For the proofreading of this thesis and scientific as well as grammatical advice, I would like to thank Robin Bolliger, Tim Brückmann, Prof. Dr. Martin Diener, Johanna Schirmer, Julian Schütz, Dr. Erik Strub, Dr. Miriam Wern, Dr. Daniel Werner und Dr. Markus Zegke – the latter in particular; thank you for your rigorous gaze and excellent expressions.

Thank you, Prof. Dr. Merilyn Manley-Harris (University of Waikato), that you recognised a potential in me and encouraged me to become a chemist.

Most of all, thank you to my friends and family, who have accompanied me on the whole journey of my studies. A special thank you to Julian Schütz for being by my side and believing in me.

Last but not least, I would like to deeply thank my wonderful parents, Ingrid und Jürgen Mattern, who enabled and encouraged me to study, strongly supported me in every idea I had and let me unfold my wings.

List of Abbreviations and Acronyms

Table 1: List of all abbreviations and acronyms used throughout this thesis.

Abbreviation	Term
4-MBA	4-mercaptobencoic acid
ADR	adrenaline
approx.	approximately
ATP	4-aminothiophenol
ATR	attenuated total reflection
b s	broad singlet (NMR)
BODIPY	boron-dipyrromethene
BOP-Cl	bis(2-oxo-3-oxazolidinyl)phosphinic chloride
BS	biogenic substance
bwt	bodyweight
CCh	carbachol
$CHCl_3$	chloroform
Cys	cysteamine
d	diameter
d	doublet (NMR)
DA	dopamine
DAH	diaminohexane
DCM	dichloromethane
demin.	demineralised
DHCA	dihydrocaffeic acid
DIC	diisopropylcarbodiimide
DIU	*N*,*N*'-diisopropylurea
DLS	dynamic light scattering
DMAP	4-(dimethylamino)pyridine
DMF	dimethyl formamide
DMSO	dimethyl sulfoxide
DTDTPA	dithiolated derivative of diethylenetriaminepentaacetic acid
EDC	*N*-(3-dimethylaminopropyl)-*N*´-ethylcarbodiimide hydrochloride

EDTA	ethylenediaminetetraacetic acid
EDX	energy-dispersive X-ray spectroscopy
EN	ethylenediamine
Eos	eosin Y
eq.	molar equivalents
ESI	electron spray ionisation
et al.	et alii/aliae/alia (*Latin* for „and others")
EtOAc	ethyl acetate
EtOH	ethanol
h	hour
HATU	hexafluorophosphate azabenzotriazole tetramethyl uronium
HPLC	high performance liquid chromatography
Hz	Hertz (NMR)
IR	infrared
J	Joule (unit)
J	coupling constant (NMR)
K	kelvin
LA	lipoic acid
m	multiplet (NMR)
MeCN	acetonitrile
MeOH	methanol
min	minute
MS	mass spectrometry
MUAM	mercaptoundecylamine
MUDA	mercaptoundecanoic acid
NaBC	sodium boranocarbonate
NEt_3	triethylamine
NMR	nuclear magnetic resonance
NP	nanoparticle
PADA	picolylamine diacetic acid
PBS	phosphate-buffered saline
PD	protein desalting

pH	potentia hydrogenii (*Latin* for „potential for hydrogen")
Ph	phenyl
q	quartet (NMR)
RCP	radiochemical purity
Rhod	rhodamine B
rpm	revolutions per minute
rt	room temperature
s	singlet (NMR)
SB	salbutamol
SEM	standard error of the mean
SDS	sodium dodecylsulfate
SEC	size exclusion chromatography
t	triplet (NMR)
^{t}Bu	tertbutyl
TEM	transmission electron microscopy
TLC	thin layer chromatography
t_R	retention time
UV/Vis	ultraviolet and visible light
XRD	X-ray diffraction

Abstract

This work concentrates on the synthesis and functionalisation of monodisperse gold nanoparticles within a size range of 5 to 30 nm. These were further functionalised with either biogenic substances such as carbachol, adrenaline or atropine or with a biomimetic compound like dihydrocaffeic acid. Different synthetic routes are described, and state-of-the-art analyses such as transition electron microscopy, multidimensional heteronuclear magnetic resonance, dynamic light scattering, optical absorption spectroscopy, high performance liquid chromatography and mass spectrometry are presented throughout and confirm the size of the nanoparticles and their successful functionalisation.

Furthermore, this thesis discusses the physiological studies of the biofunctionalised gold nanoparticles, which showed biological activity and even multivalent stimulation of various receptor types in different biological systems including intestinal, cardiac and respiratory tissues. This work demonstrates that the application of biofunctionalised gold nanoparticles can surpass the biological effects of the free parent compound by several orders of magnitude. Further prospective functionalisations are presented, such as the labelling of gold nanoparticles with fluorescent dyes, including the necessary modifications of the fluorophore.

As the biodistribution of gold nanoparticles within the whole body is of great interest, this thesis focusses strongly on investigations towards gold nanoparticles radiolabelled with ^{99m}Tc. Using a mono ligand shell (only carrying chelating ligands) or a mixed ligand shell (carrying chelating ligands as well as a biogenic substance), these radiolabelled functionalised gold nanoparticles could potentially function as probes for imaging investigations and be subject to future studies towards radiotheragnostics.

In particular, this thesis presents how the tridentate chelating ligand picolylamine diacetic acid (PADA) was used showing promising results regarding the complexation of ^{99m}Tc and its heavier group 7 homologue Re. Connecting PADA with a mercaptoalkyl linker enables the ligand to attach to the gold nanoparticle surface with the thiol group. Furthermore, a spacer with a longer alkyl chain ensures the required stability of the functionalised gold nanoparticles. The radiolabelling procedures were performed under mild conditions and in a time efficient manner, as ^{99m}Tc only has a half-life of 6 h. Special emphasis was placed on the purification and the analytical characterisation of the radiolabelled gold nanoparticles, which were obtained as stable pink dispersions and which were directly analysed by size exclusion chromatography with a γ detector. Post-labelling analyses were also carried out and confirmed the integrity of the material.

1 INTRODUCTION

Nanoparticles (NPs) in general can be man-made but have also occurred in nature long before they were artificially investigated. In particular, the terminus 'nanotechnology' was coined as late as 1974 by the Japanese scientist Norio Taniguchi, when he was describing semiconductor processes on nanoscale levels.[1]

Natural NPs occurred ever since for instance in the form of ash after a volcanic eruption.[2,3] However, engineered NPs have seen increased interest and nanoscience is a rapidly evolving field of research.

An overview of nanomaterials and their most prominent properties is presented in **Figure 1** and will be described in more detail in the following chapter.

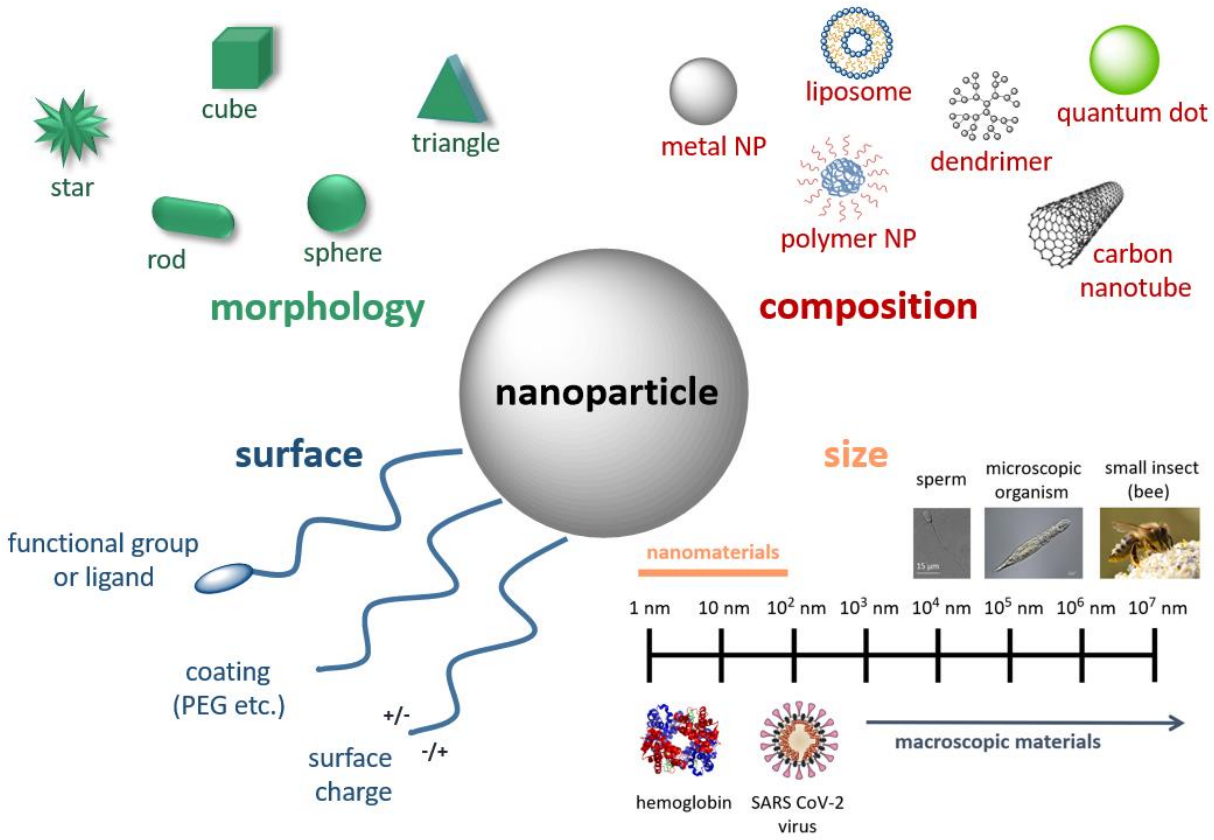

Figure 1: The key factors *composition, size, surface* and *morphology* of NPs.

1.1.1 COMPOSITION OF NANOMATERIALS

In general, the physicochemical properties of NPs differ from the chemically similar bulk material. They can be conveniently generated from noble metals Au[4], Ag,[5] Pt,[6] or Cu[7] but also from elements like carbon in form of nanotubes.[8] Further inorganic compositions like oxides ((e.g. Fe_3O_4,[9] SiO_2)[10] or nanoscale semiconductors called quantum dots, such as CdSe[5] or CdTe[11], are known.

In addition to these inorganic materials, nanoscale polymers or dendrimers are frequently reported (**Figure 1**, **top right**).[12,13] Repenko *et al*.[14] investigated polymer NPs conjugated with imidazole units, which were highly fluorescent and moreover showed promising biodegradable properties. Since their surface can be easily functionalised, various applications in imaging or drug delivery have emerged.[14] One example of the highly branched polymers called dendrimers was described by Bono *et al*.[15] Here, they showed that a polyamidoamine (PAMAM) dendrimer had a low cytotoxicity, but very good antibacterial activity against *E. coli*. Furthermore, due to an overall facile ability of a further functionalisation, the dendrimer offers potential for a gene-delivery application.[15]

Moreover, micelles and liposomes are both used in biomedical applications.[16,17] Deng *et al.*[18] encapsulated folate conjugated liposomes with a photosensitiser as well as with the antitumour drug doxorubicin. Through X-ray radiation, the photosensitiser triggered the formation of singlet O_2, which again causes the liposomal membrane to destabilise, leading to a release of doxorubicin. This system of radiotherapy coupled with chemotherapy showed satisfactory results *in vivo*, leading to cell death on a range of cancer cells with IC_{50} values as low as 1.6 µM. The same drug concentration of doxorubicin without an X-ray triggering resulted only in the death of 10% of cancer cells.[18] IC_{50} is defined as the concentration level of an inhibitor, at which a half-maximal inhibition of a specific biological function is observed. The IC_{50} value thus describes the potency of an inhibitor or a drug.

Another drug release was studied by Salgarella *et al.*[19] with micelles. These were assembled from poly(2-oxazoline) units and encapsulated with the hydrophobic anti-inflammatory drug dexamethasone, which was then released *via* ultrasound.[19] Furthermore, dexamethasone-loaded micelles demonstrated a promising potential to be applied as a treatment of rheumatoid arthritis while showing an anti-inflammatory effect after the subcutaneous injection.[20]

Since 2020, lipid NPs have been shown to function as a carrier for modified messenger ribonucleic acid (mRNA). Inside the body, ribonucleases would otherwise degrade the mRNA before it would enter the cells and reach the point of action. The coating of lipid NPs thus increases the stability of the mRNA. Furthermore, these systems have received enormous attention, as this type of NPs are currently being used worldwide as vaccines against SARS-CoV-2 in the approved injection doses of Pfizer-BioNTech and Moderna.[21,22]

In terms of their ecological impact, and in times where “micro plastic”[23] has induced a shift towards biodegradable materials, the organic frameworks used in the synthesis of nanomaterials possess generally a good biodegradability. In addition, systems based on hematite or silicon dioxide are regarded as inorganic biodegradable carrier options.[24,25]

1.1.2 Sizes of Nanomaterials

The size has a strong and significant influence on the properties of NPs. By definition, the term *nano* refers to materials whose size in at least one dimension is between 1 and 100 nm. On the metric scale (**Figure 1**, **bottom right**), nanomaterials fall in the same order of magnitude as, for example, a protein such as haemoglobin (approx. 5 nm) or a virus such as SARS CoV-2 (approx. 120 nm) and are thus 500 to 1000 times smaller than unicellular or even multicellular organisms such as bdelloid rotifers *Adineta vaga* (150 to 700 µm)[26,27] or even a human sperm (approx. 50 µm).

Nanomaterials possess a large surface to volume ratio. For instance, in NPs with a diameter of 4 nm about 50% of all atoms are surface atoms.[28] As a result, the enormous surface owns a particular importance, and it increases strongly with decreasing particle sizes. The small size of NPs furthermore leads to significantly different properties compared to macroscopic materials. NPs possess lower melting points than the corresponding bulk material[29] and a substantial depression occurs below a size of about 10 nm.[30] The surface energy even has the potential to influence the crystal structure of the formed NPs. While Rh as a bulk material usually exists as Rh *fcc* (face centred cubic), and even though the bulk energy of Rh *hcp* (hexagonal closed package) is higher, Huang *et al.*[31] described the fact that the surface energy matters so significantly for smaller Rh NPs (sizes between 1 – 5 nm) that they lead to stable *hcp* Rh NPs.[31] Even a size-dependent chemical stability of Ag NPs in an aqueous medium was observed by Molleman *et al.*,[32] when they investigated the Ag^+ release from Ag-Citrate NPs (sizes between 5 – 20 nm) and showed that smaller NPs led to a higher release of Ag^+.[32] Furthermore, a more acidic pH of the dispersion resulted in a larger Ag^+ release and thus in an oxidative dissolution of the NPs.[33] Even a size-dependent phototoxicity of near-spherical TiO_2 NPs was described by Xiong *et al.*,[34] which is stronger for smaller NPs of 10 nm in size than for the larger homologues with a size of 20 and 100 nm, respectively.[34] However, since the TEM images of the TiO_2 NPs in the mentioned study predominantly show agglomerate-like arrangements of NPs of highly different morphologies, the precision of the size determination of the primary NPs without additional error information is questioned by the author of this thesis.

Furthermore, An *et al.*[35] investigated the influence of the size on the mechanical properties of NP assemblies. The assemblies of SiO_2 NPs with diameters in the range between 10 nm to 300 nm become tighter, more rigid and harder as the NPs diameter decreases.[35] As another aspect, even the magnetic behaviour can be influenced in nanoscale materials.[29] Iron oxide NPs exhibit superparamagnetic properties,[36] which can become useful in various applications.[37–40] Furthermore, the energy band gap can be affected in nanoscale sizes, so that it increases for semiconductors with decreasing size.[41] For CdS NPs below a diameter of 3 nm, quantum effects influence the band gap.[42]

This quantum confinement occurs as soon as the dimensions of the structures are on a similar order of magnitude as the size of an electron.[42,43] The quantum size effect leads to characteristic properties for metal and also semiconductor NPs as the sizes of these nanomaterials are in a similar order of magnitude as the wavelength of visible light. Under the

influence of light and thus an oscillating electrical field, a collective oscillation of the surface conduction electrons and consequently of the electron cloud occurs (*surface plasmons*).[44] The amplified resonance of the vibratory system emerges at a certain photon frequency, so called *surface plasmon resonance*. In the case of Au NPs, the absorption maximum λ_{max} is located in the visible range of the light, thus they appear in wine red colours. The exact position of the localised surface plasmon resonance depends on size, shape, composition as well as chemical and surface environment of the NPs.[45–48]

1.1.3 Surface Functionalisation of Nanomaterials

Since nanomaterials possess a large surface energy, they tend to agglomerate in order to reduce the surface energy and to obtain an energetically more stable and favourable system. To prevent NPs from agglomeration, surface stabilisation must occur (**Figure 1**, **bottom left**), which can happen electrostatically by charged ligands on the surface of the NPs (**Figure 2**, **left**), as seen in the well-known Au-Citrate NPs. Furthermore, Monti *et al*.[49] describe an electrostatic stabilisation of Au NPs in water using sulfonated imidazolium salts. They assume a coordination of the imidazolium unit to the Au NPs and the sulfonate groups remaining outside on the ligand sphere, which again prevents aggregation through electrostatic repulsion. The respective zeta potentials support this assumption and indicate stable dispersions.[49] Another way of stabilisation occurs sterically (**Figure 2**, **centre**) due to bulky ligands on a NP surface. Here, the use of polyethylene glycol (PEG coating) or long chain alkyls is frequently described.[50–52] Polymers are also commonly chosen in order to stabilise e.g. γ-Fe_2O_3 NPs, as Priyananda *et al*.[53] described for a ferrofluid, while different nitrogen acyclic carbenes were used by Rubio *et al*. to stabilise Au NPs.[54] Even electro-steric stabilisation occurs, when both properties are present: a charged bulky ligand for an electrostatic repulsion as well as a steric stabilisation (**Figure 2**, **right**).[55,56]

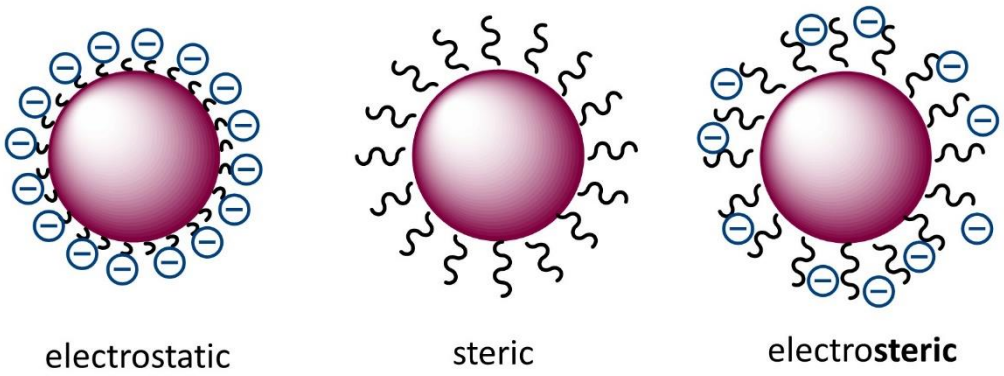

Figure 2: Representation of electrostatic (**left**), steric (**centre**) and electrosteric (**right**) stabilisation.

Coating with PEG or other polymer shells offers several advantages: The colloidal stability of NPs improves in aqueous media and especially under physiological conditions, making them feasible for biomedical applications.[57] Furthermore, PEG is an extremely hydrophilic material, which renders the NPs virtually invisible to phagocytic cells when being applied in tissue. Moreover, it ensures that the non-specific cellular uptake is reduced and, at the same time, an additional protein adsorption is diminished.[58] These processes could result in a too rapid degradation or removal from the point of action before the drug could be delivered. Therefore, PEG coated NPs possess longer blood half-lives and own a stealth effect. However, pure PEG coating is not completely biodegradable and thus could lead to accumulation in mammalian tissues.[59] Consequently, studies have been performed on PEG alternatives over the last years, for instance based on polyphosphoesters.[58] Li *et al*.[60] describe the synthesis of π-conjugated oligomeric NPs, which are coated with a PEG derivative shell; these polyphosphoesters exhibit a good biodegradability. The spherical NPs with a diameter of approximately 60 nm show the potential of being photothermal therapy agents with high efficiencies against various cancer cells.[60] Xu *et al*.[61] have investigated the influence of the PEG density on the NP surface on the overall shielding of the NPs in more detail. They synthesised NPs with different ratios of PEG and poly(lactic-co-glycolic acid) (PLGA) coating and found that they required at least 5% of PEG to shield the NPs successfully. Furthermore, they protected them in this way from interactions with mucosal components so that their targeted delivery as drug-loaded mucus-penetrating particles could still take place.[61] Another approach was described by Steiert *et al*.,[59] who presented the synthesis of a fully degradable PEG copolymer, which incorporates vinyl ether groups and thus achieves an acid degradability. Consequently, their work focuses on the development of pH-responsive protein NPs. With these, a triggered release at pH 4 of e.g. therapeutic drugs is achievable and could theoretically be used for a variety of proteins.[59]

With choosing the right stabilising ligand, further desirable compounds can be attached to the surface and thus provide not just stabilisation but also novel functionalisation of the NPs (Figure 1, bottom left). This can be applied in various areas from catalysis[62,63] to medicine. With regard to the latter one, a wide range of functional molecules and frameworks have already been attached to NPs, reaching from biogenic compounds,[4] to target ligands such as antibodies[64] and drugs[65,66] as well as proteins[67] or deoxyribonucleic acid (DNA) scaffolds.[68,69]

Furthermore, the functional group on the ligands itself can interact differently with cells. Amine stabilised NPs, for instance, are positively charged at physiological conditions and thus able to interact with nucleic acids, which are negatively charged. Hence, they can mediate transfection in mammalian cells cultures, as Sandhu *et al*.[70] reported for 2 nm sized Au NPs modified with mercaptoundecylammonium on their surface.[70] Moreover, Jiang *et al*.[71] investigated a strong correlation between surface charge and size of the NPs in regard to their uptake in cancer cells. They analysed sub 10 nm sized Au NPs and described different entering mechanisms depending on their properties. Their studies on cancer cells show that cationic NPs have a higher cellular uptake with an increasing size. In contrast, neutral, zwitterionic or negatively charged NPs show a lower uptake with larger diameters.[71] In addition, Osaka *et al*.[72] investigated the cellular uptake of NPs on different cells types. In accordance with the previously mentioned study, they

reported that positively charged NPs were taken up into cancer cells more efficiently. However, with normal endothelial cells, NPs are internalised and taken up in similar rates regardless of their charge.[72]

The surface funtionalisation and properties consequently do not only have an important impact on medical applications, the NPs' biodistribution and their effects on tissues but also on their general stability in biocompatible media. Furthermore, it can influence the shape of the NPs.

1.1.4 Morphology of Nanomaterials

A wide variety of different morphologies for NPs exists, as has been shown in **Figure 1**, **top left**. In the synthesis of NPs, the *LaMer* principle[73] can be generally used to explain NP formation. Here, the precursor molecules exist in a dissolved form and once the reducing agent is added, they will be reduced or decomposed. At a critical concentration, nuclei are formed instantaneously. Since the reaction solution is then depleted of monomers, it falls below the minimum concentration necessary for nucleation. Thus, no further nuclei are formed. Instead, the nuclei grow *via* aggregation or *Ostwald ripening* until a saturation concentration of the NPs is achieved. During growth, the NPs initially have the tendency to form the most thermodynamically stable shape, resulting in spherical NPs. In order to obtain monodisperse spheres, it is important that the phase of spontaneous nucleation is as short as possible and the following growth process proceeds more slowly. Additionally, the precursor monomers should be present in rather low concentrations.

However, if the NP synthesis is kinetically controlled, different, and also anisotropic, morphologies of NPs are achievable. A higher or changing concentration of precursor monomers, different coordinating solvents and the pH can influence the shape of the formed NPs. Furthermore, additives and surfactants can promote the formation of certain shapes by adsorbing onto defined facets of the growing NP surface and capping them. In this way, they lead to a lower surface energy and thus control the growth of these facets.[74,75] Commonly described capping agents in literature for anisotropic NP syntheses are polyvinylpyrrolidone (PVP) or cetyltrimethylammonium bromide (CTAB).[76,77]

For instance, Au nanorods are often synthesised using the additive CTAB.[78] In different syntheses, Requejo *et al.*[79] added not just CTAB but also bio additives such as glutathione or cysteine and obtained monodisperse nanorods with tuneable optical properties in either larger sizes (100 nm length and 19 nm width) or smaller sizes (40 nm length and 7 nm width), depending on if a seed-mediated or seedless synthesis was performed with the bio additives.[79] Furthermore, nanorods can be prepared from other materials. Butterfield *et al.*[80] recently obtained CuS nanorods with a lengths of 20 nm during a reaction using dodecyl thiol in an octadecene, trioctylphosphine oxide and oleylamine mixture.[80]

Moreover, nanocubes can be synthesised from a variety of starting materials. Ag nanocubes are commonly prepared using the polyol process with PVP.[81,82] Selective growth is guided by

PVP, among other factors, as Chen *et al*.[83] highlighted the particular significance of chloride ions, which are freely available during synthesis. These enter strong interactions with the NP surface and present another shape control as they selectively adsorb onto certain facets of the NP surface during synthesis.[83] This effect was also observed during the synthesis of Rh nanocubes starting from $RhBr_3$[84] or $RhCl_3$,[85] respectively. The latter synthesis was performed using PVP in ethylene glycol (EG) and different monodisperse sizes from edge lengths between 23 nm to 27 nm were isolated.[85]

In addition, nanostars have recently seen greater impact. Khoury *et al*.[86] started from Au nanoseeds coated with PVP and added PVP and DMF in a second reaction step (seed-mediated growth). In this way, nanostars of various monodisperse sizes between 45 nm and 116 nm star diameter were obtained. The nanostars dispersions showed a deep green colour and UV/Vis measurements revealed that in addition to an absorption in the red shifted region, they exhibit another even more intense plasmon resonance in the near infrared (NIR) region. Conclusively, size and morphology of the stars have a direct influence on the UV/Vis absorption, which in turn can be fine-tuned.[86] This may be of importance for biological applications.[87,88] Au nanostars can also be obtained within a single reaction instead of a seed-mediated growth process. Liebig *et al*.[89] describe a reproducible one-pot synthesis of Au nanostars in different sizes between 70 nm and 200 nm. They obtained sharp and large spikes and additionally used $AgNO_3$ as a structure directing agent during the synthesis.[89]

As a further morphology, flat nanoplates can be prepared (**Figure 1**, **top left**). Xiong *et al*.[90] describe their synthesis of Pd triangular nanoplates with a side length of 28 nm. They were able to obtain them from a slow reduction process starting from Na_2PdCl_4 dissolved in EG in the presence of PVP and additionally added $FeCl_3$.[90] Furthermore, triangle plates of Au are reported in the literature, which are stabilised with CTAB, as Huang *et al*.[91] published. Their nanoplates possess a relatively long side length of 140 nm, but they are able to adjust the thickness of the nanoplates quite accurately, ranging from 8 nm to 80 nm thickness.[91] Nambara *et al*.[92] instead use CTAC, the chloride version of CTAB, for the syntheses of their differently sized monodisperse triangular Au nanoplates with sizes from 46 nm up to 96 nm and a thickness of 30 nm. The surfaces were modified in a subsequent ligand exchange with an anionic thiol ligand, whereby the shape did not alter. A successful ligand exchange was demonstrated analytically with ^{1}H-NMR measurements. However, they were only showing the NMR data of the nanomaterials after ligand exchange, revealing “no signals” in contrast to a spectrum of a CTAB solution. To deduce a successful ligand exchange from the absence of signals and to record and to present neither a spectrum of the nanomaterials before the surface modification nor a spectrum of the new ligand, however, is considered debatable by the author of this thesis. Nambara *et al*.[92] also presented their further study on macrophagic and cancer cells: They observed that cellular uptake of the nanoplates occurred in both cell types. Moreover, a 20-fold more efficient internalisation for larger sized nanoplates (72 nm) compared to the smaller ones (66 nm) could be observed. Furthermore, they compared these results with equally modified but spherical Au NPs of a similar size (22 nm to 66 nm). However, here a controversial trend was observed: Within an increasing size, fewer spherical NPs were incorporated into the cell

types compared to smaller sizes.[92] When comparing the cellular uptake of NPs just with regard to their shapes in similar size regions, Carnovale *et al*.[93] investigated a higher internalisation tendency by cancer cells with the trend nanospheres > nanocubes > nanorods > nanoplates with having similar sizes.[93] Furthermore, Yue *et al*.[94] showed in their study a higher cellular uptake of nanospheres compared to nanostars by brain cancer cells.[94]

Overall, the science of nanomaterials presents many facets. In general, small changes can have enormous consequences on their properties and in terms of potential applications. This is what makes nanotechnology a constantly growing and evolving field of research.

1.2 Gold Nanoparticles (Au NPs)

Gold as a bulk material stands out mainly because of its unique shiny colour at first sight (**Figure 3**, **left**). Furthermore, it is a dense, soft, and ductile metal, and at the same time one of the least reactive elements of all. Its value has been highly appreciated since antiquity, and its lasting use as jewellery or in coinage remains unchallenged. Its most prominent chemistry however is represented by gold nanoparticle (Au NPs) dispersions, which are particularly recognisable because of their intense red, wine-red, or even violet colourings (**Figure 3**, **right**).

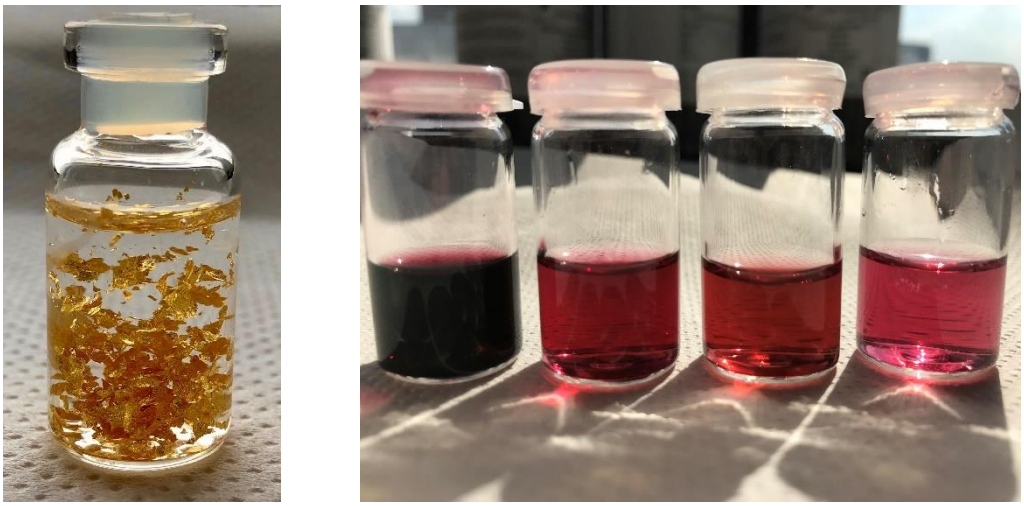

Figure 3: Bright shiny gold bulk material in a vial (**left**) and intense red gold nanoparticle dispersions (**right**).

Ever since, gold as a bulk material has fascinated people, and even alchemists tried to obtain it over centuries in supposed transmutation processes. In these, non-precious metals such as lead were tried to be converted into gold, which was believed to be achievable with the philosopher's stone.[95] Obviously, these attempts remained unsuccessful until the discovery of nuclear transmutation in the 20th century. One of the most renown chemists of the 19th century, Justus von Liebig, associated with the philosopher's stone a "most lively imagination"[96] and noted the fact that, despite this gold making process was unsuccessful, it furthered our understanding of chemical reactions and was a main contribution to the development of chemistry from alchemy.

As for macroscopic gold, also drinkable gold or potable gold has been known and Paracelsus ascribed healing properties to it.[97] Without knowledge of a precise composition and a deeper understanding of these "slightly pink solutions",[98] they were used as cures for several diseases, such as dysentery, diarrhoea or epilepsy.[99] Gold salts were also used in glass making, whereby red ruby glasses could be manufactured, which were used for church windows or in high-quality decorative objects.[100] Even if the term *colloidal gold* was already coined at that time, Michael Faraday was the first one who prepared intentionally a sample of *colloidal gold* and described its dichroistic properties in 1857.[101] He observed that he had to stabilise his "gold separated as solid particles" by addition of phosphorous in CS_2 and noticed that the "beautiful ruby fluid" was highly stable if the ratio of the added substances was accurate.[101] Surface modification and functionalisation of nanomaterials and in particular of Au NPs still constitute an important area of research.

Even though Michael Faraday was one of the first to describe *colloidal gold* as "smallest particles", it took another century before these NPs could be displayed and thus visualised using innovative electron microscopy (EM) for the first time in the 20th century, which allowed to investigate their size and morphology. However, the exact crystal structure of the gold core remained unknown for the following decades due to the non-crystallinity of the samples. But this lack of information regarding the arrangement of atoms within the particles could be overcome at the beginning of the new millennium.[102–104] Jadzinsky *et al*.[102] succeeded in obtaining crystalline material of 4-mercaptobenzoic acid (4-MBA) protected Au NPs. The structure obtained by X-ray diffraction showed 102 Au atoms in the core of the NP, which was stabilised by 44 4-MBA ligands (**Figure 4**).

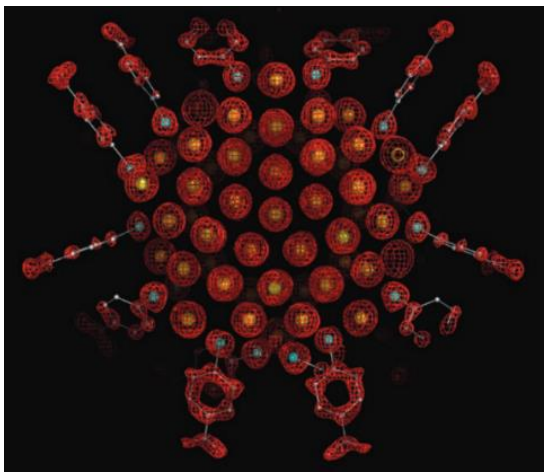

Figure 4: X-ray crystal structure determination of the Au_{102}4-MBA_{44} NP with electron density mad (red mesh) and atomic structure [gold in yellow, sulfur in cyan, carbon in grey, and oxygen in red].[101]

Furthermore, they demonstrated abundant interactions of the Au surface with the ligands, but moreover various interactions of the ligands with each other, providing additional stabilisation of the system. Lahtinen *et al*.[105] even successfully achieved to form multimeric structures of the Au_{102}4-MBA_{44} cluster containing a covalent bond (**Figure 5 A**). In a ligand exchange reaction, the linking moiety was introduced in the form of a biphenyl-4,4'-dithiol.

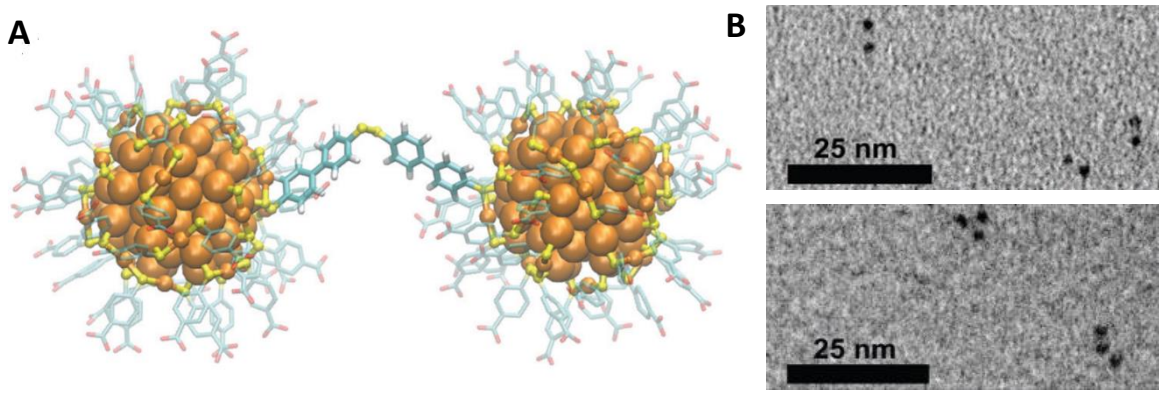

Figure 5: (**A**) Molecular density simulations of linked Au_{102}4-MBA_{44} clusters and (**B**) the corresponding TEM images of these superstructures as dimers (**top**) and trimers (**bottom**).[104]

The corresponding TEM images (**Figure 5 B**) revealed the presence of superstructures of approx. Ø 1 nm sized NPs paired as dimers (**Figure 5 B**, **top**) and trimers (**Figure 5 B, bottom**) in the dispersions. Furthermore, spectroscopic studies of the compounds were performed, showing that the Au_{102}4-MBA_{44} clusters do not possess a distinct surface plasmon resonance. On the other hand, the $Au_{\sim 250}(4\text{-MBA})_n$ multimers showed a distinct surface plasmon resonance with λ_{max} at 530 nm and thus a clear distinction between the monomeric species and the multimers could be achieved.[105]

1.2.1 Applications of Gold Nanoparticles

A variety of potential applications exists for Au NPs. In 1989, Haruta *et al.*[106] described the oxidation of CO catalysed by Au NPs; these nanomaterials have been widely studied as catalysts.[107–109] At that time, Haruta *et al.*[106] used Au NPs with sizes smaller than 10 nm, which were homogeneously deposited on a metal oxide surface such as the semiconductors Fe_2O_3 or NiO. Interaction between Au NPs and a support material nowadays allow for selective and efficiently catalysed reactions, which are mostly performed under very mild reaction conditions. Giorgi *et al.*[110] successfully used Au NPs on a support of TiO_2 or Al_2O_3 to selectively oxidise activated alcohols mainly below 100 °C in typical organic solvents under O_2 atmosphere. In addition to their catalytic properties, Au NPs have been frequently discussed in terms of their applications as switches,[111] sensors[112] or in nano electronic devices.[113,114]

The by far most extensive usage of Au NPs, however, is in the biomedical field. These applications can generally be divided into different areas: imaging & diagnostic, therapy, and transport & delivery. **Figure 6** schematically shows these areas and the respective type of functionalisation on the NP.

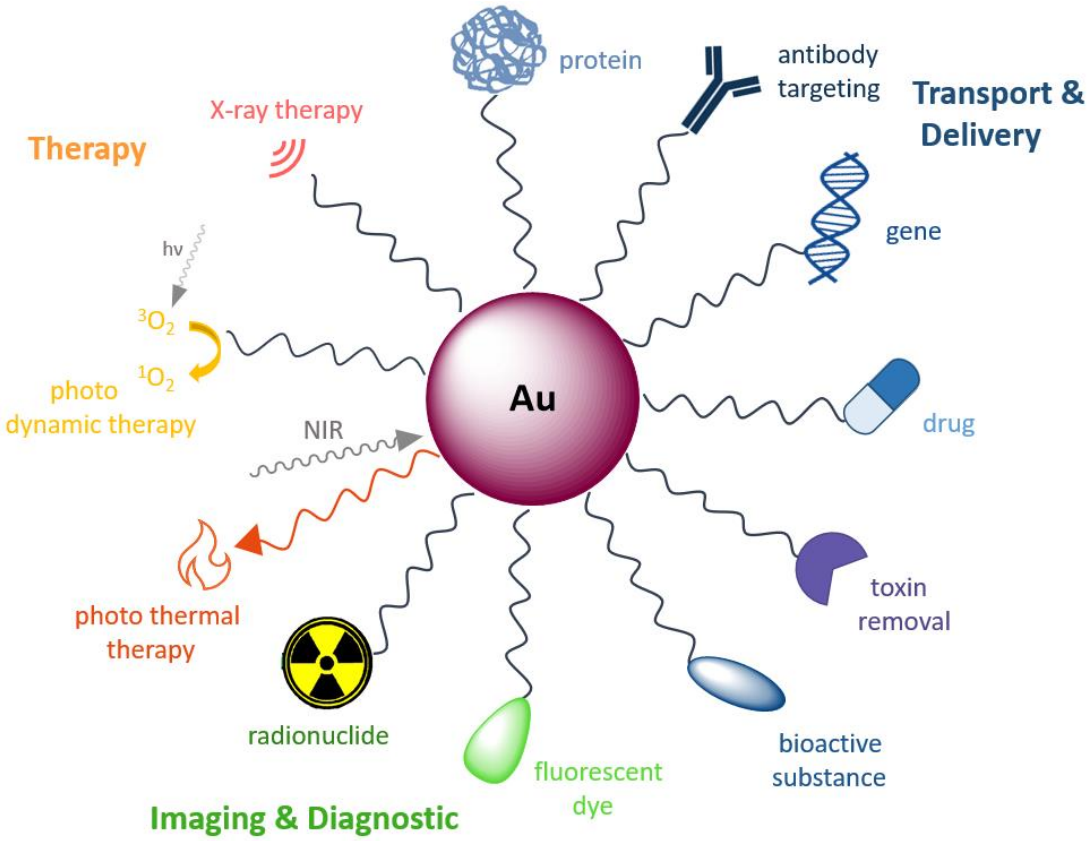

Figure 6: Biomedical applications of Au NPs and their corresponding surface functionalisation.

1.2.1.1 Therapy

Au NPs have been studied therapeutically mainly against different types of cancer. NPs or macromolecules in general accumulate in malignant tissues and thus show the *EPR* effect (*enhanced permeability and retention*). The reason for this effect is that new blood vessels with larger capillaries are formed in tumour tissues and NPs can readily permeate into them. However, the removal of NPs from them is hindered because of a lack of sufficient lymphatic drainage within the malignant cells.[115] This again causes an accumulation of these carriers within the tissue, which can be of major advantage for a therapy, as the NPs may now incapacitate or even kill the tumour or be of diagnostic use.[116]

One method that is commonly studied is photothermal therapy (PTT). This involves a hyperthermia anticancer treatment, in which the temperature of the malignant tissue is heated to 42°C – 46 °C (**Figure 6**, **lower left**), thus irreversibly damaging and destroying the cancer cells. For example, near infrared (NIR) radiation can be used for irradiation. A photosensitive agent then converts the photon energy into heat. Therefore, research is focussing on the development of effective heat mediating transmitters and Au NPs in particular represent a suitable material for this purpose.[117,118] They exhibit a defined surface plasmon resonance and if λ_{max} of the Au NPs is adjusted to the NIR region, an enormous increased absorption can be achieved. Due to the heavy mass of Au in general, Au NPs also exhibit favourable photon scattering.[119]

As an alternative, Nam *et al*.[120] even presented PTT combined with chemotherapy in their studies. In this way, synergistic effects leading to tumour tissue deaths could be achieved in a minimally invasive way.[121] Nam *et al*.[120] synthesised Au nanostars coated with different thicknesses of polydopamine. The nanostars with sizes between 60 nm and 150 nm in size and a λ_{max} around 850 nm exhibited a high PTT stability and a remarkable efficiency. After the application of the nanostars and irradiation, a subtherapeutic dose of the anticancer agent doxorubicin was administered. As a result, more than 85% of colon carcinomas were effectively treated and the therapy was also shown to be successful against a version of highly aggressive lung carcinoma. In addition, the animals exhibited a long term resistance against tumour regrowth and indicated a sort of immunological effect, which could be of interest for a further therapeutic treatment of cancer or even protection from cancers.[120]

A different approach regarding PTT was published by Schartz-Duval *et al*.[122] They used PEG clusters as a delivery vector for ionic gold. After injection into the tissues, a bioreduction to small Au NPs occurred within 30 min in the human breast cancer cells. In this cellular-driven process, the detection of the surface plasmon resonance indicated the formation of Au NPs. Afterwards, photothermal remediation was achieved by irradiation. Producing NPs inside the cells may provide a new route for ablative therapy using photothermal heating for hyperthermia applications in the future.[122] It may be criticised though that a potential disadvantage of these two studies is the fact that the drugs were administered and injected directly into the tumour tissue, so the process of transport was effectively eliminated and thus no “targeted delivery” could be observed.

Another therapy option involving the potential support of Au NPs against tumours is photodynamic therapy (PDT). Here, photosensitisers are used, which transfer energy to surrounding molecular oxygen and thereby causing the development of highly reactive oxygen species (ROS), which then lead to a rapid apoptosis or necrosis (**Figure 6**, **left**). However, most photosensitisers used, such as porphyrins or phthalocyanines, are hydrophobic: They would preferentially accumulate in non-polar sites. Therefore, for example, Au NPs that carry hydrophilic functionalities can serve as a delivery vector for these hydrophobic drugs inside them.[123–127] Cheng *et al*.[128] created highly efficient drug vectors for PDT by coating 5 nm Au NPs with PEG. These were then carrying the hydrophobic drug inside their water soluble shell. They were able to show that with the help of these carriers, faster delivery with presumably fewer side effects is possible. The intravenously injected Au NPs carry 30 phthalocyanine molecules per particle, and are able to reach the tumour selectively in less than 2 h. Phthalocyanine as a free ligand would have taken up to 2 days.[128] This type of studies were continued by Camerin *et al.*,[129] who investigated the same particles. Furthermore, they were functionalised with approx. 10 Zn-phthalocyanine derivative molecules per Au NP. These Au NPs showed an increased retention in the tumour tissues after intravenous injection, which corresponds to the EPR effect. Moreover, after subsequent irradiation, they caused destruction of melanomas in the animals. In addition, no new regrowth of tumours occurred in 40% of the animals.[129] Parallel to the two single therapy methods, some researchers combine both PTT and PDT, and hope these will lead to an even more effective treatment against cancer.[130,131]

Another common method for the treatment against cancer is radiation therapy (**Figure 6**, **upper left**). This principle is based on the fact that free radicals are formed by external irradiation. As a component of reactive oxygen species (ROS), hydroxyl radicals (·OH) are able to break molecular bonds and to oxidise DNA or other intracellular protein structures, thus causing the destruction of the cell. However, to ensure that only tumour tissue is destroyed, radiation needs to be applied only locally.[132] With regard to this methodology, researchers are investigating the applicability of Au NPs as sensitisers.[133,134] It has been shown that Au NPs significantly improve radiotherapy and increase its efficiency.[135,136] This effect is further described by the dose enhancement factor (DEF), which correlates in this study with the ratio of the radiation dose absorbed by the tumour cells in the presence of NPs to the dose absorbed in the absence of NPs.[137] In addition, due to the EPR effect, NPs in general embed and increasingly accumulate in tumour cells and thus a more targeted and at the same time more effective radiation can be achieved.[135,137]

Hainfield *et al.*[138] showed that 11 nm sized Au NPs accumulated in intracerebral malignant tumour tissues. With an immense high intravenous dose of 4 g Au/kg, they localised the NPs in brain tumour tissues with a ratio of 19:1 compared to normal brain tissue. This enabled high resolution tumour imaging *via* computer tomography (CT). After radiation, a multiplied radiotherapy dose of a calculated factor of 300% could be determined. Furthermore, they mention that 53% of the mice showed a tumour free survival in the long term compared to 9% using only radiation without Au NPs. Even though these highly aggressive and imminently lethal brain tumours were successfully treated in their study, however, the research also shows some drawbacks especially with regard to the analytical investigations of the used Au NPs. These were purchased commercially, but the authors did not provide any detailed analysis of the Au NPs, neither morphological examinations *via* TEM, nor an investigation of the surface functionality. The latter could have an enormous influence on the effect of the tumour therapy and the biodistribution of the Au NPs. Furthermore, the authors describe that the tumours removed immediately after radiation were extremely dark and black in colour, which they explained due to the high dose of Au NPs within the tumour.[138] This description suggests an agglomeration of the Au NPs which was not further elaborated on.

In another investigation, Zhang *et al.*[139] described the differences in the radiosensitivity of Au NPs depending on their sizes in *in vitro* and *in vivo* studies. They synthesised Au NPs coated with PEG in different sizes between 5 nm and 50 nm, which were then intraperitoneally injected into mice. In general, smaller Au NPs displayed a higher toxicity. But 12 nm and 27 nm Au NPs showed a wider distribution within the cells of a cervical carcinoma and thus a higher radiation DEF could be achieved as well as a higher radiosensitivity.[139] In a following study, Zhang *et al.*[140] used ultrasmall Au nanoclusters with sizes around 1.5 nm, which were coated with glutathione in order to obtain a biocompatible shell. Again, these were accumulated in cervical carcinoma tumour tissues and showed a strong enhancement of the radiotherapeutic effect. It should be highlighted that the Au NPs could be efficiently cleared off by the kidney after radiation and thus minimising potential side effects.[140]

1.2.1.2 Transport and Delivery

An important aspect of research is the transport and delivery of the nanomaterials to the point of action (**Figure 6**, **top right**). Through accurately engineered functionalisation of the NPs, their affinity to specific biological molecules and units can be increased tremendously and even targeted. Since NPs generally possess a high surface-to-volume ratio, they can be loaded with a large amount of targeted or functional moieties, while the stability may also increase at the same time,[141,142] which is particularly important for Au NPs.[143] The high number of targeting moieties on the surface ensures that their binding increases and that multivalent interactions with cell surface receptors and biomolecules may occur.[144]

Particularly with regard to the transport of drugs, the EPR effect again is significant, since the functionalised NPs have the tendency to accumulate in tumour tissue and thus reach the cancer cells more rapidly and in a targeted manner. Often, a differentiation between passive and active targeting is drawn in the literature, whereby the effect of the former derives mainly from the EPR effect. However, active targeting refers to the functionalisation of NPs with recognition moieties, such as antibodies, genes, or even small bioactive compounds that enhance the accumulation in the desired areas even further.[145]

Another approach is to encage desired drugs in order to transport them through the body. Hydrophobic active substances, which drugs often represent, may be difficult to transport through the body to the point of action. For these, it is possible to store them in the hydrophobic region of a polymer layer coated Au NP (**Figure 7**, **left**), while the hydrophilic part of the polymer layer provides sufficient stability of the NPs in aqueous media and ensures a more "fluid" transport.[146]

Figure 7: Ways of functionalisation: embedding of active substances within the polymer coating (**left**) or attachment of active substances onto the ligand shell (**right**).

In addition to embedding the active substances within the coating, the attachment of these to the capping agents on the ligand periphery is another option (**Figure 7**, **right**). The linker molecules often anchor to the NP surface on one side, while various targeted moieties can be attached to its other side.[4,147]

Furthermore, proteins can be conjugated onto Au NPs (**Figure 6**, **top**).[148,149] It is frequently noted in the literature that non-specific attachments of proteins to (functionalised) Au NPs can

occur in the cells. These proteins may form a corona layer around the Au NPs and thus masking the actual targeted functionality of the NPs.[150,151] On the other hand, an intended functionalisation of Au NPs with proteins can improve their *in vivo* stability and properties.[152] Mocan *et al*.[153] described the vector behaviour of protein functionalised Au NPs, which led to greater accumulation in liver tumour cells than non-functionalised Au NPs. They synthesised Au NPs with a diameter of 40 nm, which were coated with albumin. Since tumour cells have a higher dependence on this protein compared to normal cells, the albumin functionalised Au NPs were injected intraarterially and accumulated particularly in the malignant tissue. Irradiation in form of PTT followed and showed that the cancer could be treated with the aid of Au NP vectors in tumours, which would otherwise only allow for a poor chance of survival for the patients. [153]

Antibodies can also be immobilised on the Au NPs (**Figure 6**, **top**).[64,154–156] Byzova *et al*.[157] were able to show, that antibodies functionalised on Au NPs resulted in an improved antigen binding sensitivity with a higher specificity in the detection of the corresponding antigens.[157] Therein, antibody functionalised Au NPs have been applied in a number of antigen tests, for example pregnancy tests.[158] In these immunoassays, Au NPs have also been used in research for the diagnosis of human immunodeficiency virus (HIV) infections[159] or hepatitis.[160] Mustafaoglu *et al*.[161] were even able to successfully diagnose prostate cancer specific antigens with antibodies bound to Au NPs using dynamic light scattering (DLS). Nagatani *et al*.[162] described already in 2006 one great advantage of this detection method, as the antigen-antibody reactions can be visually observed and assessed using Au NPs on immunochromatographic test strips. A positive detection of the present antigen causes an accumulation of the antibody functionalised Au NPs.[162] This accumulation again can be observed on the lateral flow immunoassay test pad, as it possesses a different wicking velocity in contrast to the non-accumulated Au NPs, which makes it appear as a “positive” test line next to the negative control line.[163]

In addition to the use of antibody functionalised Au NPs in immunoassays, also antigens can be employed *vice versa*. Antigens and antibodies act as counterparts within the body. While antigens are present due to infection with a virus or bacteria, the body tries to fight against these antigens and stop the disease by producing antibodies. Antibodies are formed by white blood cells (lymphocytes) and are therefore detectable in blood. Consequently, the presence of antibodies can also be detected in immunoassays once a disease, such as COVID-19, has been overcome. Antigen functionalised Au NPs were used for this purpose, showing an agglomeration of the Au NPs on the immunoassay test pad, if corresponding antibodies are present in a blood sample.[164]

As a further functionalisation, genes can be applied to the Au NPs surface (**Figure 6**, **upper right**),[165–167] which can then be used in gene therapy for different genetic disorders. Various tests have shown that genes bound to Au NPs, showed stronger gene expression, higher affinity for target DNA and lower cell toxicity compared to free strands of the same sequence.[168,169] In order to attach DNA or genes in general to Au NPs, charge complexation can

be used. In this process, the highly negative gene strands can be assembled onto cationic Au NPs for a gene delivery. However, this may lead to strong interactions, causing a retardation of the loaded gene release at the desired location.[170] To counteract this scenario, a charge reversal co-polymer can be used as a coating, which allows strategic release depending on the pH.[171] Furthermore, a layer-by-layer coating can be applied, in which encapsulation of a special substance class, such as DNA and RNA, occurs, while a protective coating remains on the outside of the nanomaterial ensuring a stable transport.[172] These modifications may lead to enhanced gene delivery.

One example of gene attachment on a NP is described by Shahbazi *et al*.[173] in their work on CRISPR functionalised Au NPs, which showed to be non-toxic carriers of the sequence CRISPR into primary human blood progenitors. Here, they used 19 nm monodisperse spherical Au NPs (**Figure 8 B**, **centre**) and conjugated a PEG linker, which was attached to CRISPR on the surface. In a layer-by-layer coating, further layers were added around (**Figure 8 A**). Moreover, the CRISPR Au NPs (**Figure 8 B**, **right**) mediated gene editing proved to be efficient in different cells and tissues and thus represent a potent potential gene delivery vehicle.[173]

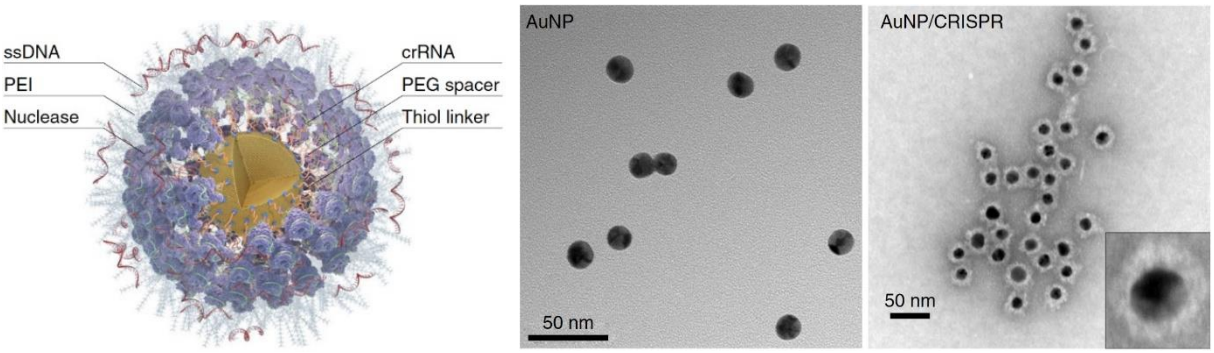

Figure 8: Schematic structure of CRISPR Au NPs (**A**) and TEM images of the unfunctionalised (**B**, **centre**) as well as CRISPR functionalised (**B**, **right**) Au NPs. [173]

RNA functionalised Au NPs are also known and have shown interfering effects on gene expression, which allows for new therapeutic approaches.[166] Lee *et al*.[174] observed a gene silencing effect of Au NPs functionalised with poly-lysine and short interfering RNA. Short interfering is also called silencing RNA as it acts within the cells by suppressing the expression of specific genes. The Au NPs were alternately coated with poly-lysine and RNA using layer-by-layer coating. Then, the RNA could be delivered into cancer cells, where a gradual and slow degradation of the biodegradable lysin coating took place. This in turn led to a slow and sustained release of RNA, which triggered an inhibition effect in the cells and thus had a gene silencing effect within the tumour.[174]

Drugs have been functionalised onto Au NP surfaces in a large variety (**Figure 6**, **right**),[175,176] since the nanomaterial serves as a carrier within the cells.[177] Brown *et al.*[178] describe the complexation of a platinum anticancer agent on the ligand shell of Au NPs, which act as the drug delivery vehicle. The 30 nm sized spherical Au NPs were further coated with PEG and

formed a supramolecular complex with oxaliplatin. The injected Au NPs showed a larger cytotoxicity compared to the free drug. Furthermore, they possessed the ability to penetrate nuclei of lung cancer cells while being also effective against colon carcinoma with possessing an IC_{50} of 0.495 nM and thus being up to 6-fold more effective than the free drug oxaliplatin (IC_{50} of 0.775 µM).[178]

When drugs are transported into cells, a drug release is often necessary, so that the drugs can fully unfold their effect. This release can be stimulated internally by chemical means, for example by molecules, such as glutathione, or by pH; or even externally by physical means, such as light.[179] In the case of the latter, Agasti *et al*.[180] describe a regulated drug release by photocleavage when a Au NP is irradiated with UV light. Their 2 nm sized Au NPs were coated with a polymer shell to which the anticancer agent fluorouracil was attached. Irradiation at 365 nm led to a controlled drug release.[180] In addition to using light as the trigger, internal stimulation *via* intracellular glutathione can also take place, as glutathione is a thiol-containing antioxidant found in almost all cells to protect them from damage. Wang *et al*.[181] report the release of thiolated anticancer drugs like captopril from their PEGylated dendrimer encapsulated Au NPs, triggered by intracellular glutathione. Furthermore, drug release is achievable in a pH sensitive manner, as Kazmi *et al*.[182] describe the release of the anticancer drug doxorubicin from Au NPs (5 nm) at a pH of 4.3. Under normal physiological conditions around pH 7, no release occurred.[182]

Even though the release mechanisms are very important, the cellular uptake of functional Au NPs must not be underestimated. Mosquera *et al*.[183] found a supramolecular strategy of a highly selective and reversible activated cellular uptake of Au NPs triggered by external additives. Their 2 nm sized Au NPs were coated with PEG and functionalised with negatively charged pyranines on the ligand periphery. A selective uptake can be activated *in situ* through the addition of cationic covalent cages, which counterbalance the negative charge of the pyranine dyes (**Figure 9**). This methodology was tested in a variety of different cancer and normal cells and showed promising results even in protein rich media.[183]

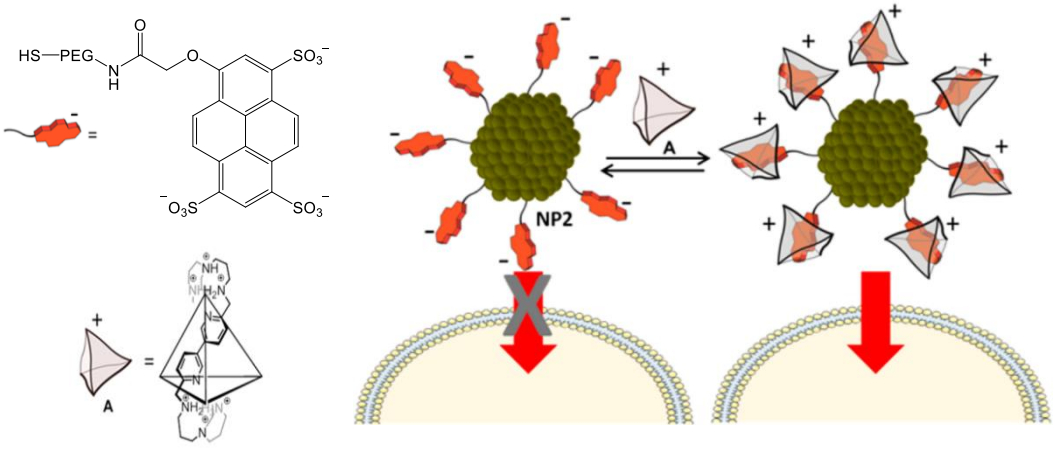

Figure 9: The activated cellular uptake of PEGylated and pyranine functionalised Au NPs.[183]

Apart from drugs, also pharmaceutically inactive compounds can be attached on Au NPs. Zhao *et al.*[184] synthesised Au NPs conjugated with a variety of amino-substituted pyrimidines, which are themselves inactive as antibiotics. The functionalised Au NPs did not exhibit any toxicity against human cells, but showed excellent efficacy as antibacterial agents.[184] Following this approach, a number of studies have shown synergic effects after the attachment of small non-antibiotic molecules to Au NPs. Even though the Au NPs themselves show only low activity, the functionalised Au NPs exhibit extensive antibacterial activity even against multi resistant bacteria.[184,185] If at all, resistance to the multi-resistant bacteria only developed with a significant delay compared to conventional antibiotics.[186] Wang *et al*.[187] describe the synthesis of functionalised Au NPs with *N*-heterocyclic molecules, which again showed efficient antibacterial activity against a broad spectrum of bacteria in their studies. Furthermore, they coated the functionalised Au NPs on the surface of a fabric and observed still an antibacterial effect including against multi resistant bacteria and moreover the prevention of a bacterial biofilm forming.[187]

Likewise, in addition to bio-inactive functionalisation, also bioactive compounds can be attached to the Au NPs (Figure 6, bottom). These substances exert similar or even increased effects in the body once being bound to Au NPs. Gasiorek *et al*.[147] showed that 14 nm sized spherical histamine functionalised Au NPs stimulated histamine receptors already in the subnanomolar range. Furthermore, they observed an enormous potentiation of the receptor activation, which they attributed to the formation of multivalent interactions.[147] These would not occur when histamine was administered as a free monovalent drug.

In the literature, Au NPs are also used to bind toxins such as toxic ions and remove them from the environment (Figure 6, lower right).[188–190] Ojea *et al*.[191] described 9 nm sized Au-Citrate NPs that initiated a reduction of Hg^{2+} ions to amalgam in aqueous solutions contaminated with Hg^{2+} ions. In this way, mercury was successfully removed from the system by precipitation.[191] Chen *et al*.[192] also chose Au-Citrate NPs and effectively detected and removed Hg^{2+} ions. They even established this technique on a membrane filter for an easier application.[192] For other types of NPs, detoxification applications were likewise investigated.[193,194] Pang *et al*.[195] used NPs to treat serious organophosphate poisoning. They used biomimetic polymeric NPs conjugated with acetylcholinesterase. The toxin would usually block this enzyme and irreversibly inactivate it, leading to death. Whereas here, the toxin binds preferentially to the functionalised NPs and improves the chances of survival.[195]

1.2.1.3 Imaging and Diagnostics

Furthermore, Au NPs can be used in imaging and diagnostics (Figure 6, bottom). Some of these applications have already been addressed in the subchapters above, but a variety will be highlighted and described here. Au NPs have often been studied as X-ray contrast agents due to their high X-ray absorption and scattering properties.[196–198] With these characteristics, they represent tuneable alternatives to other used contrast agents for CT such as $BaSO_4$ or iodine.[199]

However, since CT imaging has a lower sensitivity in soft tissues, combinatorial systems can be used, that provide further tools such as photoacoustic or fluorescence imaging, which can be done by attaching fluorescent dyes to the Au NPs (Figure 6, bottom). Nonetheless, if organic fluorophores are located close to an Au NP core, fluorescence quenching will occur. There is an energy transfer from the donor (fluorophore) to the acceptor (Au NP) and this results in a lower fluorescence intensity. However, Sanchez *et al*.[200] were able to successfully synthesise fluorescent 2 nm sized polyaminocarboxylate coated Au NPs, which where functionalised with an NIR organic dye. After intravenous application, they were able to monitor the Au NPs and localise them precisely in the tissue despite quenching effects. Furthermore, they observed their accumulation in tumours.[200]

Zhang *et al*.[201] chose a different path by using dual modal fluorescence/CT imaging and completely prevented the quenching effect by storing Au NPs and organic dyes into larger PEG micelles. In this one pot ultrasonic emulsification preparation, they successfully obtained 120 nm sized micelles, which showed excellent fluorescent and CT imaging effects. As non-invasive *in vivo* agents, the functionalised micelles showed good tumour targeting ability.[201] Jing *et al*.[202] addressed a similar goal in their work. However, they used a simultaneous combination of photoacoustic/CT imaging. Again, the aim was to achieve a better soft tissue contrast[203] in order to target cancer cells. Jing *et al*.[202] used Prussian Blue coated Au NPs with a size of 17 nm in their work. Prussian Blue acts as a photoabsorbing agent for photoacoustic imaging but also for photothermal therapy. In photoacoustic imaging, light energy is absorbed and subsequently a photoacoustic signal is emitted. These signals are detected in order to obtain an image of the optical absorption properties of the internal tissue structure.[204,205] After intravenous application of Prussian Blue coated Au NPs, simultaneous photoacoustic /CT imaging was performed and showed a very promising soft tissue contrast. These findings were directly used to perform a precise irradiation for photothermal therapy. The tumours of the human colon cancer cell line were successfully ablated after one irradiation and no new tumour growth was observed.[202] The last example in particular shows very impressively how imaging and diagnostics also go hand in hand with therapy and how all the different aspects are combined within this piece of research.

Furthermore, Au NPs serve as a platform in radiochemistry or in nuclear medicine to enable imaging or diagnostics (Figure 6, bottom). Biodistribution and pharmacokinetics are investigated using typical setups in radiology such as single photon emission computed tomography (SPECT) or positron emission tomography (PET). Again, also combinations of these methods with CT or fluorescence imaging are used. In general, even subnanomolar dosages of the radiopharmaceuticals retain enough radioactivity to be sufficiently used for diagnostics. These include *γ* emitters, which are detected *via* special *γ*-cameras with high sensitivity. There exist different procedures for applying radionuclides to Au NPs, e.g. radiohalogens can adsorb directly onto the surface of the Au NP.[206] Another possibility offers the incorporation of radionuclides, such as ^{64}Cu, into the Au NP core in order to obtain ^{64}Cu:Au NPs.[207–209]

Thereby, it is possible to directly incorporate radionuclides of Au, such as ^{198}Au or ^{199}Au.[210–212] In addition, functionalisation of radionuclides *via* conjugation at the ligand is also a commonly used method.[213–215] Pretze *et al*.[216] describe the multifunctionalisation of 3 nm sized Au NPs on the one hand with a chelating ligand for complexing the radionuclide and on the other hand with another type of ligand carrying prostate tumour targeting peptides next to further PEG stabilisation chains. Directly after radiolabelling, the functionalised Au NPs were administered intravenously and analysed using NIR fluorescence imaging and PET. Pretze *et al*.[216] observed a higher tumour uptake of the Au NPs functionalised with the tumour targeting peptides in contrast to the ones only functionalised with the radionuclide chelating ligand. Furthermore, the targeted Au NPs remained inside the tumour with over 85% of the total dosage after 4 h, which enable the precise localisation of the prostate tumour.[216]

Depending on the radionuclide, different therapeutic treatments are possible. While ^{68}Ga is suitable for diagnostics, ^{177}Lu can be used for the corresponding therapy since both radionuclides can be complexed by similar chelating ligands.[217,218] For therapy with radionuclides, α- or β- emitters are used, such as ^{198}Au, ^{131}I, ^{90}Y, ^{188}Re. Al-Yasiri *et al*.[210] describe the synthesis of radioactive Au NPs that are already doped with ^{198}Au in their core. Right in the synthesis, they add mangiferin to the radioactive gold precursor, which serves as a reducing agent, as well as stabilising the ligand. Mangiferin itself has been shown as a glucose containing phytochemical, which is found in mango peels and thus supports the authors' "green chemistry" approach. They investigated the mangiferin functionalised Au NPs as a potential anticancer agent. Due to the high tumour metabolism, there is a higher demand for glucose within tumour cells. The researchers exploited this property in order to obtain an accumulation of glucose in the tumour cells. Here, the radioactive 35 nm sized Au NPs were applied intravenously and a retention of more than 80% of the total injected dosage was found in the prostate tumours after 24 h. Furthermore, a 5-fold reduction of the tumours was observed after 3 weeks, thus indicating that these radioactive Au NPs functionalised with mangiferin may be a potential anticancer agent with regard to prostate tumours. However, no additional analysis of the functionalised Au NPs were performed with regard to their organic framework. Thus, there is no clear evidence whether intact mangiferin is still present on the surface of the Au NPs and whether or not these may have caused or influenced the effects.[210]

All these aspects only show a small part of the actual as well as the potential application of Au NPs in biomedical research. Even though this overview of applications and functionalisations represented and discussed these within the subheadings transport & delivery, imaging & diagnostics and therapy, the crossovers and connections between these are constantly present. This complexity serves as Au NPs main advantage and leads directly into the field of "multivalency", discussed in the next chapter.

1.2.2 MULTIVALENCY

Multivalent interactions have been a recognised phenomenon in various biological systems.[219–223] There are monovalent interactions, where a monovalent ligand engages in only one ligand-receptor complex at a time (**Figure 10**, **left**). In contrast, when multiple simultaneous recognition events occur at similar receptors on the surface of a cell, they are referred to as multivalent receptor activations (**Figure 10**, **right**).[224] Inspired by nature, it has been recognised that multivalent interactions lead to higher selectivity and furthermore, ultra-sensitivity, and thus they rapidly gained interest in medical science such as drug delivery research. Complexes triggering multivalent interactions have been studied on different cell and tissue types.[147,225–227]

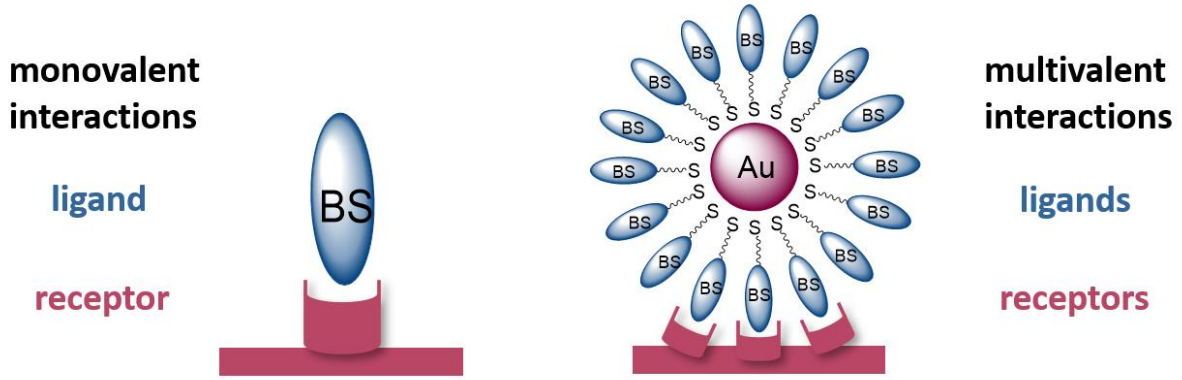

Figure 10: Monovalent (**left**) in contrast to multivalent (**right**) interactions at the ligand-receptor level.

Kiessling *et al*.[228] reported different binding modes of multivalent ligands at the receptors. Different model assumptions exist in the literature; today, some researchers assume an exactly uniform distribution of receptors on the membrane, however, earlier publications describe receptor clustering as the main model.[222,229] Nonetheless, there has been a consensus in the literature that, with regard to drug delivery, receptors in general occur in excess. Moreover, multivalent systems have been promising candidates for the use as high affinity drugs, but each one requires distinctive studies on a balanced core size, a flexible ligand system with tuneable linker lengths and furthermore an accurate comparison to monovalent ligand affinities.[230] Since different entering mechanisms and behaviours depending on the loading were observed, precise investigations on cellular uptake are essential. This is why Moradi *et al*.[231] investigated the internalisation of folate stabilised NPs with different ligand densities on the surface. They prepared folate stabilised polymer NPs with a hydrodynamic radius of around 60 nm and showed their behaviour on bronchial epithelial cells in *in vitro* models. They observed a higher cellular uptake with higher folate loading, but only up to a saturation level.[231] This was also shown by other studies, where the effects caused by multivalent interactions increased only up to a saturation plateau.[232,233]

Another important aspect in medical research concerns the fact that the effect of a substance can be dependent on whether it is presented monovalently or multivalently (**Figure 10**). This

was demonstrated by Wang *et al*.[234] in their studies on either transferrin or transferrin receptor antibodies functionalised NP. They observed a highly specific transferrin receptor mediated uptake by several human tumour cell lines. Furthermore, they were able to show that the individual ligands presented monovalently had no or only little toxicity. However, the functionalised NPs exhibited a high toxicity, selective towards the Ramos lymphoma cell line, which is important in malignant lymphoma tumours. Again, they observed a strong correlation between ligand density on the NP surface and cellular uptake, which can be influenced and adjusted by the amount of ligands present on the NP shell. Moreover, by conjugating the non-toxic transferrin or transferrin receptor antibodies onto NPs, targeted drug delivery or even cancer therapy can be achieved, which is expected to show low immune responses, as transferrin itself is an endogenous protein and one of the most abundant in human blood.[235]

In addition to cancer therapy, multivalency contributes to the development of HIV-1 infection therapies. Again, researchers have been able to design highly active drugs from ligands, which were inactive when used monovalently, and which have become active when used multivalently in the form of functionalised NPs. Bowman *et al*.[236] suggested that NPs, as carriers, often possess similar sizes to proteins. Thus, they theorised that the sufficiently modified NPs could possibly effectively disrupt protein-protein interactions, which would ordinarily promote diseases. This interference caused by the NPs could then achieve a therapeutic effect. For their studies, Bowman *et al*.[236] chose 2 nm sized Au NPs with a proposed empirical formula $Au_{144}(4\text{-MBA})_{52}$, which, like proteins, are monodisperse and atomically precise. These were functionalised with modified co-receptors, which were originally responsible for the transmission of HIV-1 strains within the cells. Bowman *et al*.[236] were able to show that the functionalised Au NPs served as effective inhibitors of HIV fusion and thus can have a therapeutic benefit as multivalent administered drugs. In addition, Bastian *et al*.[237] postulated in their studies of functionalised Au NPs on HI viruses a potential mechanism of the inactivation of the virus. They used slightly larger Au NPs in the range of 13 nm to 93 nm, which were also functionalised with a peptide based triazole derivative. In their studies, these NPs ensure an antiviral effect through the multivalent attachment to the virus' envelope spikes. Bastian *et al*.[237] suggest that these multivalent spike connections trigger a metastability of the virus envelope, which in turn irreversibly inactivated HIV-1 and thus leads to a collapse of the virus, before the host cell is attacked and damaged. Bastian *et al*.[237] even assume that this theory can be generalised, which could be of importance for other viral diseases as well.

1.2.3 Gold Nanoparticles in Bronchial Tissue or in the Gastrointestinal Tract

In the following, the application of drugs and NP based drugs will be highlighted for two different systems, which are relevant to this thesis. One system is the lung epithelial system with regard to potential asthma or chronic obstructive pulmonary disorder (COPD) research. Colonic epithelial tissues are included in the other system with different biomedical approaches.

The influence and effect of NPs – or drugs in general – on the G protein coupled receptors present in tissues is the key focus of this research. G protein coupled receptors represent one of the largest super family of cell surface receptors in mammalian cells.[238] A large variety of drugs target receptors of this family and cause cellular responses, which are of high interest in general biomedical research.[239] Furthermore, these mediated signalling processes are particularly attractive for therapeutic applications.[240] COPD and asthma present common diseases worldwide, especially asthma being one of the most prevalent chronic diseases.[241] Currently, anti-inflammatory agents and bronchodilators serve as therapeutic treatments.[242] However, it is believed that up to 50% of patients are not able to control their symptoms well with these drugs.[242] Further development of potential treatments with less side effects remains an important part of current research.[243,244] β agonists are frequently used in the treatment of asthma and COPD, activating β_2-adrenoreceptors, which are distributed throughout the respiratory tract, and providing a bronchodilator effect on the smooth muscles. Back in 1969, salbutamol was described as an agent selectively acting on bronchial muscles;[245] it is still widely used today as a common short-term acting β agonist in therapy.[246] Furthermore, it is unambiguously quite similar in its chemical structure to the neurotransmitters adrenaline or noradrenaline, which are already present in mammalian cells. Various nanomaterials have already been investigated for the treatment of asthma, often showing anti-inflammatory effects and no hyperresponsiveness.[247–249] A limited number of studies have been performed using Au NPs, mainly with Au-Citrate NPs, which also served as starting NPs in this thesis. Omlor *et al*.[250] described the behaviour of intranasally administered Au-Citrate or Au-PEG NPs, each with a size of 5 nm, and indeed observed that a greater uptake of the NPs occurred when the animals were sensitised with ovalbumin to cause airway hypersensitivity (equals asthma-like symptoms). In addition, Omlor *et al*.[250] were able to determine a high anti-inflammatory effect and the inhibition of airway hyperreactivity, especially for Au-Citrate NPs. Barreto *et al*.[251] only used unfunctionalised 6 nm sized Au-Citrate NPs, which were administered intranasally and minimised asthma symptoms in their studies. The researchers even distinguished between allergy-induced asthma and genetically caused asthma. Au-Citrate NPs demonstrated anti-inflammatory effects and a reduction in airway hyperreactivity. In fact, in the case of allergy-induced asthma, at least 70% of the allergen-induced features were inhibited.[251]

Au NPs do not only play a role in medical applications in the lungs. If pharmaceutically relevant substances are orally administered, they will often be absorbed by the intestinal epithelial membrane. Therefore, it is also important to investigate the effects of Au NPs on intestinal epithelial cells. Regarding to the uptake of Au NPs, Smith *et al*.[252] investigated 2 nm sized Au NPs with different stabilising ligands, and measured their absorption in the gastrointestinal tract after oral administration. 4-mercaptobenzoic acid (4-MBA), glutathione and various PEG chains were used as ligands, but only a significant absorption and thus a bioavailability of the Au NPs could be measured for Au NPs with the short chain PEG-4 ligand. These Au NPs were found in the blood even after 24 h and thus passed the epithelial barrier successfully.[252] Yao *et al*.[253] investigated Au-Citrate NPs and the influence of their size on the transport across the epithelial membrane from the apical side towards the lumen into the basolateral side towards the blood.

They analysed 100 nm, 50 nm and 15 nm sized Au-Citrate NPs and found that the smaller the NPs, the faster the migration. In case of the 100 nm sized Au-Citrate NPs, not only a slower excretion on the basolateral side was observed, but an increasing accumulation appeared, which in turn led to cytotoxicity. Again, the smaller the NP size, the lower the tendency to accumulate. 50 nm sized Au-Citrate NPs were successfully transported across the barrier and also excreted on the basolateral side. Au-Citrate NPs with a size of 15 nm migrated the fastest, but these were also, at least in part, internalised into the cells more quickly.[253]

Au NPs can also have therapeutic effects in the gastrointestinal tract. Li *et al*.[254] used 4,6-diamino-2-pyrimidinethiol coated Au NPs with a size of 16 nm, which were investigated for the treatment of bacterial infections in the gut. Conventional antibiotics occasionally cause an imbalance of the intestinal microflora, which can result in symptoms similar to those of chronic metabolic diseases. The new type of nano-antibiotics showed an antibacterial effect after oral administration, but without damaging the intestinal microflora. Long term studies of 28 days administration revealed no toxicity to other organs such as the kidneys or the liver, but showed that the richness of the microflora remained intact.[254] Thus, functionalised Au NPs are promising alternatives to conventional antibiotics, which do not lead to an imbalance of the intestinal microflora.

As a potential major complication in the gastrointestinal tract, an imbalance of electrolytes after a major surgery can lead to postoperative ileus.[255] This temporary standstill of the regulated intestinal peristalsis occurs after 17.4% of colorectal operations[256] and is associated with longer hospital stays and thus higher additional costs. It also leads to symptoms such as abdominal pain and vomiting.[256] A crucial step in treatment of ileus is to stimulate and reactivate the gastrointestinal functions.[256] Some of the literature recommends to chew chewing gum in order to stimulate the motility of the intestines,[257–259] but the effect of this on ileus is highly questioned.[257,260] Nevertheless, it is useful to investigate a potential change of the neurotransmitter receptor activation,[255] and thereby causes a reactivation of the gastro-intestinal function.[261] For example, Diener *et al*.[261] describe the effects of histamine as a mediator stimulating histamine H_1 and H_2 receptors. This stress-induced activity can be useful to remove potential antigens from the lumen.[261] When the receptors are activated, ion transport occurs as a physiological process and the induced chloride secretion across the colon epithelium can be measured. To balance the charge, sodium ions are transported to the lumen together with H_2O,[262] whereby a higher flow rate is achieved towards the lumen, which in turn can benefit the motility of the gastrointestinal tract. Saada *et al*.[263] describe the enhancement of activation using histamine functionalised on Au NPs, which was higher compared to the reaction of free ligands. Gasiorek *et al*.[147] also used histamine functionalised Au NPs and showed that they act as regulators of physiological processes. A 10^6-fold potentiation of receptor activation was observed, which they attributed to multivalent interactions. Thus, functionalised Au NPs are also suitable for potentiated activation of receptors in the gastrointestinal tract.

1.2.4 BIODISTRIBUTION

With a variety of biomedical applications, one question usually emerges almost all the time: What happens to the Au NPs within the body?

Various studies already focused on different Au NPs and their behaviour in mammalian tissue. Parveen *et al*.[264] described Au NPs, which were synthesised using a clove bud aqueous extract and $HAuCl_4 \times 3\ H_2O$. Their spherical non-monodisperse NPs range in sizes between 5 nm to 100 nm and showed no toxicity nor harmful effects on the investigated organs after intravenous administration of daily doses up to 500 µg/kg bwt/day for 28 days.[264] However, the validity of this study is debated by the author of this thesis, since the enormous discrepancy in NP size of almost 100 nm represents a rather unspecific experimental set-up. In addition, the surface of the Au NPs synthesised in this way was not examined more closely, and as we and others have shown, this precisely affects the behaviour and potential effects of materials within a body immensely.[265–268] Bailly *et al*.[269] investigated in 2019 the biodistribution of laser synthesised dextran coated Au NPs with an average size of 21 nm. These were administered intravenously at a dose of 1 mg/kg and were rapidly eliminated from the blood stream. However, the dextran Au NPs mostly accumulated in the liver (Kupffer cells) and in the spleen (macrophages), though no hepatic or renal toxicity nor a histological damage or inflammation in tissues was observed.[269] Several studies showed that inorganic NPs often accumulate in these two organs when administered intravenously.[270–273] A closer look into the biodistribution of inhaled Au NPs took Durantie *et al*.[274] They investigated the behaviour of 14.5 nm 2-mercaptopropionylglycine stabilised and with a polymer mixture of polyvinyl alcohol and polyallyl amine coated Au NPs at the lung epithelial tissue barrier and found that the majority of Au NPs were taken up inside the cells and remained there, while less than 5% translocated to the basolateral side. They compared single NPs to distinct Au NPs aggregates with an average of 4 single NPs clustered per aggregate and gained similar translocation results for both, but observed that the aggregated Au NPs showed a significantly faster cellular uptake than the single Au NPs.[274] The influence of different NP sizes between 2 and 80 nm was investigated in more detail by Bachler *et al*.[275] Here, they used a variety of monodisperse sizes of Au-Citrate NPs. Bachler *et al.* examined the Au-Citrate NPs for their translocational behaviour across lung tissues particularly on human and mouse alveolar epithelial cellular monolayers. In their studies, they observed that translocation is inversely proportional to the NP size but independent of the dose (up to 100 ng/cm²). Ultrasmall Au NPs could easily cross these epithelial monolayers. For NPs smaller than the capillary pores of the kidney, excretion even occurred *via* the urine. Bachler's approach furthermore was to combine *in vitro* and *in silico* methods to reduce or even replace short term animal *in vivo* experiments, as they obtained similar results in all settings.[275]

1.2.4.1 Functionalisation with Fluorescent Dyes and Radiolabelling with Radionuclides

Biodistribution on a microscopic level can also be investigated with fluorescent imaging. For this purpose, Au NPs can be modified and functionalised with fluorescent dyes. Even though a quenching effect of the fluorescence occurs, if the dye molecules are present in the vicinity of the Au NPs, tracking remains viable with lower fluorescence intensity, since a higher number of fluorescent molecules are present.[276,277]Lee *et al*.[277] use BODIPY functionalised Au NPs as fluorochromogenic sensors for Cu^{2+} ions. BODIPY itself represents a well-known versatile fluorophore with a wide range of potential applications and was first described by Treibs and Kreuzer in 1968.[278] Lee *et al.*[277] employed spherical Au NPs with a size of 10 nm and functionalised them with lipoic acid to the BODIPY derivative. The functionalised Au NPs showed an emission λ_{max} at 704 nm (λ_{Ex} = 598 nm) in fluorescence measurements, which was gradually quenched, whenever the Cu^{2+} concentration was increased. The quenching effect was reversible: As soon as EDTA solution was added to the system and the Cu^{2+} was preferentially complexed by EDTA, the fluorescence intensity increased again. Sanchez *et al*.[200] even intend to potentially use functionalised 5 nm sized Au NPs for imaging guided radiotherapy by performing *in vivo* fluorescence imaging. They synthesised Au NPs with a polyaminocarboxylate shell. A derivative of these functionalised Au NPs (Au-DTDTPA) is commonly used in magnetic resonance imaging (MRI) or nuclear imaging, when complexed or labelled with Gd or ^{99m}Tc,[279–281] and showed that they are temporarily retained in solid brain tumours.[282] Sanchez *et al*.[200] have additionally functionalised the Au NPs with an organic dye derivative of cyanine 5 and observed an internalisation of the Au NPs in fluorescence imaging studies on cells. In addition, they demonstrated in *in vivo* fluorescence imaging a preferential accumulation of the Au NPs in breast cancer tumour tissues as well as in the kidneys and investigated their biodistribution within the whole body. Although a quenching effect occurs with fluorophore functionalised Au NPs, previous studies indicate their potential application as agents for the study of their biodistribution at the microscopic level as well as through the body.

Another possibility of investigating the biodistribution is diagnostic imaging with radiotracers. One of the most commonly used radionuclides in nuclear medicine is ^{99m}Tc. It possesses a half-life of 6 h and emits an easily detectable *γ* radiation of 140 keV. These excellent properties together with a relatively low price and good availability due to its easy production as a pertechnetate ($^{99m}TcO_4^-$) eluate from commercial generators, make it an ideal radionuclide for diagnostics.[283] Radiolabelled NPs are currently used for the imaging of cardiovascular diseases and also cancer diagnosis.[284–287] The concept of radiolabelled Au NPs acting as imaging agents has been validated by Alric *et al*.,[281] when they injected functionalised radiolabelled Au NPs into healthy animals and proved their renal excretion. They used 3 nm sized Au NPs functionalised with the previously described polyaminocarboxylate shell (Au-DTDTPA). These showed a longer retention time in brain or breast cancer tumour tissues in former studies.[200,282] Here, Alric *et al*.[281] obtained a greater sensitivity with nuclear imaging and they showed that shortly after the intravenous injection of the radiolabelled Au NPs, radioactivity was detected in the heart, kidneys, liver and bladder. However, 30 min after the administration, the radioactive NPs only remained in the kidney and the bladder, which indicates that the radioactive Au NPs are

mainly removed by renal excretion.[281] Moreover, during the whole imaging process, no radioactivity was detected in the thyroid, glands and stomach. These would be targeted by free pertechnetate, which would occur, if $^{99m}TcO_4^-$ as the starting material remained in the injection or if the DTDTPA as a chelate would have released the ^{99m}Tc from the complex under physiological conditions. Since this is not the case, Au-DTDTPA-^{99m}Tc NPs appear to form stable complexes even under physiological conditions. In the literature, different Tc chelators are described.[286,288] Felber *et al*.[289] focused in their studies on the synthesis of different linker-chelator ligands for Fe_3O_4-Au core-shell NPs and investigated the most suitable one for the ^{99m}Tc labelling. In a further study,[66] they used the most suitable chelating moiety 2,3-diaminopropionic acid (DAP). This ligand was used to either chelate the ^{99m}Tc after radiolabelling or to conjugate to a biomolecule, such as the prostate-specific membrane antigen (PSMA). With this, multifunctional radiolabelled Au NPs could be synthesised containing both a radioisotope as well as the targeting molecule PSMA with relevance to prostate cancer on the ligand surface. *In vivo* microSPECT imaging and *ex vivo* biodistribution studies showed a fast clearance from the blood but also low tumour uptake.[66]

Even though a higher intracellular uptake of the radiolabelled NPs into tumour tissues could not be confirmed in this particular study, the concept shows that it may be fruitful to continue investigating radiolabelled multifunctional NPs.

2 AIM OF THE THESIS

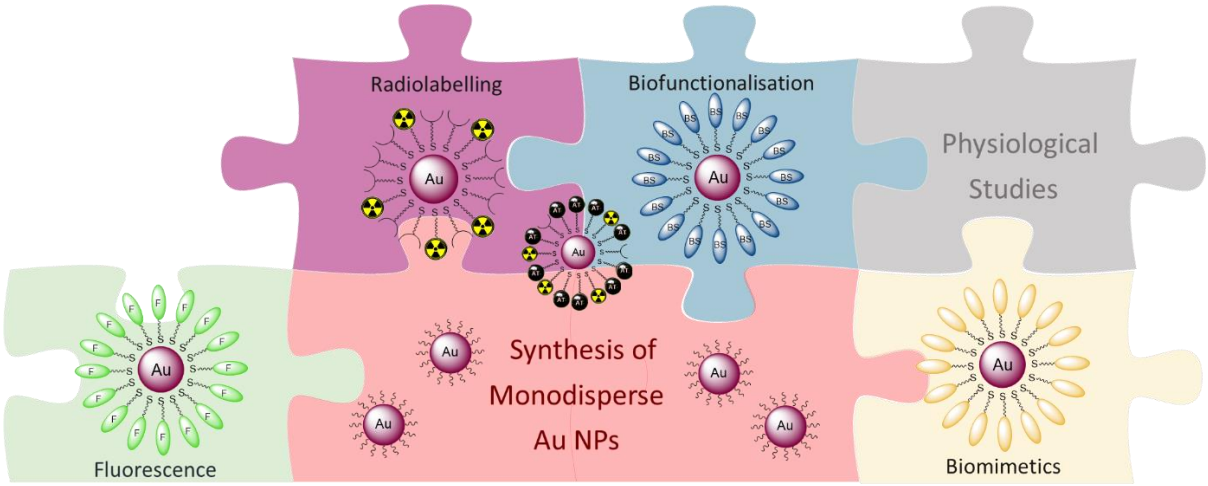

Figure 11: Building blocks of this thesis.

As a fundamental component for further functionalisation, **Chapter 3.1** discusses the synthesis of monodisperse Au NPs with a narrow size distribution. The focus of this work is placed on spherical Au NPs in the size range between 5 nm to 30 nm, which serve as starting particles for various functionalisation approaches. A wide range of biofunctionalisations will be explored in the context of **Chapter 3.2** *via* various synthetic routes. In particular, the attachment of catecholamines onto the Au NP surface is discussed as well as a potential functionalisation with the drug salbutamol. Finally, these functionalised Au NPs are investigated by our collaboration partners in physiological studies on their receptor activation in different biological systems, in particular the tracheal tract and the gastrointestinal tract. For the latter, further biologically active molecules are immobilised on the Au NPs' surface such as the physiologically important muscarinic receptor antagonists carbachol and atropine. **Chapter 3.3** describes another synthetic strategy to mimic a biogenic substance. Here, not the biologically active molecule itself is attached on to the Au NPs, but dihydrocaffeic acid (DHCA), a molecule that is similar to the biologically active compounds dopamine or noradrenaline. DHCA functionalised Au NPs thus may potentially be able to cause similar receptor effects in physiological studies.

In addition to biologically active Au NPs, **Chapter 3.4** focuses on a specific functionalisation with fluorescent dyes. These Au NPs may be of interest for microscopic investigations or relevant as a diagnostic tool using optical spectroscopy. Furthermore, **Chapter 3.5** discusses in detail how Au NPs are labelled with the radionuclide ^{99m}Tc in order to perform biodistribution studies on a macroscopic level. For this purpose, a suitable ligand design is required to guarantee the attachment onto the Au NPs on one hand and a strong complexation of the radionuclide on the other hand.

3 Results and Discussion

3.1 Nanoparticle Syntheses

NPs synthesised during this work were prepared with the intention of applying them as carriers for biologically active molecules and to investigate their behaviour of activating the respective receptors in animal tissue. Thus, it was essential to obtain monodisperse NPs with a narrow size distribution. All NPs were synthesised in wet chemical approaches using the *bottom up* method and could be made in various sizes and from different starting materials.

3.1.1 Syntheses of Monodisperse Gold Nanoparticles

The focus of this work is placed on spherical Au NPs in the size range of 5 nm and 30 nm. Different synthetic procedures were investigated, of which two methods in particular showed excellent results as a very good size control of the NPs could be achieved. The NPs from these approaches fulfilled the requirements and were biofunctionalised in further steps. Performing the *Turkevich* citrate reduction method according to a size selective procedure by Frens *et al.*[290] led to good reproducible results in aqueous media. Furthermore, carrying out a modified method based on Stucky and coworkers[291] performed in DMSO yielded monodisperse NPs with an extremely precise size control. Moreover, biocompatibility could be provided with the selection of H_2O or DMSO as the solvents used during these syntheses.

Syntheses using the citrate reduction

To perform the citrate reduction, shown in **Scheme 1**, tetrachloroauric acid trihydrate was dissolved in demineralised H_2O and heated to reflux. Sodium citrate dihydrate was added quickly under vigorous stirring and was heated to 80 °C for 2 h.

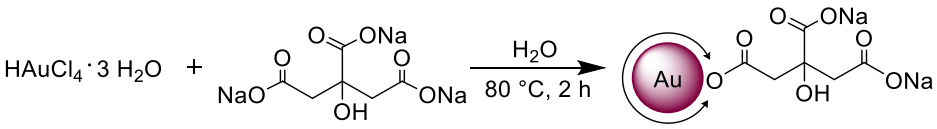

Scheme 1: Synthesis of Au-Citrate NPs in H_2O according to Frens *et al.*[290]

A change in colour from yellowish over blue to an intense red indicated the formation of NPs within a few minutes. After 120 min, the dispersion was cooled in an ice bath to stop the progressing reaction and thus prevent a further growth of the NPs.

All NP dispersions were characterised with TEM, DLS and UV/Vis spectroscopy to investigate the morphology and homogeneity of the Au NP core. Additionally, NMR and IR spectroscopy were performed to determine the structure of the organic ligands on the NP surface. Different approaches were performed in which the ratio of tetrachloroauric acid and citrate were varied.

TEM images of the different Au-Citrate NP approaches are displayed in **Figure 12** and show that the synthesised NPs have a spherical shape and are monodisperse. No agglomeration of the NPs was observed. On the contrary, some NPs have even arranged themselves hexagonally presumably during the drying of the TEM grid (**Figure 12**, **centre**). This again indicates an extreme narrow size distribution of the synthesised NPs.

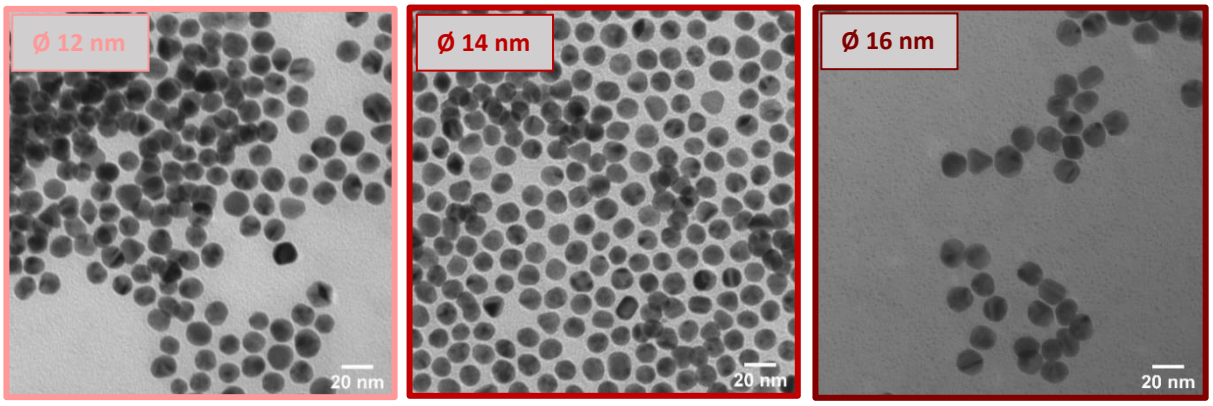

Figure 12: TEM images of Au-Citrate NPs, synthesised in H_2O with an average diameter of 12 nm (**left**), 14 nm (**centre**) and 16 nm (**right**) (according to Frens *et al.*[290]).

In this synthesis, $HAuCl_4 \cdot 3\ H_2O$ as a gold precursor was reacted with sodium citrate dihydrate operating as both a mild reducing agent and the stabilising ligand, simultaneously. Key figures of the performed Au-Citrate NPs approaches are listed in **Table 2**, indicating the following trend: The higher the percentage of citrate in the solution compared to tetrachloroauric acid, the smaller the obtained NP diameter. This can be explained with a larger amount of reducing agent present at the nucleation state. Moreover, more potential ligands available can saturate a larger overall surface. Or to put it in another way: a smaller ratio of $HAuCl_4$ and citrate leads to larger NP due to the fact that fewer ligand molecules are available to stabilise the NP surface. With a larger individual NP diameter, there exists a smaller overall surface related to the entire system, making it energetically more favourable.

Table 2: Au-Citrate NP approaches with different ratios resulting in different diameters, absorption maxima and concentrations.

sample	ratio of $HAuCl_4$: citrate	d_{TEM}	λ_{max} (UV/Vis)	concentration
Ø 11 nm	1 : 15	11.2 ± 0.9 nm	523 nm	14.6 nmol/l
Ø 12 nm	1 : 10	12.2 ± 1.2 nm	523 nm	11.9 nmol/l
Ø 13 nm	1 : 6.7	12.9 ± 1.3 nm	522 nm	9.7 nmol/l
Ø 14 nm	1 : 5.8	13.8 ± 1.2 nm	521 nm	7.8 nmol/l
Ø 16 nm	1 : 4.0	15.9 ± 1.1 nm	521 nm	5.1 nmol/l

Another trend can be observed: The concentration of the NP dispersion increases as the diameter gets smaller. This is a logical consequence, since the same amount of precursor is now distributed over a larger number of smaller NPs.

This consideration is based on the assumption that the precursor is completely reduced to NPs. This is supported by TEM images showing only monodisperse NPs and no remaining gold seeds. Uniform and homogenous growth leads to the formation of NPs with a narrow size distribution.

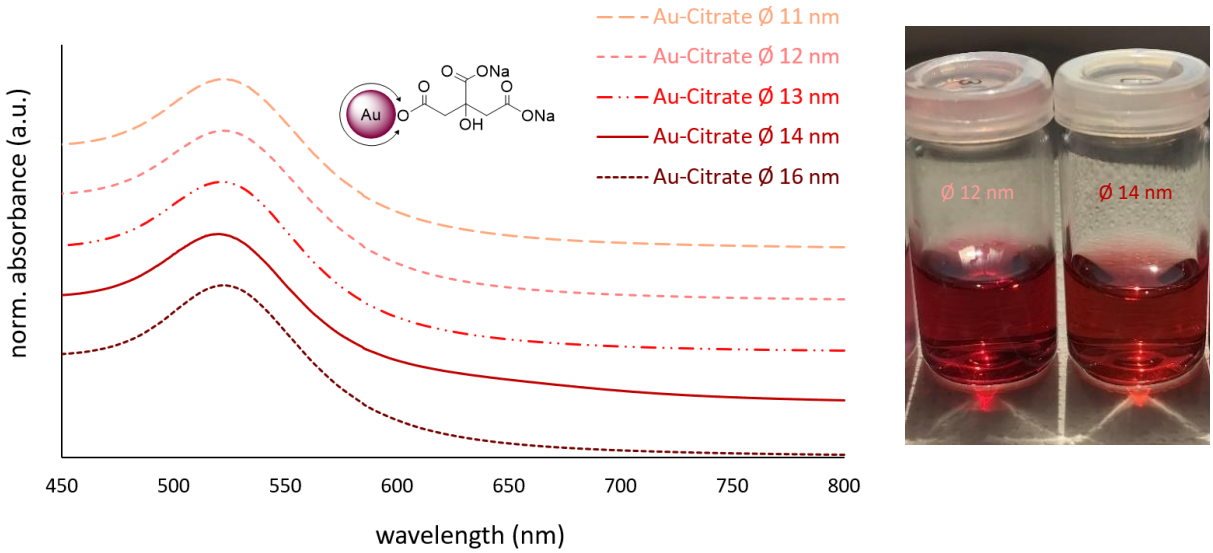

Figure 13: UV/Vis spectra of Au-Citrate NPs (**left**) and wine red stable Au-Citrate NP dispersions (**right**).

Since Au NPs have a distinctive plasmon resonance, they can be further characterised by UV/Vis spectroscopy. The measured UV/Vis spectra of the Au-Citrate NPs, displayed in **Figure 13** (**left**), revealed their positions of the absorption maximum (λ_{max}) being in a similar range: λ_{max} of Au-Citrate NPs are 523 nm (Ø 11 nm), 522 nm (Ø 13 nm) or 521 nm (Ø 16 nm), respectively. **Figure 13**, **right** shows a picture of the bright coloured Au-Citrate NP samples.

The maximum concentration of NPs that is achievable by this method is limited to approx. 20 nM, since citrate has only a relatively weak stabilising character. Thus, higher concentrated NP dispersions cannot be prevented from agglomerating during and also after the synthesis. Citrate ligands only stabilise the Au NPs electrostatically and thus only weak interactions between ligands and particle surface occur. However, this allows them to function as excellent starting particles for ligand exchange reactions.

Moreover, since citrate has only a weak reducing character, the obtained NPs possess relatively large diameters. Au-Citrate NP sizes smaller than 10 nm synthesised according to the *Turkevich* citrate reduction method are rarely known in literature.[292]

However, when applying a lower equivalent of citrate molecules, even larger Au-Citrate NPs were synthesised. Here, a slightly different procedure was chosen, with the Au NPs being reacted at reflux but only in the shorter reaction time of 30 min, as displayed in **Scheme 2**.

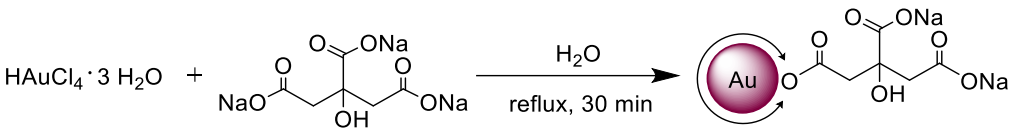

Scheme 2: Synthesis of Au-Citrate NPs in H_2O according to Panigrahi *et al*.[293]

Stable Au-Citrate NPs were obtained in both approaches, listed in **Table 3**. Furthermore, these NPs possessed wine red intense colours and owned a distinct λ_{max} around 530 nm.

Table 3: Properties of Au-Citrate NPs synthesised according to Panigrahi *et al*.

size	ratio of $HAuCl_4$: citrate	d_{TEM}	λ_{max} (UV/Vis)	concentration
Ø 25	1 : 2.2	24.9 ± 1.2 nm	528 nm	0.5 nmol/l
Ø 28	1 : 1.7	28.1 ± 2.4 nm	532 nm	0.4 nmol/l

The corresponding TEM images (**Figure 14**) reveal that monodisperse and mainly spherical Au-Citrate NPs have formed. Using a $HAuCl_4 \cdot 3\ H_2O$: sodium citrate × 2 H_2O ratio of 1.0 : 2.1, the Au-Citrate NPs have an average size of d_{TEM} = 24.9 ± 1.2 nm (**Figure 14**, **left**). If less stabilising and reducing agent is used, the diameter increases again, such as in the approach with a ratio of 1.0 : 2.1, where an average size of d_{TEM} = 28.1 ± 2.4 nm was obtained (**Figure 14**, **right**). Even though also larger stable Au-Citrate NPs were obtained, the ones with sizes over 20 nm were not used for further functionalisations, as they did not possess a highly spherical shape.

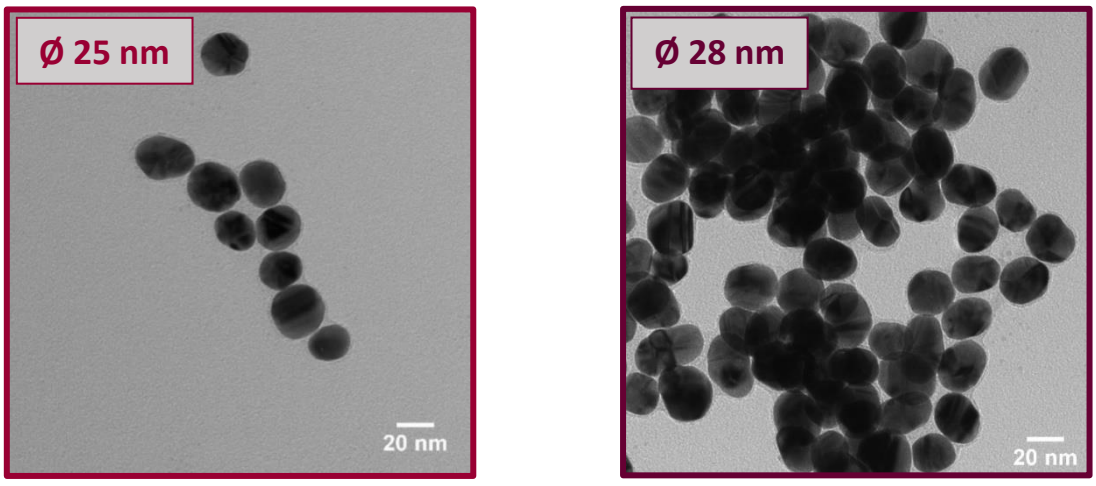

Figure 14: TEM images of Au-Citrate NPs with d_{TEM} = 24.9 ± 1.2 nm (**left**) and d_{TEM} = 28.1 ± 2.4 nm (**right**).

Nevertheless, these studies reflect the enormous impact of the reducing agent on the NP formation. More detailed interactions of the citrate ligands with the Au NPs were discussed by Al-Johani *et al.*[294], who postulated a binding coordination of these ligands on to the Au surface. In their studies, they investigated that the surface atoms predominantly exist in oxidation state ±0 with a very minor presence of gold atoms that are partially charged and described as "$Au^{+\delta}$" species. In addition, they assume that at room temperature a monocarboxylate interacts with the Au surface, and they base this on their investigations including ^{23}Na NMR spectroscopy, which suggests that the displaced Na^+ ion remains near the Au surface and in the vicinity of the citrate.[294] Therefore, the study of Al-Johani *et al.*[294] confirms the present coordination situation at the Au-Citrate NPs. According to this model, the schemes of Au-Citrate NPs were drawn in this thesis.

Furthermore, it was observed that due to the limited stabilising effect of the citrate ligands, purification *via* centrifugation is not always possible. Since this leads to an agglomeration of the NPs and thus, they cannot be redispersed in H_2O again. Purification *via* dialysis is possible but potentially results in a less stable NP dispersion less likely to be functionalised any further. Moreover, a pH sensitive handling was required when working with Au-Citrate NPs. To prevent the dispersion from agglomeration, the pH had to be controlled accurately. Au-Citrate NPs are stable between pH 5 and pH 7 (physiological conditions). At lower pH, NPs started to precipitate and even the addition of different bases such as NaOH or NEt_3 can cause precipitation. Furthermore, NPs in aqueous media can be stored in a fridge at 4 °C to prevent a significant growth or even agglomeration of the NPs, as this is favoured at higher temperatures due to a larger kinetic energy of the system.[295,296]

Their agglomeration can be further investigated by slow evaporation of the Au NP dispersions. Au-Citrate NPs showed no agglomeration when their volume was reduced to 80% of the initial volume, also TEM investigations showed no changes in their morphology. However, if the volume was reduced to about 50% of the initial volume, the Au-Citrate NPs agglomerated irreversibly.

In order to investigate how the synthetic conditions affect the outcome, the citrate reduction method is presented as the method of choice because only a small number of chemicals is used. Because of the mild conditions during the synthesis, the purity of the starting material may have a large impact. In this work, $HAuCl_4 \cdot 3\ H_2O$ (Sigma Aldrich) also $HAuCl_4 \cdot 1\ H_2O$ (Sigma Aldrich) and $HAuCl_4 \cdot x\ H_2O$ (synthesised in teaching labs) were tested as starting materials for the NP synthesis (Scheme 3).

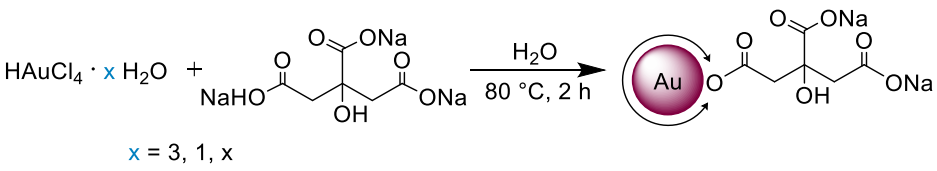

Scheme 3: Synthesis of Au-Citrate NPs in H_2O with different starting materials.

Table 4: Properties of Au-Citrate NPs synthesised with different gold precursors.

Starting material	ratio of $HAuCl_4$: citrate	d_{TEM}	λ_{max} (UV/Vis)	concentration
$HAuCl_4 \cdot 3\ H_2O$	1 : 5.8	13.8 ± 1.2 nm	521 nm	7.8 nmol/l
$HAuCl_4 \cdot 1\ H_2O$	1 : 5.8	13.5 ± 1.0 nm	522 nm	8.5 nmol/l
$HAuCl_4 \cdot x\ H_2O$	1 : 5.8	14.5 ± 1.0 nm	522 nm	6.8 nmol/l

In all approaches, stable red Au-Citrate NPs dispersions were obtained. All revealed a distinct plasmon resonance with an absorption maximum around 520 nm, each (**Table 4**). Using TEM, diameters of the Au NPs in these dispersions were determined and showed no significant changes in NP sizes and shapes (**Figure 15**). Instead, Au-Citrate NPs with a rather narrow size distribution were obtained in all approaches. Furthermore, predominantly spherical NPs could be observed.

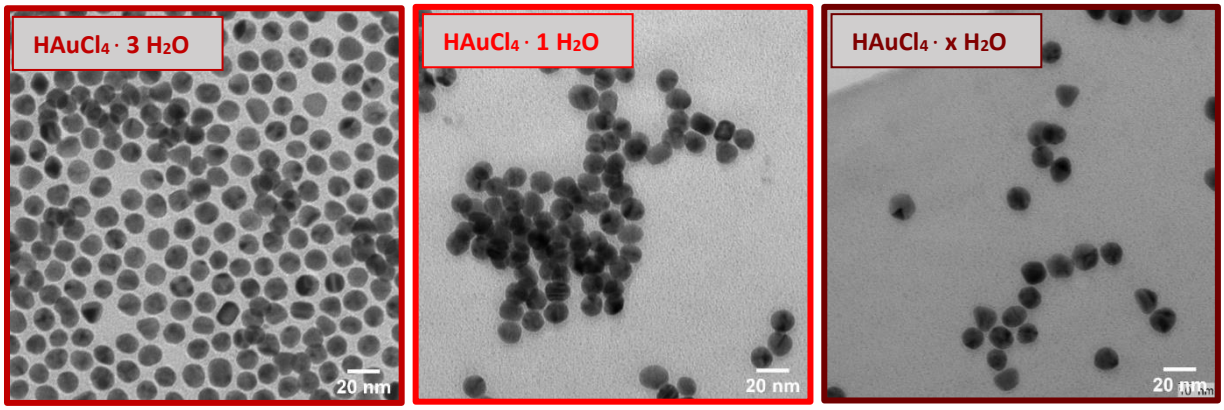

Figure 15: TEM images of Au-Citrate NPs synthesised with $HAuCl_4 \times 3\ H_2O$ (**left**), $HAuCl_4 \times 1\ H_2O$ (**centre**) and $HAuCl_4 \times x\ H_2O$ (**right**).

In addition, the concentration of the dispersions or the volume of H_2O used during the synthesis plays an important role in the outcome. The aim of the following studies was to investigate whether Au-Citrate NPs can still be stabilised in higher concentrations or whether agglomeration occurs during synthesis or storage. Starting from the standard concentration of 7.5 nM for Ø 14 nm Au-Citrate NPs, the volume of the reaction mixture was reduced in increments, while the amount of substances added stayed the same. **Table 5** displays the size of the Au NPs and their concentration in dispersion with respect to the performed synthesis.

Table 5: Size and concentration of Au-Citrate NPs from different syntheses.

	V (ml)	ratio of $HAuCl_4$: citrate	d_{TEM}	λ_{max} (UV/Vis)	concentration
1-fold	100	1 : 5.8	13.8 ± 1.2 nm	521 nm	7.5 nmol/l
1.5-fold	75	1 : 5.8	12.6 ± 1.1 nm	520 nm	13.7 nmol/l
2.0-fold	50	1 : 5.8	12.0 ± 1.3 nm	523 nm	23.8 nmol/l
4.0-fold	25	1 : 5.8		agglomerated	

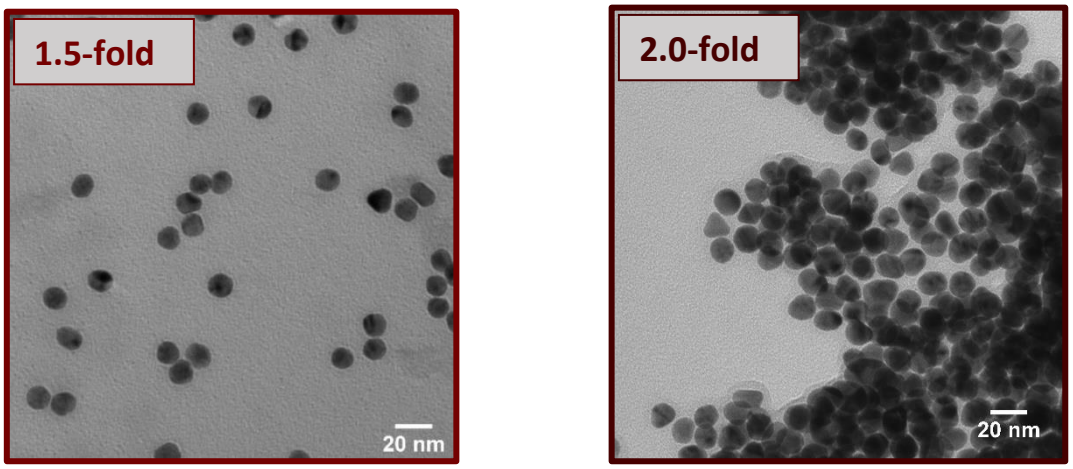

Figure 16: TEM images of Au-Citrate NPs synthesised in reduced volumes of 75 ml (**left**) or 50 ml (**right**) instead of 100 ml H_2O.

The corresponding TEM images (**Figure 16**) reveal the formation of stable Au NPs up to a 2.0-fold concentration. A higher concentration during the synthesis resulted in a slightly smaller diameter of the NPs formed, and monodisperse and mainly spherical NPs could be obtained. Due to the smaller size of the NPs (d_{TEM} = 12.6 ± 1.1 nm) the concentration has almost doubled (13.7 nM) when the volume was limited to 75 ml (1.5-fold; (**Figure 16**, **left**)). However, in a volume of 50 ml (2.0-fold) Au-Citrate NPs with a size of d_{TEM} = 12.0 ± 1.3 nm were isolated (**Figure 16**, **right**), whereas at a volume of 25 ml (4-fold), Au NPs were obtained as stable red dispersions during synthesis but agglomerated when cooled to room temperature.

Syntheses using ^{t}Bu-amine borane complex as the reducing agent

Since Au-Citrate NPs are reasonably low concentrated and have comparatively larger diameters (Ø > 10 nm), the synthesis of smaller Au NPs with a higher concentration was investigated further. Thus, syntheses of a modified version of the Stucky method were performed with ^{t}Bu-amine borane complex ($^{t}BuNH_2{:}BH_3$) as a stronger reducing agent. Furthermore, mercaptoundecanoic acid (MUDA) was used as the capping ligand, ensuring stable Au NPs. In these approaches, MUDA was used as a thiol containing ligand. In this way, a stable Au-S bond to the Au core can be formed. Furthermore, its long alkyl chain provides steric stabilisation of the formed Au NPs. In order to obtain Au-MUDA NPs, a modified version of the synthesis described by Stucky and coworkers[291] was performed, as displayed in Scheme 4.

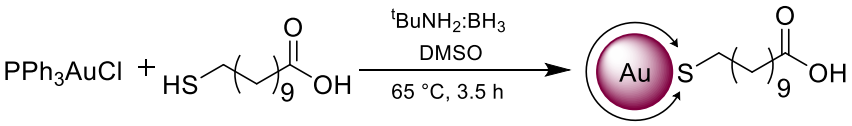

Scheme 4: Direct synthesis of Au-MUDA NPs according to a modified Stucky method.[291]

The Au precursor PPh_3AuCl was dissolved in DMSO with MUDA and heated to 65 °C. $^{t}BuNH_2{:}BH_3$ in DMSO was quickly added and stirred at 65 °C for 3.5 h before being cooled down in an ice bath. The resulting Au NPs are more stable than those obtained by the citrate reduction method, and thus they can be purified *via* centrifugation. As an important additional difference to the method described by Stucky *et al.*,[291] the Au NPs were redispersed in H_2O after being washed several times *via* centrifugation and dialysed against H_2O for an additional further purification. In this way, it was possible to obtain and maintain stable Au NPs in an aqueous medium. In some cases, diluted NaOH was added during the redispersion step to obtain a slightly basic pH in order to sufficiently stabilise the free acid of the ligand shell. Since the ligand shell contains acid groups in their ligand sphere, slightly basic conditions lead to stabilised NPs. With changing the ratios of starting materials, different core sizes of the NPs were obtained (Figure 17 A). The following tendency could be observed with regard to the size control: The larger the equivalent of reducing agent, the smaller the sizes of the formed Au NPs.

A

size	Ø 8 nm (Au-MUDA) B	Ø 9 nm (Au-MUDA) C	Ø 10 nm (Au-MUDA) D
PPh_3AuCl	1.0 eq.	1.0 eq.	1.0 eq.
ligand MUDA	4.6 eq.	1.0 eq.	0.7 eq.
$t_{Bu}NH_2:BH_3$	10 eq.	10 eq.	0.7 eq.
TEM	d = 7.9 ± 0.9 nm	d = 9.0 ± 0.9 nm	d = 9.7 ± 1.0 nm
DLS	d_{hydr} = 12 ± 3 nm	d_{hydr} = 14 ± 4 nm	d_{hydr} = 12 ± 3 nm
UV/Vis	λ_{max} = 528 nm	λ_{max} = 526 nm	λ_{max} = 525 nm
concentration c	212 nM	143 nM	115 nM

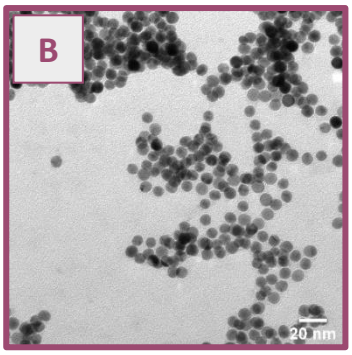

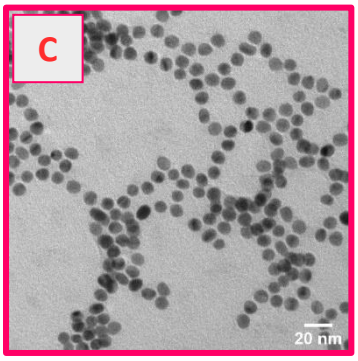

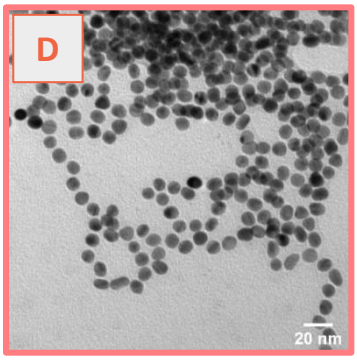

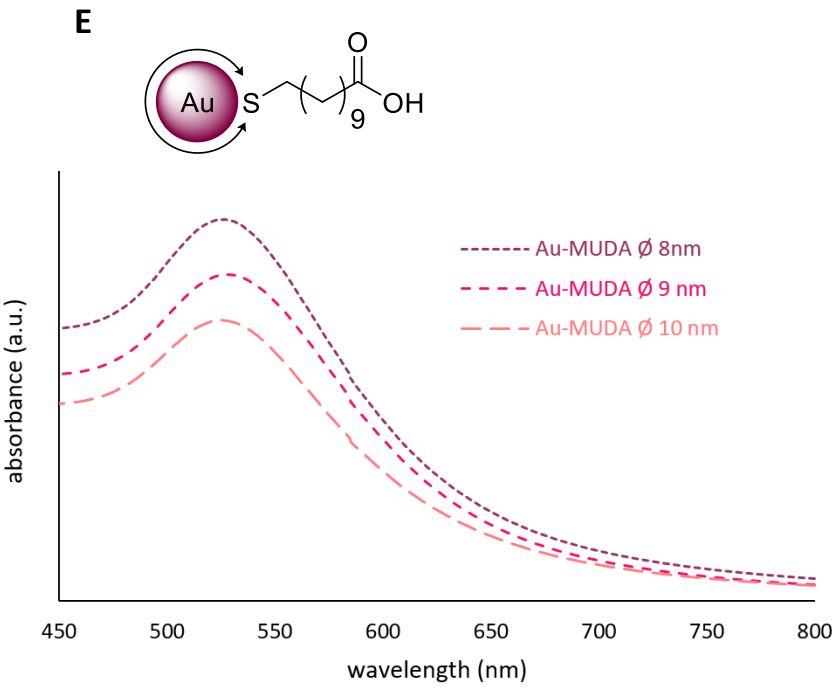

Figure 17: (**A**) Properties of the synthesised Au-MUDA NPs, corresponding TEM images of Au-MUDA NPs with a size of (**B**) Ø 8 nm, (**C**) Ø 9 nm and (**D**) Ø 10 nm and (**E**) their UV/Vis spectra.

Furthermore, TEM images of the synthesised NPs reveal predominantly spherical NPs with a narrow size distribution and without visible agglomeration. Using a ratio of PPh_3AuCl : MUDA : $^tBuNH_2:BH_3$ of 1.0 : 4.6 : 10, NPs with a size of d_{TEM} = 7.9 ± 0.9 nm were obtained (**Figure 17 B**). Slightly larger Au-MUDA NPs were synthesised using the same method. The PPh_3AuCl : MUDA : $^tBuNH_2:BH_3$ ratio of 1.0 : 0.7 : 0.7 resulted in Au NPs with an average diameter of d_{TEM} = 9.7 ± 1.0 nm (**Figure 17 D**). Their hydrodynamic diameter d_{hydr}, determined using DLS, showed slightly larger d_{hydr} than their corresponding d_{TEM} sizes (**Figure 17 A**), as expected. This is due to the fact that DLS considers the entire NP with its ligand shell, whereas in TEM only the gold core of the NP can be measured. Important to mention is that this consideration is based on the assumption that the precursors are completely reduced to NPs and a 100% conversion occurred. The measured absorptions of all synthesised pink and clear Au NP samples are displayed in **Figure 17 E**. All Au-MUDA NPs possess an absorption maximum λ_{max} around 525 nm. Overall, a very narrow size distribution and furthermore a very good size control could be achieved in the direct synthesis using MUDA as the capping agent.

Further studies were performed in order to investigate whether a different type of thiol ligand provided the same stability of the NPs. 4-mercaptobenzoic acid (4-MBA) was used, as displayed in **Scheme 5**. 4-MBA possesses, next to a free acid function, a thiol moiety in order to bind to the Au NPs. These units are connected only by an inflexible phenyl ring.

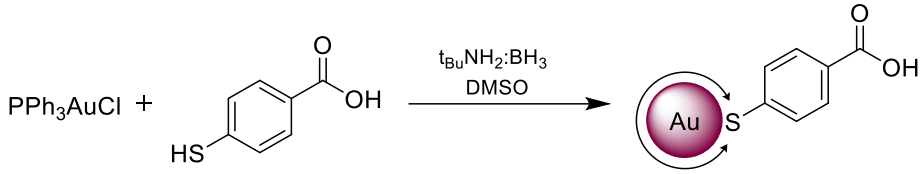

Scheme 5: Direct synthesis of Au-4MBA NPs.

Again, PPh_3AuCl was dissolved in DMSO with the ligand 4-MBA and heated up to 65 °C or 60 °C, respectively. The reducing agent was added either dissolved in DMSO or as a solid and the reaction mixture was stirred at the respective temperature before being cooled in an ice bath. In various approaches, stable red NPs dispersions were obtained. A homogenous addition of the reducing agent $^{t}BuNH_2:BH_3$ dissolved in DMSO as well as a heterogenous addition of solid $^{t}BuNH_2:BH_3$ led to a rapid formation of Au NPs. Under similar conditions with a reaction temperature of 65 °C for 4 h, similarly sized Au NPs were formed. TEM images of both approaches reveal spherical NPs with a monodisperse morphology and an excellent size distribution (**Figure 18**).

Using a ratio of PPh_3AuCl : 4-MBA : $^{t}BuNH_2:BH_3$ of 1.0 : 0.6 : 6.8, the Au-4-MBA NPs have an average size of d_{TEM} = 8.3 ± 0.8 nm (**Figure 18 A**), when the reducing agent was added as a solid, and d_{TEM} = 8.0 ± 1.1 nm (**Figure 18 B**), when it was dissolved in DMSO.

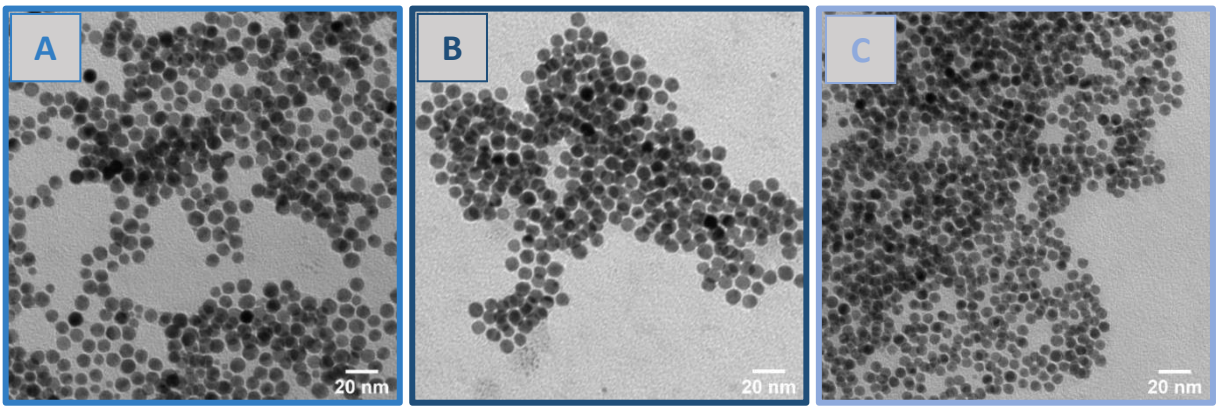

Figure 18: TEM images of Au-4-MBA NPs with (**A**) d_{TEM} = 8.3 ± 0.8 nm ($^{t}BuNH_2:BH_3$ solid), (**B**) d_{TEM} = 8.0 ± 1.1 nm ($^{t}BuNH_2:BH_3$ dissolved) and (**C**) d_{TEM} = 6.0 ± 0.9 nm.

By changing the ratio of PPh_3AuCl : 4-MBA : $^{t}BuNH_2:BH_3$ to 1.0 : 1.2 : 7.1 and the reaction conditions slightly (60 °C for 90 min), slightly smaller Au NPs were obtained with a diameter of d_{TEM} = 6.0 ± 0.9 nm (**Figure 18 C**). Furthermore, UV/Vis measurements revealed that all samples possess a distinct plasmon resonance between λ_{max} 520 and 530 nm (**Figure 19 A**).

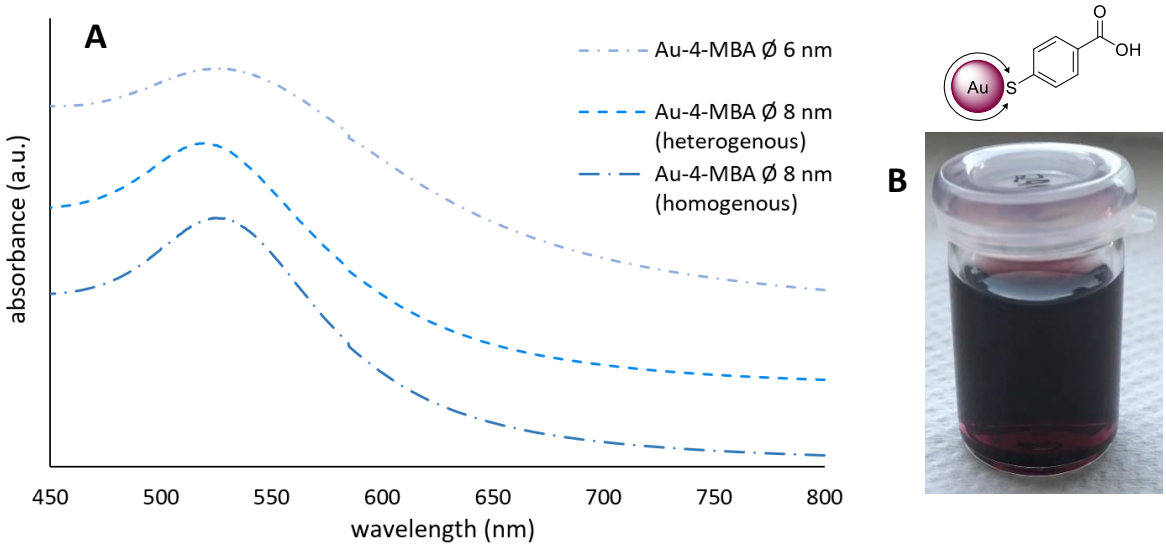

Figure 19: (**A**) UV/Vis spectra of Au-4-MBA NPs and (**B**) synthesised Au-4-MBA NPs in a glass vial.

Overall, all Au NP samples showed a good stability and monodisperse behaviour in dispersion. Red, clear dispersions were obtained in all approaches (**Figure 19 B**). It has been demonstrated that the direct synthesis of Au NPs with different thiol ligands is applicable and thus presents an alternative to the Au-Citrate NPs. When handled appropriately, a successful transfer into an aqueous medium is possible with both, sterically demanding and additionally stabilising ligands as well as short chain and rather stiff ligands. Although these thiol ligands are attached to the Au NPs more strongly than the merely electrostatically coordinating citrate molecules in Au-Citrate NPs, the Au NPs obtained in direct syntheses may also be used for various functionalisations.

3.2 BIOFUNCTIONALISED AU NPS

In order to functionalise Au NPs with biogenic substances (BS), different synthetic strategies can be chosen (**Figure 20**). Irrespective of the choice of the functionalisation route, NPs were synthesised first as described in **Chapter 3.1.1** and displayed in **Figure 20**, **red**.

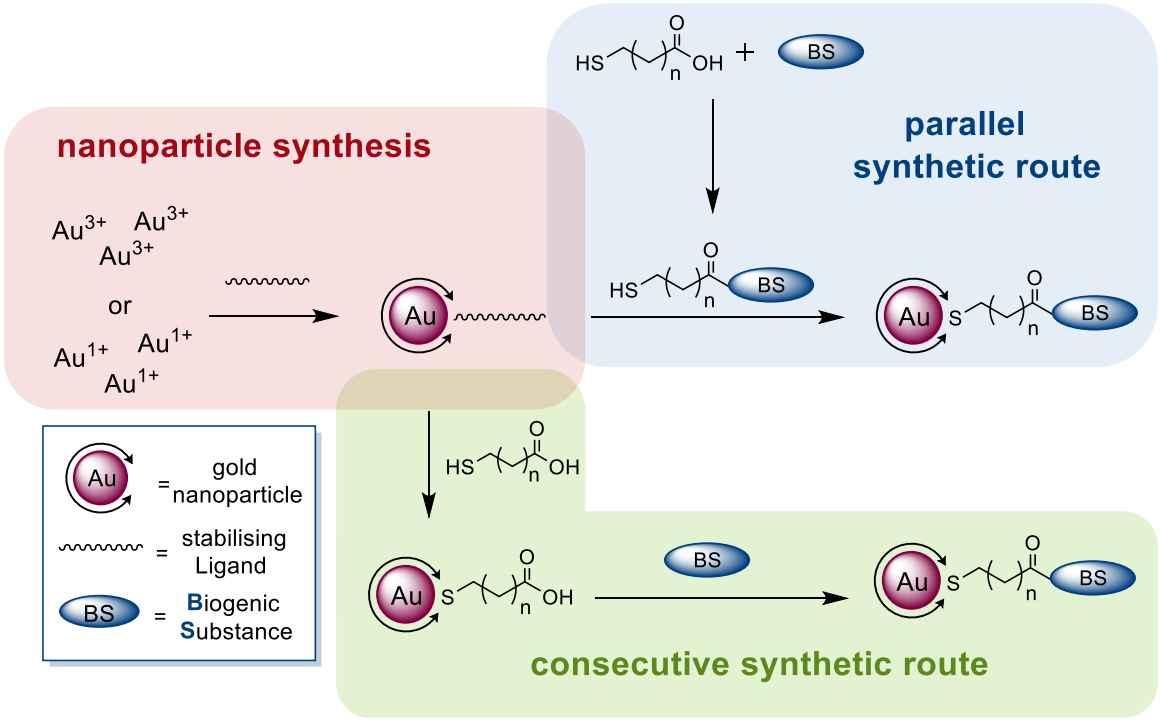

Figure 20: Synthetic strategies towards biofunctionalised Au NPs: after the NPs were synthesised (red), they were functionalised either in a consecutive route (green) *via* a ligand exchange and a consecutive reaction at the ligand periphery or using a parallel synthetic route (blue), in which the ligand was prepared independently and afterwards immobilised onto the Au NP surface.

Two different synthetic pathways for a biofunctionalisation were performed during this work. The consecutive route started with a ligand exchange reaction, in which a bifunctional thiol linker (mercapto acid) was attached to the Au NP surface. In the next step, a biogenic substance was linked to the ligand sphere *via* a free acid moiety in a reaction at the ligand periphery (**Figure 20**, **green**). This pathway provides the advantage of working in an aqueous and thus biocompatible medium throughout. However, a drawback of this route certainly is the fact that a precise surface analysis has to be performed after each reaction step to ensure a successful surface exchange. For this purpose, at least 4 ml of NP dispersion out of an up to 10 ml batch – an immense amount of the NP dispersion – is utilised and cannot be reused in further investigations. Furthermore, depending on their functional groups, only specific biogenic substances can be functionalised onto the Au NPs *via* this procedure, e.g. an amide bond to an amine may be formed, whereas an esterification linkage to an alcohol would be less successful in aqueous media. In here, the biogenic amine carbachol (CCh) was attached using amide bond formation.

Alternatively, a parallel synthetic route can be chosen for several biogenic substances (**Figure 20**, **blue**). Here, a bifunctional ligand was prepared starting from a mercapto acid acting as both a bifunctional thiol linker and spacer. The biogenic substance was then added under inert conditions in an organic solvent, as biomedically interesting catecholamines tend to undergo oxidation when being exposed to oxygen.[297] Moreover, oxidation also occurred in an aqueous medium at the air-water interface.[298] In this way, even compounds sensitive towards water or air could be reacted. Afterwards, the obtained ligand was immobilised on the synthesised Au NPs in one step, using again degassed H_2O and inert conditions.

As an advantage, the elaborated characterisation of functionalised Au NPs had to be performed only once during the whole pathway and thus only a small amount of the total dispersion was utilised for analytics.

3.2.1 Biofunctionalisation of Au NPs *via* a Consecutive Route

In the following, the stepwise biofunctionalisation of Au NPs with carbachol (CCh) is described (**Scheme 6**). Carbachol represents a pharmacologically interesting compound since it is a stable derivative of acetylcholine. Being a synthetic choline ester with a positively charged quaternary ammonium unit, this molecule exhibits effects on nicotinic and muscarinic acetylcholine receptors similar to native acetylcholine. Carbachol itself is used therapeutically as a glaucoma treatment or to stimulate motility of the gastrointestinal or the urogenital tract, thus carbachol functionalised Au NPs offer potential therapeutic applications.

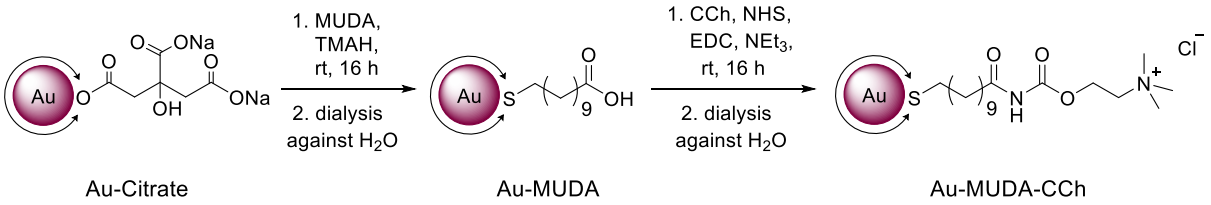

Scheme 6: Synthesis of carbachol functionalised Au NPs *via* a stepwise route. Au-Citrate NPs (**left**) were reacted with mercaptoundecanoic acid (MUDA) to obtain Au-MUDA NPs (**centre**) in a ligand exchange reaction, followed by a peptide coupling at the ligand periphery in order to link carbachol to the ligand sphere and obtain Au-MUDA-CCh (**right**).

First, Au-Citrate NPs were reacted with mercaptoundecanoic acid (MUDA) (**Scheme 6**, **left**). In this ligand exchange reaction, relatively weak coordinating citrate ligands were substituted by the thiol linker MUDA and led to strong covalent Au-S-bonds. Additionally, the Au NPs were further stabilised through steric interactions induced by the long flexible chain of MUDA. The ligand was added as a solid in a large excess and since the surface of the Au NPs was modified, the pH had to be monitored in order to ensure a stable NP dispersion. Since free carboxylic acid moieties were present on the ligand shell during the ligand exchange, a basic environment (pH > 8) prevented the NPs from agglomeration. The reaction mixture was purified *via* dialysis against H_2O (in MWCO 12000, 6 × 2 h). In the following synthetic step, the biogenic amine was linked to the ligand periphery by peptide coupling (**Scheme 6**, **right**).

N-hydroxysuccinimide (NHS) and *N*-(3-dimethylaminopropyl)-*N´*-ethylcarbodiimide hydrochloride (EDC) were added first to form an *in situ* active ester, which then reacted with carbachol (CCh) to an amide. Again, all reagents were added in excess and a slightly basic pH was maintained by the addition of triethyl amine (NEt_3). Subsequently, the obtained pink stable Au-MUDA-CCh NP dispersion was purified *via* dialysis against H_2O (in MWCO 12000, 6 × 2 h). In addition to low concentrated Au-MUDA NPs, which were obtained after the ligand exchange reactions, also Au-MUDA NPs obtained in the direct syntheses were used as starting particles for the functionalisation described above. In this way, Au-MUDA-CCh NPs with slightly smaller sizes were obtained in slightly higher concentrations. TEM images of the approaches revealed that no change in the morphology of the NPs occurred during the functionalisation (**Figure 21 A** and **B**) and spherical monodisperse Au-MUDA-CCh NPs with a size of d_{TEM} = 13.9 ± 1.4 nm (**Figure 21 A**) and d_{TEM} = 9.0 ± 0.9 nm (**Figure 21 B**) were obtained.

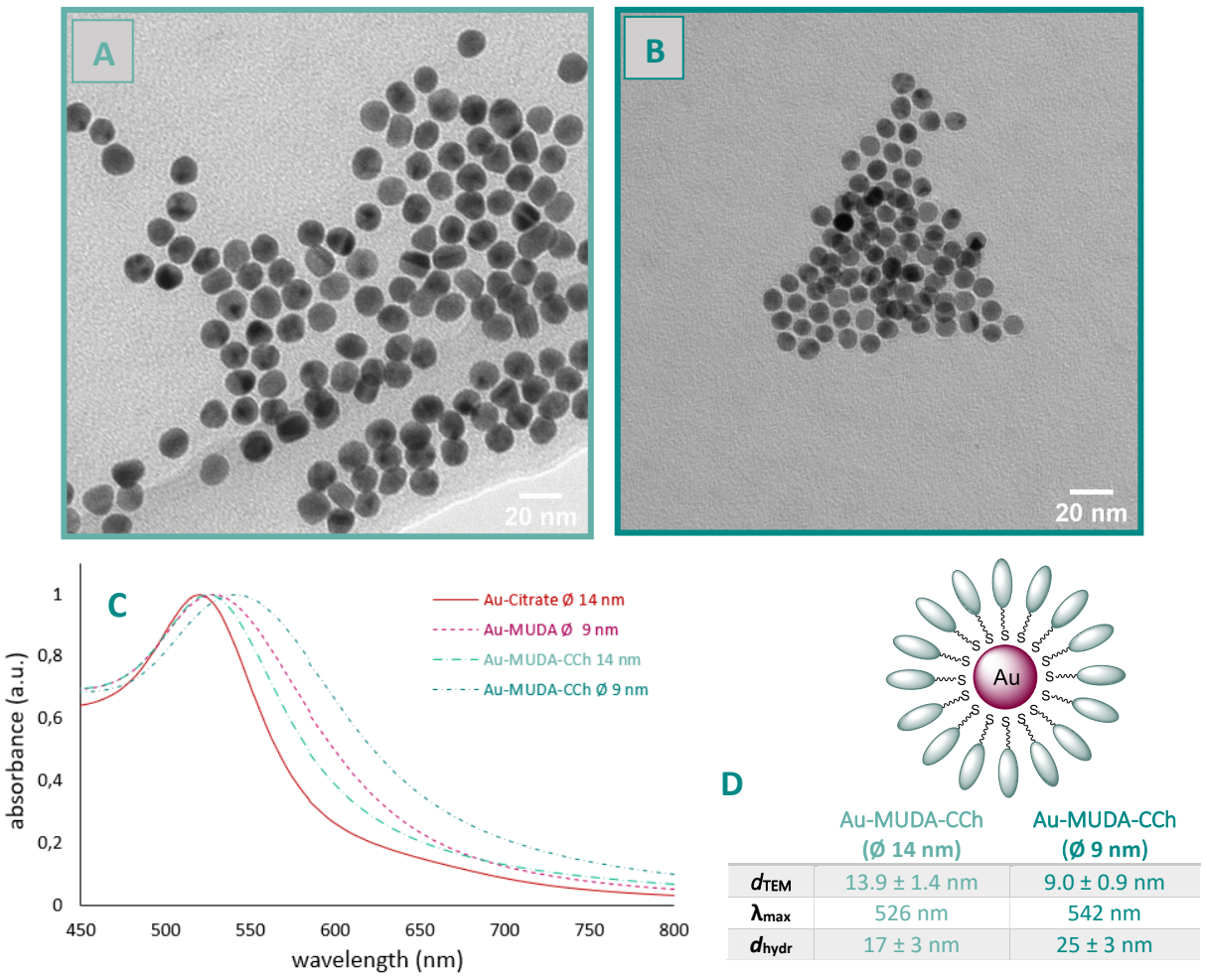

	Au-MUDA-CCh (Ø 14 nm)	Au-MUDA-CCh (Ø 9 nm)
d_{TEM}	13.9 ± 1.4 nm	9.0 ± 0.9 nm
λ_{max}	526 nm	542 nm
d_{hydr}	17 ± 3 nm	25 ± 3 nm

Figure 21: TEM images of Au-MUDA-CCh NPs (Ø 14 nm) (**A**) and (Ø 9 nm) (**B**),(**C**) UV/Vis spectra of Au-Citrate NPs (Ø 14 nm), Au-MUDA NPs (Ø 9 nm), Au-MUDA-CCh NPs (Ø 14 nm) and Au-MUDA-CCh NPs (Ø 9 nm), (**D**) corresponding data of Au-MUDA-CCh NPs (Ø 14 nm) and Au-MUDA-CCh NPs (Ø 9 nm).

UV/Vis spectra of Au-MUDA-CCh (**Figure 21 C**) showed that slight bathochromic shifts occurred due to their new surface modification in comparison to the starting particles. Au-MUDA-CCh NPs (Ø 14 nm) has λ_{max} = 526 nm and Au-MUDA-CCh NPs (Ø 9 nm) possesses an absorption maximum at 542 nm. However, the hydrodynamic diameters of both dispersions resemble (**Figure 21 D**) the values of d_{TEM}, with d_{DLS} = 17 ± 3 nm for Au-MUDA-CCh NPs (Ø 14 nm) and d_{DLS} = 25 ± 3 nm for Au-MUDA-CCh NPs (Ø 9 nm).

The successful reaction at the ligand periphery was investigated with ^{1}H-NMR measurements by comparing the obtained spectra to the spectra of the initial NP dispersions as well as native CCh as a reference. The spectra show all predicted proton resonances of the long chain MUDA spacer and furthermore reveal two proton signals around 4.50 ppm and 3.70 ppm, which can be assigned to the two methylene groups of CCh. The surface functionalisation of the Au-MUDA-CCh NPs was further verified by IR spectroscopy and compared with the spectra of the starting particles and materials as references (**Figure 22**). Au-MUDA-CCh NPs (**Figure 22**, **2nd** from **bottom**) has distinctive ν_{C-H} bands around 3000 cm^{-1}, which can be assigned to the long MUDA spacer (also present in **Figure 22**, **2nd** from **top**).

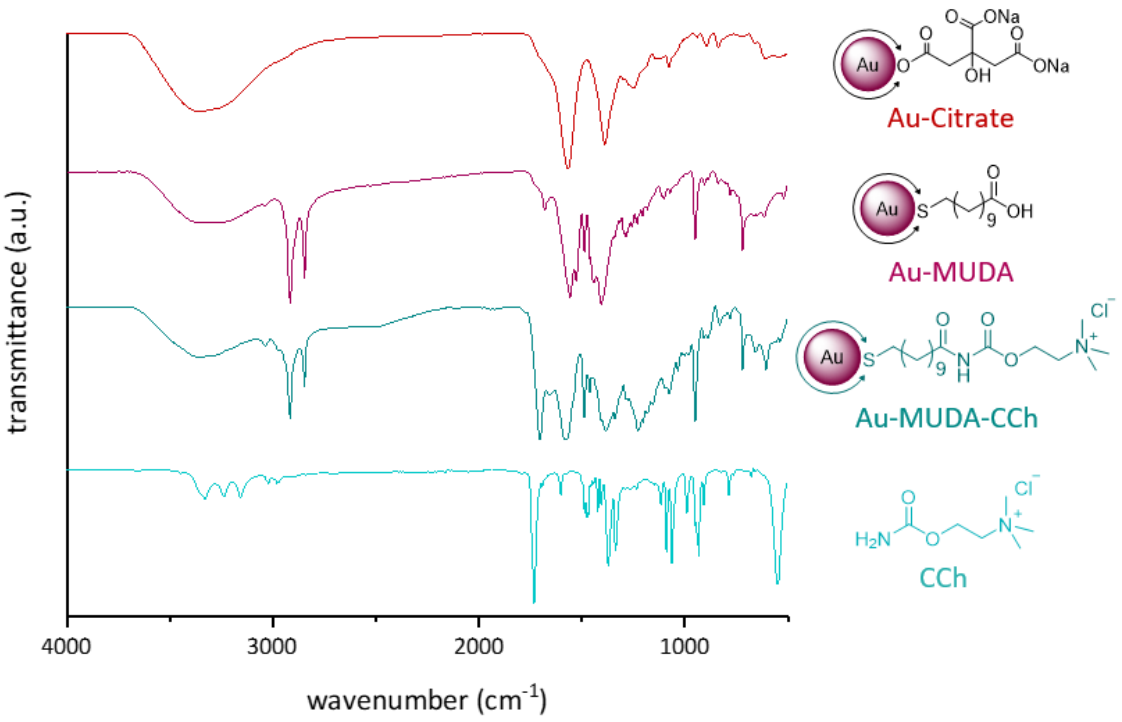

Figure 22: IR spectra of Au-MUDA-CCh NPs (**2nd from bottom**) in comparison to Au-Citrate NPs (**top**), Au-MUDA NPs (**2nd from top**) and CCh (**bottom**).

Furthermore, an intense sharp $\nu_{C=O}$ resonance at 1704 cm^{-1} corresponds to the carbonyl unit of carbachol (also present in (**Figure 22**, **bottom**)). The spectrum of Au-MUDA-CCh NPs (**Figure 22**, **2nd from bottom**) reveals characteristic vibrations of the amide bond formed, such as resonances at 1580 cm^{-1} (δ_{N-H}) and 650 cm^{-1} (δ_{O-C-N}). Taken together, these data unambiguously prove the successful functionalisation of Au NPs with CCh.

Physiological testing of Au-MUDA-CCh (Ø 14 nm)

The physiological studies of all functionalised Au NPs within this thesis were performed by the research group of Prof. Diener at the Institute of Veterinary Physiology and Biochemistry at the Justus Liebig University Giessen. In the present study, rat colonic mucosa was mounted in Ussing chambers (detailed experimental setup is described in **Chapter 5.9.2.1**). Here, the receptor activities of muscarinic or nicotinic acetylcholine receptors were studied, which can both be activated by carbachol (CCh). CCh represents a potent secretagogue as it activates chloride secretion across mammalian colonic epithelium. The setup was administered with either native CCh or Au-MUDA-CCh NPs and their effect on the measured short circuit current (I_{SC}) was investigated. A stimulation of the muscarinic or nicotinic acetylcholine receptors would be displayed in an increase of the measured I_{SC}. As displayed in **Figure 23 A**, Au-MUDA-CCh NPs induced a concentration-dependent increase of I_{SC}.

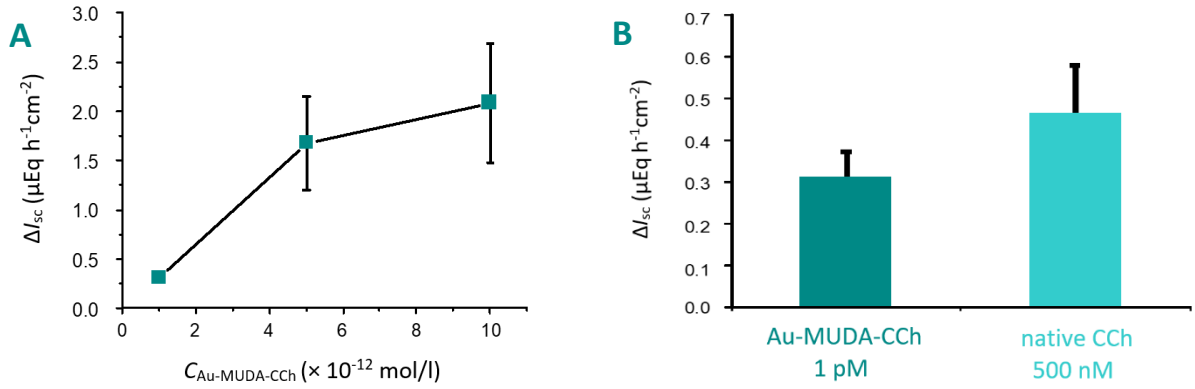

Figure 23: (**A**) Au-MUDA-CCh NPs induced a concentration-dependent increase in I_{SC}. Values are given as increase in I_{SC} above baseline in short-circuit current ΔI_{SC}) just before administration of the corresponding drug and are means ± SEM, n = 6, (**B**) 0.5 µM native CCh and 1 pM Au-MUDA-CCh NPs yielded approximately the same response in Ussing chambers experiments.

Moreover, even very low concentrations of Au-MUDA-CCh NPs (pM) caused a detectable stimulation of the receptors. In comparison with the native agonist, it was found that 500 nM native CCh was nearly equieffective to 1 pM Au-MUDA-CCh NPs (**Figure 23 B**) and thus showing a 10^6-fold potentiation of the induced receptor activation.

To better determine this potentiation, molecular approaches based on the signalling cascade of acetylcholine-induced activation of muscarinic receptors were used. For this purpose, FRET (Förster Resonance Energy Transfer) measurements on **h**uman **e**mbryonic **k**idney cells (**HEK** 293T) were performed by the research group of Prof. Bünemann at the Institute of Pharmacology and Clinical Pharmacy at the Philipps University Marburg. Since muscarinic receptors are G protein coupled receptors, different protein subunits were conjugated to a fluorescent protein (**Figure 24 A**). The Gα subunit was conjugated to the yellow fluorescence protein (YFP) and the $G\gamma_2$ subunit to the cyan fluorescence protein (CFP).

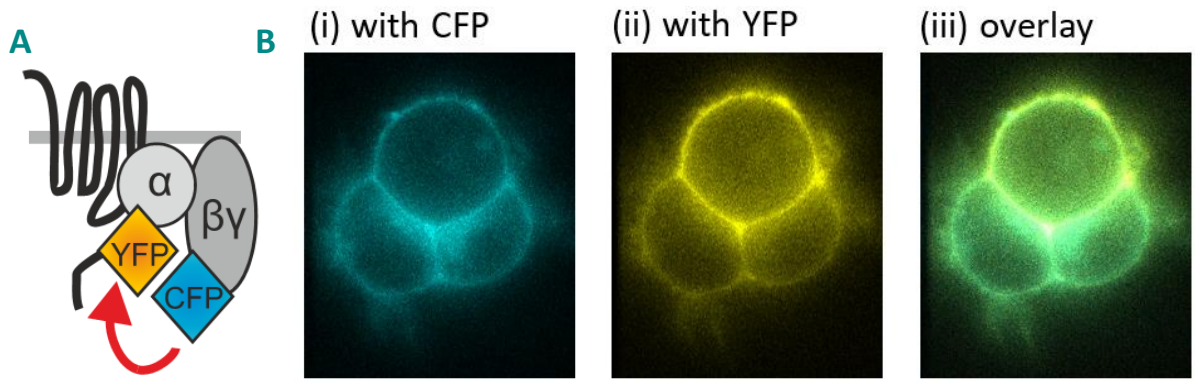

Figure 24: (**A**) Scheme of a G protein-coupled receptor, e.g. muscarinic receptor, and its subunits Gα and $G\gamma_2$ coupled to the yellow fluorescence protein (YFP) or cyan fluorescence protein (CFP), respectively. (**B**) Images of transiently transfected HEK293T cells with CFP (**i**), YFP (**ii**) and overlay (**iii**) staining were taken using an inverted fluorescence microscope with a 100× oil immersion objective, 100 ms exposure time, 2% YFP (500 nm) and/or CFP (425 nm) LEDs intensity).

FRET measurements were performed, confirming the energy transfer (**Figure 24 B**). The observed fluorescence confirms the activation of the Gα and G $\beta_1\gamma_2$ subunits of the G protein, and thus the activation of the receptor by Au-MUDA-CCh NPs. The fluorescence data (not shown) confirm the 10^6-fold activation of the G protein.

3.2.2 Biofunctionalisation of Au NPs *via* a Parallel Route

In this synthetic pathway, the entire ligand is first synthesised separately, before immobilisation onto the Au NPs takes place (**Figure 25**).

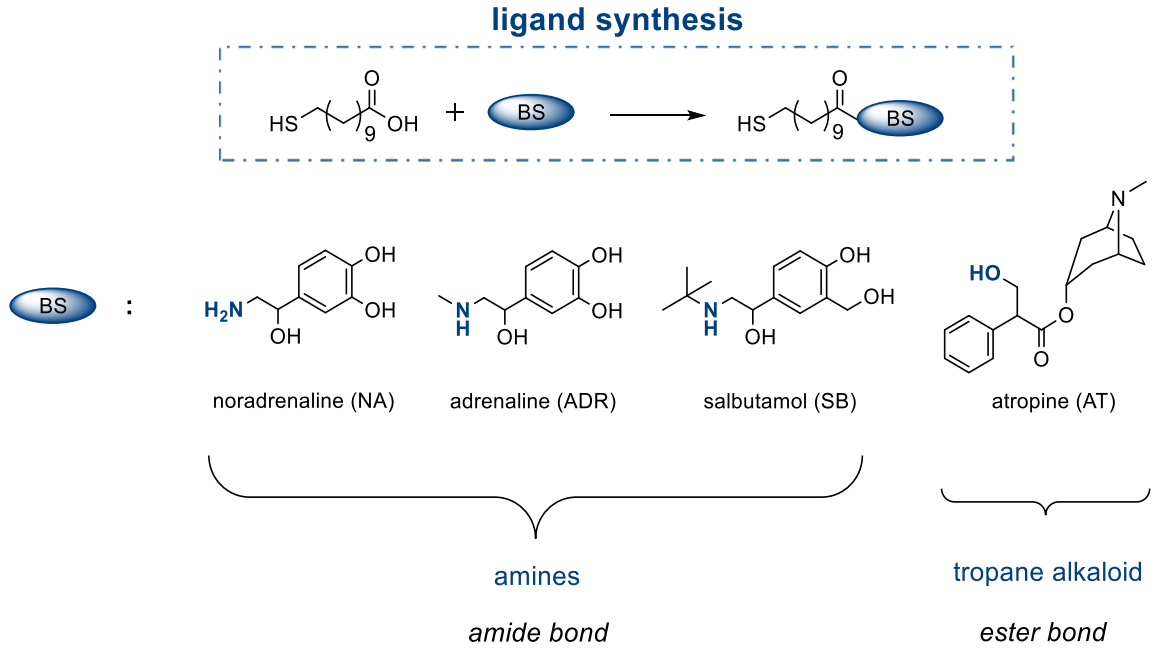

Figure 25: Scheme of the parallel ligand synthesis (**top**) and biogenic substances used with amine groups (noradrenaline, adrenaline, salbutamol (**bottom left**)) and an alcohol group containing tropane alkaloid (atropine (**bottom right**)).

To do so, the bifunctional thiol linker (mercapto acid), which serves as a connection and stability component for the NPs at a later stage, is linked to the biogenic substance (**Figure 25**, **top**). Depending on the functional linking unit on the biogenic substance, a differentiation is drawn between biogenic amines (**Figure 25**, **bottom left**) and biogenic substances with e.g. an alcohol group (**Figure 25**, **bottom right**), corresponding to whether the biogenic component is connected to the spacer *via* an amide or an ester bond.

3.2.2.1 Biofunctionalisation of Au NPs with adrenergic amines

Adrenergic amines fulfil essential functions in biological systems. The catecholamines investigated herein, noradrenaline (NA) and adrenaline (ADR), both act as endogenous transmitter in the sympathetic nervous system, functioning as hormones with the catechol unit in their structure and causing a stimulation of adrenergic receptors.[299,300] These receptors are found in numerous organ systems and have an impact on smooth muscle contractions, epithelial secretion and cardiac functions. Thus, it is of interest to investigate whether Au NPs functionalised with adrenergic amines can interact with adrenergic receptors in different biological systems.

Ligand syntheses

The syntheses were carried out according to a modified procedure by Abed *et al.*[301] The spacer molecule MUDA was reacted with the coupling reagents *N*-hydroxysuccinimide (NHS) and diisopropylcarbodiimide (DIC) in absolute pyridine at room temperature in order to form an active ester with NHS (**Scheme 7**).

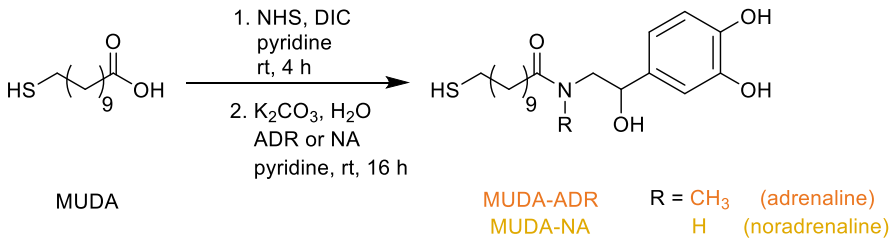

Scheme 7: Ligand syntheses of MUDA-ADR and MUDA-NA with the biogenic amines adrenaline (ADR) and noradrenaline (NA), respectively.

The reaction is a well-established amide coupling and its mechanism was described frequently.[302,303] After 4 h, the biogenic amine (either adrenaline (ADR) bitartrate or noradrenaline (NA) bitartrate) dissolved in pyridine is added simultaneously with K_2CO_3 in degassed H_2O. Now, the active ester reacts *in situ* with the amine under mildly basic conditions.

The ligands were purified in an aqueous work-up followed by column chromatography. However, traces of the side product *N*,*N*'-diisopropylurea (DIU) remained next to the pure ligands and could only be removed completely using preparative HPLC. Nonetheless, the

presence of DIU was tolerated during the functionalisation since the bifunctional ligand with its thiol moiety is more likely to be attached to the Au NPs in a ligand exchange reaction than any DIU side product. Moreover, free molecules and by-products are removed from the Au NP dispersion in the subsequent dialysis.

Attempts of crystallisation were made with the pure ligands but without any success. However, analytical characterisations were carried out using NMR, IR and ESI-MS. ^{1}H-NMR spectra show all expected proton resonances. Furthermore, the characteristic aromatic proton signals in the range from 6.76 ppm to 6.52 ppm correspond to the aromatic protons of the biogenic amines (ADR or NA). Moreover, intense resonances between 1.57 ppm and 1.17 ppm are assigned to the long alkyl chain of the thiol linker MUDA.

IR spectroscopy was used to further identify the existing binding types within the ligands. The spectra of both ligands show a strong $\nu_{O\text{-}H}$ vibration around 3300 cm^{-1}, which can be attributed to the hydroxyl groups. The formation of amide bonds was verified with $\delta_{C\text{-}N}$ resonances around 1240 cm^{-1} as well as sharp $\nu_{C=O}$ bands in the range between 1650 cm^{-1} and 1600 cm^{-1}. A further small $\nu_{N\text{-}H}$ vibration can be observed for MUDA-NA around 3100 cm^{-1}, which is not present in MUDA-ADR since it lacks an NH-group due to its *N*-methylation. In ESI MS measurements, the molecule ion [M-H]$^{-}$ of *m/z* 380.20 was found for MUDA-ADR and [M-H]$^{-}$ of *m/z* 368.20 for MUDA-NA. Both match the calculated ligand masses.

Nanoparticle functionalisation

As a next step, functionalisation of the synthesised Au NPs took place using ligand exchange reactions with the synthesised ligands MUDA-ADR or MUDA-NA, as displayed in **Scheme 8**.

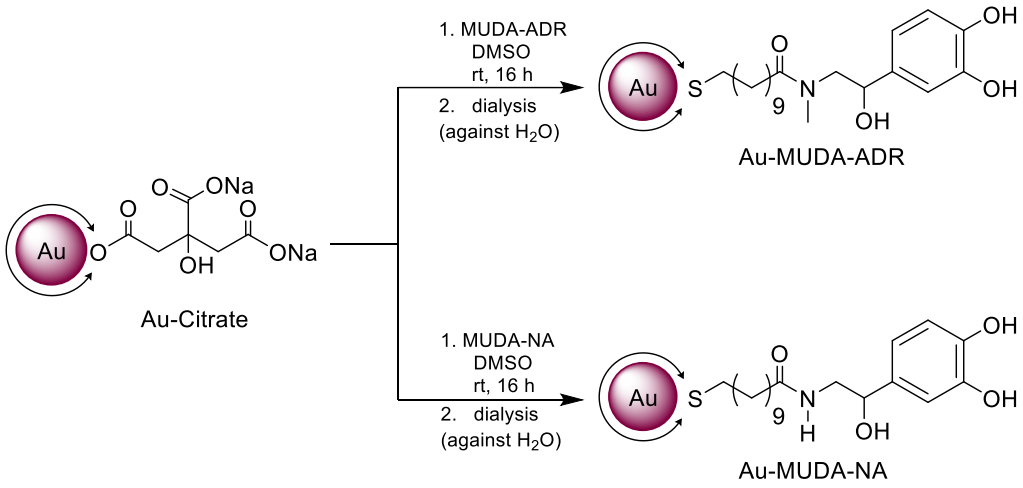

Scheme 8: Functionalisation in a ligand exchange reaction with the synthesised catecholamine carrying ligands (MUDA-ADR or MUDA-NA).[304]

The Au NP dispersion of the preferred size was degassed with argon prior to the addition of the ligand. The ligand was dissolved in DMSO and slowly added in a large excess (ca. 10^{6}-fold) under vigorous stirring. A benefit of adding the ligand in a dissolved form is a rapid and efficient

homogenisation. Furthermore, agglomeration of the Au NPs upon the addition of bulk material is prevented. To ensure a stable Au NP dispersion during the reaction, the pH was adjusted by adding NEt_3. The obtained pink and stable Au NP dispersion was subsequently purified *via* dialysis in order to remove remaining free ligands and other side products.

All pink and stable Au NP dispersions were characterised by UV/Vis spectroscopy, displaying a slight bathochromic shift in the measured absorption maxima λ_{max} (**Figure 26 A**). The existence of only one relatively narrow absorption band with a noticeable rise indicates that a stable NP dispersion with fairly monodisperse NPs is present.

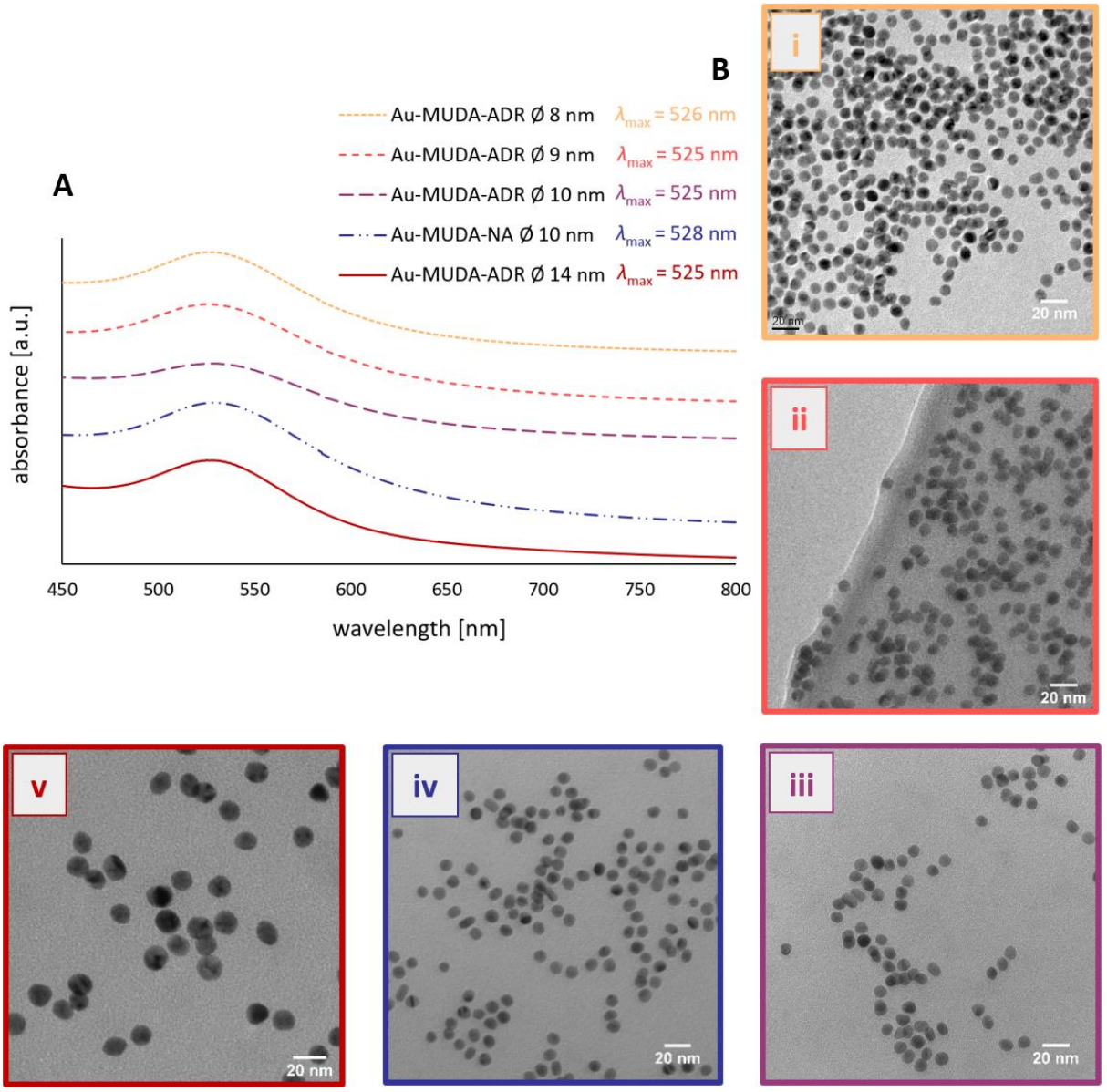

Figure 26: (**A**) UV/Vis spectra of the functionalised Au NPs Au-MUDA-ADR Ø 14 nm, Ø 10 nm, Ø 9 nm, Ø 8 nm and Au-MUDA-NA Ø 10 nm and (**B**) their corresponding TEM images of (**i**) Au-MUDA-ADR d = 8.1 ± 0.6 nm, (**ii**) Au-MUDA-ADR d = 8.9 ± 0.8 nm, (**iii**) Au-MUDA-ADR d = 9.9 ± 0.9 nm, (**iv**) Au-MUDA-NA d = 9.9 ± 0.8 nm and (**v**) Au-MUDA-ADR d = 13.9 ± 1.2 nm.

Moreover, TEM images reveal that no remarkable change in the morphology of the NPs occurred during their functionalisation with MUDA-ADR or MUDA-NA, respectively

(Figure 26 B (i)-(v)). Furthermore, no agglomeration was observed and the Au NPs remain with a spherical shape in their expected diameters with a small size distribution.

In addition to the TEM investigations, DLS measurements were performed (displayed in Table 6), showing that the determined d_{hydr} remain in the expected range and thus supporting the conclusion that a stable NP dispersion is present.

Table 6: Properties of the synthesised functionalised Au NPs.

size	8 nm	9 nm	10 nm	14 nm	10 nm
sample	Au-MUDA-ADR				Au-MUDA-NA
d_{TEM} / nm	8.1 ± 0.6	8.9 ± 0.8	9.9 ± 0.9	13.9 ± 1.2	9.9 ± 0.8
d_{hydr} / nm	17 ± 5	13 ± 3	13 ± 5	16 ± 4	17 ± 4
λ_{max} / nm	526	525	523	525	528
concentration	157 nM	191 nM	101 nM	7.1 nM	35 nM

The organic ligand structures around the Au NPs were further analysed using IR and NMR spectroscopy in order to confirm a successful ligand exchange during each functionalisation reaction. ^{1}H-NMR spectra of the functionalised Au NPs were recorded and compared to the spectra of MUDA-ADR and MUDA-NA, respectively. It was possible to assign the proton signals of the synthesised ligands on the Au NP surface as the spectra show all desired proton resonances. The aromatic protons of the biogenic amines (ADR or NA) show resonances in the range from 6.77 to 6.52 ppm (Figure 27 A, left). Furthermore, intense resonances between 1.57 ppm and 1.17 ppm are assigned to the long alkyl chain of the spacer (Figure 27 A, right).

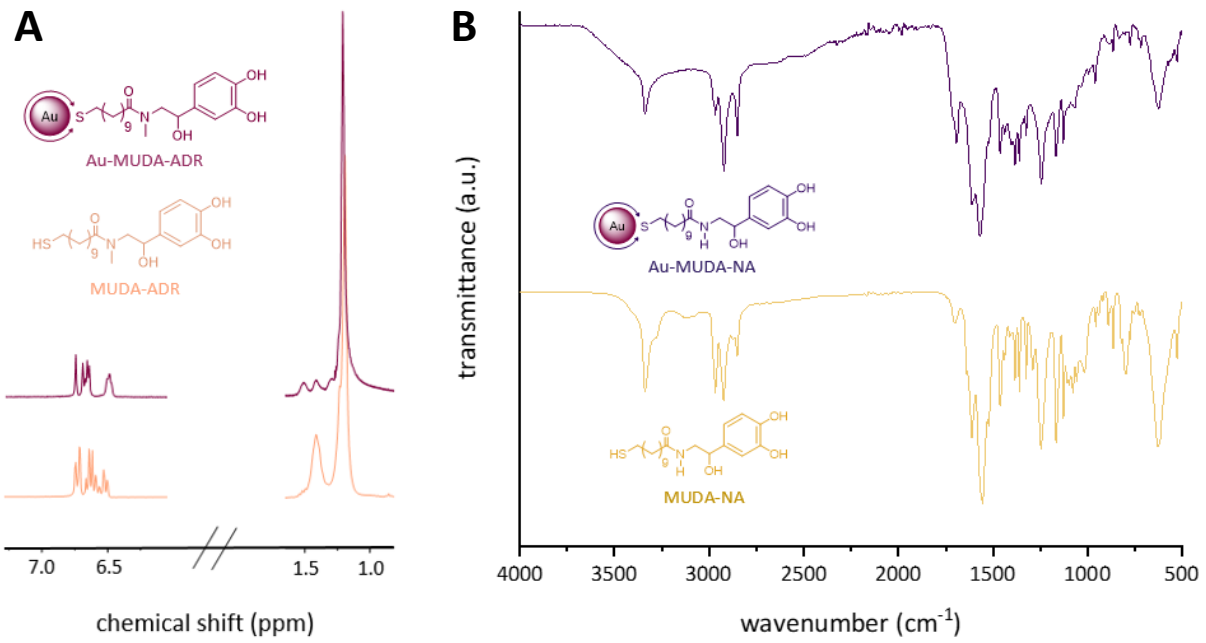

Figure 27: (A) NMR spectra sequence of Au-MUDA-ADR (top) and MUDA-ADR (bottom) and (B) IR spectra of Au-MUDA-NA (top) and MUDA-NA (bottom).

IR spectra of the Au NP samples were recorded and compared with the free ligands. With the spectra of Au-MUDA-NA NPs (Figure 27 B, top) and MUDA-NA (Figure 27 B, bottom) as an

example, unambiguous similarities were observed. Both samples show a characteristic ν_{O-H} resonance around 3300 cm^{-1} that is assigned to the hydroxyl groups. Again, intensive ν_{C-H} absorptions in the range of 3000 cm^{-1} to 2800 cm^{-1} suggest the presence of the long chain MUDA. Distinct $\nu_{C=O}$ bands between 1650 cm^{-1} and 1600 cm^{-1} originate from the amide bonds within the ligands. Moreover, both spectra show a characteristic ν_{C-S} resonance around 625 cm^{-1} next to multiple further similarities within the entire fingerprint area. In summary, these data demonstrate the successful functionalisation of Au NPs with the catecholamines adrenaline and noradrenaline.

Biological actions of the functionalised Au NPs

The physiological studies at respiratory smooth muscle and intestinal epithelia with the functionalised Au NPs were performed by Rebecca Claßen as part of her PhD thesis in the research group of Prof. Diener at the Institute of Veterinary Physiology and Biochemistry at the Justus Liebig University Giessen. The contractility studies at isolated rat cardiomyocytes were carried out by the research group of Prof. Schlüter at the Physiological Institute at the Justus Liebig University Giessen.

Since adrenaline causes an activation of adrenergic receptors and a stimulation of β_2-receptors on smooth muscle tissue, which induces a bronchodilation,[305] adrenaline functionalised Au NPs could be of medical interest with regard to asthma therapy when applied to the respiratory tract. However, native adrenaline loses its potency due to desensitisation effects,[306] making long-term medication with this drug for the treatment of asthma impractical. Nevertheless, in order to compare the effect of adrenaline functionalised Au NPs and native adrenaline on the smooth trachea muscle, the contractibility of the upper respiratory tract was determined under isometric contraction experiments in an organ bath using bronchial tissue from rats (detailed experimental setup is described in **Chapter 5.9.1.1**).

The results of these studies are shown in **Figure 28**. The restrained rat trachea muscles were pre-contracted with carbachol (CCh) to adjust the muscle to a stable standard condition. Then, the reagents (Au-MUDA-ADR NPs ∅ 9 nm, **Figure 28**, **left**) or native ADR (**Figure 28**, **right**) were added and the tension of the relaxing muscle was measured. After a subsequent washing step, the reagents were applied again in order to investigate the desensitisation effects.

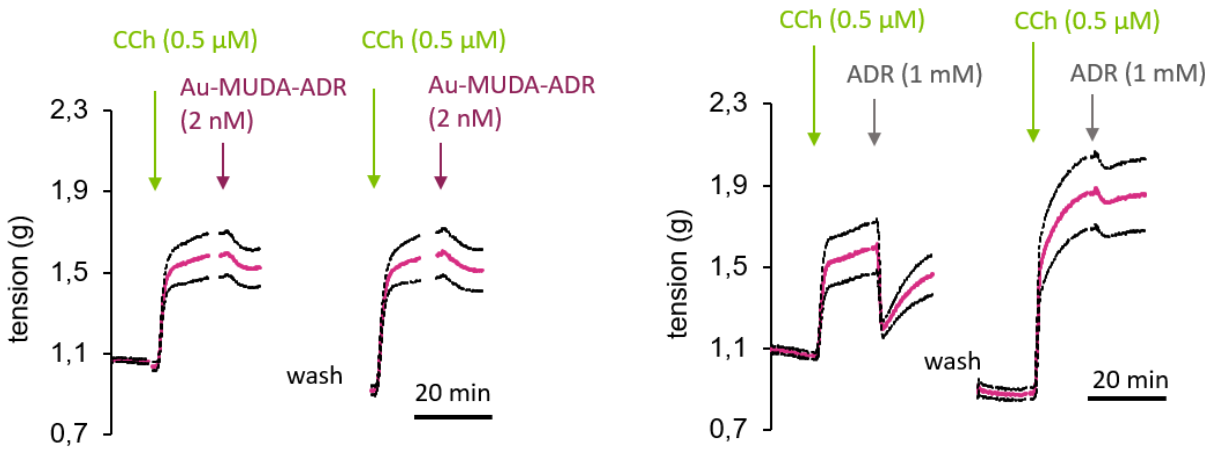

Figure 28: Results from isometric contraction measurements with adrenaline functionalised Au NPs (Au-MUDA-ADR Ø 9 nm) (**left**) or native adrenaline (ADR) (**right**). Rat tracheal rings were restrained in an organ bath, pre-contracted with CCh (0.5 µmol, green arrows) and relaxation was measured after the addition of Au-MUDA-ADR (2 nM, **left**) or native ADR (1 mM, **right**). After a washing step, the same substances were applied to detect a possible desensitisation. Values are mean (pink line) ± SEM, n = 6.

The data show that, in contrast to native ADR, no significant desensitisation of the relaxing effect of adrenaline functionalised Au NPs is observed. Au-MUDA-ADR NPs continue to have the same relaxing effect after the washing step (**Figure 28**, **left**). As already known, native ADR shows hardly any relaxing effect after it was applied a second time (**Figure 28**, **right**). Since these studies showed promising results, further investigations were made in order to inhibit the relaxation when a β_2-receptor blocker (ICI-118551) was present. In this way it was investigated whether the relaxing effect of Au-MUDA-ADR NPs on the tracheal rings in fact originated from a stimulation of a β_2-receptor. The results are displayed in **Figure 29**.

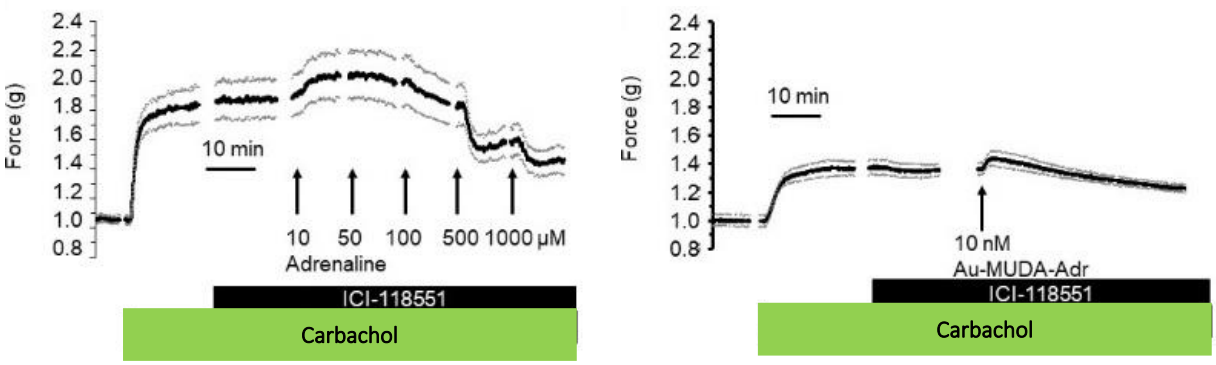

Figure 29: Concentration-dependent relaxation of segments from rat tracheal rings (upper respiratory tract) by adrenaline (arrows) after pretreatment with the β_2-blocker ICI-118551 (10 µmol · l^{-1}; black bar) (**left**). Missing effect of Au-MUDA-ADR (10 nmol · l^{-1}; arrows) after pretreatment with ICI-118551 (10 µmol · l^{-1}; black bar) (**right**). All segments were pre-contracted with CCh (0.5 µmol · l^{-1}; green bar). Data are means (thick line) ± SEM (dotted lines), n = 5 – 8.

This relaxation was inhibited, when adrenaline was administered in the presence of the β_2-receptor blocker ICI-118551 (**Figure 29**, **right**). However, Au-MUDA-ADR NPs induced after a

transient contractile response a slow fall in muscle tone, which was not altered after preincubation with ICI-118551 (10 µmol·1^{-1}) (**Figure 29**, **left**). At the end of each experimental series, a viability control (not shown) was performed with KCl (30 mmol·l^{-1}) demonstrating the viability of the preparations.

In order to find out whether the missing effect on β_2-receptors of Au-MUDA-ADR NPs might be caused by unfavourable spatial conditions, different Au core sizes ranging from 8 to 14 nm were tested. However, none of the tested NPs induced a significant relaxation at the isolated tracheal rings. This was also the case with noradrenaline functionalised Au NP (Au-MUDA-NA (Ø 10 nm)). These studies confirm that no particular stimulatory effect on β_2-receptors on smooth muscle tissues was induced by the functionalised Au NPs.[304]

However, it is possible that the functionalised Au NPs might cause a stimulation of β_1-receptors. These are predominantly expressed in cardiac tissues. Therefore, contractility studies at isolated rat cardiomyocytes were performed with the functionalised Au NPs. In this set-up, the stimulation of β_1-receptors exert a positive inotropic effect and thereby increase cellular contraction.

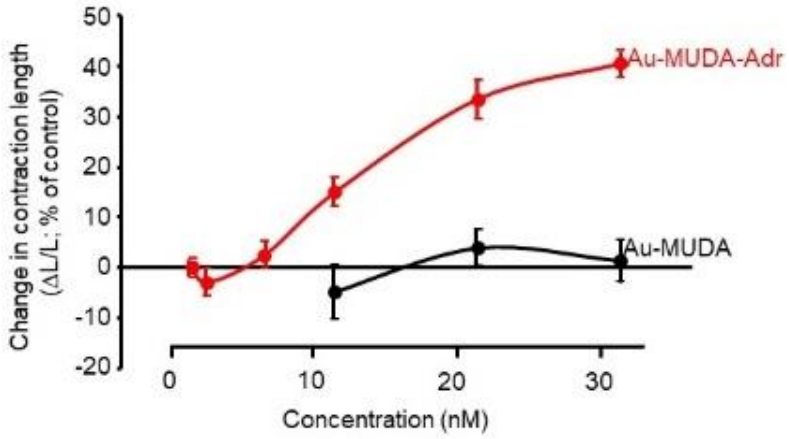

Figure 30: Concentration-dependent increase in contractility of isolated rat cardiomyocytes (measured as cell shortening) by Au-MUDA-ADR (red symbols; n = 53 – 81), but not by Au-MUDA (reference without adrenaline) (black symbols; n = 27 – 36).[304]

Au-MUDA-ADR NPs (Ø 9 nm) indeed increased cellular shortening in a concentration-dependent manner, i.e. exerted a positive inotropic action and thus stimulated the receptors (**Figure 30**). On the other hand, this was not observed for Au-MUDA NPs (Ø 9 nm) as a non-catecholamine carrying reference (**Figure 30**). The increase in contractility induced by the highest concentration used of Au-MUDA-ADR NPs (30 nmol·l^{-1}) reached about 2/3 of the increase in contractility induced by native ADR (5 µmol·l^{-1}) (not shown). The stimulatory effect of Au-MUDA-ADR NPs was significantly inhibited by pretreatment with β_1-receptor blocker atenolol (10 µmol·l^{-1}) (not shown).[304]

These functionalised Au NPs show biological activity in the nanomolar range in various biological systems, where β_1-adrenergic receptors are involved in the control of physiological processes such as intestinal secretion or cardiac contractility.

3.2.2.2 Biofunctionalisation of Au NPs with the Artificial β_2-Receptor Agonist Salbutamol

Since adrenaline or noradrenaline functionalised Au NPs did not induce a stimulation of β_2-receptors on tracheal smooth muscle in contrast to the native compounds, a further approach was conducted this time with an artificial short-acting β_2-receptor agonist. Salbutamol is widely used as a sympathomimetic in the treatment of bronchial asthma and chronic obstructive pulmonary disease (COPD). Salbutamol (SB) exhibits a structural similarity to ADR and NA. However, the presence of the tertbutyl group on the N atom greatly increases its selectivity for β_2-receptors.[307] Thus, the synthesis of salbutamol functionalised Au NPs is presented in the following section.

Ligand synthesis

The synthesis was performed according to a modified procedure by Abed *et al*.[301] As mentioned before, the linker molecule MUDA was reacted with the coupling reagents *N*-hydroxysuccinimide (NHS) and diisopropylcarbodiimide (DIC) in absolute dimethyl formamide at room temperature in order to form an active ester with NHS (Scheme 9).

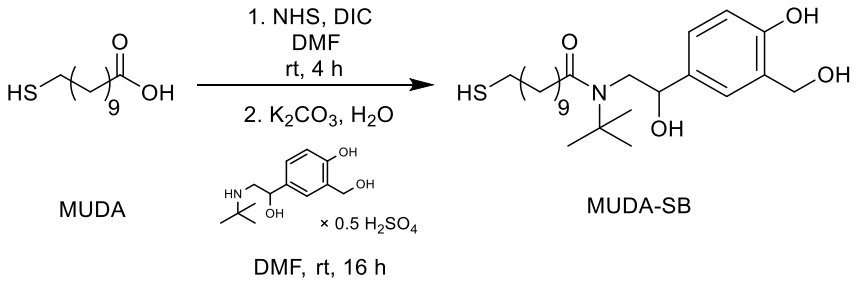

Scheme 9: Ligand synthesis of MUDA-SB using the coupling reagents NHS and DIC according to Abed *et al*.[301]

Salbutamol was dissolved in DMF, added to the solution and reacted with the active ester to an amide under mildly basic conditions. Aqueous work-up as well as purification *via* column chromatography proceeded. However, the product was only obtained in a small yield (20%) with an impurity of DIU. A reason for the low yield might be the sterically very demanding ^{t}Bu group on SB. A further synthetic approach was performed using **h**exafluorophosphate **a**zabenzotriazole **t**etramethyl **u**ronium (**HATU**) as a coupling reagent. HATU is particularly suitable for the formation of amide bonds of sterically demanding amines.

MUDA was dissolved in DMF and cooled to 0 °C. NEt_3 and HATU were added and after 5 min salbutamol hemisulfate (SB) dissolved in DMF was added to the reaction mixture (Scheme 10).

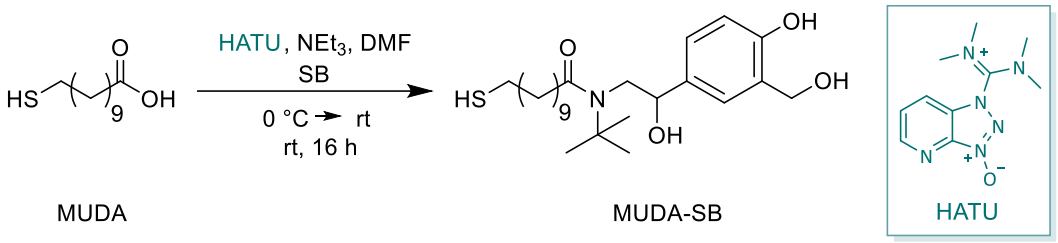

Scheme 10: Ligand synthesis of MUDA-SB using the coupling reagent HATU.

During this reaction, an active ester was formed, which reacted with the nucleophilic amine to the desired amide. Aqueous work-up was performed in order to obtain the product. However, the use of HATU in this synthetic procedure did not result in a higher yield or a higher purity. The structure of MUDA-SB was investigated using NMR, IR and ESI-MS. ^{1}H-NMR spectra show all expected products including aromatic proton resonances between 7.20 ppm and 6.51 ppm, which are attributed to the phenol ring of SB. A significant singlet at 1.15 ppm can be assigned to the ^{t}Bu rest of SB. Furthermore, proton resonances of MUDA are present, such as intense resonances in the range of 1.65 ppm to 1.12 ppm. In ESI MS measurements, the molecule ion $[M\text{-}H]^-$ of *m/z* 438.26 was found for MUDA-SB. This matches with the calculated ligand mass.

Nanoparticle functionalisation

As a following step, surface functionalisation with MUDA-SB was performed on Au-Citrate NPs in a ligand exchange reaction, as displayed in **Scheme 11**. Au-Citrate NP (Ø 13 nm) dispersion was degassed with argon prior to the dropwise addition of MUDA-SB dissolved in DMSO. To ensure a pink and clear NP dispersion during the ligand exchange, the dispersion was adjusted to pH 8 by adding NEt_3. The reaction mixture was stirred at room temperature before it was purified *via* dialysis in order to remove free ligands and unbound species from the functionalised NP dispersion.

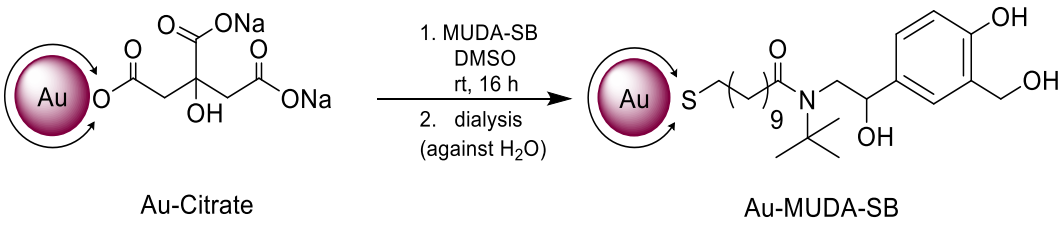

Scheme 11: NP functionalisation in a ligand exchange reaction with MUDA-SB.

TEM images show that the morphology of the functionalised NPs has not changed during the ligand exchange reaction (**Figure 31 A**). Spherical monodisperse Au NPs remain present with a diameter of d_{TEM} = 13.0 ± 1.0 nm. Furthermore, the Au-MUDA-SB NPs reveal a distinct plasmon resonance with λ_{max} at 531 nm. The organic framework of the functionalised Au NPs was investigated using NMR and IR spectroscopy. The ^{1}H-NMR spectrum of Au-MUDA-SB NPs shows

the majority of the expected proton resonances, like the aromatic proton resonances between 7.14 ppm to 6.57 ppm, which are attributed to the phenyl ring of SB. However, not all proton resonances were resolved sufficiently, and the resonances in the range of 1.32 ppm and 1.09 ppm are located under solvent signals and can therefore not be determined. Furthermore, in addition to the NMR resonances of residual H_2O and added NEt_3, there is another solvent impurity from DMF as well as the side product DIU present in the sample. **Figure 31 B** shows the IR spectrum of Au-MUDA-SB NPs (**Figure 31 B**, **bottom**) in comparison to the free ligand MUDA-SB (**Figure 31 B**, **top**). Both spectra reveal correspondences, such as the distinct $\nu_{C=O}$ vibration around 1650 cm^{-1}, which can be assigned together with the δ_{C-N} oscillation around 1245 cm^{-1} to the amide bond formed.

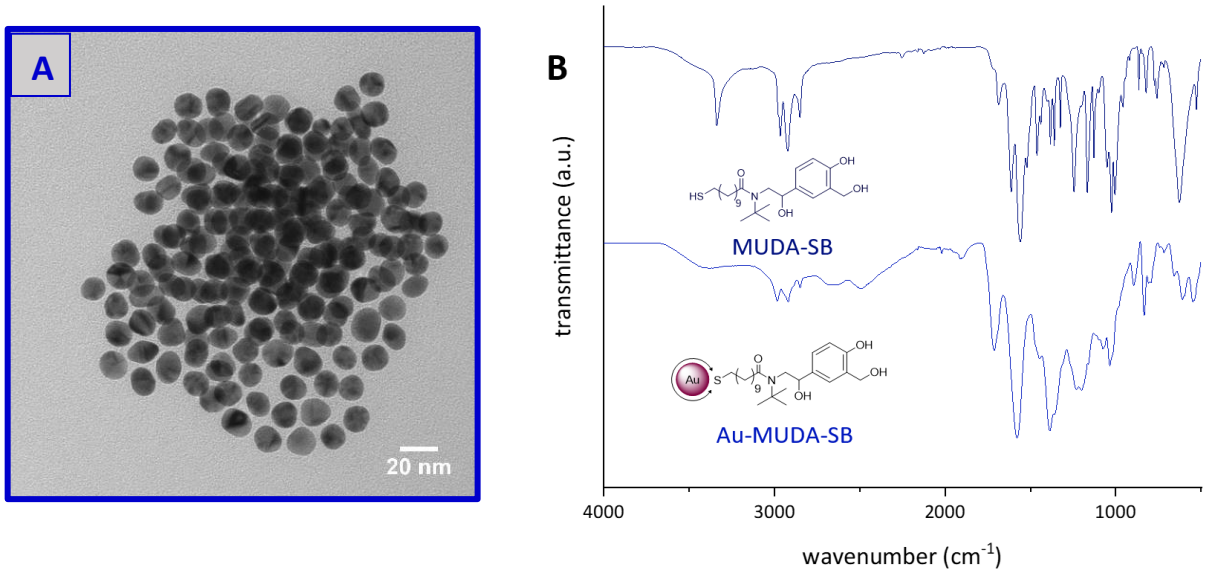

Figure 31: (**A**) TEM image of Au-MUDA-SB NPs and (**B**) corresponding IR spectra in comparison to the free ligand MUDA-SB (**top**).

Moreover, characteristic absorptions between 3000 cm^{-1} and 2800 cm^{-1} are attributed to the long alkyl chain of MUDA. Furthermore, the distinct ν_{C-S} band around 620 cm^{-1} indicates the presence of the free thiol in the ligand (**Figure 31 B**, **top**) as well as the thiolate unit attached on to the Au NP surface in the spectrum of Au-MUDA-SB NPs (**Figure 31 B**, **bottom**). These IR spectra reveal quite distinctly that the IR spectra of functionalised NPs frequently show a broadening of the bands. In addition, the Au-MUDA-SB NP sample displayed here was not completely dry, as can be readily recognised from the water band around 3350 cm^{-1}.

The analytical characterisation indicates a possible functionalisation of Au NPs with SB. However, future ligand syntheses need to be optimised, in order to obtain higher yields and to increase the purity. Only then, salbutamol functionalised Au NPs can be studied in biological systems.

3.2.2.3 Biofunctionalisation of Au NPs with a tropane alkaloid

Hereinafter, the biofunctionalisation of Au NPs with atropine is described using a separate synthetic pathway. In nature, atropine is found as the poison of the deadly nightshade "*atropa belladonna*" (**Figure 32**, **left**). As a biogenic substance, atropine chemically already contains an ester function. Therefore, mild conditions in further reactions are required. Since the molecule itself offers a free hydroxyl group, an ester bond with a spacer can be formed.

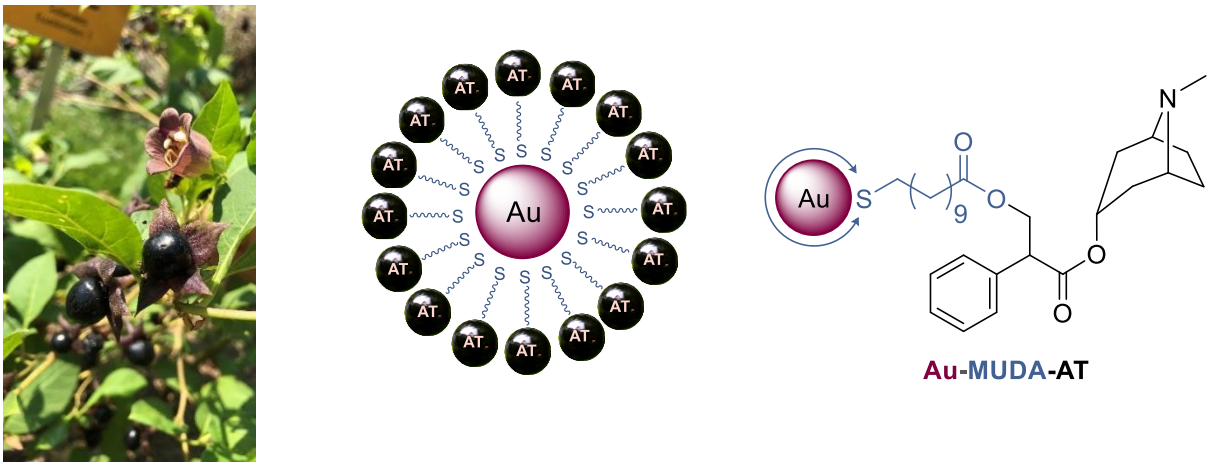

Figure 32: Image of deadly nightshade "*atropa belladonna*" (photo: Annabelle Mattern) (**left**), scheme (**centre**) and structure of atropine functionalised Au NPs (**right**).

Inside the body, atropine competes with acetylcholine and acts as a synaptic toxin by blocking M_3 receptors so that acetylcholine or derivatives are unable to act. The detailed mechanism of how atropine is taken up through the gastrointestinal tract (on the apical side of the epithelial membrane) and how it acts on the M_3 receptors on the basolateral side remains not fully understood. Thus, there is interest in whether Au NPs can function as carriers and still overcome this barrier to act on the basolateral side in order to gain potential new insights into this system. Furthermore, atropine is currently used to treat spasms in the gastrointestinal tract, so atropine functionalised Au NPs (**Figure 32**, **right**) could have potential therapeutic applications.

Ligand synthesis

The esterification was performed in an anhydrous medium and under inert atmosphere according to a modified procedure described by Steglich *et al.*[308] For this purpose, MUDA was dissolved in anhydrous DCM and catalytic amounts of 4-(dimethylamino)pyridine (DMAP) (0.1 eq.) were added (**Scheme 12**). Increasing concentrations of DMAP up to 3 eq. did not lead to a higher yield in these syntheses.

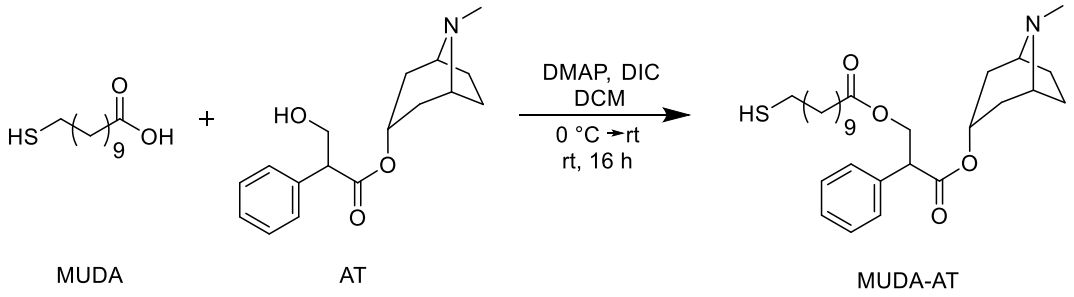

Scheme 12: Synthesis of MUDA-AT in a Steglich esterification.[308]

The coupling reagent diisopropyl carbodiimide (DIC) was added to the cooled solution and then the reaction mixture was treated with the alcohol atropine. As shown in **Scheme 13**, the acid is initially deprotonated and the active DIC ester (*O*-acylisourea) is formed (**Scheme 13**, **top right**).

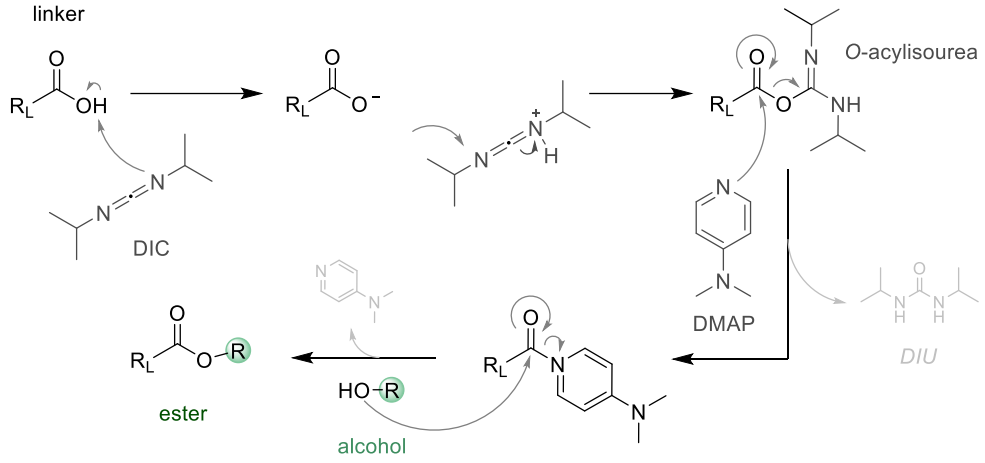

Scheme 13: Potential reaction mechanism of a Steglich esterification.

DMAP is added as an acyl transfer reagent, as it is a stronger nucleophile than the present alcohol, thus preventing a 1,3 rearrangement, which may irreversibly form *N*-acylisourea. DMAP now nucleophilically attacks the partial positively charged C atom of the active DIC ester. This produces diisopropylurea (DIU) as a side product, which precipitates (**Scheme 13**, **bottom right**). Furthermore, a DMAP conjugate results as an intermediate, which no longer undergoes any intramolecular side reactions and instead has a polarised acyl group, enabling a rapid reaction with the alcohol forming the desired ester (**Scheme 13**, **bottom left**). In particular, sterically demanding and acid-labile reactants may undergo reactions under mild conditions at

room temperature in this approach. Remaining acid and other side products were removed in the subsequent aqueous work-up. The crude product was purified over a silica plug. Again, traces of the side product *N*,*N*'-diisopropylurea (DIU) remained and could not be removed completely during various work-up steps. As mentioned before, remaining traces of DIU were tolerated, as the desired biofunctional ligand possesses a thiol moiety, which binds more favourably to the NPs.

The ligand was analysed by NMR, IR and ESI-MS. Attempts of crystallisation were performed but without any success. The ^{1}H-NMR spectrum shows all expected proton resonances. Furthermore, the characteristic intense resonances between 1.63 ppm and 1.10 ppm can be assigned to the long alkyl chain of the thiol spacer MUDA. Moreover, aromatic proton signals in the range from 7.30 ppm to 7.18 ppm correspond to the phenyl unit of atropine and suggest a successful ligand synthesis. IR measurements were performed to verify the existing binding types within the product. First, the spectrum of MUDA-AT (**Figure 33**, **bottom**) reveals distinct $\nu_{C\text{-}H}$ resonances in the range of 3000-2800 cm^{-1}, which are significantly stronger than in the spectrum of AT (**Figure 33**, **top**) and thus indicate the long alkyl chain of MUDA. Furthermore, MUDA-AT shows an intense $\nu_{C\text{-}S}$ vibration at 629 cm^{-1}, suggesting the existence of a thiol.

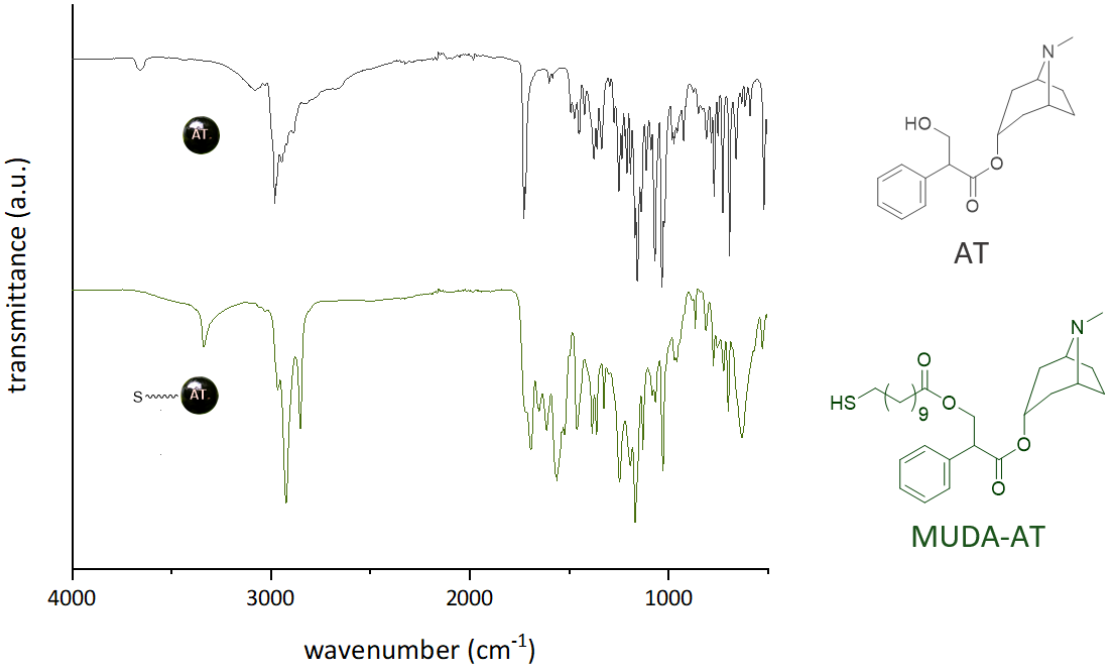

Figure 33: IR spectra of MUDA-AT (**bottom**) and atropine (AT) (**top**).

In addition, unambiguous similarities appear between AT and MUDA-AT, e.g. the strong $\nu_{C\text{-}O}$ bond at 1156 cm^{-1} or the intense $\nu_{C\text{-}N}$ vibration around 1025 cm^{-1}. It is apparent that significantly more absorptions are found in the range of 1750-1600 cm^{-1} in MUDA-AT than in the individual AT, which may be attributed to the two ester moieties next to one another.

The molecular mass of MUDA-AT was confirmed using ESI-MS. The molecule ion $[M\text{-}H]^-$ of 488.23 was found, which matches with the calculated ligand mass.

Nanoparticle functionalisation

As a next step, functionalisation of the synthesised Au NPs took place in ligand exchange reactions with the synthesised MUDA-AT ligand, as displayed in **Scheme 14**.

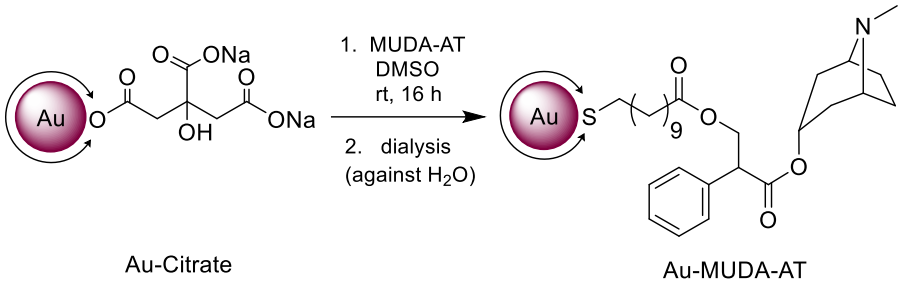

Scheme 14: NP functionalisation in a ligand exchange reaction with MUDA-AT.

The Au NP dispersion of the preferred size was degassed with argon prior the addition of the ligand. MUDA-AT was dissolved in DMSO and slowly added in a large excess (approx. 10^6-fold) under vigorous stirring. To ensure a stable Au NP dispersion during the reaction, the pH was adjusted by adding NEt_3. The obtained pink and stable Au NP dispersion was subsequently purified *via* dialysis in order to remove remaining free ligands and other side products. TEM images of Au-MUDA-AT NPs show (**Figure 34** (**A**)-(**F**)) that no remarkable change in the morphology of the NPs occurred during their functionalisation with MUDA-AT.

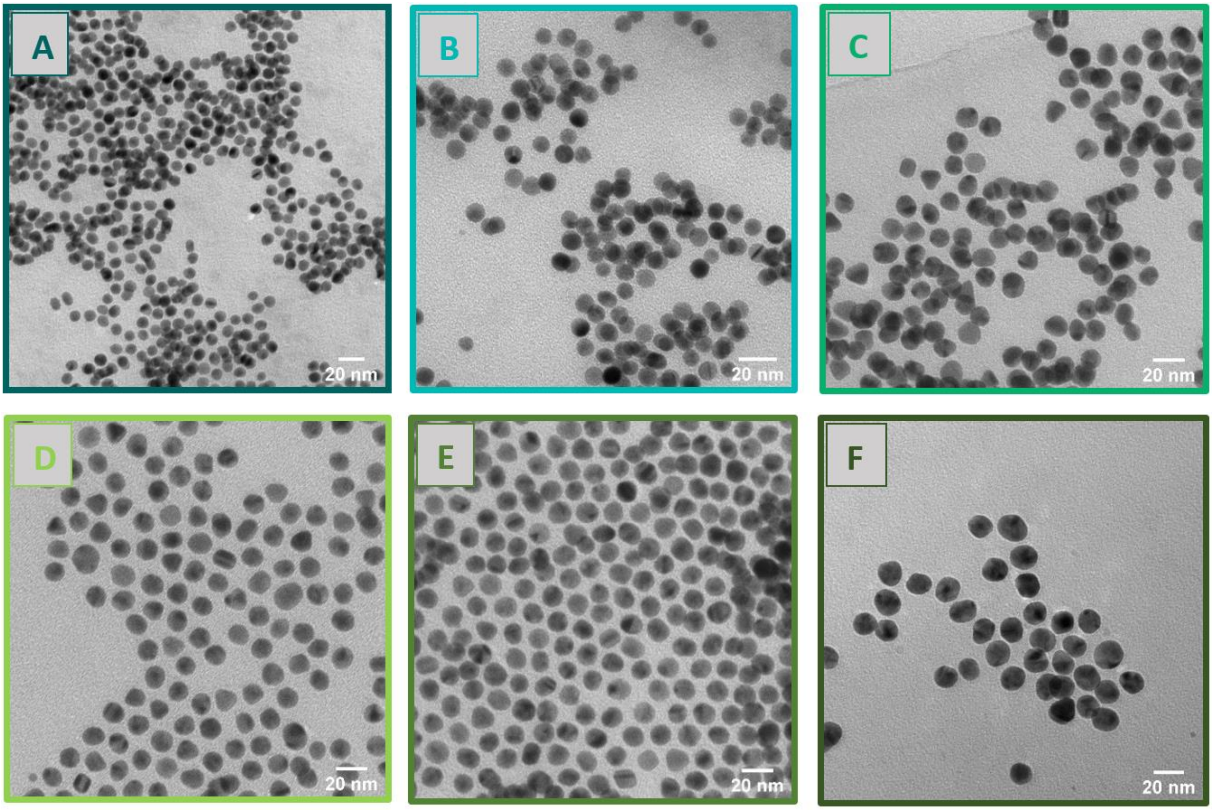

Figure 34: TEM images of Au-MUDA-AT NPs with a size of Ø 8 nm (**A**), Ø 10 nm (**B**), Ø 12 nm (**C**), Ø 13 nm (**D**), Ø 14 nm (**E**) and Ø 16 nm (**F**).

Indeed, the images reveal that MUDA-AT is a suitable ligand to sufficiently stabilise the Au NPs, resulting in no agglomeration. The determined values of d_{TEM} remain in the range of the sizes found for the corresponding starting particles (**Figure 35 A**). The ligand shells appear to increase slightly in all approaches due to the new sterically demanding ligand. This is evidently shown in the d_{hydr} values (**Figure 35 A**), all of which were slightly larger after the functionalisation with MUDA-AT.

A

size	8 nm	10 nm	12 nm	13 nm	14 nm	16 nm
sample	Au-MUDA-AT					
d_{TEM} / nm	8.1 ± 0.7	9.7 ± 0.9	12.0 ± 1.0	12.9 ± 1.0	14.0 ± 1.0	15.9 ± 1.1
d_{hydr} / nm	29 ± 8	33 ± 4	112 ± 59	105 ± 42	31 ± 13	53 ± 19
λ_{max} / nm	530	530	529	528	527	528

B

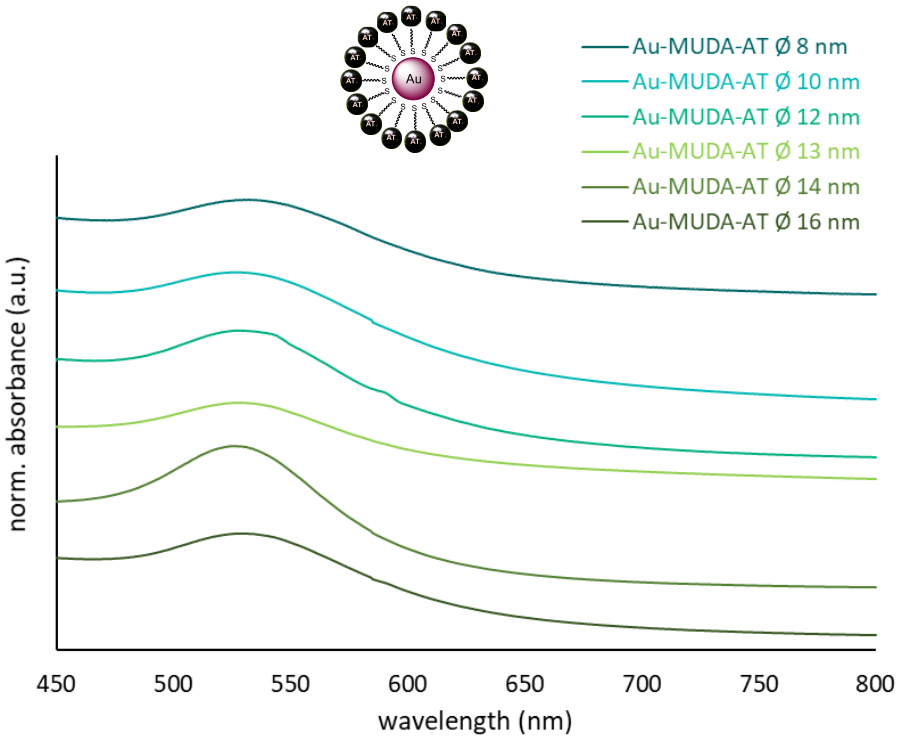

Figure 35: (**A**) Properties of the functionalised Au-MUDA-AT samples in different sizes and (**B**) their corresponding UV/Vis spectra.

The UV/Vis spectra of the Au-MUDA-AT NPs (**Figure 35 B**) show a distinct plasmon resonance with an absorption maximum λ_{max} each in the range around 530 nm. The existence of only one relatively narrow absorption band with a noticeable rise indicates that a stable NP dispersion with monodisperse NPs is present.

The ^{1}H-NMR spectra of Au-MUDA-AT NPs were compared with the spectrum of the synthesised ligand MUDA-AT and show all desired proton resonances. Aromatic proton signals between 7.49 ppm and 7.19 ppm correspond to the phenyl unit present in atropine. Furthermore, significant signals in the range from 1.74 ppm to 1.15 ppm are associated to the long alkyl chain of MUDA-AT.

Similarly, the IR spectrum of the Au-MUDA-AT NP sample (**Figure 36**, **bottom**) was compared with the one of the free ligand MUDA-AT (**Figure 36**, **top**). Thereby, unambiguous similarities were observed, especially the intensive $\nu_{C\text{-}H}$ absorptions in the range of 2900 cm^{-1} confirm the presence of the long chain MUDA.

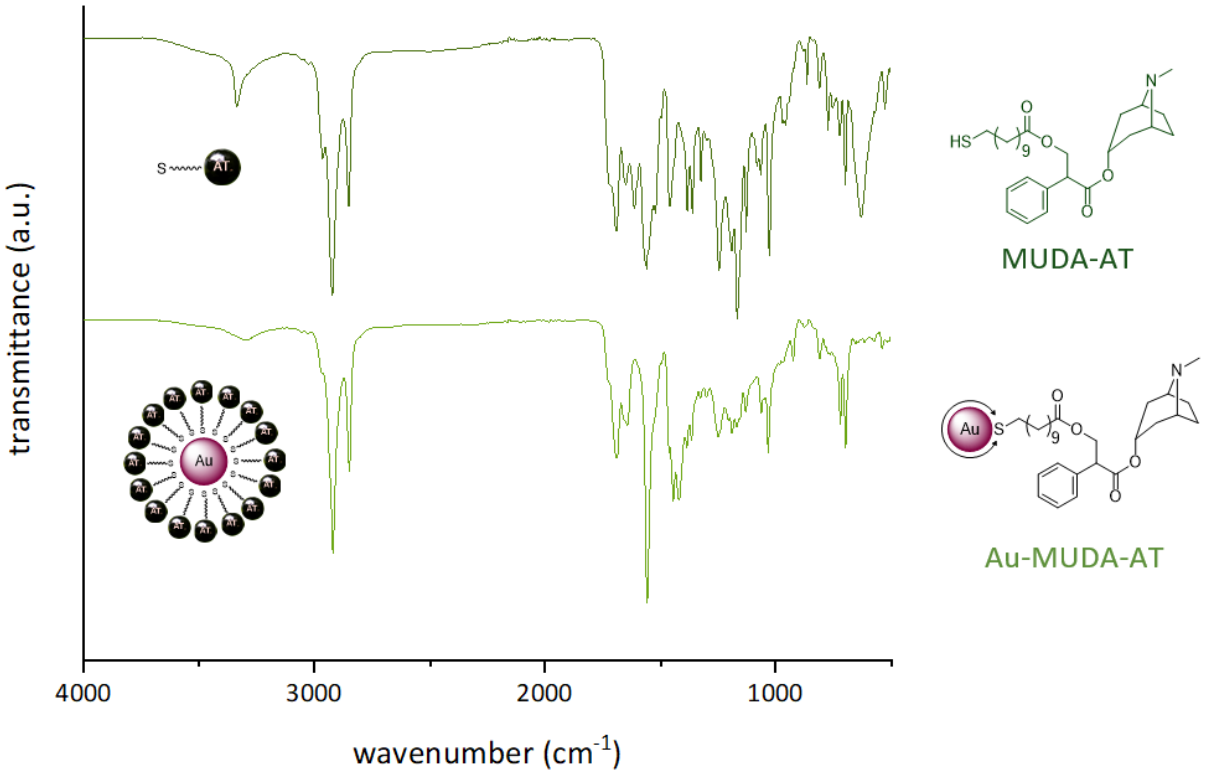

Figure 36: IR spectra of Au-MUDA-AT NPs (**bottom**) and the corresponding free ligand MUDA-AT (**top**).

Furthermore, both $\nu_{C=O}$ absorptions between 1730 cm^{-1} and 1650 cm^{-1} and the $\delta_{C\text{-}O}$ vibrations around 1200 cm^{-1} reveal the ester groups on the organic ligand sphere of the NP samples (**Figure 36**, **bottom**). Even a characteristic $\nu_{C\text{-}N}$ absorption at 1029 cm^{-1} was found in both samples. Moreover, the entire fingerprint areas resemble one another very closely.

In summary, the data of all analytical characterisations unambiguously confirm that Au NPs were successfully functionalised with atropine (AT) and monodisperse NP in selected sizes were obtained.

Biological actions of the atropine functionalised Au NPs

The physiological studies of the functionalised Au NPs were performed by Rebecca Claßen as part of her PhD thesis in the research group of Prof. Diener at the Institute of Veterinary Physiology and Biochemistry at the Justus Liebig University Giessen. In further studies, Au-MUDA-AT NPs were investigated in Ussing Chamber experiments regarding their receptor activities. The intention here was to find out whether Au NPs can function as carriers of the biologically relevant compound atropine across the epithelial membrane, and whether M_3 receptors on the basolateral side get blocked. Furthermore, a size dependent tendency of the effects on M_3 receptors caused by Au-MUDA-AT NPs should be examined.

Results of "Reversed Ussing Chamber" Experiments with Au-MUDA-AT Ø 14 nm

Standard Ussing Chamber experiments are conducted according to the procedure described above. In a reversed experiment the agent of interest is now added on the opposite side of the receptors. The receptors focused on were the muscarinic type 3 (M_3) receptors, which are situated on the basolateral side of the epithelial membrane of rat jejunal tissue. **Scheme 15** illustrates the setups and **Figure 37** and **Figure 38** show the results of such an experiment.

i. control (without NPs)

A control measurement was performed without adding NPs showing that no M_3 receptors are blocked and thus can still be activated.

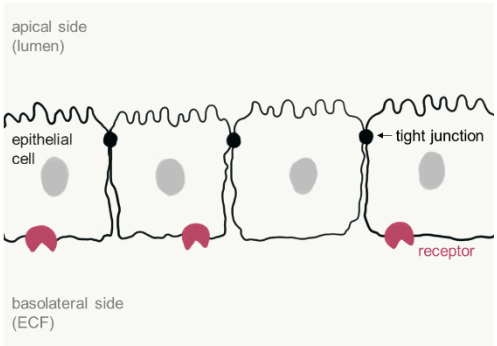

ii. NP treatment

Au-MUDA-AT NPs Ø 14 nm (75 pM) were added on the apical side of a rat jejunal epithelium.

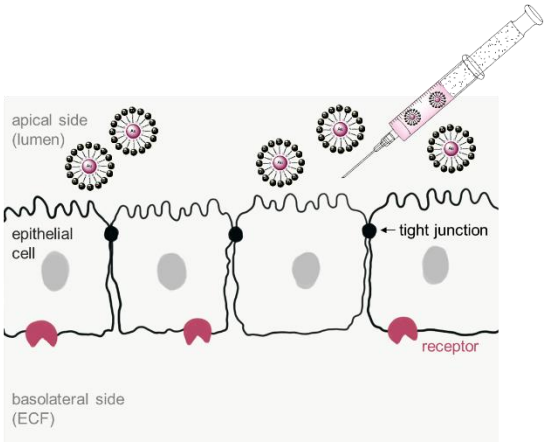

iii. 30 min incubation with NPs

After an incubation time of 30 min the NPs pass the epithelial barrier and block some receptors, but some receptors (not blocked yet) can still be activated.

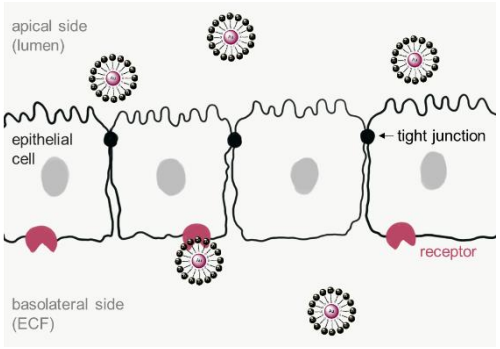

iv. 2 h incubation with NPs

After an incubation time of 2 h the NPs achieve a complete blocking on the basolateral side. Thus, no M_3 receptors can be activated.

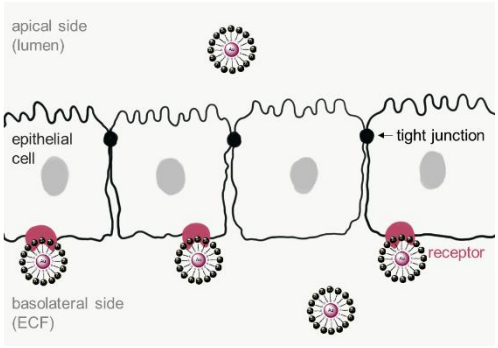

Scheme 15: Experimental implementation in a "Reverse Ussing Chamber Setup" and the obtained results.

In this approach, the agent of interest (Au-MUDA-AT NPs Ø 14 nm) was injected on the apical side (**Scheme 15 ii**), before the secretagogue carbachol (CCh, M_3 receptor agonist) was added on the basolateral side to attempt a stimulation of the receptors. Such an activation of receptors would be displayed in an increase of the measured short circuit current (I_{sc}). Furthermore, these measurements were performed with different incubation times (**Scheme 15 iii** and **iv**) to determine whether the NPs can cross the epithelial barrier, act on the basolateral side and block the receptors there. At the end of each experiment, forskolin (Forsk., another secretagogue) was added to proof if the functional viability of the tissue was still existing. This would be displayed again in an increase of I_{sc}.

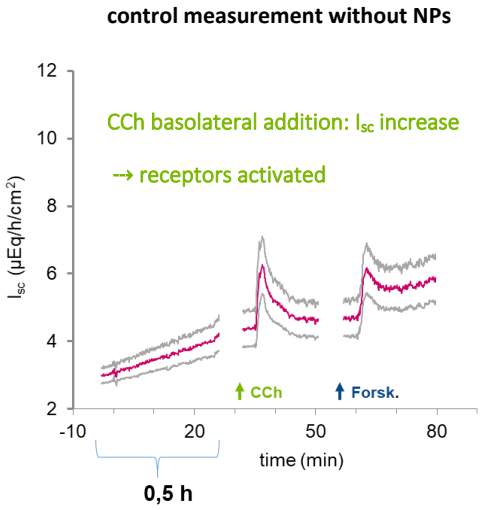

Figure 37: Measured short-circuit current (I_{sc}) over time on rat jejunal epithelium mounted in an Ussing Chamber. No treatment with the NPs took place (control measurement). Carbachol (50 µM; CCh, M_3 receptor agonist) was added to stimulate the receptors displayed as an increase in I_{sc}. Then, forskolin (5 µM; Forsk., another secretagogue) was added resulting in an increase of I_{sc} in order to reveal the functional viability of the tissue. Data are given in mean values ± SEM, n=7-8.

First, a time-dependent control measurement was performed without adding the agent of interest, shown in Scheme 15 (i). After 30 min, CCh was added on the basolateral side and an increase of the measured short circuit current was observed (Figure 37). This proves that the M_3 receptors are stimulated and not blocked.

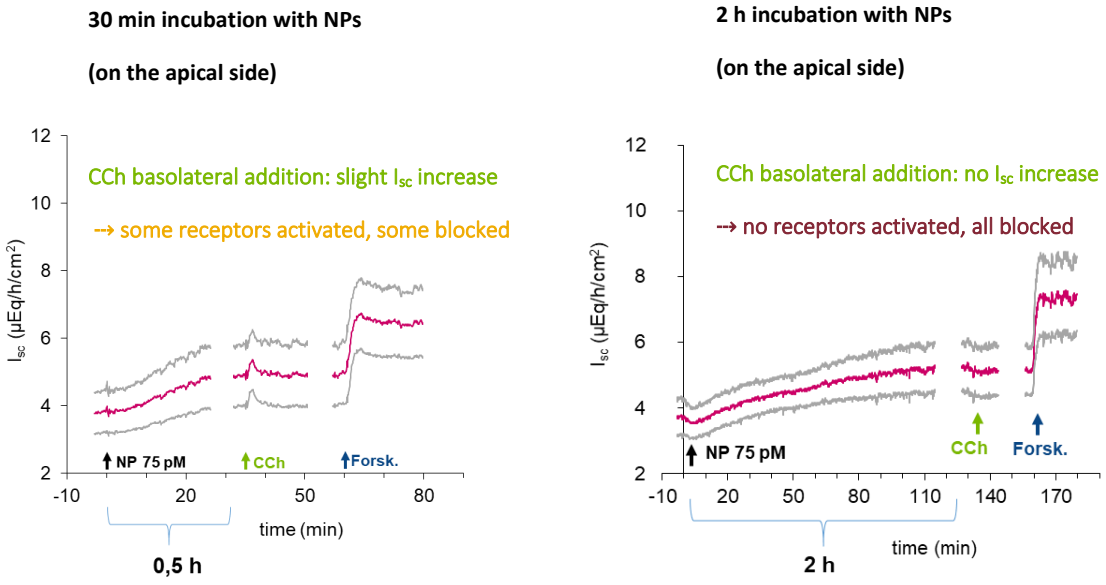

Figure 38: Measured short-circuit current (I_{sc}) over time on rat Jejunal epithelium mounted in an Ussing Chamber. A treatment with the NP (75 pM) took place on the apical side of the tissue before the secretagogue carbachol (50 µM; CCh, M_3 receptor agonist) was added to stimulate the receptors displayed as an increase in I_{sc}. Then, forskolin (5 µM; Forsk., another secretagogue) was added resulting in an increase of I_{sc} in order to reveal the functional viability of the tissue. Incubation of the tissues with Au-MUDA-AT reduced (**left**) or abolished (**right**) the response to CCh, without impairing tissue viability. Data are given in mean values ± SEM, n=7-8.

In a next experiment, the Au-MUDA-AT NPs (75 pM) were added on the apical side (**Scheme 15 ii**) and incubated for 30 min (**Scheme 15 iii**). The response to CCh was reduced, displayed only in a slight increase of I_{sc} (**Figure 38, left**) and thus indicating that only a part of the receptors could be activated, while the other part of receptors were already blocked (**Scheme 15 iii**). This again implies that the NPs cross the epithelial barrier.

In another experiment, the incubation time was extended to 2 h in total (**Scheme 15 iv**). When CCh was applied, no increase of I_{sc} could be observed. (**Figure 38, right**). This suggests that no receptors are stimulated because all are blocked. This may lead to the conclusion that the passage of Au-MUDA-AT NPs is complete in less than 2 h and a complete blocking effect can be observed on the basolateral side. This is the first time that atropine functionalised Au NPs are reported to cross the epithelial barrier and act on the basolateral side as a receptor poison.

Impact of Au NPs Core Sizes on Blocking of M_3 receptors by Au-MUDA-AT NPs

In further Ussing chamber experiments, the Au-MUDA-AT NP's direct ability to block M_3 receptors was investigated without overcoming a barrier beforehand but in dependence of the Au NP core sizes used. For this purpose, standard Ussing chamber set-ups were chosen: Au-MUDA-AT NPs (20 nmol) of the preferred size were applied to the basolateral side of the jejunum of a rat (**Figure 39 A**). After 20 min, native CCh (50 µmol) was added on the basolateral side and the change in I_{SC} was measured (**Figure 39 B**). The control groups (**Figure 39 B**, black bar, pooled control from all experiments) were not treated with NPs. The results of the different Au NPs core sizes were compared with each other (**Figure 39 B**, coloured bars, each n = 8-9) as well as with the control group.

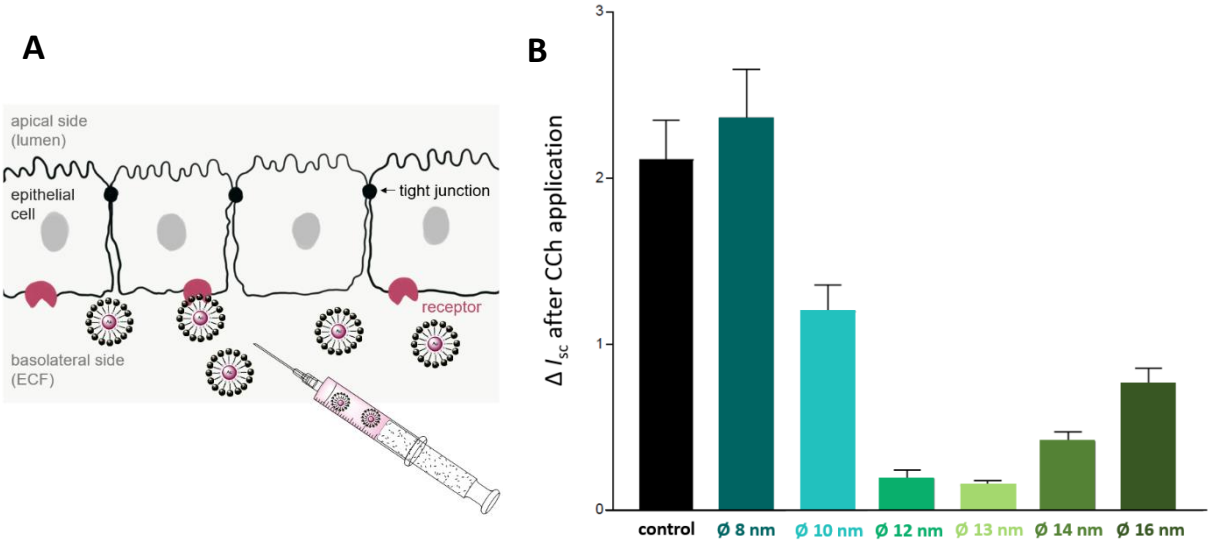

Figure 39: (**A**) Scheme of the experimental implementation in a "standard Ussing Chamber Setup" on an epithelial membrane (jejunum) of a rat and (**B**) change of the measured short circuit current I_{SC} after the application of CCh (50 µmol) on the basolateral side of Jejunal epithelium, which was treated with Au-MUDA-AT NPs (20 nmol) of a selected size on the basolateral side 20 min before.

The diagram in **Figure 39 B** illustrates a size dependent effect of the used atropine functionalised Au NPs on ΔI_{SC} after CCh application. Following a treatment with for instance Ø 12 nm or Ø 14 nm Au-MUDA-AT NPs, only slight changes of the I_{SC} were observed. Like in previous experiments, the reason for this is that the majority of M_3 receptors are blocked by either of the two and therefore cannot be activated after the addition of the secretagogue CCh. Expanding the range of sizes a bit further, one can observe larger ΔI_{SC} after treatment with Ø 10 nm or Ø 16 nm Au-MUDA-AT NPs. Hence, fewer M_3 receptors are blocked and these NPs appear to be less effective. The addition of Ø 8 nm Au-MUDA-AT NPs increases the ΔI_{SC} even stronger than the control group (**Figure 39 B**, black bar), which received no treatment. However, the large error bar of the Ø 8 nm NP measurements renders this experiment less precise. Nevertheless, in order to achieve the optimal size for a strong effect, Ø 13 nm Au-MUDA-AT NPs were synthesised. Taking into account the standard deviation of the size with d_{TEM} = 12.9 ± 1.0 nm, these NPs show an even smaller ΔI_{SC} and thus an improved effect compared to the other NP sizes.

Figure 39 B thus shows a correlation between size and ΔI_{SC}, and it was determined that Au-MUDA-AT NPs with a size of Ø 13 nm are the most effective in our experimental set up. Furthermore, our experiments show that atropine functionalised Au NPs with a size of Ø 14 nm cross the epithelial barrier and act on the basolateral side as a receptor poison. Thus, this system is of high interest for further studies also on a microscopic level, in order to obtain an in-depth investigation of the Au NPs within the tissues.

3.3 Amine stabilised Au NPs and Biomimetic Functionalisation

Amine stabilised Au NPs have been described rarely in the literature. However, a free amine moiety on the ligand sphere offers the opportunity to attach a wide variety of relevant acidic compounds to the ligand surface using peptide bond formation (**Figure 40**, **yellow**).

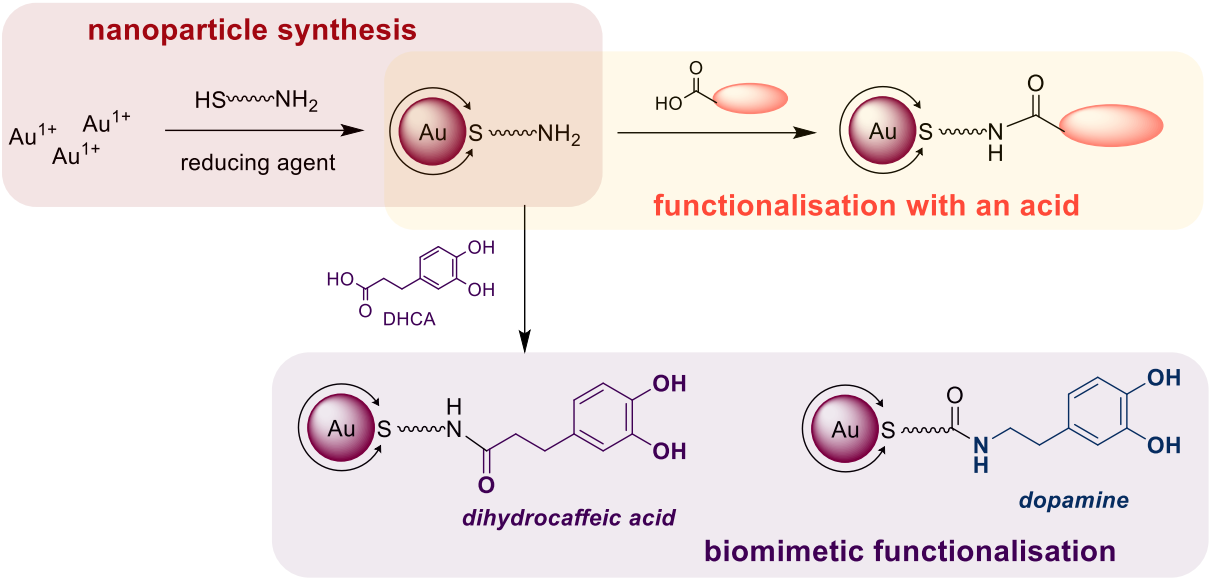

Figure 40: Synthetic strategy towards amine stabilised Au NPs (**red**) and their subsequent functionalisation with an acidic compound (**yellow**). A biomimetic functionalisation (**violet**) is possible when compounds mimic biogenic substances, e.g. dihydrocaffeic acid (DHCA) mimics dopamine (DA).

If the acidic compound resembles another biogenic substance, this may be referred to as *biomimetic functionalisation*. The binding moiety is present on the ligand shell that is significant for e.g. the stimulation of a receptor, and thus simulates the presence of a biogenic substance, although this biogenic compound is in fact not linked to the NPs. Here, we used dihydrocaffeic acid (DHCA; 3(3,4-dihydroxy-phenyl) propionic acid) (**Figure 40**, **violet**), which was linked to the amine stabilised Au NPs by its free acid moiety by a peptide bond formation. Similarly to dopamine, it exhibits a free catechol unit relevant for adrenergic receptor stimulation.

Worth mentioning is that although long chain and shorter chain aminothiols are commercially available – which are structurally similar to the already used mercapto acids – the aminothiols are very expensive. Therefore in a first step, low cost aminothiols were used as alternatives in initial trials. Cysteamine (Cys or 2-Aminoethanethiol) has already been mentioned in the literature when stabilising Au NPs; 4-aminothiolphenol (ATP) was chosen additionally.

Nanoparticle syntheses with short chain mercaptoamines

Au-Cys NPs were synthesised according to a procedure described by Lee *et al.*[309] $HAuCl_4 \cdot 3\ H_2O$ was dissolved in H_2O and cysteamine hydrochloride (Cys · HCl) was added. After 20 min of stirring in the dark, freshly prepared $NaBH_4$ solution was added and the mixture was stirred at room temperature in the dark for 16 h (**Scheme 16**).

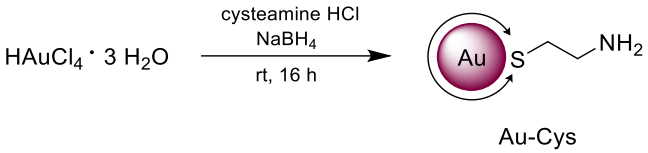

Au-Cys

Scheme 16: Synthesis of Au-Cys NPs using the approach by Lee *et al.*[309]

Subsequently, the violet NP dispersion was purified *via* dialysis. However, the NP dispersion seems to interact with the dialysis membrane, which, after a while, resulted in a less stable dispersion that agglomerated quickly. **Figure 41** shows the TEM images of Au-Cys NPs before (**Figure 41**, **left**) and after (**Figure 41**, **right**) purification *via* dialysis. Initial agglomeration could be observed especially after the purification, which is in accordance with the visual findings.

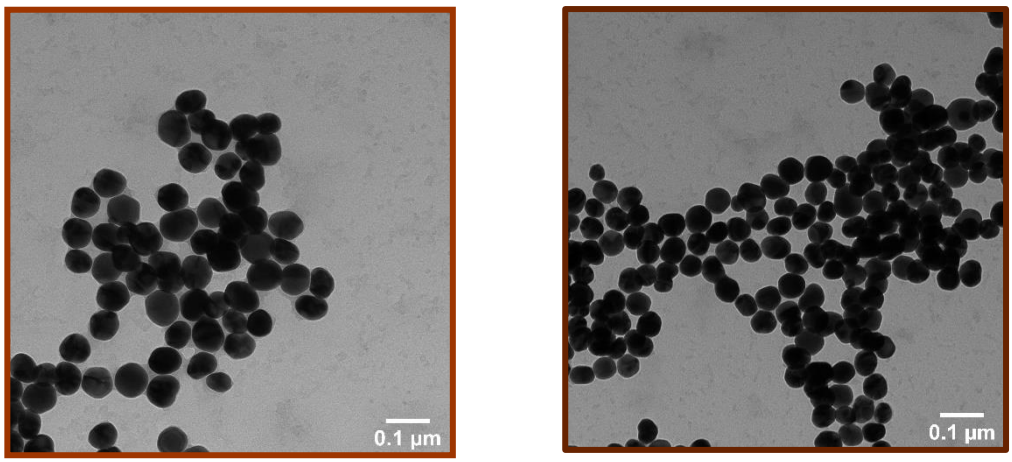

Figure 41: TEM images of Au-Cys NPs before (**left**) and after (**right**) purification via dialysis implying agglomeration of the NPs.

As an alternative purification method, centrifugation was performed, but the NP were not able to get redispersed again.

Furthermore, a ligand exchange starting from Au-Citrate NPs was performed with Cys · HCl, but agglomeration occurred immediately after the new ligand was introduced, even if the reactions were attempted at different pH values. Since neither a direct synthesis with $NaBH_4$ nor a ligand exchange reaction led to stable amine stabilised Au NPs, no further analysis (UV/Vis, DLS, IR, NMR) was performed. Instead, 4-aminothiolphenol (ATP) was used for further investigations as a new ligand type. Its phenyl ring could provide additional stability in order to obtain more stable Au NPs.

Syntheses of a modified version of the Stucky method were performed while PPh_3AuCl was dissolved in DMSO, the ligand ATP was added and heated to 60 °C. Then, a solution of $^tBuNH_2$:BH_3 in DMSO was added quickly under vigorous stirring. The solution was stirred at 60 °C in the dark for 1 h before being cooled in an ice bath (Scheme 17).

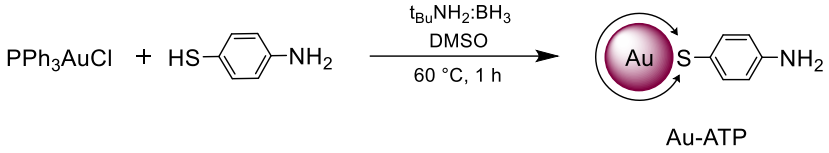

Scheme 17: Synthesis of Au-ATP NPs.

The NPs were purified *via* centrifugation. Precipitation with EtOH or acetone was possible. Even though TEM images (not shown) show that spherical NPs formed, these could not be completely redispersed after centrifugation. Furthermore, TEM images revealed next to agglomerated NPs a large amount of remaining solvent and presumably other impurities encapsulating the Au NPs. On the other hand, precipitation with acetonitrile (MeCN) was possible and the Au NPs were redispersed in acidic H_2O (pH 3) before further washing procedures with MeCN were performed (4 × 30 min, 8000 rpm). Afterwards the Au NPs were redispersed in H_2O, acidified with hydrochloric acid to pH 1, forming a red dispersion. The TEM image shows that spherical, nearly monodisperse Au NPs were obtained. No organic solvent residues, no excess nucleation nuclei and almost no agglomeration were observed. In conclusion, a precipitation with MeCN and redispersion in acidic H_2O works well, while nor stable or purified Au-ATP NPs could be obtained in precipitation with EtOH or acetone.

Even though redispersion in acidic H_2O was possible, the Au NPs did not appear to resist centrifugation completely without any damage. Therefore, the milder purification method of dialysis was used for further approaches. The Au NPs withstood the dialysis (12 h or 36 h, respectively) and clean Au NPs were obtained. However, an excessively long dialysis (more than 48 h at a stretch) also led to an incipient agglomeration of the Au NPs; they seemed to react with the tube material.

In the described manner, Au-ATP NPs were synthesised in two different sizes. The higher the equivalent of ligand and reducing agent added, the smaller the diameter of the obtained Au NPs (Table 7).

Table 7: Properties of the synthesised Au-ATP NPs.

sample	ratio of PPh_3AuCl: ATP : t_{Bu}-NH_2BH_3	d_{TEM}	λ_{max} (UV/Vis)	concentration
Ø 8 nm	1.0 eq. : 0.6 eq. : 8.9 eq.	7.9 ± 0.8 nm	537 nm	238 nmol/l
Ø 6 nm	1.0 eq. : 1.0 eq. : 9.6 eq.	5.8 ± 0.8 nm	538 nm	570 nmol/l

Within 10 min, a colour change occurred and the NP dispersion turned increasingly into deep red over time, e.g. noticeable after 50 min (**Figure 42 A**). The TEM images of the purified samples reveal monodisperse, spherical Au NPs with a size of d_{TEM} = 7.9 ± 0.8 nm (**Figure 42 B**) and d_{TEM} = 5.8 ± 0.8 nm (**Figure 42 C**), respectively. Moreover, the Ø 6 nm Au-ATP NPs arranged themselves hexagonally on the TEM grid, indicating a particularly high monodispersity. UV/Vis spectra display a distinct plasmon band each with λ_{max} around 540 nm. However, the Ø 6 nm Au-ATP NP dispersion was not stable over a longer time period (< 2 months).

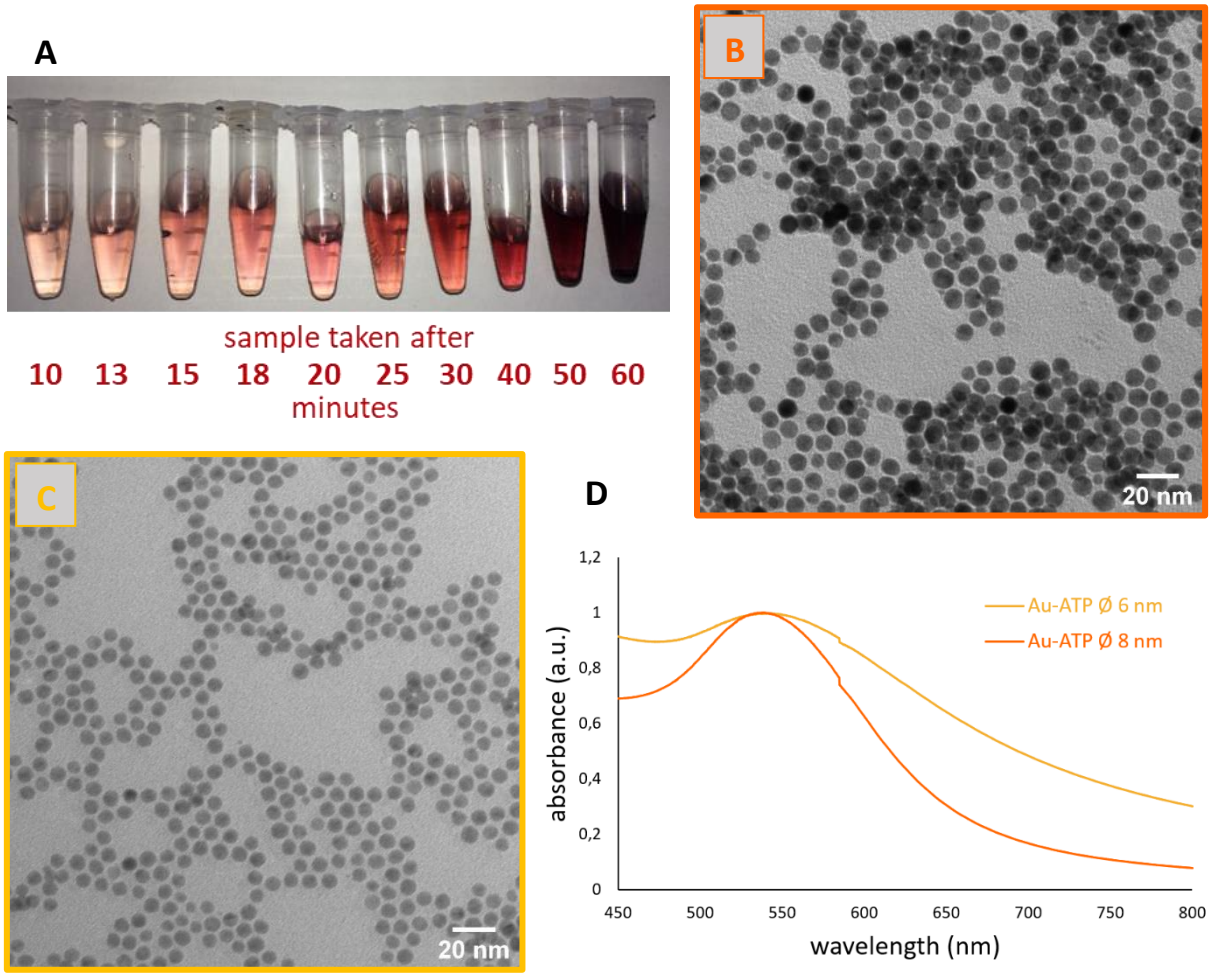

Figure 42: (**A**) Optical monitoring of the synthesis over time; Au NP solution turns increasingly dark red. TEM images of Au-ATP NPs Ø 8 nm (**B**) and Ø 6 nm (**C**) and their corresponding UV/Vis spectra (**D**).

Additionally, ^{1}H-NMR and IR spectroscopy clearly reveal the presence of ATP on the Au NP surface. The ^{1}H-NMR spectrum shows two aromatic proton signals at 7.55 ppm and 7.23 ppm, which are assigned to the phenyl ring of the linker. However, the amine protons were not detected as the spectrum was measured in D_2O.

Figure 43 displays the IR spectrum of Au-ATP NPs (**Figure 43**, **bottom**) in comparison to the free ligand ATP (**Figure 43**, **top**). Both samples reveal distinct similarities in the observed bands. However, the NP sample contains additional bands not found in the free ligand. These intense $\nu_{C\text{-}H}$ resonances in the range 3000 cm^{-1} to 2800 cm^{-1} and the significant $\nu_{S=O}$ oscillation at 1071 cm^{-1} are assigned unambiguously to DMSO as remaining solvent in the sample. Other remaining bands can be attributed to the ligand ATP, such as the weak absorption in the range between 3450 cm^{-1} to 3300 cm^{-1}. These $\nu_{N\text{-}H}$ vibrations together with $\delta_{N\text{-}H}$ oscillations at 1581 cm^{-1} as well as the $\nu_{C\text{-}N}$ bands around 1300 cm^{-1} strongly indicate the presence of an amine on the ligand shell. Furthermore, weak benzene overtone $\delta_{C\text{-}H}$ bands around 1970 cm^{-1} are assigned to the aromatic ring. A distinct $\nu_{C\text{-}S}$ vibration around 600 cm^{-1} refers to the thiolate moiety attached to the Au core. Taken together, these data indicate that monodisperse Au-ATP NPs were synthesised in a direct approach with the short chain ligand ATP.

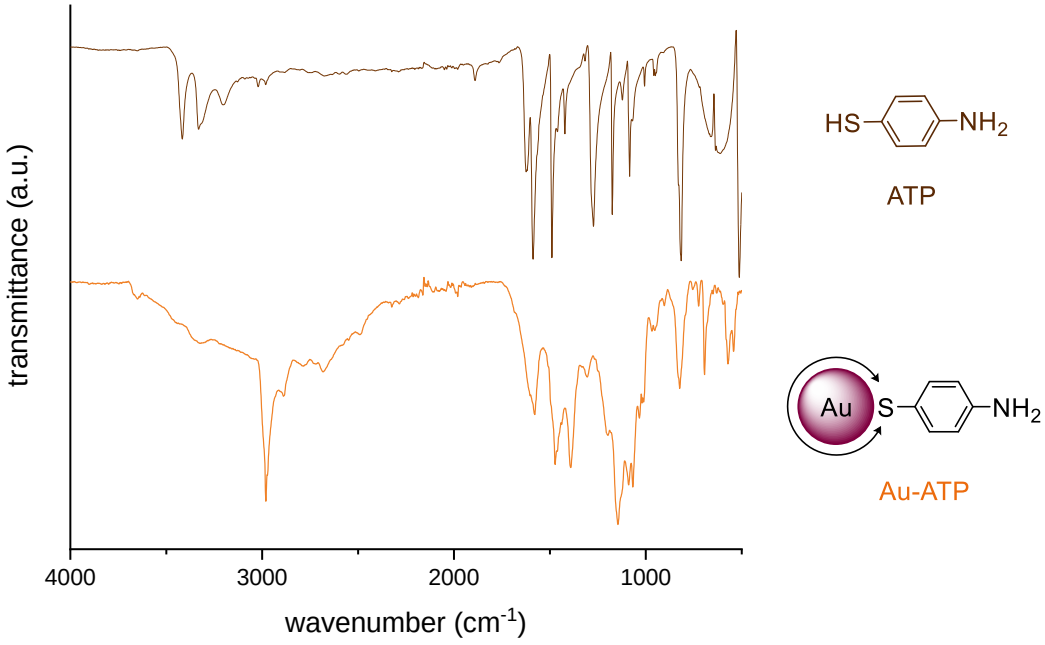

Figure 43: IR spectra of the ligand ATP (**top**) and Au-ATP NPs (**bottom**).

In order to prepare amine stabilised Au NPs with even longer shelf lives (> 2 months), ligands with a longer chain may increase the stability, due to their steric bulkiness, which was already observed in similar systems with long chain mercapto acids as ligands, e.g. MUDA. Moreover, a comparable long-chain mercaptoamine could be introduced in order to compare these systems. However, mercaptoundecylamine (MUAM) is in fact commercially available, but extremely expensive compared to the acid (MUDA: about 15 €/g; MUAM: about 10000 €/g). Due to the high price, the MUAM ligand was prepared using a four step approach (**Scheme 18**). The experimental work of the MUAM synthesis was performed jointly with Sebastian Habermann (advanced module of the master student under the supervision of the author).

3.3.1 Synthesis of Mercaptoundecylamine

Starting from 11-bromoundecanol, the phthalimide protecting group was introduced in a salt metathesis (**Scheme 18**, **top right**)).[310] Then, the remaining hydroxyl group was converted with bromine in an Appel-reaction (**Scheme 18**, **centre**).[311]

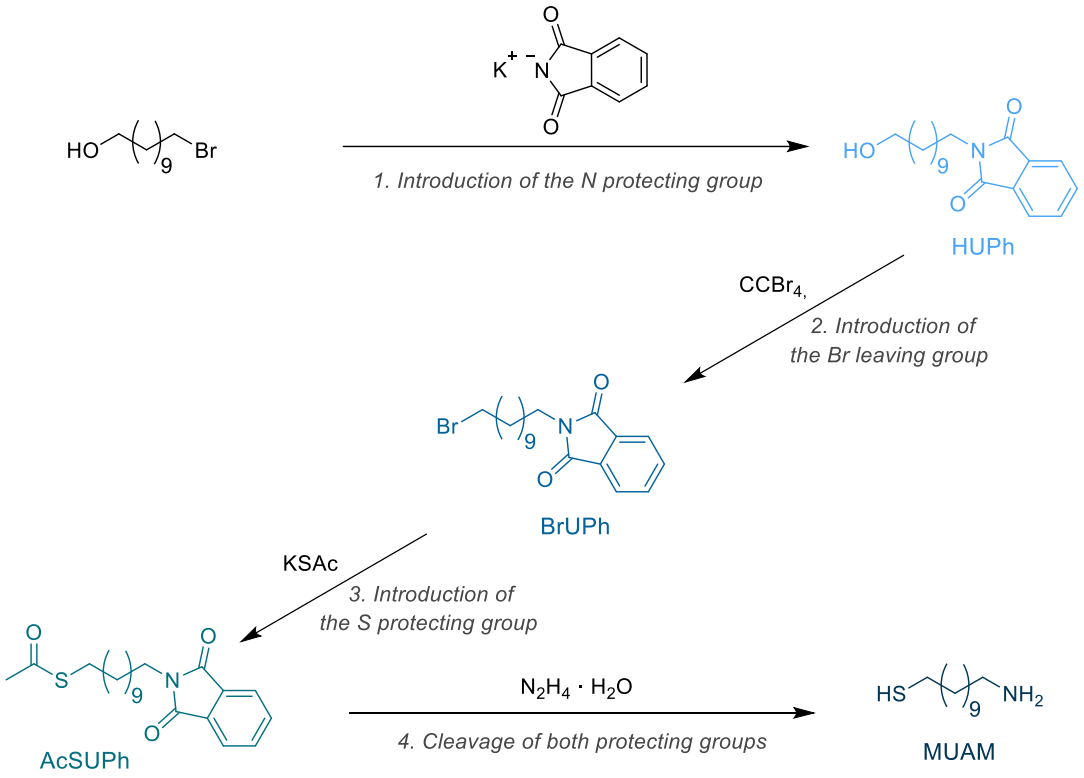

Scheme 18: Four step synthesis of mercaptoundecylamine (MUAM).

With this new attractive leaving group, again a salt metathesis was performed in order to introduce the sulfur containing thioacetate protecting group in the third step (**Scheme 18**, **bottom left**). Afterwards, both protecting groups were released in one step with hydrazine hydrate in order to obtain MUAM with a free thiol and a free amine moiety (**Scheme 18**, **bottom right**).

The Gabriel synthesis[310] in the first step of the approach was performed according to a procedure described by Perez *et al*.[312] and is displayed in **Scheme 19**.

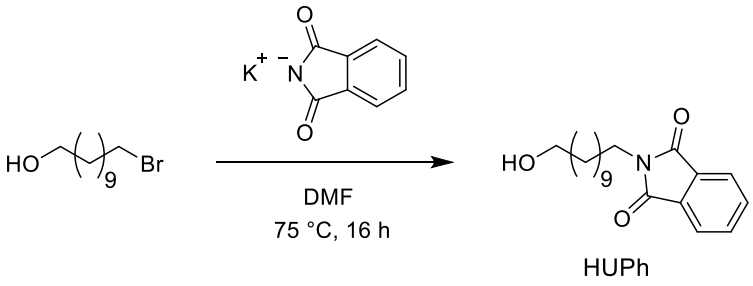

Scheme 19: Synthesis of 11-hydroxyundecylphthalimide (HUPh).

11-Bromoundecanol was reacted with potassium phthalimide in anhydrous DMF at 75 °C. The polar side product potassium bromide precipitated as a colourless material and was filtered off. After aqueous work-up, the product 11-hydroxyundecylphthalimide (HUPh) was obtained as colourless crystalline solid in a very good yield (97%). The product was characterised using NMR, IR and ESI MS. The ^{1}H-NMR spectrum shows all desired proton resonances. Furthermore, two characteristic signals were observed at 7.84 ppm and 7.71 ppm, which can be attributed to the symmetric aromatic protons of the phthalimide protecting group. Intense resonances in the range of 1.67 ppm to 1.34 ppm refer to the long alkyl chain. Moreover, the spectrum shows two triplets at 3.67 ppm and 3.60 ppm, which were shifted to higher frequencies. These were determined using 2D experiments and were assigned through their long range coupling correlations. The proton signal at 3.60 ppm refers to the methylene group next to the nitrogen of phthalimide and the triplet at 3.67 ppm was assigned to the adjacent methylene group of the hydroxyl group.

IR spectroscopy was performed to additionally verify the existing binding types within the compound as described on the next page. The molecular mass was confirmed using ESI MS. The molecule ion $[M+Na]^{+}$ of *m/z* 340.20 was found for HUPh, which matches the calculated mass.

As a next step the hydroxyl group was converted into a bromine moiety, which again represents a good leaving group for a further reaction. This Appel reaction[311] was performed according to a procedure described by Jarboe *et al.*[313](Scheme 20).

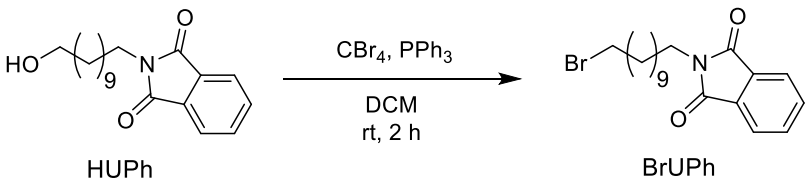

Scheme 20: Synthesis of 11-bromoundecylphthalimide (BrUPh).

HUPh was dissolved in tetrabromomethane (CBr_4) and anhydrous DCM, triphenylphosphine (PPh_3) was added and the mixture was stirred at room temperature. The crude product was purified by column chromatography (hexane : ethyl acetate, 10:1) to obtain the 11-bromoundecylphthalimide (BrUPh) as a colourless solid in a good yield (70%).

The formation of the side product triphenylphosphine oxide with its strong P=O bond is the driving force of this process and related to the Mitsunobu reaction.[314]

Only slight changes in the compound's structure occurred, nevertheless the ^{1}H-NMR spectrum shows a distinct difference to the starting material HUPh. Since the hydroxyl group was exchanged by a bromine atom, the electronic environment of the adjacent protons changed. Thus, a signal at 3.39 ppm results from the methylene group next to the bromine which is now shifted to a lower frequency compared to the starting material's resonance at 3.60 ppm. All other proton signals remained similar to the chemical shifts present in the starting material.

For instance, the characteristic signals between 1.65 ppm and 1.21 ppm refer to the long alkyl chain and two distinct resonances at 7.83 ppm and 7.70 ppm are assigned to the aromatic ring of the phthalimide protecting group. **Figure 44** shows the IR spectra of both compounds synthesised in the first two steps: HUPh (**Figure 44**, **top**) and BrUPh (**Figure 44**, **bottom**).

Both samples show intense $\nu_{C\text{-}H}$ absorptions in the range of 3000 cm^{-1} to 2800 cm^{-1}, suggesting the presence of the long alkyl chain. Furthermore, each spectrum shows a sharp $\nu_{C=O}$ vibration around 1700 cm^{-1}, which corresponds to the imide and indicates the successful introduction of the phthalimide protecting group in the first step of the synthesis.

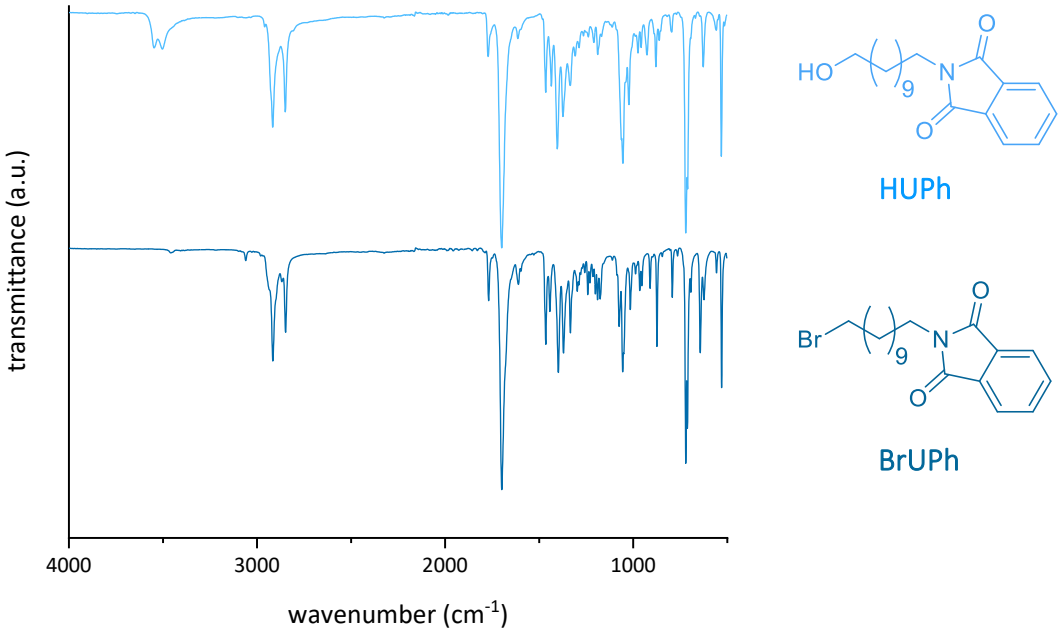

Figure 44: IR spectra of 11-hydroxyundecylphthalimide (HUPh) (**top**) and 11-bromoundecylphthalimide (BrUPh) (**bottom**).

Moreover, HUPh (**Figure 44**, **top**) shows characteristic $\nu_{O\text{-}H}$ resonances around 3500 cm^{-1}, which are assigned to its hydroxyl group. These bands were no longer observed in the spectrum of BrUPh (**Figure 44**, **bottom**), indicating a successful exchange of the hydroxyl group by bromine. Instead, BrUPh reveals a stronger $\nu_{C\text{-}Br}$ vibration at 640 cm^{-1}, which corresponds to the introduced halogen.

In ESI MS measurements, the molecule ion $[M+Na]^+$ *m/z* 404.10 was found for BrUPh, which matches the calculated mass. Taken together, these data unambiguously prove the successful synthesis of pure BrUPh in a good yield.

BrUPh was further reacted in a salt metathesis in order to introduce the sulfur containing thioacetate protecting group. The synthesis was performed according to a procedure described by Wang *et al.*[315] and is displayed in **Scheme 21**.

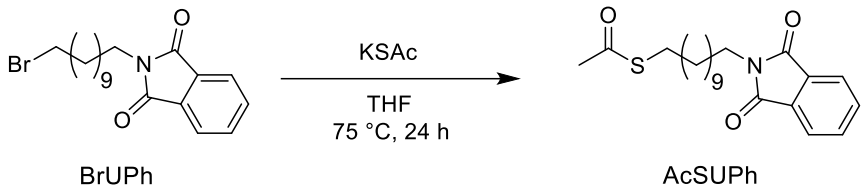

Scheme 21: Synthesis of 11-(*N*-phthalimido)undecyl thioacetate (AcSUPh).

BrUPh was dissolved with potassium thioacetate (KSAc) in anhydrous THF and heated to reflux. The pure product 11-(*N*-phthalimido)undecyl thioacetate (AcSUPh) was obtained after aqueous work-up as a brown solid in a very good yield (92%). Again, during this salt metathesis potassium bromide formed as a side product and could be removed during purification.

The ^{1}H-NMR spectrum reveals that the product possesses intense resonances in the range between 1.65 ppm to 1.15 ppm, which can be assigned to the long alkyl chain. Furthermore, the aromatic proton signals at 7.83 ppm and 7.70 ppm can be attributed to the phthalimide protecting group. These results prove that one side of the molecule did not change during the reaction. Moreover, the bromine was substituted by a thioacetate group and thus, a different shift was observed for the adjacent methylene group with a triplet at 2.85 ppm. Again, this resonance is shifted to lower frequency because of the lower electronegativity of sulfur. In addition, the spectrum of AcSUPh shows a distinct singlet resonance at 2.31 ppm, which was assigned to the methyl group of thioacetate. IR spectroscopy was performed to additionally verify the existing binding types within the compound. The results are described on the following page. Furthermore, the molecular mass was confirmed using ESI MS and showing the molecule ion $[M+H]^{+}$ of *m/z* 376.20, which matches the calculated mass for AcSUPh.

As a final step, both protecting groups were cleaved off in a reaction with hydrazine hydrate according to a procedure described by Wang *et al.*[315] and displayed in Scheme 22.

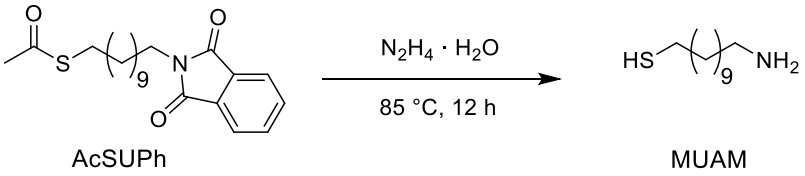

Scheme 22: Synthesis of mercaptoundecylamine (MUAM).

AcSUPh was dissolved in dry EtOH and hydrazine hydrate was added at 0 °C. Then, the reaction mixture was slowly heated to 85 °C. Aqueous work-up proceeded at various pH values and the product mercaptoundecylamine (MUAM) was obtained as a slightly brown solid in a good yield (75%).

During this reaction, hydrazine attacks the imide nucleophilically, resulting in the formation of the free amine and phthalhydrazide. Moreover, hydrazine attacks the carbonyl of the thioacetate. After a rearrangement, this forms the side product acethydrazide as well as the

thiolate, which leads to a thiol under acidic conditions. In summary, two different reactions occur next to each other during this synthetic step.

The ^{1}H-NMR spectrum reveals that no aromatic protons are present, indicating the successful cleavage of the phthalimide protecting group. Furthermore, a distinct singlet around 2.31 ppm, which was assigned to the thioacetate moiety, was not observed in the spectrum of MUAM. This implies the sulfur protecting group being released as well. Moreover, the compound still shows characteristic intense resonances in the range between 1.68 ppm and 1.12 ppm, which are assigned to the long alkyl chain. **Figure 45** shows the IR spectra of AcSUPh (**Figure 45**, **top**) and MUAM (**Figure 45**, **bottom**).

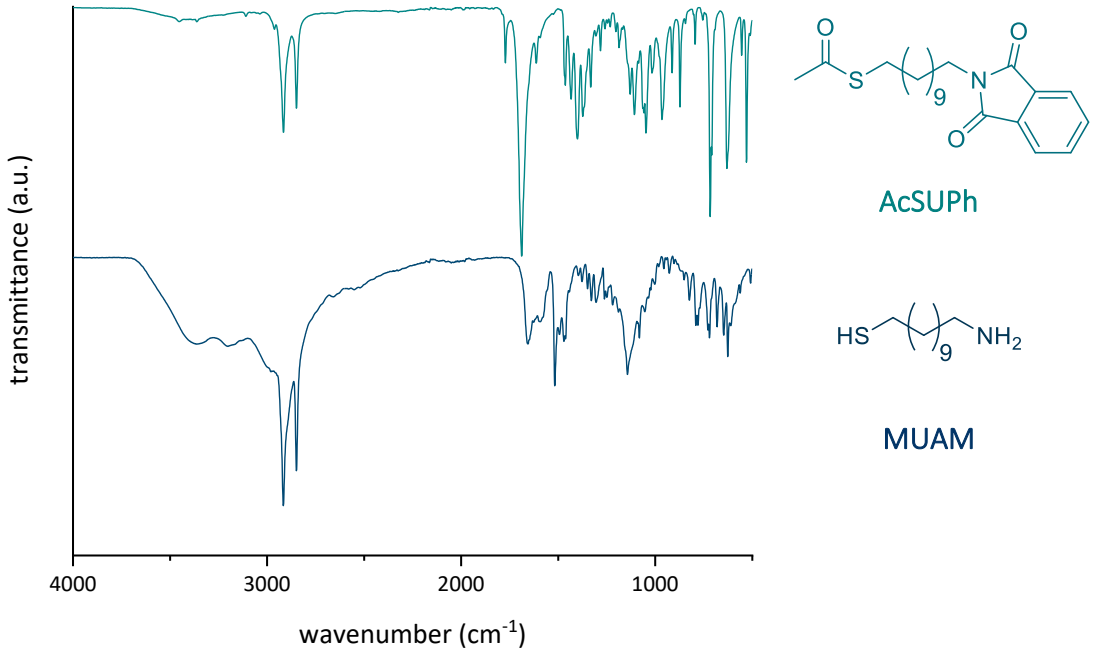

Figure 45: IR spectra of 11-(*N*-phthalimido)undecyl thioacetate (AcSUPh) (**top**) and mercaptoundecylamine (MUAM) (**bottom**).

The spectrum of AcSUPh (**Figure 45**, **top**) shows $\nu_{C\text{-}H}$ vibrations in the range between 3000 cm^{-1} and 2800 cm^{-1} attributed to the long alkyl chain. Moreover, the distinct $\nu_{C=O}$ vibration around 1700 cm^{-1} was observed, which can be assigned to the imide as well as the thioacetate carbonyl unit. A significant indication of a successful introduction of thioacetate gives the presence of a strong $\nu_{C\text{-}S}$ band at 624 cm^{-1}, which did not exist in the starting material BrUPh.

In the spectrum of MUAM (**Figure 45**, **bottom**), $\nu_{C\text{-}H}$ vibrations between 3000 cm^{-1} and 2800 cm^{-1} reveal the presence of the long alkyl chain. However, the characteristic strong $\nu_{C=O}$ resonance around 1700 cm^{-1} is not detected anymore and thus indicates a successful cleavage of the phthalimide protecting group. Furthermore, phthalhydrazide as a potential side product was completely removed from the mixture during the work-up. Moreover, $\nu_{N\text{-}H}$ vibrations at

3367 cm^{-1} and 3194 cm^{-1} can be assigned to the free primary amine. The presence of a free thiol group can be deduced from a $\nu_{C\text{-}S}$ band at 624 cm^{-1} as well as a weak $\nu_{S\text{-}H}$ vibration around 2550 cm^{-1}. The latter one appears typically very weak. Summarising these results, the spectrum of MUAM reveals the cleavage of both protecting groups. In ESI MS measurements, the molecule ion $[M+H]^+$ of *m/z* 204.20 was found, which matches the calculated mass of MUAM.

As a conclusion, these data unambiguously prove the successful synthesis of MUAM. Thus, this compound was used as a ligand for further syntheses of amine stabilised Au NPs.

Nanoparticle syntheses using the long chain ligand MUAM

Au-MUAM NPs were synthesised using the modified version of Stucky and coworkers,[291] but slightly changed to the Au-ATP NPs preparation.

Again, PPh_3AuCl was dissolved in DMSO with the ligand mercaptoundecylamine (MUAM) and heated to 60 °C, 55 °C or 40 °C, respectively (**Scheme 23**). Then, $^t BuNH_2{:}BH_3$ was added quickly under vigorous stirring. The solution was stirred at the respective temperature in the dark for 1 h before being cooled in an ice bath.

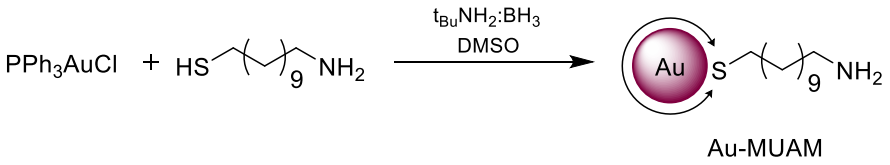

Scheme 23: Synthesis of Au-MUAM NPs.

The following paragraphs will describe the investigation as to how subtle changes in temperature, in this case a difference of 5 K, affect the formation of the NPs.

In several approaches, the reducing agent was added as a solid, as described in the original Stucky method.[291] Thus, the reaction mixture initially is a heterogeneous system during the synthesis until the reducing agent is completely solvated and mixed thoroughly. The NP dispersion turned distinctly red after a short time.

The samples shown in **Figure 46 A** were heated for 1 h at 60 °C. Even after purification, a stable dispersion was obtained, which, as shown in **Figure 46 A**, has mainly spherical NPs with a good size distribution. In the majority of approaches $^{t}BuNH_2$:BH_3 was added dissolved in DMSO. This offers the advantage of a homogeneous and rapid mixing. Again, dark red NP dispersions were obtained. Some NP batches precipitated towards the end of the heating phase, presumably because the formed amine shell NPs are not sufficiently stabilised in the medium DMSO. Though, after purification, stable Au MUAM dispersions were obtained, revealing only spherical Au NPs with a good monodisperse size distribution, as shown in **Figure 46 B**.

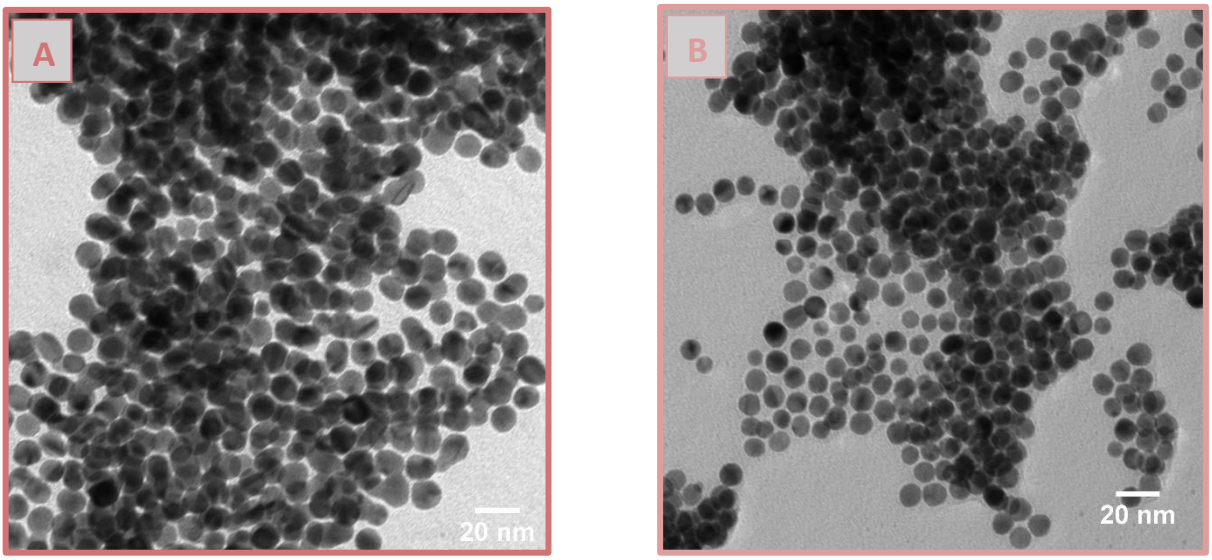

Figure 46: TEM images of Au-MUAM NPs synthesised with $^{t}BuNH_2$:BH_3 added (**A**) as a solid (d_{TEM} = 11.7 ± 1.7 nm (Au-MUAM NPs Ø 12 nm)) or (**B**) dissolved in DMSO (d_{TEM} = 10.7 ± 1.3 nm (Au-MUAM NPs Ø 11 nm)) at 60 °C for 1 h.

In contrast to the synthesis described above, the following samples were heated for 1 h at 55 °C in order to obtain stable Au NP dispersions during the syntheses since the temperature was reduced. As above, stable dark red Au NP dispersions were obtained after the usual work-up. The two approaches were performed using the ratios of PPh_3AuCl : MUAM : $^{t}BuNH_2$:BH_3 (1 eq. : 0.75 eq. : 9.75 eq.). TEM images (**Figure 47**) of these NPs reveal slightly smaller sizes compared to the ones obtained at a higher reaction temperature of 60 °C. **Figure 47 A** shows the particles obtained from the synthesis when the reducing agent was added as a solid (heterogenous). **Figure 47 B** shows the NP formed during the approach when $^{t}BuNH_2$:BH_3 was added dissolved in DMSO (homogenous). Mainly spherical Au NPs were obtained in both batches, whereas the NPs formed with solid $^{t}BuNH_2$:BH_3 (**Figure 47 A**) possessed marginal larger diameters than those in the batch with the homogenously added reducing agent (**Figure 47 B**). Even though the sizes of the Au NPs synthesised in both approaches only hardly deviate, stable Au NPs dispersions were obtained at a slightly lower reaction temperature throughout the syntheses.

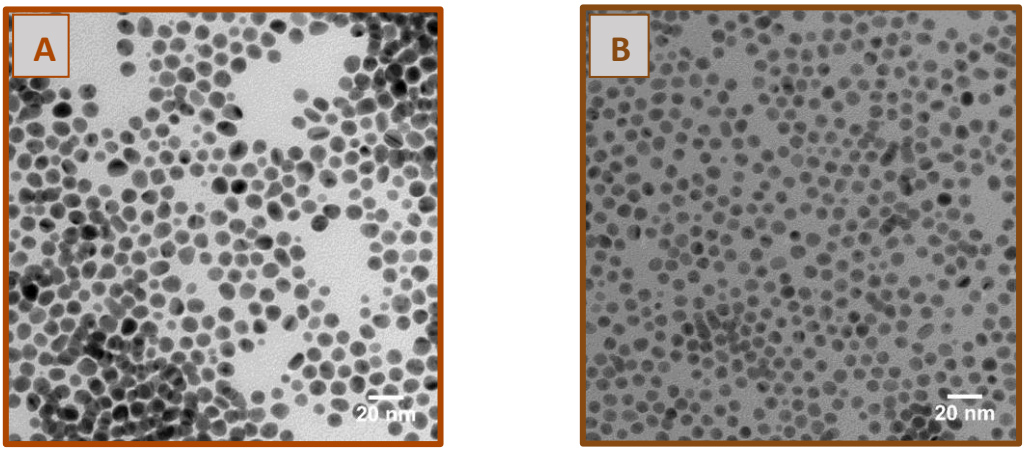

Figure 47: TEM of Au-MUAM NPs synthesised with $^{t}BuNH_2$:BH_3 added (**A**) as a solid (d_{TEM} = 8.0 ± 0.9 nm) or (**B**) dissolved in DMSO (d_{TEM} = 6.3 ± 0.7 nm) at 55 °C for 1 h.

A further method to avoid an agglomeration of the formed Au NPs during the synthesis was to adjust the reaction mixture to a slightly acidic pH by adding diluted HCl. In this way, stable NPs in a dark red or violet dispersion were obtained throughout the syntheses. Nevertheless, even the precipitated Au NPs were further purified. After centrifugation, they were successfully redispersed in slight acidic H_2O. The violet stable dispersions were easily additionally purified *via* dialysis. Again, the Au NPs initially resisted dialysis and only showed a reaction with the tube material at very long intervals (longer than ca. 48 h).

In the following paragraph, the differences of NP size distribution were investigated by carefully changing either reaction temperature or reaction time. Lower temperature and longer reaction times were compared simultaneously. The results are as follows: **Figure 48** reveals that predominantly spherical Au NPs were obtained during the syntheses at 60 °C for 1 h (**Figure 48 A**) with Ø 17 nm, at 40 °C for a slightly longer reaction time of 2 h (**Figure 48 B**) with Ø 8 nm and at 45 °C for 1 h (**Figure 48 C**) with Ø 5 nm. Particularly at Au-MUAM Ø 5 nm, a few Au NPs larger than the average diameter were observed. This was described by Stucky *et al.*[291] before and the authors attribute it to the potential formation of more thermodynamically stable, randomly formed intermediates.

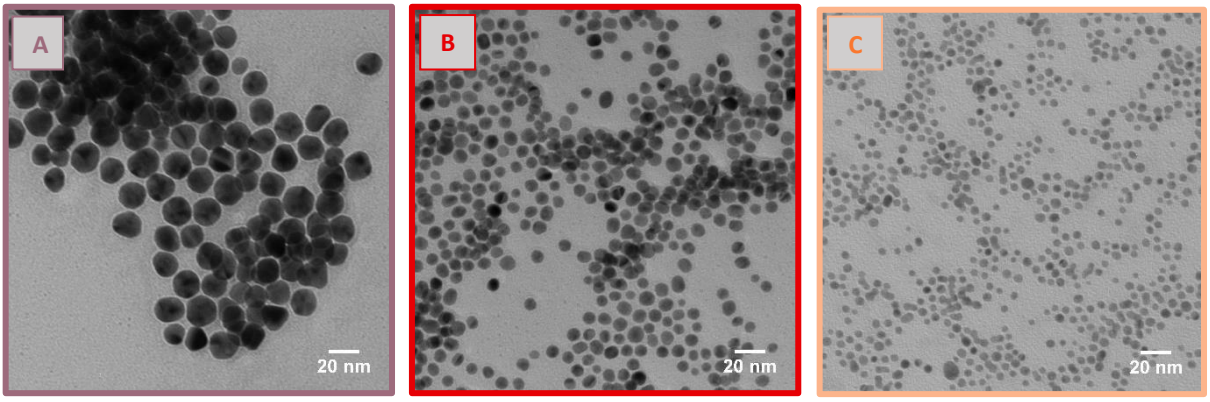

Figure 48: TEM images of Au-MUAM NPs synthesised at (**A**) 60 °C for 1 h with d_{TEM} = 16.8 ± 1.4 nm, at (**B**) 40 °C for 2 h with d_{TEM} = 7.8 ± 0.9 nm or at (**C**) 45 °C for 1 h with d_{TEM} = 5.0 ± 0.7 nm.

In general, lower reaction temperatures decrease the size of the Au NPs, whereas longer reaction times increase the size. However, Au-MUAM NPs tended to agglomerate more easily at higher temperatures over time. Consequently, it is advisable to use longer reaction times only at lower temperatures. Nevertheless, in all of the above syntheses with the ligand MUAM, stable Au NPs were obtained throughout the synthesis. In case of precipitation during the synthesis, they were successfully redispersed in H_2O after purification by adjusting the dispersion to a slightly acidic pH in order to sufficiently stabilise the free amine moiety.

In addition to this direct synthetic approach, Au MUAM NPs were synthesised in a ligand exchange reaction as displayed in **Scheme 24**.

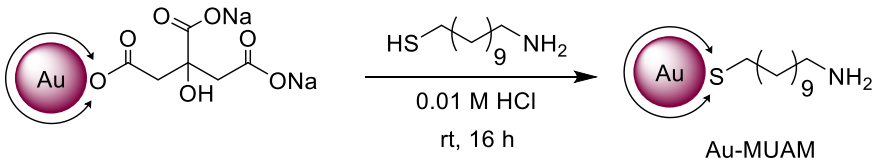

Scheme 24: Ligand exchange reaction towards Au-MUAM NPs.

Starting from Au-Citrate NPs, the new ligand MUAM dissolved in 0.01 M HCl was added dropwise. Further semi concentrated HCl was added to ensure a stable, violet reaction mixture, which was stirred at room temperature. After 3 h, MUAM was added a second time to achieve a higher ligand exchange. The NP dispersion was purified *via* dialysis to obtain stable, violet Au-MUAM NPs. **Figure 49 A** reveals that no change in the morphology of the Au NPs occurred during the ligand exchange. Monodisperse spherical Au NPs with a size of d_{TEM} = 13.2 ± 1.1 nm were obtained. MUAM was found to be a capable ligand in order to ensure a sufficient stabilisation of the Au NPs even throughout a ligand exchange.

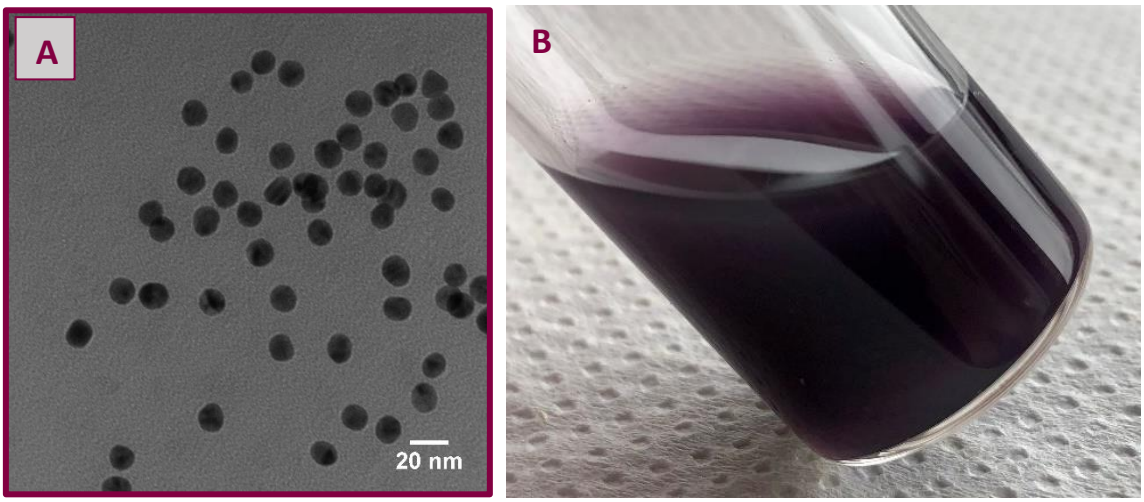

Figure 49: (**A**) TEM images of Au-MUAM NPs synthesised during a ligand exchange reaction starting from Au-Citrate NPs and (**B**) vial filled with Au-MUAM NPs.

The properties of the main synthesised Au-MUAM NP approaches are listed in Figure 50 A. Nevertheless, different sizes of Au-MUAM NPs in the range from 5 nm to 17 nm were obtained and thus comparably sized to the Au NPs already mentioned during this work. All NP samples possess larger d_{hydr} than d_{TEM}, referring to an expanded hydrodynamic shell of the amine stabilised Au NPs.

A

size	5 nm	8 nm	11 nm	12 nm (solid)	17 nm	13 nm (ligand exchange)
sample	Au-MUAM					
d_{TEM} / nm	8.1 ± 0.7	9.7 ± 0.9	12.0 ± 1.0	12.9 ± 1.0	14.0 ± 1.0	15.9 ± 1.1
d_{hydr} / nm	29 ± 8	33 ± 4	112 ± 59	105 ± 42	31 ± 13	53 ± 19
λ_{max} / nm	530	530	529	528	527	528

B

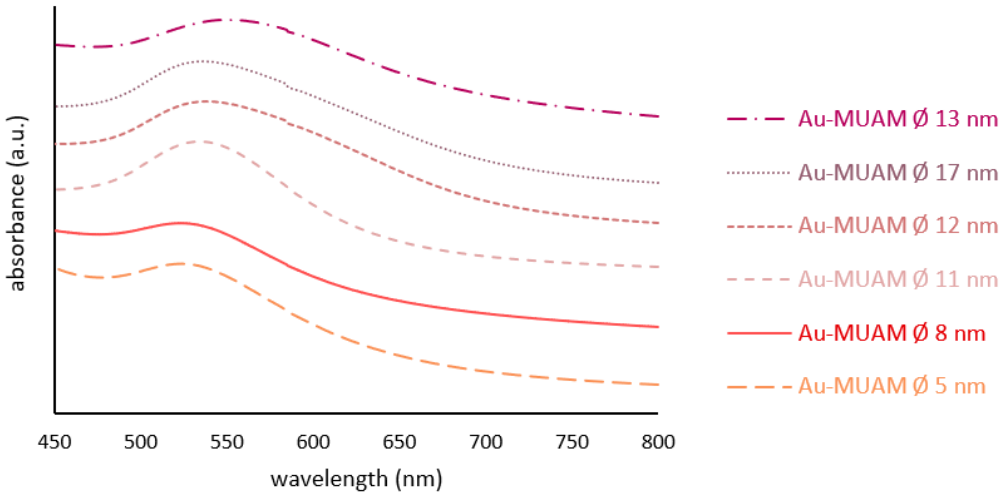

Figure 50: (A) Properties of Au-MUAM NP approaches and (B) their UV/Vis spectra.

The UV/Vis spectra of the Au-MUAM NPs (Figure 50 B) all show a distinct plasmon resonance with an absorption maximum λ_{max} each in the range between 524 nm to 550 nm.

The organic structure of the ligands attached to the Au NPs was investigated using NMR and IR spectroscopy. The ^{1}H-NMR spectrum of Au-MUAM NPs shows all desired proton signals. The intense resonances between 1.60 ppm and 1.12 ppm being the most characteristic ones and are assigned to the long alkyl chain of the MUAM ligand. Furthermore, the spectrum reveals signals in the range of 2.98 ppm to 2.52 ppm, which are shifted towards higher frequencies and thus are assigned to the protons adjacent to the heteroatoms N and S, respectively. For a further investigation of the surface, IR spectroscopy was performed.

Figure 51 displays the IR spectra of the different kinds of Au-MUAM NPs in comparison to the free ligand MUAM (**Figure 51**, **top**). An extremely high similarity of all spectra can be observed, extending over characteristic vibrations as well as the overall fingerprint area. Furthermore, it strongly reinforces that a similar product was obtained from both, the direct synthesis (**Figure 51**, **centre**) as well as the ligand exchange reaction (**Figure 51**, **bottom**).

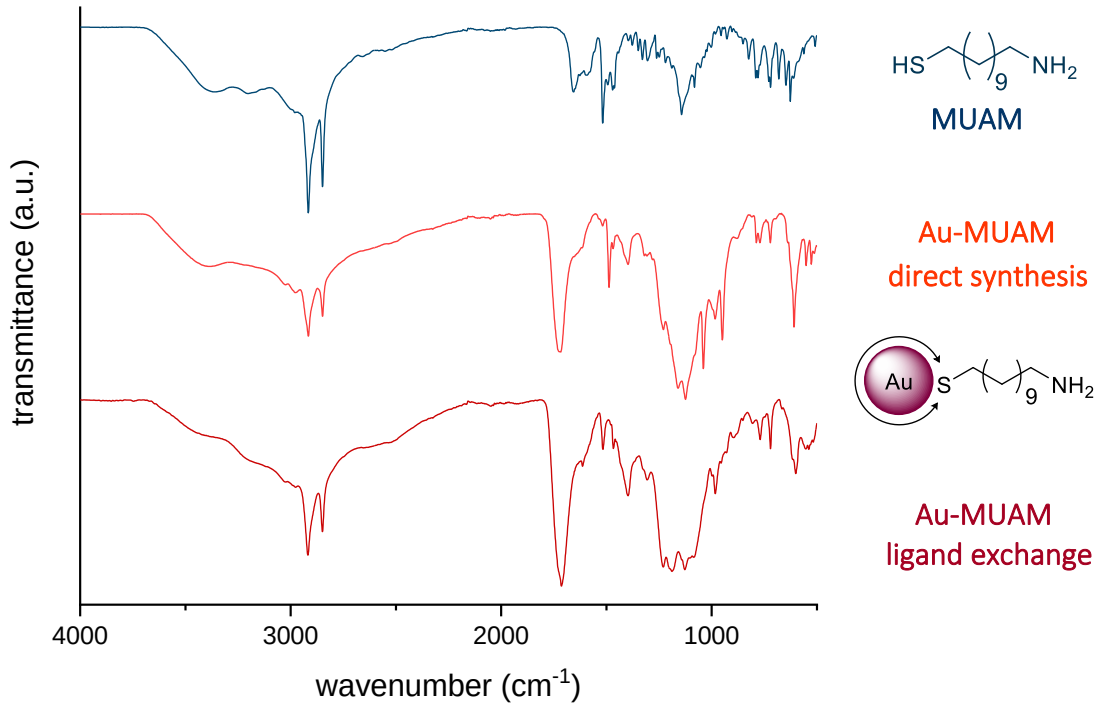

Figure 51: IR spectra of the free ligand MUAM (**top**), Au-MUAM NPs prepared in a direct synthesis (**centre**) or in a ligand exchange reaction (**bottom**).

Weak $\nu_{N\text{-}H}$ vibrations were observed between 3420 cm^{-1} and 3200 cm^{-1}, which can be assigned to the free amine moiety present on the ligand sphere. This is further underlined by $\delta_{N\text{-}H}$ bands around 1600 cm^{-1} as well as $\nu_{C\text{-}N}$ resonances around 1120 cm^{-1}. Moreover, characteristic $\nu_{C\text{-}H}$ vibrations in the range from 3000 cm^{-1} to 2800 cm^{-1} are assigned to the long alkyl chain of MUAM. Furthermore, a distinct oscillation around 600 cm^{-1} appears in all spectra, referring to the $\nu_{C\text{-}S}$ vibration of the thiolate attached onto the Au NP surface.

Consequently, these data show that MUAM is present as a stabilising ligand around the NPs. Furthermore, stable, monodisperse and spherical Au-MUAM NPs were obtained during these syntheses which are suitable as starting NPs for further functionalisations.

3.3.2 Functionalisation of Au-MUAM NPs and Potential Biomimetic Approaches

As a next step, further functionalisation of the Au NPs can be performed on the free amine moiety. For instance, reactions with ketones or aldehydes lead to imines. Furthermore, diverse acids can be attached by amide bonds.

Since our motivation was to mimic a biogenic substance, for this work we chose the peptide coupling using the reagents 1-ethyl-3-(3-dimethylaminopropyl)carbodiimide (EDC) and *N*-hydroxysuccinimide (NHS). In previous studies, dopamine was functionalised onto the Au NP surface. These NP samples showed ambivalent effects when they were tested on smooth trachea muscles of a rat in isometric contraction measurements.[316] Depending on the solvent, Au NPs in H_2O had a contracting effect, presumably stimulating D_1-like receptors and leading to a contraction of the trachea muscle. In contrast, Au NPs in DMSO caused a bronchodilation, potentially caused by the stimulation of D_2-like receptors, leading to a relaxing effect of the trachea muscle.

Nevertheless, it is of general interest to investigate whether biomimetically functionalised Au NPs also exert an effect on the trachea muscles or other biological systems (epithelial membranes, etc.). Here, we chose dihydrocaffeic acid (DHCA) which is closely linked to the structure of dopamine (DA) and thus being similar to catecholamines in general. Therefore, there is a possibility that adrenergic receptors could be stimulated by the catechol moiety of this substance as well as by its biogenic amine-like structure.

Nanoparticle functionalisation

A first attempt of a functionalisation of Au-MUAM NPs was made using dihydrocaffeic acid (DHCA), as displayed in Scheme 25.

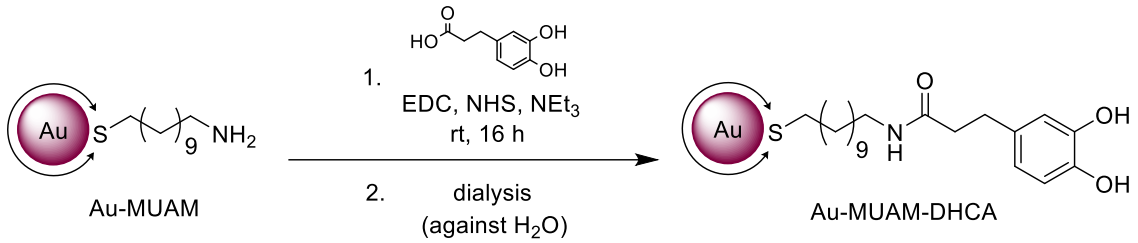

Scheme 25: Functionalisation of Au-MUAM NPs with DHCA using a peptide coupling at the ligand periphery.

For the air sensitive reaction, the peptide coupling reagents *N*-hydroxysuccinimide (NHS), *N*-(3-dimethylaminopropyl)-*N´*-ethylcarbodiimide hydrochloride (EDC) and triethylamine (NEt_3) were dissolved in degassed H_2O. Dihydrocaffeic acid (DHCA) was dissolved in DMSO and added to the mixture, which was stirred for 2 h at room temperature while still being purged with argon. In the meantime, an Au-MUAM NP dispersion was degassed with argon. The ligand mixture was added slowly to the NP dispersion under vigorous stirring. All reagents were added in large excess to obtain maximal conversion. The pink or violet dispersion, respectively, was

stirred for 16 h at room temperature under argon atmosphere and subsequently purified *via* dialysis against H_2O (in MWCO 6000, 3 × 2 h). These coupling reactions were performed with Au-MUAM NPs of the size Ø 5 nm, Ø 8 nm and Ø 13 nm. TEM images of all approaches show no agglomeration (**Figure 52**). Furthermore, the morphology of the NPs did not change during the functionalisation step and remain spherical with a good overall monodispersity. Using this method, Au-MUAM-DHCA NPs with d_{TEM} = 5.0 ± 0.8 nm (**Figure 52**, **left**), with d_{TEM} = 8.0 ± 0.8 nm (**Figure 52**, **centre**) and with d_{TEM} = 13.0 ± 0.8 nm (**Figure 52**, **right**) were obtained.

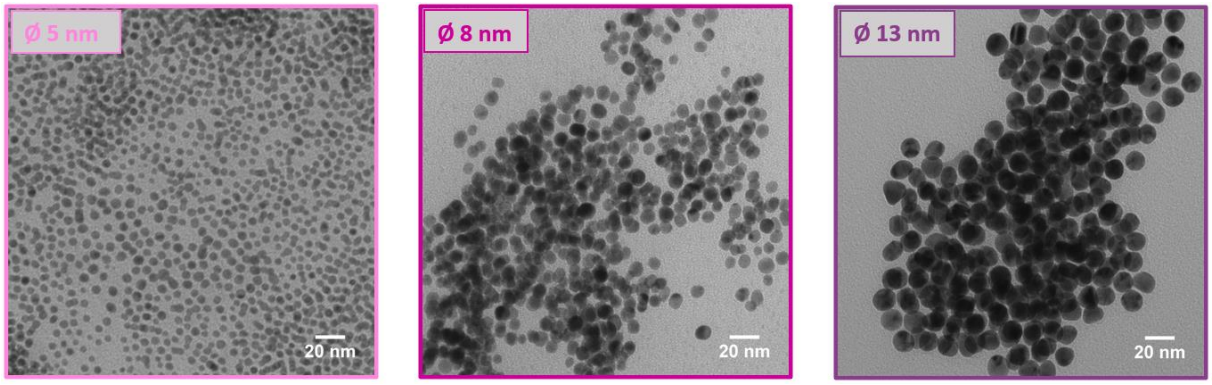

Figure 52: TEM images of Au-MUAM-DHCA with d_{TEM} = 5.0 ± 0.8 nm (**left**), with d_{TEM} = 8.2 ± 0.9 nm (**centre**) and with d_{TEM} = 13.0 ± 1.0 nm (**right**).

An indication of the successful functionalisation can be seen from d_{hydr}, which increased significantly in all approaches after the reaction at the ligand periphery (**Figure 53 A**).

A

size	5 nm	8 nm	13 nm
sample	Au-MUAM-DHCA		
d_{TEM} / nm	5.0 ± 0.8	8.2 ± 0.9	13.0 ± 1.0
d_{hydr} / nm	100 ± 27	101 ± 39	164 ± 39
λ_{max} / nm	545	550	556

B

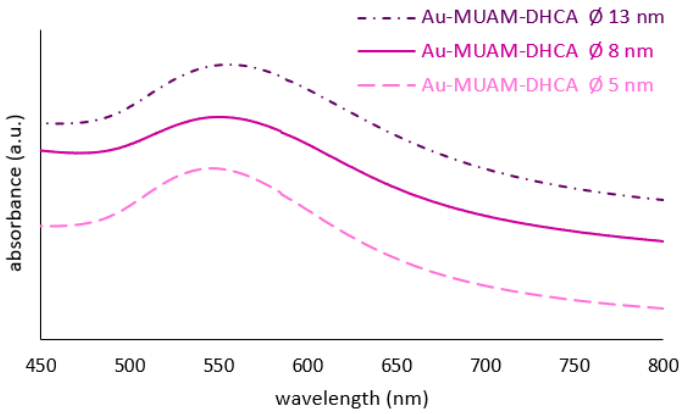

Figure 53: (**A**) Properties of the Au-MUAM-DHCA approaches and (**B**) their corresponding UV/Vis spectra.

Furthermore, a bathochromic shift occurred for all samples showing a distinct plasmon resonance with an absorption maximum λ_{max} each in around 550 nm (**Figure 53 B**) and thus shifted either 21 nm (for Ø 5 nm), 26 nm (for Ø 8 nm) or only 8 nm (for Ø 13 nm) towards longer wavelengths, respectively.

An important impact on the assumption of a successful functionalisation gave the zeta potential data, which should underwent a significant change due to the surface alteration from a positive amine stabilisation (Au-MUAM, ζ = +29.67 ± 1.16 mV) towards rather negatively charged catechol units (Au-MUAM-DHCA, ζ = -48.07 ± 1.99 mV). The data are displayed in **Figure 54**.

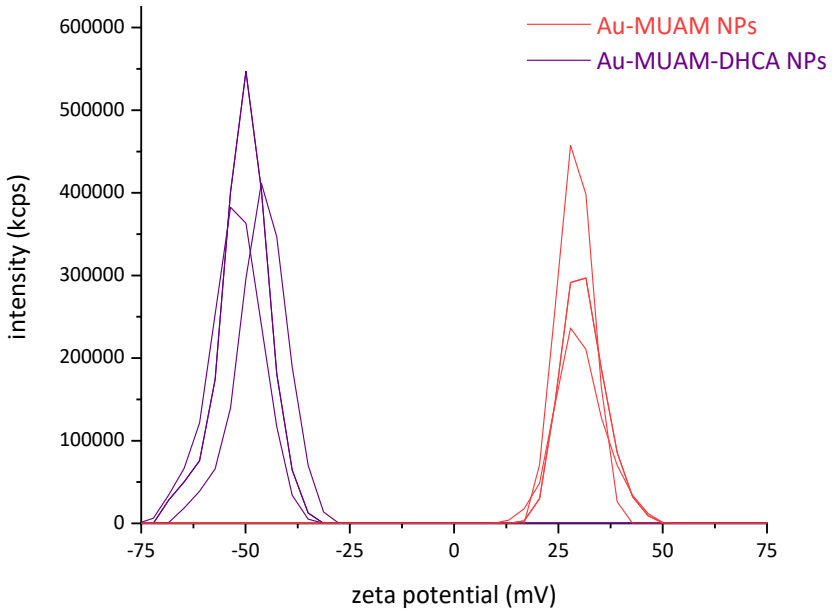

Figure 54: Zeta potential curves of Au-MUAM NPs (**red**) and Au-MUAM-DHCA NPs (**violet**).

The organic structure of the NPs framework was investigated using NMR and IR spectroscopy. ^{1}H-NMR spectrum shows all desired proton signals including the ones of DHCA. Proton signals of MUAM were identified, such as the intense resonances in the range of 1.61 ppm to 1.12 ppm, which are assigned to the alkyl chain. In addition to these, the spectrum shows aromatic proton signals between 6.59 ppm and 6.39 ppm, referring to the phenol ring of DHCA and this clearly confirms the successful attachment of DHCA.

IR spectroscopy was performed in order to obtain further information about the bonds formed in the organic framework. **Figure 55** shows the IR spectra of functionalised Au-MUAM-DHCA NPs (**Figure 55**, **bottom**) in comparison to the starting NPs Au MUAM (**Figure 55**, **centre**) and the compound 3,4-DHCA (**Figure 55**, **top**).

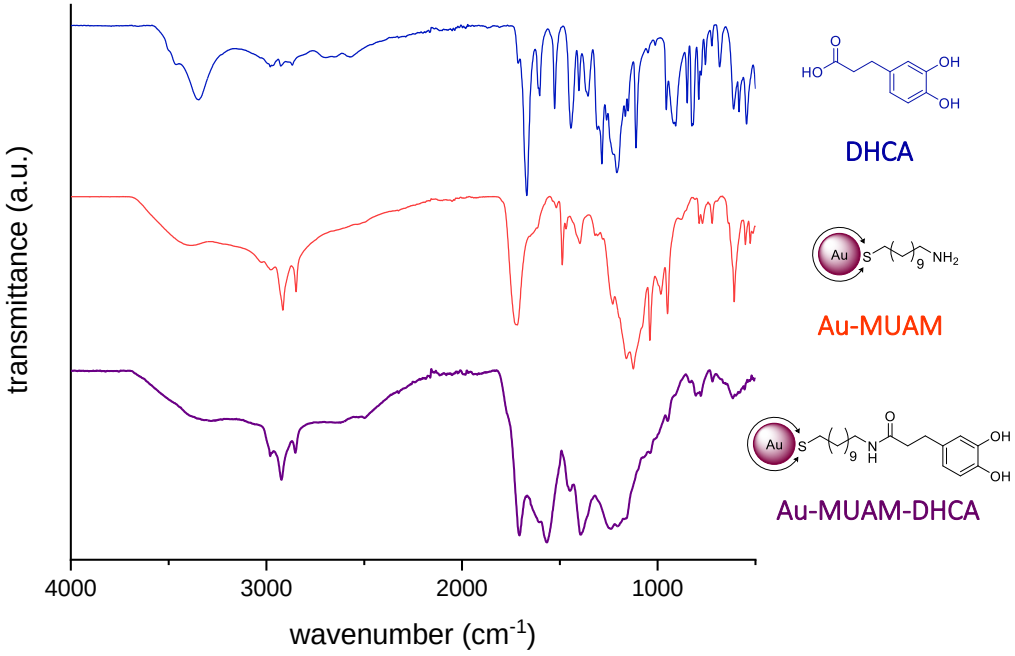

Figure 55: IR spectra of the compound DHCA (**top**), Au-MUAM NPs (**centre**) and Au-MUAM-DHCA NPs (**bottom**).

Although the vibrations of Au-MUAM-DHCA NPs (**Figure 55**, **bottom**) appear quite broadened and therefore not as clearly resolved, correspondences with both, starting NPs (**Figure 55**, **centre**) as well as the attached DHCA (**Figure 55**, **top**), can be seen. Au-MUAM-DHCA NPs show additional vibrations at 1705 cm^{-1}, which can be assigned to the carbonyl unit of the amide bond formed. Furthermore, distinct oscillations around 1560 cm^{-1} ($\delta_{O\text{-}H}$) and 1209 cm^{-1} ($\nu_{C\text{-}O}$), respectively, can be unambiguously attributed to the catechol unit of DHCA. Slight benzene overtone $\delta_{C\text{-}H}$ vibrations around 2000 cm^{-1} refer to the aromatic ring of the newly attached compound. Distinct bands between 3000 cm^{-1} and 2800 cm^{-1} are assigned to the long alkyl chain of MUAM. The characteristic band of $\nu_{C\text{-}S}$ appears at 640 cm^{-1}, still indicating the presence of the thiolate unit attached on to the Au NP surface. Compared to the initial NPs (**Figure 55**, **centre**), a shift of the $\nu_{C\text{-}N}$ vibration was observed. This is no longer present as a free amine above 1100 cm^{-1}, but instead now in Au-MUAM-DHCA NPs (**Figure 55**, **bottom**) as an amide slightly below 1100 cm^{-1}. The IR spectra are identical for all the different sizes of the Au NPs.

To sum up, these data jointly prove the successful synthesis and characterisation of Au-MUAM-DHCA NPs in different sizes. These samples may be used to study their effect in biological systems for their receptor interactions. Although no actual biogenic amine is present in these Au NPs, the introduced catechol unit could provide sufficient receptor activity.

3.4 Labelling of Au NPs with a Fluorescent Dye

3.4.1 Labelling of Au NPs

In addition to the studies mentioned in the introduction, it is equally of interest to study the functionalised Au NPs mentioned in the previous chapters within the body; both on a microscopic level and in relation to the whole system. Herein, the labelling with fluorescent dyes or other luminescent substances, which can be performed extrinsically or intrinsically, will be described. A second approach will be the labelling with radioactive tracers.

In the present work, the fluorescent dyes were modified, so that an attachment to the Au NP surface was possible. These modified Au NPs are then ideally suited for the determination and investigation on a microscopic level in order to find out where the Au NPs are located, as they migrate within the membranes, and which cell processes may be triggered, such as endocytosis.

The radioactive labelling of the Au NPs will be described in **Chapter 3.5**. At first, specific ligand syntheses are described, followed by comparative complex reactions as well as the labelling and investigations of (bio)functionalised Au NPs with the radionuclide ^{99m}Tc. The highly sensitive nature of radiolabelling provides an excellent diagnostic tool for the investigation of a biodistribution throughout entire biological systems.

3.4.2 Fluorescent Dye Functionalised Au NPs

Two organic dyes were used in the following approaches: Rhodamine B (Rhod) and Eosin Y (Eos). They are rather inexpensive compounds and their structures both possess free carboxylic acid groups on the phenyl moiety for a further derivatisation as displayed in **Scheme 26**.

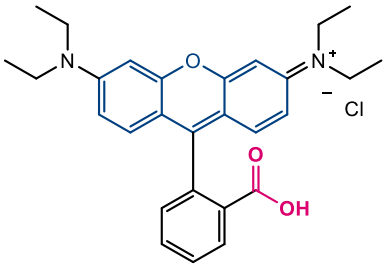

Rhodamine B (Rhod)

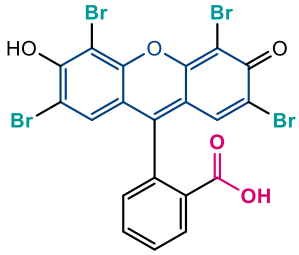

Eosin Y (Eos)

Scheme 26: Structures of the fluorescent dyes Rhodamine B (Rhod, **left**) and Eosin Y (Eos, **right**).

Both dyes consist of a xanthene scaffold. Rhodamine B possesses two diethylamine groups. However, Eosin Y, being more similar to fluorescein in general, owns four ortho bromine substituents. With these heavy atoms, further analytical approaches might be accessible, such as a more effective crystallisation of the synthesised compounds.

Furthermore, the heavy atoms enable further analytical methods, such as EDX, which can be used to investigate the entire organic framework more closely once it is attached on the NPs.

A variety of modified Rhod derivatives have been described in the literature, and a fine tuning of the characteristics regarding e.g. biocompatibility or photophysical properties were also described.[317–321] First, Rhod is reacted with a thiol containing linker in order to obtain a ligand which can be attached onto the Au NP surface in a ligand exchange reaction, as displayed in Scheme 27.

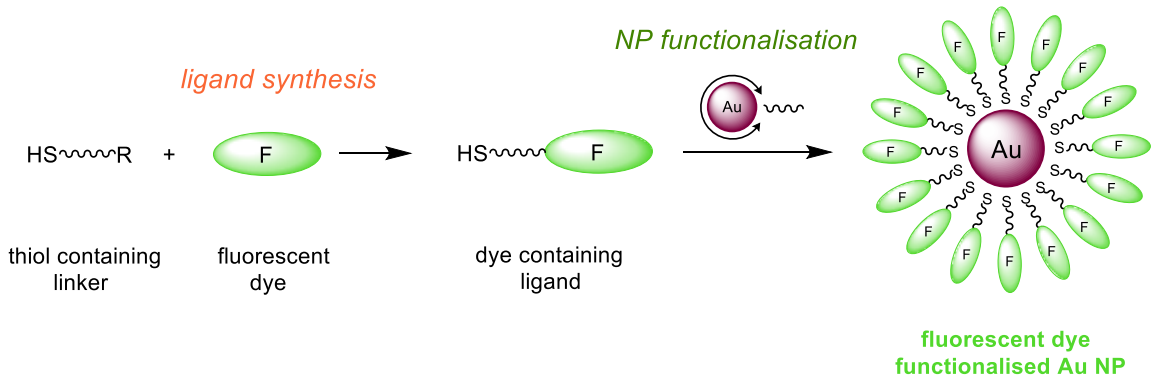

Scheme 27: Potential labelling procedure of Au NPs with a fluorescent dye.

Different approaches for the ligand syntheses were performed, leading not to the desired products (Scheme 28). A Steglich esterification[308] of Rhod with mercaptoundecanol (MUDOL) in order to obtain the ester bond was unsuccessful (green pathway). Approaches using short chain aminothiols, such as 4-aminothiolphenol (ATP) and mercaptoundecylamine (MUAM) did also not lead to the desired peptide ligands (blue pathways). However, a consecutive route using a short chain diamine, such as ethylenediamine (EN) as a spacer and a further reaction with a mercapto acid, such as lipoic acid (LA) leads to a ligand of the composition Rhod-EN-LA, of which the synthesis is described in the following section (orange/red pathway).

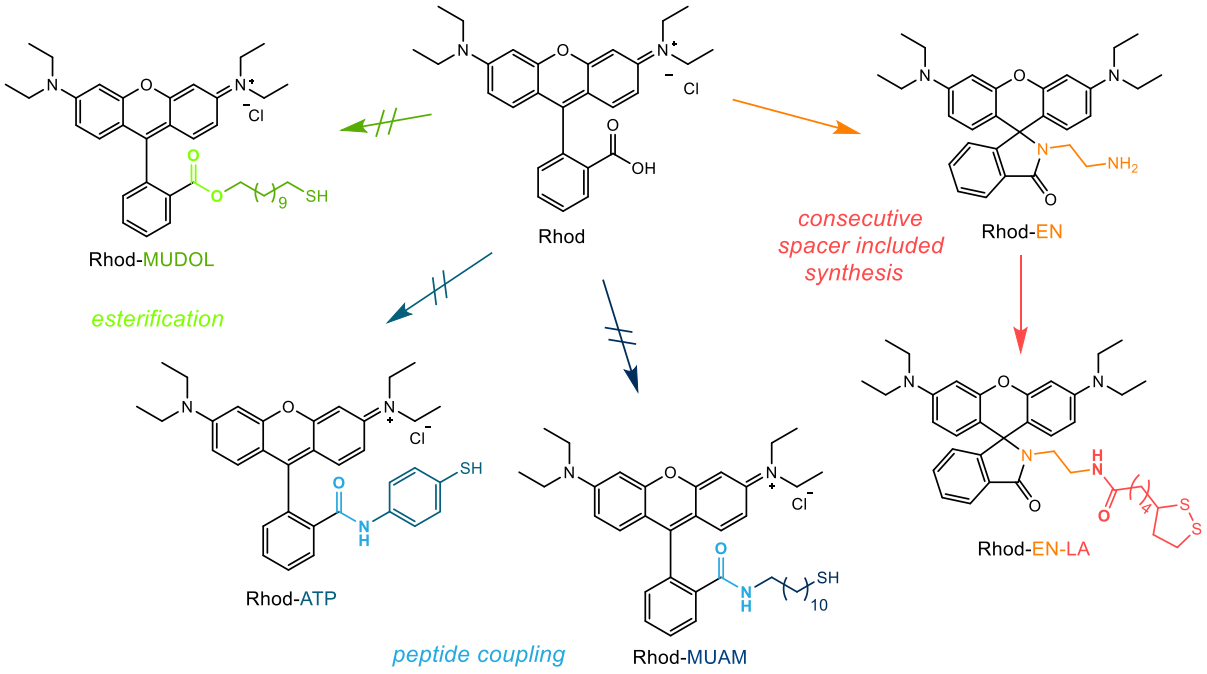

Scheme 28: Different synthetic approaches for a ligand containing a thiol unit as well as the fluorescent dye Rhod.

Noteworthy is the fact that further investigations, especially with the second fluorescent dye Eosin Y, were performed during two student projects as well as a master's project under the author's supervision and are therefore not described in detail in this thesis (**Scheme 29**).

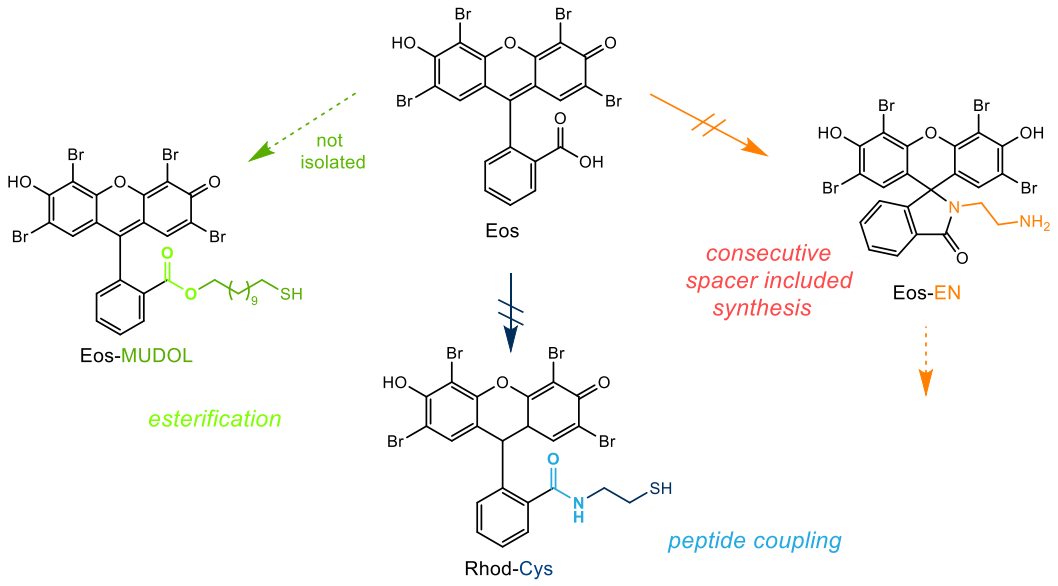

Scheme 29: Different synthetic approaches for a ligand containing a thiol unit as well as the fluorescent dye Eosin Y.

Ligand syntheses

The synthesis was performed according to a modified version of the approach by Eling *et al.*,[322] displayed in **Scheme 30.** Rhod and ethylenediamine (EN) or diaminohexane (DAH) were separately dissolved in anhydrous EtOH. The Rhod solution was heated to 90 °C and the EN or DAH solution was slowly added dropwise under vigorous stirring. Afterwards, the reaction mixture was heated under reflux for 16 h with EN and 3 d with DAH. The solvent was removed and the orange residue was further purified in an aqueous work-up using EtOAc. Rhod-EN was obtained as a colourless (occasionally slightly orange) crystalline solid in a good yield of 85% or 84% for Rhod-EN and Rhod-DAH, respectively.

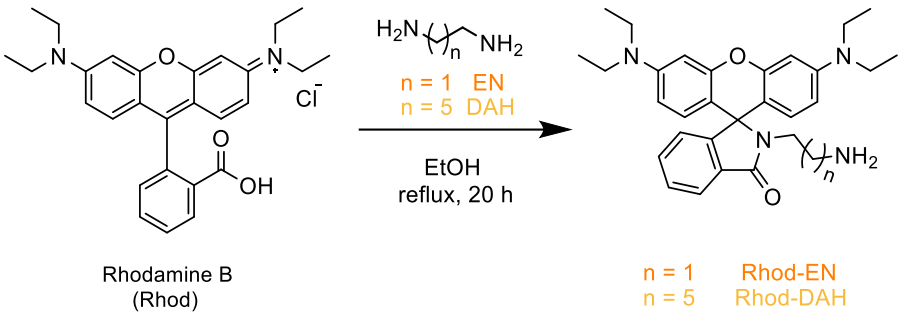

Scheme 30: Synthesis of the compounds Rhod-EN and Rhod-DAH using Rhodamine B (Rhod) and ethylenediamine (EN) or diaminohexane (DAH), respectively.

The organic structures of both compounds were investigated using NMR and IR spectroscopy. The NMR spectra of Rhod-EN and Rhod-DAH both show the expected proton signals, which were further determined using 2D experiments and assigned through their long range coupling. Aromatic proton resonances between 8.03 ppm and 7.07 ppm can be attributed to the 1,2-disubstituted phenyl ring of the rhodamine dye. Furthermore, a variety of proton signals in the range of 6.58 ppm to 6.29 ppm are assigned to the xanthene framework. Proton resonances at 3.35 ppm and around 1.20 – 1.06 ppm refer to the four ethyl groups on the xanthene structure. In the ^{1}H-NMR spectrum of Rhod-EN, the two proton signals 3.21 ppm and 2.44 ppm are assigned to the methylene groups of EN and are shifted towards slightly higher frequencies as they are adjacent to the nitrogen atoms. These resonances also occurred in the ^{1}H-NMR spectrum of Rhod-DAH, in addition to intense proton signals in the range of 1.69 ppm to 1.05 ppm, which are attributed to the longer alkyl chain of DAH. Furthermore, IR measurements were performed in order to investigate the existing binding types within the synthesised compounds. The spectra of Rhod-EN (**Figure 56**, **centre**) and Rhod-DAH (**Figure 56**, **bottom**) were compared to the starting material Rhod (**Figure 56**, **top**).

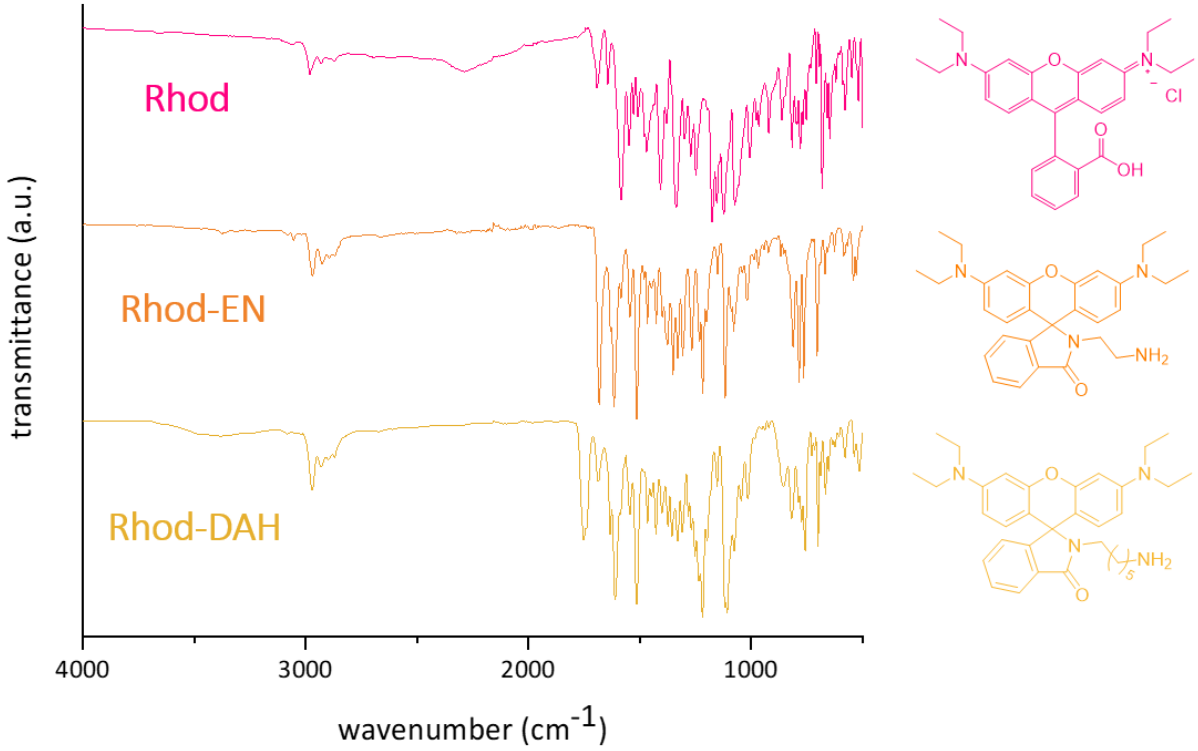

Figure 56: IR spectra of Rhodamine B (Rhod (**top**)), Rhod-EN (**centre**) and Rhod-DAH (**bottom**).

Due to the large organic scaffold, all three spectra generally contain a series of different vibrations with significant correspondences in the entire frequency range. All spectra show low intensities of $\nu_{C\text{-}H}$ vibrations between 3000 cm^{-1} and 2800 cm^{-1}. Similar structures describing the existing aromatic system in more detail are also observed within the fingerprint area: A $\delta_{C\text{-}H}$ oscillation around 840 cm^{-1} as well as a $\delta_{C=C}$ vibration at 800 cm^{-1} are assigned to the 1,2,4-trisubstituted xanthene fragments. Furthermore, a $\delta_{C\text{-}H}$ band around 780 cm^{-1} as well as an $\delta_{C=C}$ absorption at 700 cm^{-1} refer to the 1,2-disubstituted phenyl ring of the rhodamine scaffold. In addition to these similarities, several differences indicate the successful reaction of the starting material dye to its derivatives. The spectra of both synthesised compounds (**Figure 56**, **centre and bottom**) contain an intense vibration at 1680 cm^{-1} each, which is assigned to the carbonyl group of the amide bond. Its formation is further confirmed by a $\delta_{N\text{-}H}$ band around 1515 cm^{-1}. Furthermore, Rhod-DAH (**Figure 56**, **bottom**) has in addition to marginally more intense $\nu_{C\text{-}H}$ vibrations around 2900 cm^{-1} also a distinct $\delta_{C\text{-}H}$ oscillation, which refers to the slightly longer alkyl chain of DAH. As mentioned before, Rhod and its derivatives Rhod-EN and Rhod-DAH have an open and a closed form and the formation is pH dependent. At higher pH values, the closed form with a spirocyclic ring is formed.[322] In ESI MS measurements, the molecule ion $[M+H]^+$ of *m/z* 485.31 was found for Rhod-EN and $[M+H]^+$ of *m/z* 541.35 for Rhod-DAH. Both match the calculated masses for the closed forms.

Taken together, these data prove that the derivatives of Rhod were synthesised with both, a short diamine linker (EN) as well as a longer one (DAH). Furthermore, the structure of the closed form was confirmed by X-ray crystallographic analysis (**Figure 57**). Crystals of Rhod-EN were obtained by slow diffusion of *n*-pentane into a deuterated chloroform solution and were measured at the DESY synchrotron in Hamburg.

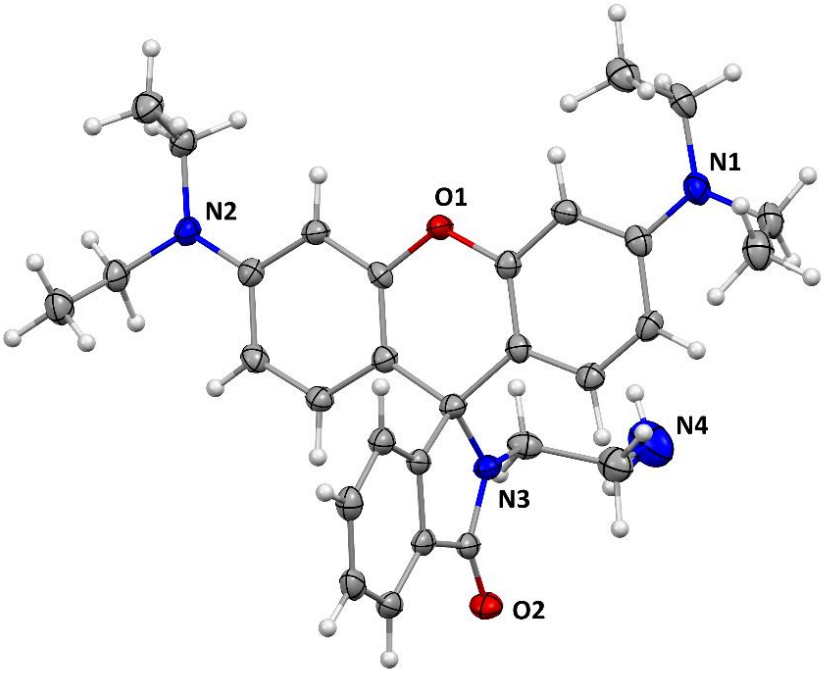

Figure 57: Molecular structure of Rhod-EN (displacement ellipsoids are drawn at 50% probability).

The data solution was performed in the triclinic space group *P*-1, with an R_1 of 5.95%, wR_2 = 13.56% and an R_{int} of 8.46%. The cell parameters are a = 11.097(2), b = 11.539(2), c = 12.280(3) Å and α = 80.45(3)°, β = 63.33(3)° and γ = 64.82(3)°. The molecular structure of Rhod-EN reveals the successful derivatisation with the short diamine linker EN. Moreover, in the closed spirolactam moiety exists a central sp^3-hybridised C atom. This causes the conjugation of the xanthene π system to be reduced, whereby the system loses its high fluorescence in the solid state and results in colourless crystals.

These derivatives present excellent starting materials for a further reaction with a thiol spacer in order to obtain a ligand suitable for attachment onto a Au NP surface, in this case lipoic acid (LA). The synthesis was performed as displayed in **Scheme 31**.

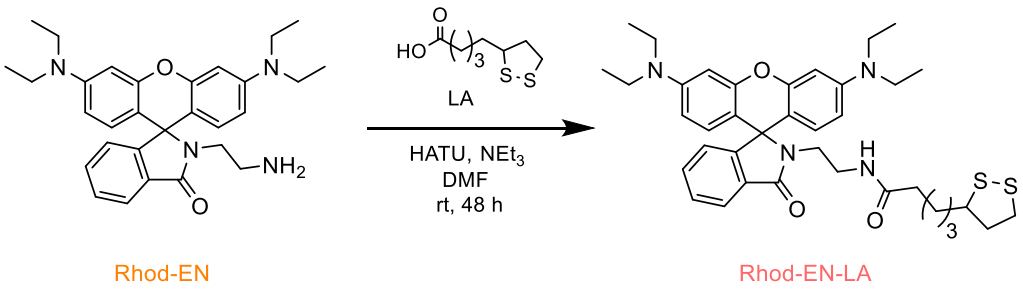

Scheme 31: Synthesis of Rhod-EN-LA.

LA was dissolved in anhydrous DMF and cooled to 0 °C. NEt_3 and the coupling reagent **h**exafluorophosphate **a**zabenzotriazole **t**etramethyl **u**ronium (HATU) was added and stirred for 10 min at 0 °C. Rhod-EN was dissolved in anhydrous DMF and was slowly added dropwise. The dark violet reaction mixture was stirred under argon atmosphere at room temperature. After 48 h, the pink reaction mixture was quenched with H_2O. Diluted HCl was added and aqueous work-up proceeded. The product was obtained as a pink solid in a poor yield (21%). Furthermore, traces of Rhod remained in the pure product. This was not further purified, as in the following Au NP functionalisation the bifunctional ligand will be added in excess, and it connects with its thiol moiety, which binds more favourably to the Au NPs.

The structure of the ligand was investigated using NMR, IR and ESI-MS. The ^{1}H-NMR spectrum shows all expected proton signals. Again, the aromatic proton resonances in the range of 7.92 ppm to 6.24 ppm are assigned to the aromatic system of Rhod. Moreover, its derivatisation with EN can be confirmed with the proton resonances of the methylene groups of EN between 3.18 ppm and 3.00 ppm. The successful ligand synthesis of Rhod-EN-LA is supported by further proton resonances in the range between 3.38 ppm to 1.23 ppm, which are attributed to LA. **Figure 58** shows the IR spectra of Rhod-EN-LA (**Figure 58**, **bottom**) compared to the starting materials LA (**Figure 58**, **centre**) and Rhod-EN (**Figure 58**, **top**).

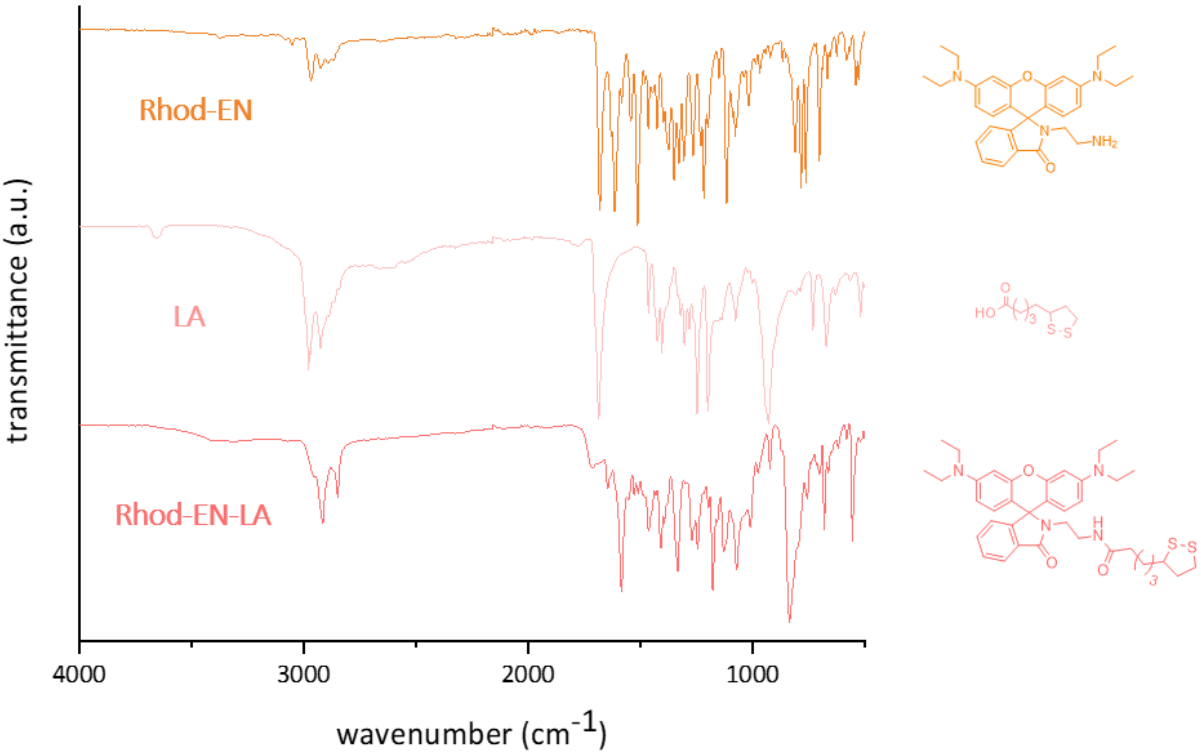

Figure 58: IR spectra of Rhod-EN (**top**), lipoic acid (LA, **centre**) and Rhod-EN-LA (**bottom**).

The spectrum of Rhod-EN-LA (**Figure 58**, **bottom**) contains distinct similarities with its starting material Rhod-EN (**Figure 58**, **top**). Several vibrations in the range of 1650 cm^{-1} to 1200 cm^{-1} still indicate the formation of amides, such as $\nu_{C=O}$ oscillations around 1640 cm^{-1}, a δ_{N-H} band around 1585 cm^{-1} and ν_{C-N} absorptions between 1350 cm^{-1} and 1200 cm^{-1}. However, additional bands imply a successful reaction with LA (**Figure 58**, **centre**). The broad ν_{N-H} vibration above 3300 cm^{-1} is slightly more defined than in Rhod-EN. Furthermore, the ν_{C-H} absorptions in the range of 3000 cm^{-1} and 2800 cm^{-1} appear more intense than in Rhod-EN (**Figure 58**, **top**), which may be due to the slightly longer alkyl chain of LA. This is confirmed by the presence of δ_{C-H} oscillations around 1450 cm^{-1}, which were not observed in the starting dye. Moreover, a strong vibration around 840 cm^{-1} is presumably assigned to δ_{H-C-S} and thus supports the assumption that LA was successfully connected. However, this broad intense band overlaps with the benzene vibrations (δ_{C-H} and $\delta_{C=C}$), which would indicate the 1,2,4-trisubstituted xanthene framework. Oscillations of δ_{C-H} around 760 cm^{-1} and $\delta_{C=C}$ at 704 cm^{-1} are attributed to the 1,2-disubstituted phenyl residue. Furthermore, the new appearing oscillation of ν_{C-S} around 680 cm^{-1} is assigned to the thiol moiety.

In ESI MS measurements, the molecule ion $[M+Na]^+$ of *m/z* 695.31 was found for Rhod-EN-LA, which matches its calculated mass for the closed spirolactam form.

Nanoparticle functionalisation

The functionalisation of the Au NPs was performed with the Rhod-EN-LA, as displayed in Scheme 32. A dispersion of Au-Citrate NPs (Ø 13 nm) was degassed with argon prior to the addition of the ligand. Rhod-EN-LA was dissolved in DMSO and slowly added in a large excess (10^6-fold) under vigorous stirring. Then, the pH was adjusted to 8 by adding NEt_3 and the mixture was stirred at room temperature. The obtained Au NPs were first purified using centrifugation and *via* dialysis in a second step.

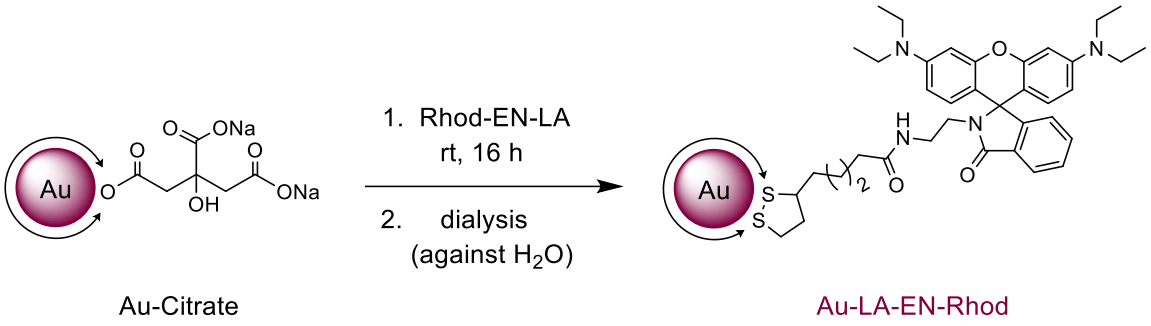

Scheme 32: Functionalisation of Au-Citrate NPs with Rhod-EN-LA.

As displayed in Figure 59 A, the TEM images reveal that the morphology of the Au-LA-EN-Rhod NPs did not change during the ligand exchange with Rhod-EN-LA. Monodisperse spherical Au NPs with a size of d_{TEM} = 12.9 ± 0.9 nm were obtained. Furthermore, the Au NPs reveal a distinct plasmon resonance at 542 nm.

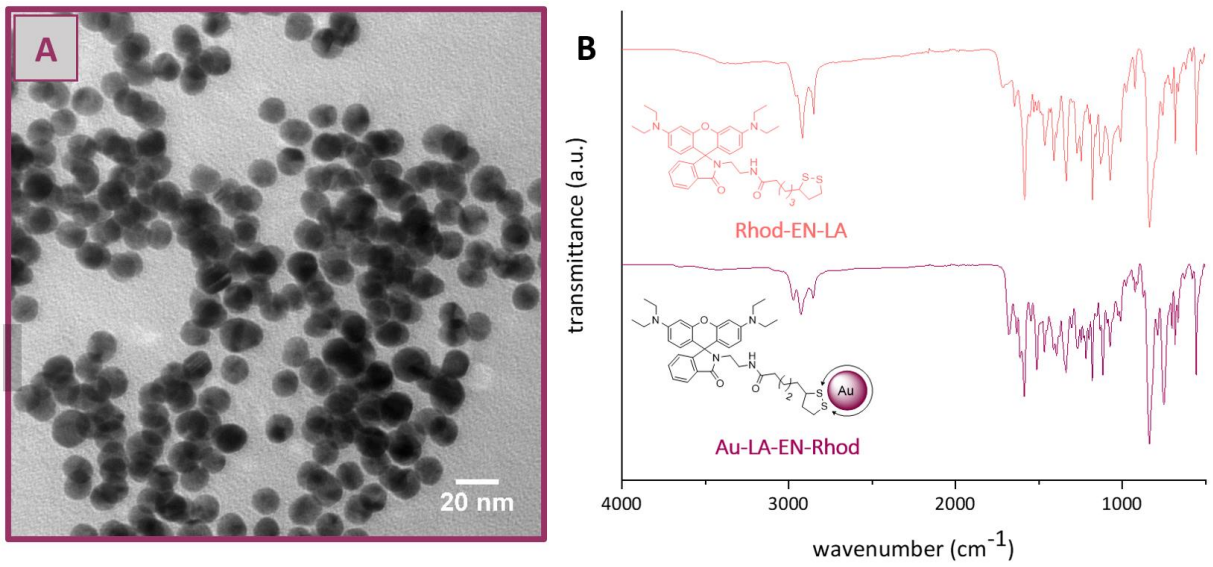

Figure 59: (A) TEM image of Au-LA-EN-Rhod NPs and (B) corresponding IR spectrum in comparison to the ligand Rhod-EN-LA.

The plotted IR spectra in Figure 59 B indicate a successful change in surface functionalisation. The spectrum of Au-LA-EN-Rhod NPs (Figure 59 B, bottom) reveals strong similarities to the

free ligand Rhod-EN-LA (**Figure 59 B, top**), which was immobilised onto the Au-Citrate NPs during the ligand exchange reaction. In particular, the characteristic $\nu_{C\text{-}H}$ absorptions in the range 3000 cm^{-1} to 2800 cm^{-1} as well as the $\nu_{C=O}$ vibration in around 1650 cm^{-1} appear in both spectra. Furthermore, high similarities in the range between 800 cm^{-1} and 600 cm^{-1} indicate the presence of lipoic acid with its $\nu_{C\text{-}S}$ and $\nu_{S\text{-}S}$ absorptions.

Taken together, the data imply that Rhod dyes were successfully attached on Au NPs. However, the synthesis of a suitable fluorescent dye ligand appeared to be rather challenging with rather low yields. For this reason, this thesis was extended to a further method of labelling, which will be discussed in the following chapter in more detail.

3.5 Multifunctional Au NPs Labelled with ^{99m}Tc

Since the biofunctionalised NPs were prepared in order to use them for biomedical applications, their biodistribution within the whole body was of great interest. In order to gain further knowledge about it in future studies, the intention of this work was to synthesise radiolabelled Au NPs as a probe for imaging investigations.

3.5.1 Ligand Syntheses

For this purpose, a new bifunctional ligand type was designed (**Scheme 33**, **top**). On one terminus, the ligand contains a thiol moiety that allows attachment to the Au NP surface. On the other side, it possesses a chelating unit capable of complexing ^{99m}Tc as the chosen radiolabel. With this bifunctional ligand, radiolabelled NPs were prepared *via* different synthetic routes.

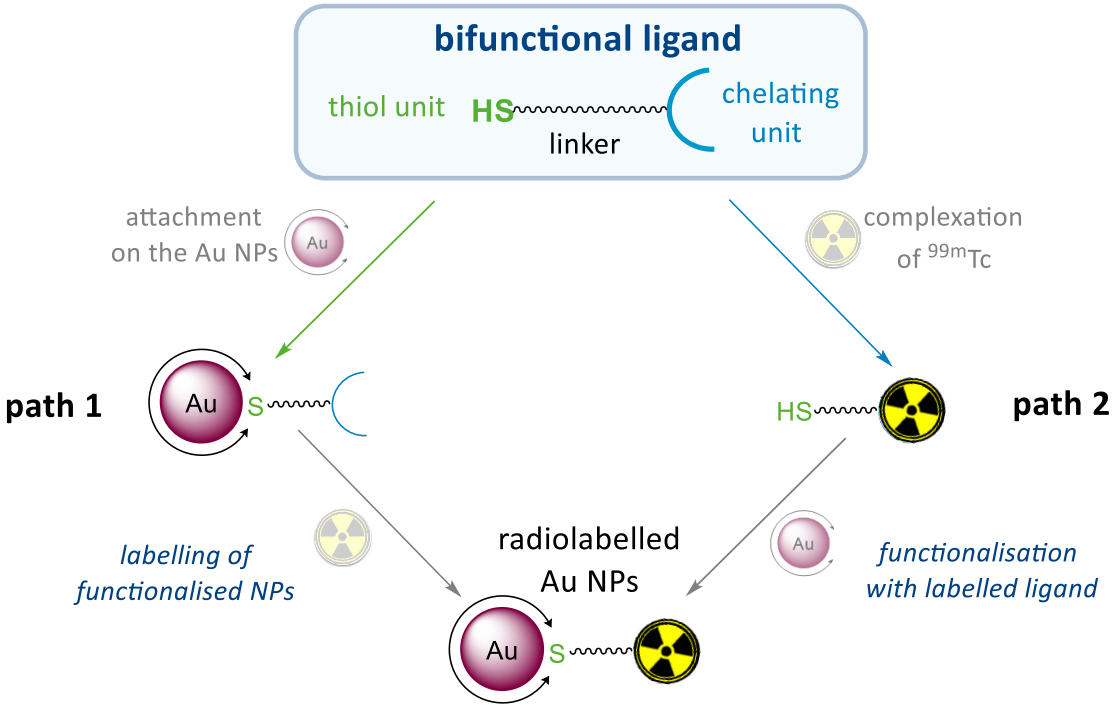

Scheme 33: Synthetic pathway to radiolabelled Au NPs. A bifunctional ligand (**top**) that carries both a thiol group to bind on a Au NP surface (**centre, left**) and a chelate moiety to complex ^{99m}Tc (**centre, right**). The functionalisation takes places either by attaching the ligand to the Au NP before radiolabelling with the radionuclide ("*labelling of functionalised NPs*", **left,** path 1), or by labelling of the ligand followed by functionalisation of the Au NPs ("*functionalisation with labelled ligand*", **right**, path 2).

One pathway involved the attachment of the bifunctional ligands on the NPs first, then the radiolabelling with the functionalised Au NPs was performed (**Scheme 33**, **left** path). An alternative route included the complexation of the bifunctional ligand with the radionuclide in the first step. In this consecutive route, the NPs were directly functionalised with the

radiolabelled ligands afterwards (**Scheme 33**, **right** path). In this manner, mono ligand shell Au NPs were synthesised, which were only carrying the chelator ligand type on their surface (**Figure 60**, **left**) and could act as a probe for imaging itself. In addition to these, mixed ligand shell functionalised Au NPs were synthesised (**Figure 60**, **right**). These contained next to the chelator ligands also a secondary biofunctionalisation with a pharmacologically relevant compound.

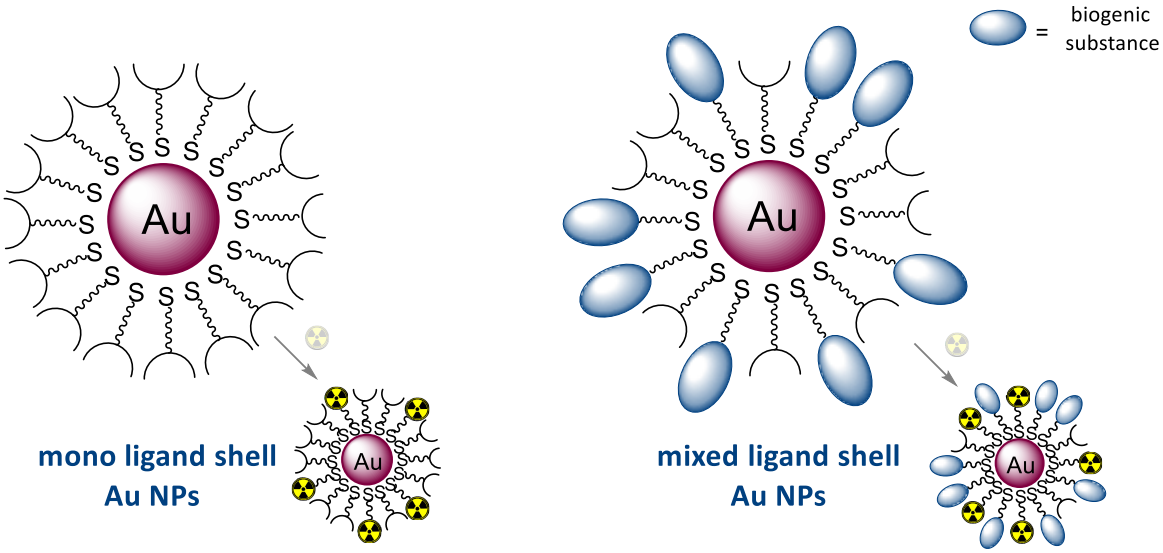

Figure 60: Schematic structure of mono ligand shell Au NPs (**left**) next to mixed ligand shell Au NPs (**right**).

In this way, multifunctional mixed shell Au NPs were prepared, which offer therapeutic effects as well as being a potential radiotheragnostic agent. In particular, the bioactive ligands can be modified, selected and adapted to a variety of requirements, such as the laboratory conditions and the specific illness. This allows for a range of different radiotheragnostics to be developed from the method presented herein. However, multifunctional mixed ligand shells do not necessarily contain the same amount of bioactive ligands within different batches, so that this could influence their effect on the receptors and furthermore a cross-batch comparison will be rather challenging. Nevertheless, the benefits of a radiotheragnostic application predominate, since the effect of the biofunctionalised Au NPs and their biodistribution can be studied simultaneously using this approach.

In this work, picolylamine diacetic acid (PADA) was chosen as the chelating unit, as displayed in **Scheme 34** (**top left**). This tripodal ligand is known in literature and is capable of binding strongly to the *fac*-{M(CO)$_3$}$^+$ core (M = Re/^{99m}Tc), shown in (**Scheme 34**, **bottom left**).

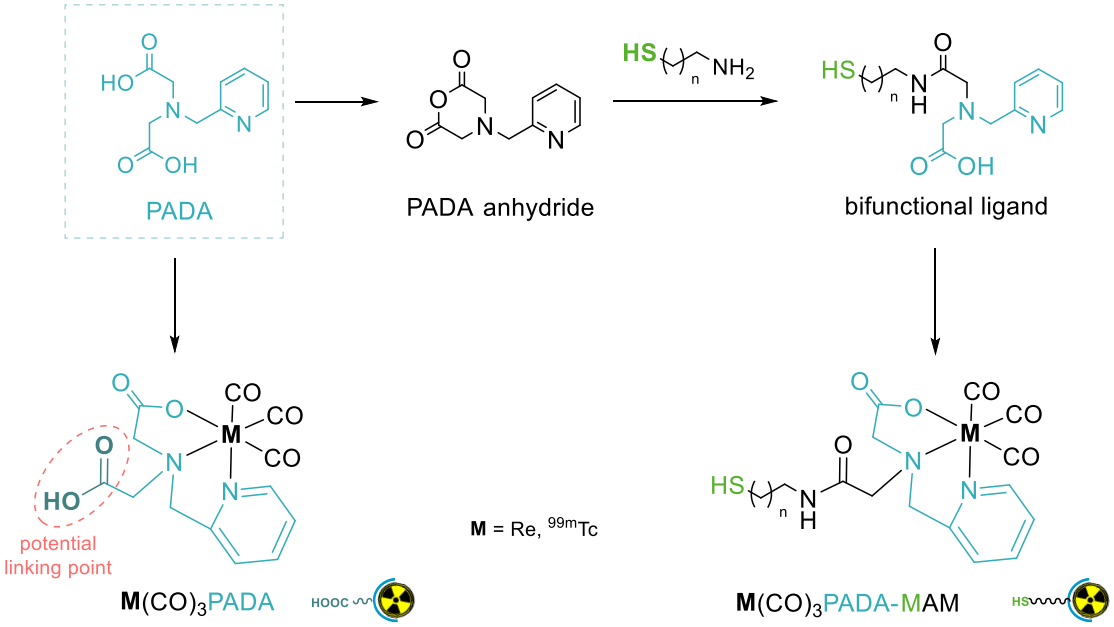

Scheme 34: Synthetic pathway to complexes with the *fac*-[**M**(CO)$_3$]$^+$ core (M= Re, ^{99m}Tc). Using PADA as the chelating unit (**top, left**) with PADA anhydride (**top, centre**) as an intermediate, directly linked to a spacer (mercaptoamine, MAM) in order to obtain the bifunctional ligand (**top, right**).

Furthermore, it provides the possibility to link another relevant species to this coordination site with its additional free acid unit (highlighted in **Scheme 34**, **bottom left**). For this purpose, various binding options exist, e.g. esterification or amide bonds.

Here, we decided to follow the approach of forming the anhydride (**Scheme 34**, **top centre**), which was further reacted *in situ* with a linker to obtain the desired ligand in a good yield (**Scheme 34**, **top right**). Various mercaptoamines (cysteamine (Cys) or mercaptoundecylamine (MUAM)) were used as linkers, which were either purchased or synthesised in the lab, as previously described in **Chapter 3.3.1**. The synthesis of PADA was performed according to a procedure described by Shepherd *et al.*[323] and is displayed in **Scheme 35**.

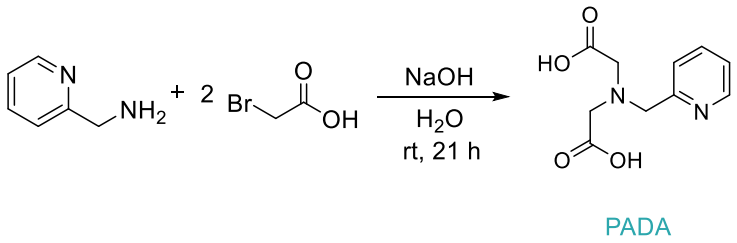

Scheme 35: Synthesis of picolylamine diacetic acid (PADA) according to Shepherd *et al.*[323]

Starting from 2-picolylamine and two equivalents of bromoacetic acid in H_2O, the chelator was formed during a nucleophilic substitution in a basic environment. After acidic work-up and recrystallisation from EtOH/H_2O (3:1), PADA was obtained as a colourless crystalline solid in good yield.

A thiol moiety was introduced in order to modify PADA as a chelating unit in a way that the ligands can be attached on the surface of Au NPs. Due to the strong Au-S bond (HSAB principle) thiol ligands are highly favoured to stabilise Au NPs. Thus, mercaptoamines were chosen as linking units. As the structure of the ligand has an important influence on the stability of a NP dispersion, bulky ligands with long chains were often used, leading to steric stabilisation. However, we decided to design two different bifunctional ligands, which differ in their spacer lengths. With these, their impact on stability of the functionalised Au NPs as well as their behaviour during a radiolabelling process were investigated. Therefore, cysteamine (Cys, mercaptoethylamine) was chosen as a very short spacer in contrast to mercaptoundecylamine (MUAM) applied as the long chain alternative. The syntheses were performed according to a modified version reported by Chiotellis *et al*.[324] and are displayed in Scheme 36.

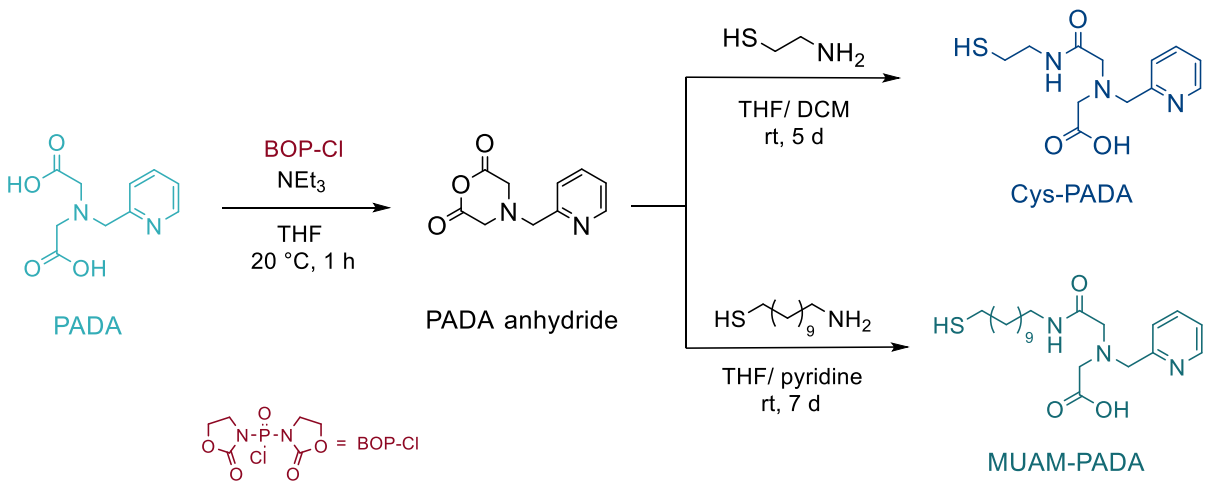

Scheme 36: Syntheses of the short chain ligand Cys-PADA starting from PADA and cysteamine (Cys, **top**) and the long chain ligand MUAM-PADA starting from PADA and mercaptoundecylamine (MUAM, **bottom**).

PADA was dissolved in anhydrous THF and the dehydration agent bis(2-oxo-3-oxazolidinyl)phosphinic chloride (BOP-Cl) as well as 3 eq. NEt_3 were added to the mixture under vigorous stirring. The synthesis of the anhydride proceeded under very mild conditions at room temperature under argon atmosphere and was complete after 1 h. Since PADA anhydride was sensitive towards heat and decomposes upon storage, the orange solution was directly subjected to the *in situ* reaction with the amine. Thereby, the anhydride solution was cooled to 0 °C and the mercaptoamine suspended in DCM or pyridine was added dropwise under vigorous stirring. After several days, the reaction mixture turned from orange to a pale yellow indicating the consumption of the anhydride. The solvent was removed *in vacuo* and aqueous work-up proceeded. Noteworthy is the fact that the short chain ligand Cys-PADA remained in the aqueous phase, whereby all by-products could be removed during several washing steps

with various organic solvents. Furthermore, the long chain ligand MUAM-PADA was extracted into the organic phase and separated from side-products. Cys-PADA could be obtained as a yellow solid in a good yield, while MUAM-PADA was a yellow gel obtained in a moderate yield.

The ligands were fully characterised by detailed NMR studies showing all predicted proton resonances: All ligands show aromatic protons of the pyridyl unit of PADA in the range from 8.87 ppm to 7.21 ppm. In particular, two distinctive triplets at 3.53 ppm and 2.85 ppm in the spectrum of Cys-PADA can be attributed to the short chain in Cys and thus supports the successful synthesis of Cys-PADA. Furthermore, the ligand MUAM-PADA shows characteristic intense resonances between 1.62 ppm and 1.26 ppm, which can be assigned to the long alkyl chain of MUAM as a spacer.

IR spectroscopy was performed to additionally verify the existing binding types within the ligands. Both bifunctional ligands (MUAM-PADA (**Figure 61**, **centre**) and Cys-PADA (**Figure 61**, **below**) carry characteristic bands, which are also present in the mother ligand PADA (**Figure 61**, **top**).

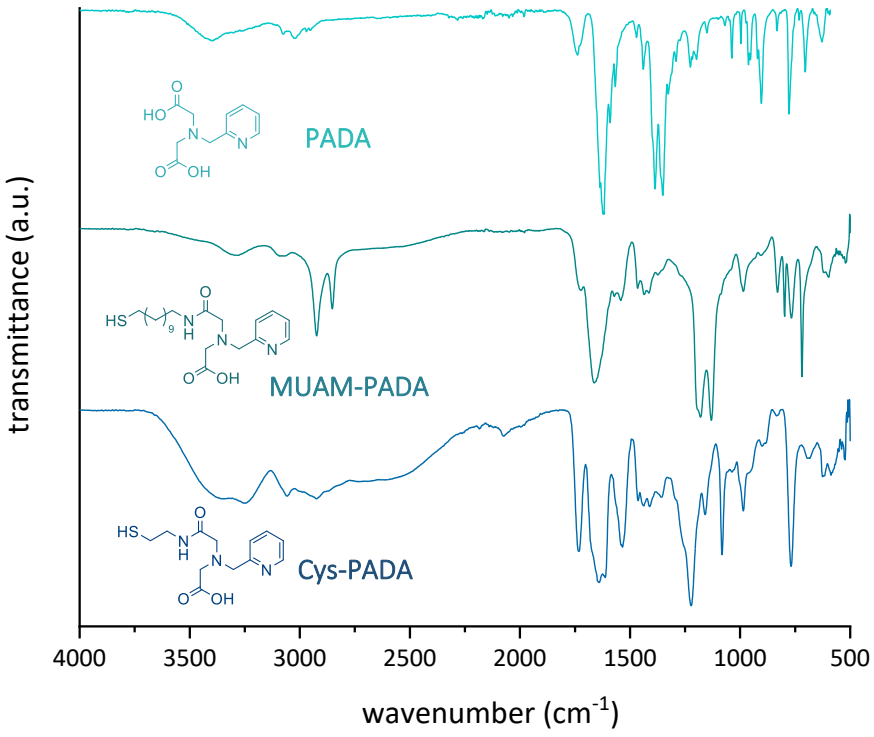

Figure 61: IR spectra of PADA (**top**), MUAM-PADA (**centre**) and Cys-PADA (**bottom**).

Each of these shows an intense sharp $\nu_{C=O}$ resonance around 1630 cm^{-1}, which is assigned to the carbonyl group of the free acid. Furthermore, broad ν_{O-H} bands in the range from 3400 – 3250 cm^{-1} indicate the presence of hydroxyl groups. Both MUAM-PADA and Cys-PADA show – next to the acid carbonyl stretching vibration – an additional strong $\nu_{C=O}$ absorption at

1540 cm^{-1} indicating the presence of an amide. This statement is supported by $\delta_{C\text{-}N}$ vibrations around 1200 cm^{-1}. These, together with weak $\nu_{N\text{-}H}$ absorption in the region between 3075 cm^{-1} and 3053 cm^{-1}, confirm the formation of primary amide bonds. Furthermore, they both possess $\nu_{C\text{-}S}$ vibrations around 600 cm^{-1}, indicating the presence of a thiol unit and thus supporting the successful synthesis of the thiolated bifunctional ligands MUAM-PADA and Cys-PADA. Moreover, slight differences in the intensities of the measured resonances in the pure ligands can be identified in the region around 2920 cm^{-1}, directly corresponding to the different lengths of the alkyl chains within these two ligands: MUAM-PADA has a moderately intense vibration, whereas the $\nu_{C\text{-}H}$ resonance of Cys-PADA is very small. In addition to that, molecular masses of all ligands were confirmed using ESI MS. The molecule ion $[M\text{-}H]^-$ of *m/z* 408.20 was found for MUAM-PADA and $[M\text{-}H]^-$ of *m/z* 282.10 for Cys-PADA. Both match the calculated masses.

3.5.2 Surface Functionalisation

Mono Ligand Shell Gold Nanoparticles

As a next step, the ligands were immobilised onto the Au NPs in ligand exchange reactions according to our published procedure as shown in **Scheme 37**. The Au-Citrate NP dispersion of interest was degassed with argon prior to the dropwise addition of the desired ligand. This was taken in a large excess of around 10^6-fold and dissolved in DMSO under vigorous stirring, in order to obtain a rapid intermixing. To ensure a pink and clear NP dispersion during the ligand exchange, the dispersion was adjusted to a slightly basic pH by adding NEt_3. Since the ligand shell changes in the exchange reaction, the properties as well as the stabilities of the resulting NPs change. In this case, they contain acid groups in their ligand sphere after the reaction, so that slightly basic conditions lead to stabilised NPs.

The reaction mixture was stirred at room temperature before it was directly purified *via* dialysis in order to remove free ligands and unbound species from the functionalised NP dispersion.

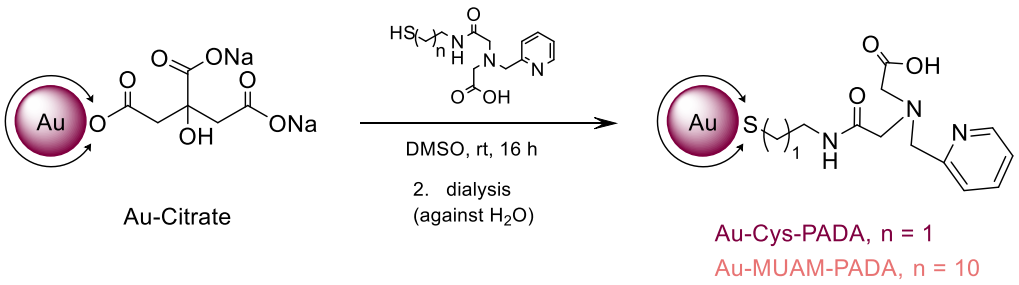

Scheme 37: NP functionalisation in a ligand exchange reaction according to Mattern *et al.*[304], starting from Au-Citrate NPs with either the short chain ligand Cys-PADA (n = 1) or the long chain ligand MUAM-PADA (n = 10) in order to obtain the corresponding functionalised mono ligand shell Au NPs.

TEM images show that the morphology of the functionalised NPs has not changed during the ligand exchange reaction. Spherical monodisperse Au NPs remain present in both samples with a diameter of d_{TEM} = 14.0 ± 0.9 nm for Au-MUAM-PADA (**Figure 62 A**) and d_{TEM} = 13.9 ± 1.1 nm

for Au-Cys-PADA (**Figure 62 D**). Furthermore, the hydrodynamic diameters, determined by DLS, indicate stable NP dispersions, with d_{hydr} = 19 ± 4 nm for Au-MUAM-PADA and d_{hydr} = 19 ± 6 nm for Au-Cys-PADA. These are typically slightly larger than the diameters determined by TEM since the entire ligand shell is considered in the measurements. Nevertheless, d_{hydr} are in the range of d_{TEM}, indicating that no large agglomerates have been formed, but stable dispersions are present. The observed absorptions plotted in **Figure 62 C** each show a maximum of the plasmon resonance at around 520 nm and thus illustrate the existence of monodisperse stable Au NP dispersions.

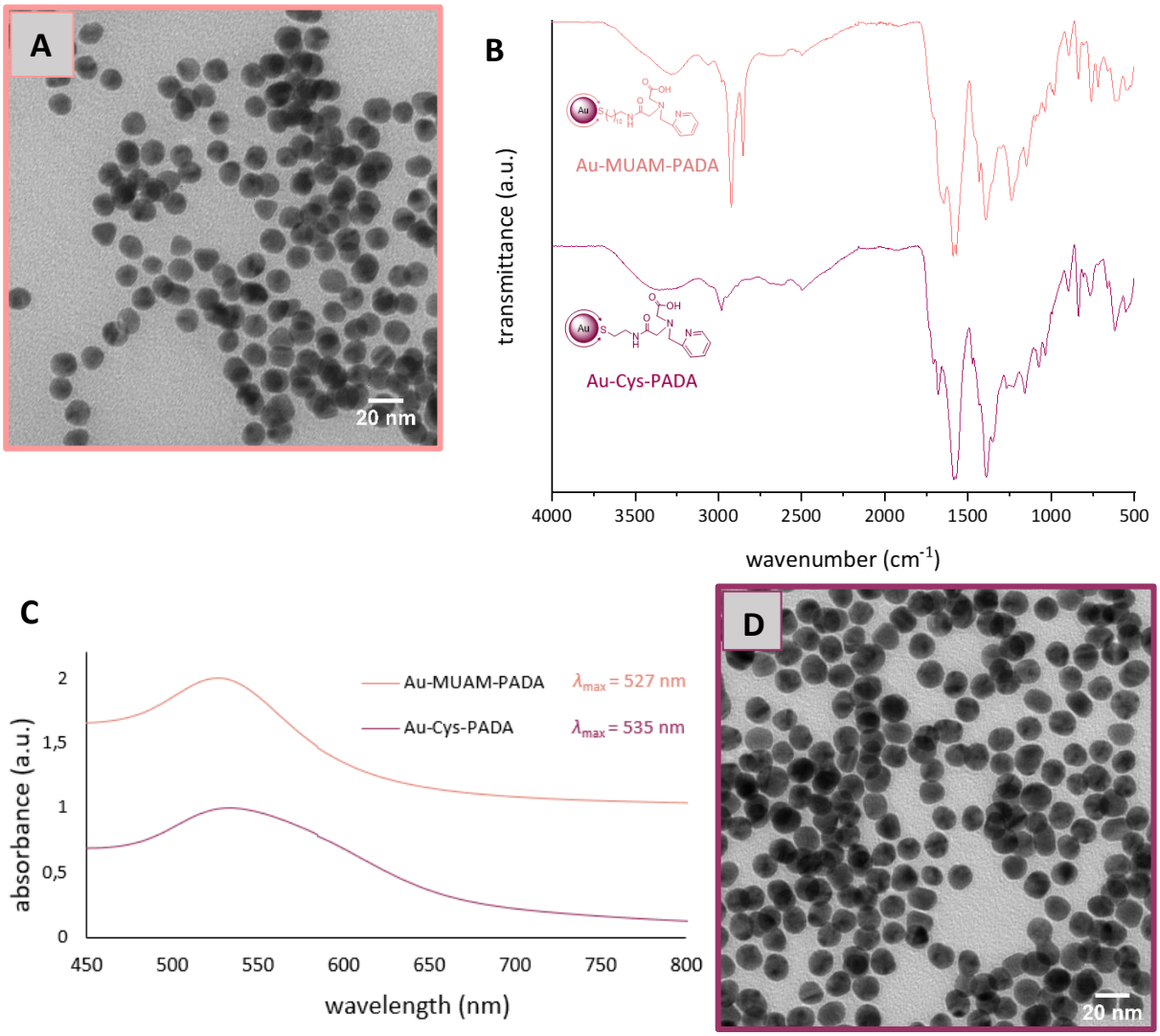

Figure 62: (**A**) TEM image of Au-MUAM-PADA NPs with d_{TEM} = 14.0 ± 0.9 nm, (**B**) IR spectra of Au-MUAM-PADA NPs and Au-Cys-PADA NPs, (**C**) their absorptions measured on an UV/Vis spectrometer and (**D**) TEM image of Au-Cys-PADA-NPs with d_{TEM} = 13.9 ± 1.1 nm.

The plotted IR spectra in **Figure 62 B** indicate a successful change in surface functionalisations of the Au NPs formerly stabilised only with citrates. The spectra of the organic ligand shells now unambiguously correspond to the desired bifunctionalised ligand.

Both, Au-MUAM-PADA NPs and Au-Cys-PADA NPs show two strong $\nu_{C=O}$ bands, each at around 1660 cm^{-1} and 1580 cm^{-1}, which belong to the carboxylic acid and the amide group, respectively. Furthermore, broad ν_{O-H} resonances at 3300 cm^{-1} correspond to the hydroxyl group of the acid. Both spectra are similar in the entire fingerprint area, including the ν_{C-S} vibration at 618 cm^{-1}. This indicates that similar ligand types are present on each respective NP surface. However, as mentioned before with the free ligands, the intensities of the ν_{C-H} oscillations around 2900 cm^{-1} vary in the two samples. These appear stronger for the long alkyl chain of Au-MUAM-PADA NPs than for the short chain in Au-Cys-PADA NPs. The successful ligand exchange was further confirmed with ^{1}H-NMR measurements by comparing the obtained spectra to the spectra of the initial Au-Citrate NP dispersions as well as the bifunctional ligands (MUAM-PADA or Cys-PADA). The spectra show all predicted proton resonances of the new ligands. The aromatic protons in the range of 8.56 ppm to 7.14 ppm are very characteristic. Furthermore, Au-Cys-PADA has two resonances between 3.48 ppm and 2.77 ppm, which correspond to the short cysteamine chain. In contrast, Au-MUAM-PADA shows intense resonances in the range of 1.80 ppm to 1.04 ppm. These are assigned to the long alkyl chain of the MUAM spacer.

In conclusion, Au NPs were successfully functionalised in various approaches with two different and freshly synthesised ligands. These mono ligand shell Au NPs now contain a chelator unit (PADA) on their surface, which enables them to form a complex with the radionuclide ^{99m}Tc and thus serve as an imaging probe in future studies.

Mixed Ligand Shell Gold Nanoparticles

In addition to Au-Cys-PADA NPs and Au-MUAM-PADA NPs, mixed shell Au NPs were prepared in the next step, carrying both a chelator ligand and a bioactive ligand. We have chosen (MUDA-AT (atropine) and MUDA-ADR (adrenaline), respectively, whose syntheses are described in Chapters 3.2.2.1 and 0. In this way, the ligand sphere was supplemented by a bioactive species and thus these mixed shell Au NPs represent pharmacologically relevant samples for potential theragnostic applications.

For their syntheses, the initial Au-Citrate NP dispersions were degassed with argon. As stated in Scheme 38, both ligand types (chelator ligand as well as bioactive ligand) were dissolved in DMSO separately and added dropwise to the NP dispersion simultaneously. Concurrent addition of the ligands and thorough mixing was essential, especially in these approaches, in order to ensure that both – chelator as well as bioactive – ligands were attached to the surface of the Au NPs.

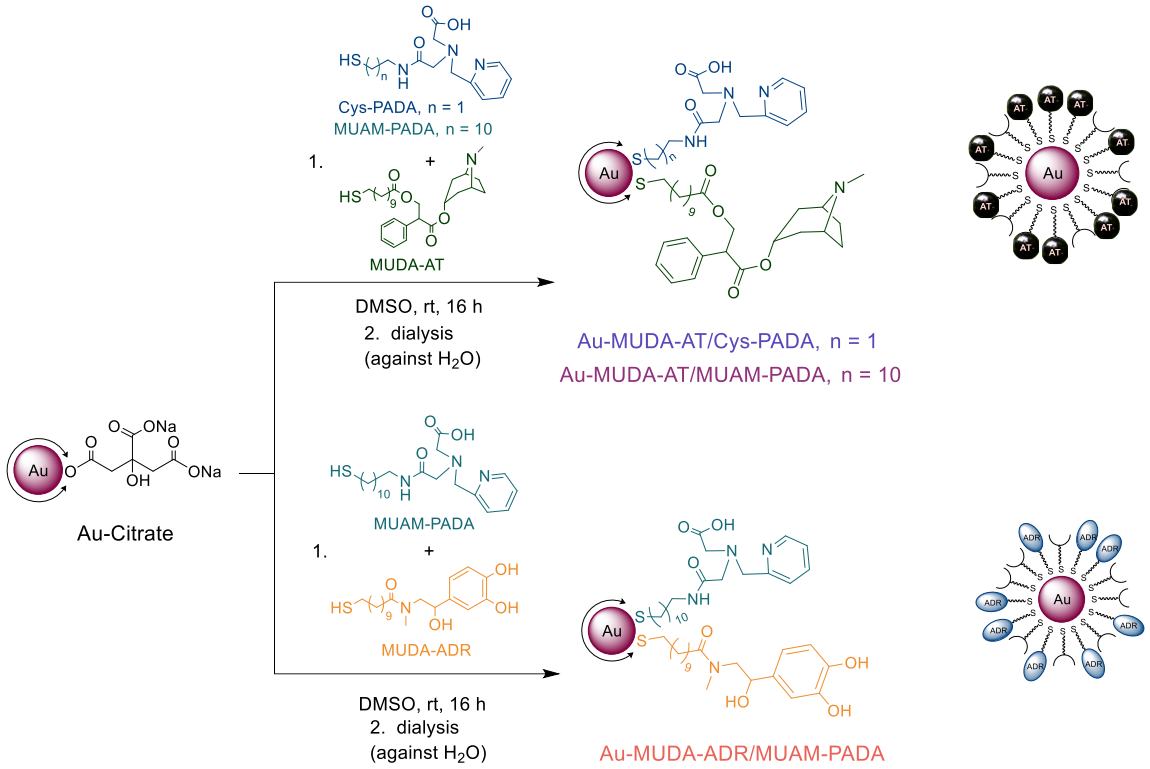

Scheme 38: Syntheses of mixed ligand shell Au NPs, starting from Au-Citrate NPs with either the short chain ligand Cys-PADA (n = 1) or the long chain ligand MUAM-PADA (n = 10) containing the chelator unit and a bioactive ligand with atropine (MUDA-AT) or adrenaline (MUDA-ADR).

Furthermore, a simultaneous addition of both ligands was repeated after a few hours. This procedure led to satisfying results in the NP approach with adrenaline. To ensure a stable NP dispersion, the pH was adjusted to 8 by the addition of NEt_3. The pink, stable dispersions were stirred at room temperature and directly purified *via* dialysis.

TEM investigations (displayed in **Figure 63**) revealed that the morphology of the spherical monodisperse NP samples did not change by their new surface functionalisation, nor did their sizes.

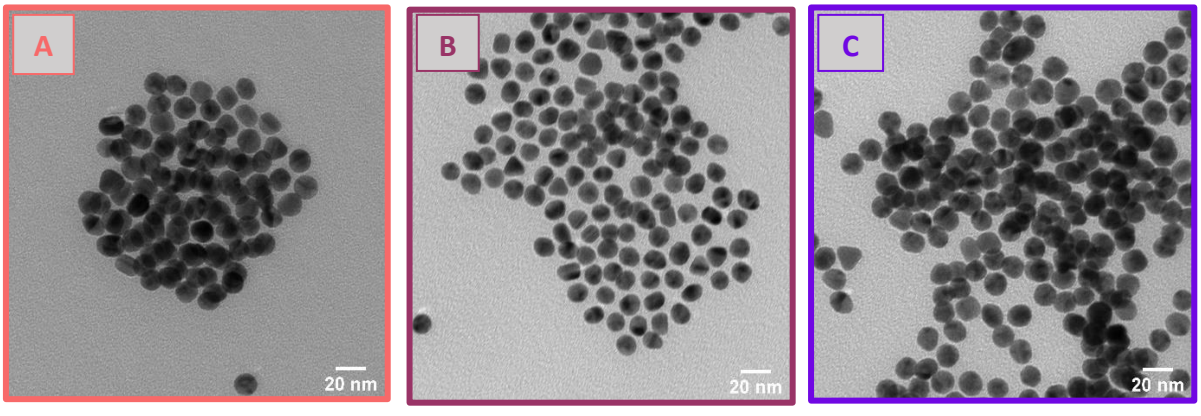

Figure 63: TEM images of Au-MUDA-ADR/MUAM-PADA NPs with d_{TEM} = 13.9 ± 1.2 nm (**A**), Au-MUDA-AT/MUAM-PADA NPs with d_{TEM} = 12.0 ± 1.0 nm (**B**) and Au-MUDA-AT/Cys-PADA NPs with d_{TEM} = 13.8 ± 1.1 nm (**C**).

Furthermore, the hydrodynamic diameters show corresponding values, indicating stable NP dispersions. Au-MUDA-ADR/MUAM-PADA NPs have a size of d_{TEM} = 13.9 ± 1.2 nm (**Figure 63 A**) and d_{hydr} = 20 ± 5 nm, Au-MUDA-AT/MUAM-PADA NPs possess d_{TEM} = 12.0 ± 1.0 nm (**Figure 63 B**) and d_{hydr} = 20 ± 6 nm. Both samples show a uniform plasmon resonance with λ_{max} around 530 nm (**Figure 64**) and thus confirm the existence of stable monodisperse Au NPs. However, Au-MUDA-AT/Cys-PADA NPs have a size of d_{TEM} = 13.8 ± 1.1 nm (**Figure 63 C**) and d_{hydr} = 29 ± 11 nm. The measured UV/Vis absorption of this sample has λ_{max} at 545 nm (**Figure 64**) and the band shows a broad and slowly flattening shoulder towards longer wavelengths, indicating a slightly less stable dispersion.

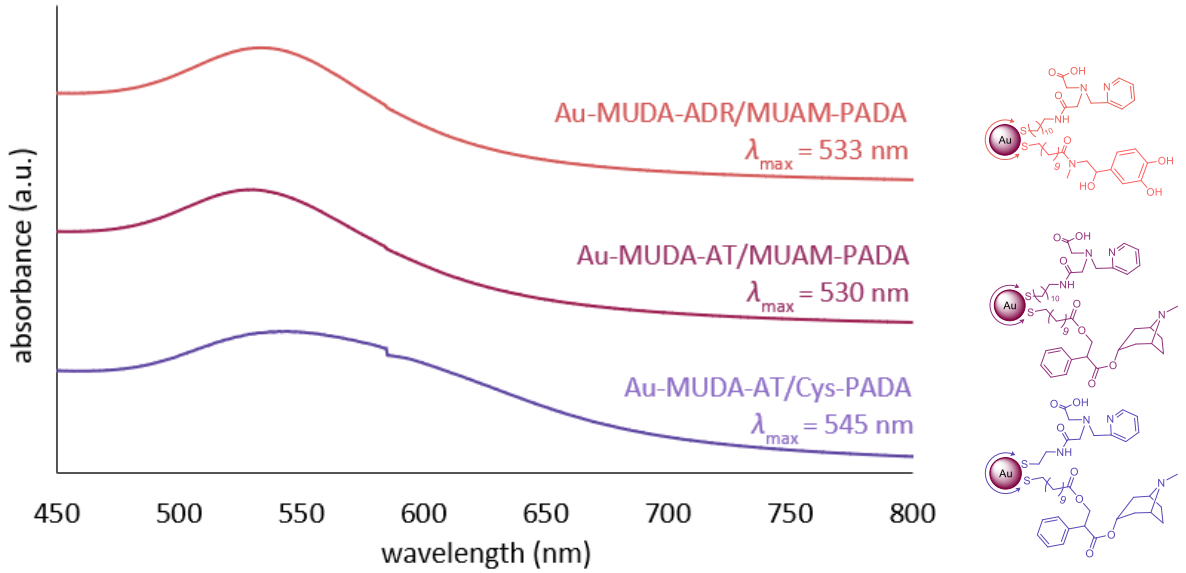

Figure 64: UV/Vis spectra of Au-MUDA-ADR/MUAM-PADA NPs (**top**), Au-MUDA-AT/MUAM-PADA NPs (**centre**) and Au-MUDA-AT/Cys-PADA NPs (**bottom**) and their corresponding absorption maxima λ_{max}.

A successful functionalisation with both ligand types was further investigated by NMR and IR, as already described for the other NPs. Again, the obtained spectra were compared with those of the two starting ligands. With the spectrum of Au-MUDA-AT/MUAM-PADA NPs as an example, **Figure 65** illustrates the presence of characteristic resonances particularly in the range of aromatic protons, showing that the mixed ligand shell Au NPs clearly possess resonances of both ligand types.

Four proton resonances in the range between 8.40 ppm and 7.69 ppm can unambiguously be assigned to the pyridyl unit of MUAM-PADA as the chelator ligand (**Figure 65**, **top** & **centre**). Moreover, the spectrum shows proton signals at 7.53 ppm to 7.19 ppm, which correspond conclusively to the phenyl group of the tropane alkaloid moiety in MUDA-AT (**Figure 65**, **top** & **bottom**). IR spectra likewise show correspondences of the mixed shell Au NPs with both ligand types and thus confirm a successful mixed ligand shell functionalisation.

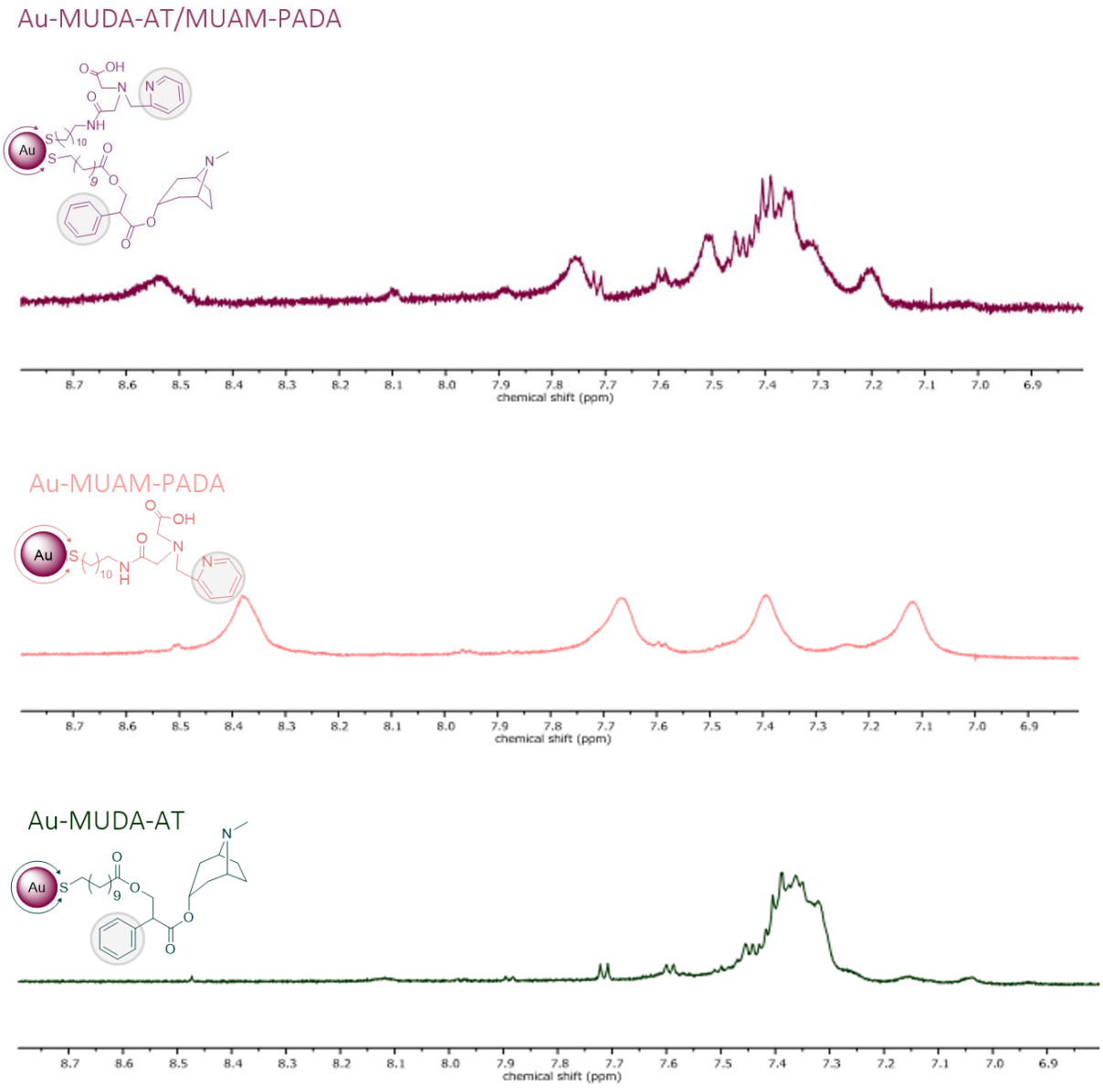

Figure 65: (Detailed) ^{1} H-NMR spectra of Au-MUDA-AT/MUAM-PADA NPs (**above**), Au-MUAM-PADA NPs (**centre**) and Au-MUDA-AT NPs (**bottom**) in the range between 8.80 ppm and 6.80 ppm, showing the aromatic proton resonances of all samples.

The ^{1}H-NMR spectrum of the mixed ligand shell Au-MUDAADR/MUAM-PADA NPs also revealed proton resonances corresponding to both ligand types.

Figure 66 displays with the IR spectrum of Au-MUDA-ADR/MUAM-PADA NPs (**Figure 66**, **top**) as an example that bands of both ligand types can be observed by comparing the spectrum of the mixed ligand shell Au NP sample to the mono ligand shell Au NPs Au-MUDA-ADR (**Figure 66**, **centre**) and Au-MUAM-PADA (**Figure 66**, **bottom**).

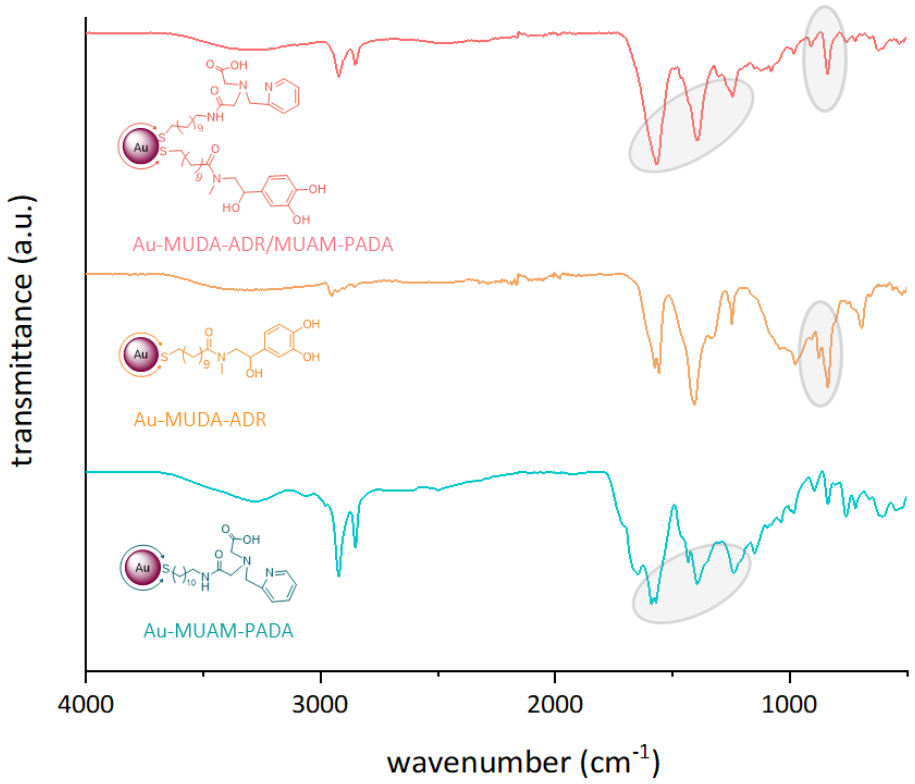

Figure 66: IR spectra of the mixed ligand shell Au-MUDA-ADR/MUAM-PADA NPs (**top**) in comparison to the mono ligand shell NPs Au-MUDA-ADR (**centre**) and Au-MUAM-PADA (**bottom**).

Comparing the spectra of the mixed ligand shell Au NP (**Figure 66**, **top**) and mono ligand shell Au-MUAM-PADA NPs (**Figure 66**, **bottom**), they show a similar intensity distribution of vibrations in the range between 1600 cm^{-1} and 1200 cm^{-1}, some of which include characteristic $\nu_{C=O}$ resonances, as they are present, e.g. in the acid of Au-MUAM-PADA NPs. Furthermore, Au-MUDA-ADR/MUAM-PADA NPs have a distinctive absorption at 840 cm^{-1}, which also occurs in Au-MUDA-ADR NPs (**Figure 66**, **centre**). Presumably, this is a $\delta_{C\text{-}H}$ *out of plane* (deformation) oscillation, which originates from the 1,2,4-trisubstituted benzene moiety in adrenaline.

Taken together, these data demonstrate that mixed ligand shell Au NPs were successfully synthesised carrying both a chelator ligand as well as a pharmacologically relevant species.

3.5.3 Syntheses of Re-Complexes with the Ligands

As a proof of principle, Re complexes of the ligands (PADA and PADA-MUAM) were synthesised, since the analytical characterisations by NMR, IR or CHNS can more conveniently be carried out with the non-radioactive heavier group 7 homologue Re instead of ^{99m}Tc. In order to compare Re-complexes with the corresponding ^{99m}Tc-complexes later on, a $Re(CO)_3$-precursor was synthesised, carrying, similar to ^{99m}Tc, three stable carbonyl ligands. $(NEt_4)_2[ReBr_3(CO)_3]$ represents a commonly used Re-precursor with three labile bromide ligands.[325] In coordinating solvents, this precursor will form $[Re(CO)_3(OH_2)_3]^+$, so that the aqua ligands can easily be exchanged by the chelating ligands, similar to the radiolabelling process with ^{99m}Tc.

$(NEt_4)_2[ReBr_3(CO)_3]$ was synthesised in a two-step process starting from $[Re_2(CO)_{10}]$ according to a procedure by Alberto *et al.*,[325] as displayed in **Scheme 39** and **40**. $[Re_2(CO)_{10}]$ was reacted with bromine in dry DCM and stirred at room temperature until a colourless precipitate formed (**Scheme 39**).[326] The product $[ReBr(CO)_5]$ was obtained as a colourless powder in a good yield (84%).

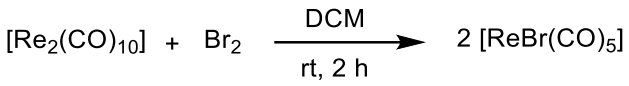

Scheme 39: Synthesis of $[Re(CO)_5Br]$ according to a modified approach of Schmidt *et al*.[326]

In the second synthetic step, $[ReBr(CO)_5]$ was reacted with NEt_4Br in diglyme (**Scheme 40**). The reaction mixture was heated at 115 °C for 19 h in order to form the product as a colourless precipitate in a yellow solution.

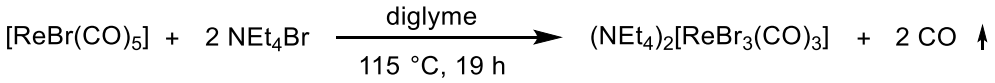

Scheme 40: Synthesis of $(NEt_4)_2[ReBr_3(CO)_3]$ according to a procedure by Alberto *et al*.[325]

The crude product was filtered off, washed with cold EtOH and dried *in vacuo* to obtain a colourless solid in a good yield (73%). The purity of $(NEt_4)_2[ReBr_3(CO)_3]$ was confirmed using elemental analysis, showing no excess of NEt_4 being present in the product. Complex formations were now performed using $(NEt_4)_2[ReBr_3(CO)_3]$. The synthesis of $[Re(CO)_3PADA]$ was carried out according to a procedure described by Alberto *et al.* (**Scheme 41**).[327]

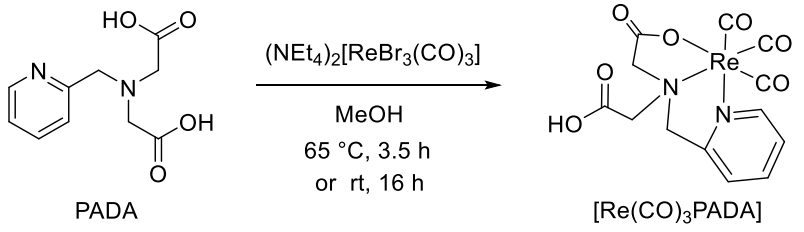

Scheme 41: Synthesis of $[Re(CO)_3PADA]$ according to a procedure by Alberto *et al*.[327]

$(NEt_4)_2[ReBr_3(CO)_3]$ was dissolved in MeOH. A solution of PADA in MeOH was added to the $(NEt_4)_2[ReBr_3(CO)_3]$ solution under vigorous stirring. The reaction mixture was heated to 65 °C for 3.5 h before the volume was reduced *in vacuo*. Then, the flask was stored at 4 °C and colourless crystals were obtained after several days. The crystals were filtered, and the pure $[Re(CO)_3PADA]$ was obtained in a moderate yield of 49%. Alternatively, the reaction was performed under milder conditions at room temperature, however, even after a longer reaction time, the obtained yield was lower (35%).

The purity of the compound was confirmed using NMR, IR and XRD. The ^{1}H-NMR spectrum shows all expected proton resonances. Aromatic proton resonances in the range from 8.81 ppm to 7.55 ppm are assigned to the pyridyl unit of PADA. $[Re(CO)_3PADA]$ contains a stereogenic centre at the central nitrogen atom, resulting in a splitting of the methylene proton resonances adjacent to this nitrogen. These proton resonances are present as six doublets in the range between 5.25 ppm and 3.86 ppm.

Figure 67 displays the IR spectra of $[Re(CO)_3PADA]$ in comparison to its starting materials PADA and $(NEt_4)_2[ReBr_3(CO)_3]$. The most significant new introduced resonances in $[Re(CO)_3PADA]$ (**Figure 67**, **bottom**) are the intense and characteristic $\nu_{C\equiv O}$ oscillations around 2000 cm^{-1}. These vibrations are assigned to the carbonyl ligands, as already observed in $(NEt_4)_2[ReBr_3(CO)_3]$ (**Figure 67**, **top**).

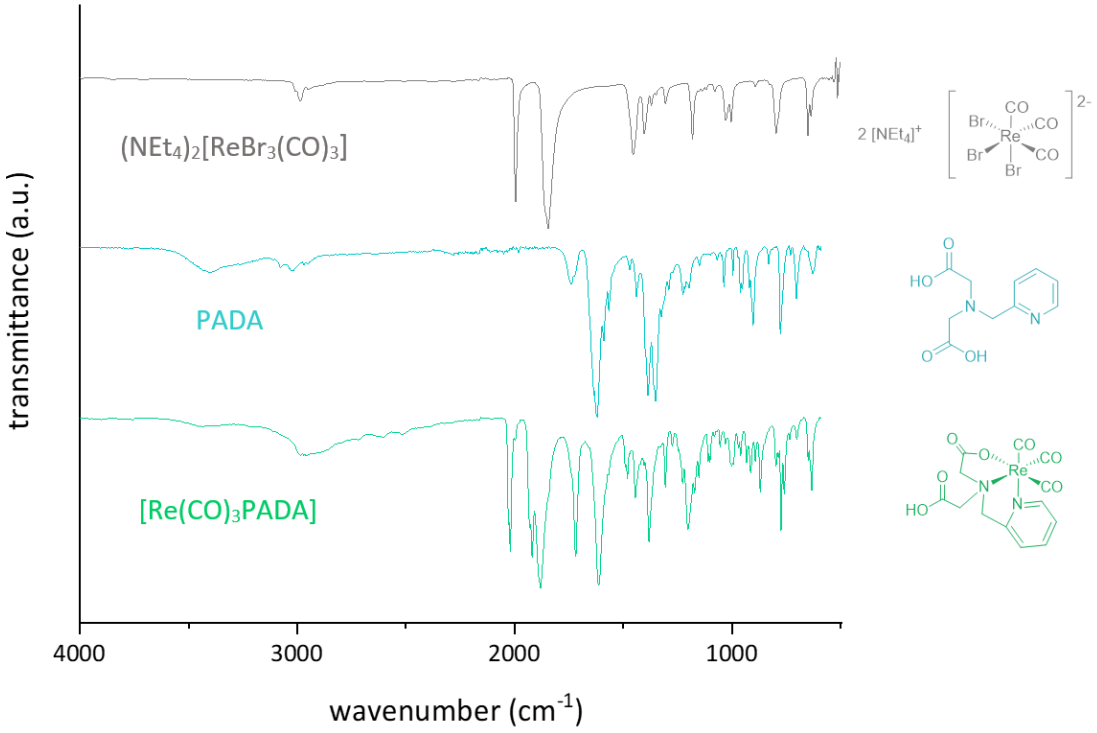

Figure 67: IR spectra of the starting materials $(NEt_4)_2[ReBr_3(CO)_3]$ (**top**) and PADA (**centre**) and the complex $[Re(CO)_3PADA]$ (**bottom**).

Furthermore, the spectrum of $[Re(CO)_3PADA]$ reveals the presence of the chelating ligand PADA (**Figure 67**, **centre**) in the target structure with distinct $\nu_{C=O}$ vibrations around 1600 cm^{-1}, a δ_{C-O} band below 1400 cm^{-1} and a δ_{O-H} vibration at 860 cm^{-1}, which are attributed to the carboxyl units. The ^{1}H-NMR spectrum shows all expected proton resonances: Aromatic proton resonances in the range from 8.81 ppm to 7.55 ppm assigned to the pyridyl unit of PADA. $[Re(CO)_3PADA]$ contains a stereogenic centre at the central nitrogen atom, resulting in a splitting of the methylene proton resonances adjacent to this nitrogen. These proton resonances are present as 6 doublets in the range between 5.25 ppm and 3.86 ppm. These characterisations clearly indicate the formation of the complex $[Re(CO)_3PADA]$.

Since crystals of $[Re(CO)_3PADA]$ were obtained, the exact structure was further confirmed by X-ray crystallographic analysis (**Figure 68**). The solution reveals the already-known bonding motif as reported by Marti *et al.*[328] However, the data solution was performed in the monoclinic space group $P2_1/c$, with an R_1 of 2.07%, wR_2 = 4.80% and an R_{int} of 5.27%. The cell parameters are a = 7.6084(3), b = 24.1148(11), c = 7.7772(3) Å and β = 91.146(2)°. This is in contrast to the reported values by Marti *et al.* of a = 14.567 (1), b = 13.145 (1), c = 14.865 (1) Å in the orthorhombic space group *Pbca*, with an R_1 of 4.95%, wR_2 = 9.52% and an R_{int} of 8.07%.

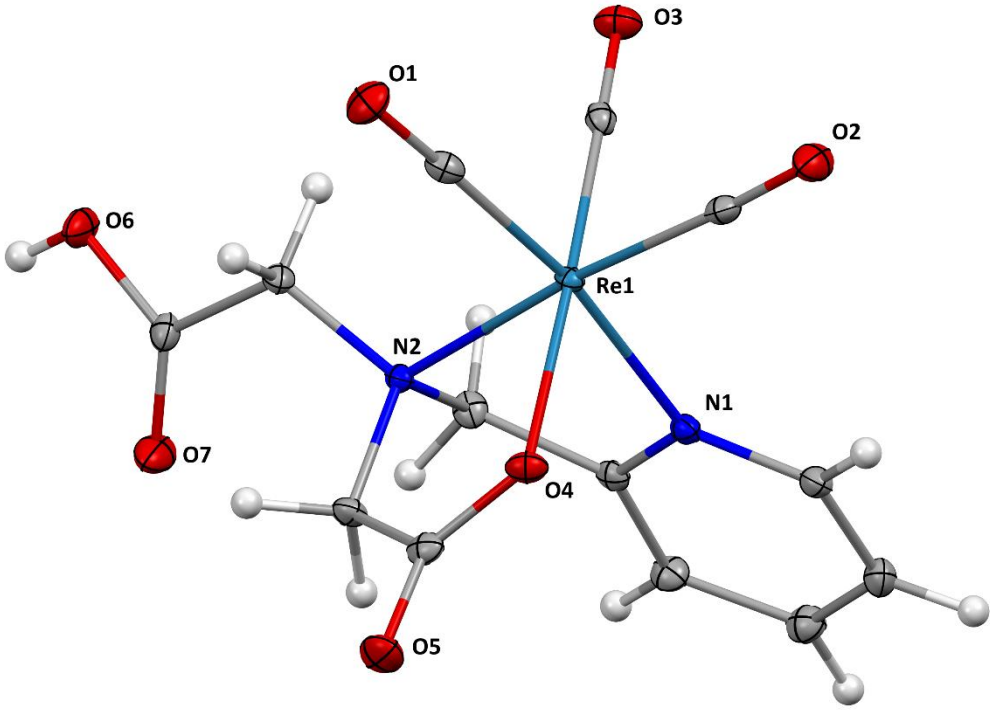

Figure 68: Molecular structure of $[Re(CO)_3PADA]$ (displacement ellipsoids are drawn at 50% probability).

Most importantly, these data reveal the exact binding behaviour within the $[Re(CO)_3PADA]$ complex. With this knowledge, a similar complexation of the radioactive isotope ^{99m}Tc can be assumed.

As a next step, [Re(CO)$_3$PADA-MUAM] was synthesised. Assuming a similar coordination chemistry in this complex compared to [Re(CO)$_3$PADA], a free thiol moiety of the MUAM-linker is available in order to attach the whole complex onto a Au NP surface. The experimental work of the [Re(CO)$_3$PADA-MUAM] synthesis as well as its functionalisation onto Au-Citrate NPs was performed jointly with Patrick Scholz (advanced module of the master student under the supervision of the author).

For the synthesis of [Re(CO)$_3$PADA-MUAM] (**Scheme 42**), (NEt$_4$)$_2$[ReBr$_3$(CO)$_3$] was dissolved in purged MeOH and PADA-MUAM dissolved in MeOH was added quickly before the reaction mixture was heated to reflux. The complex was purified using column chromatography and was obtained as a brown solid in a rather low yield (33%).

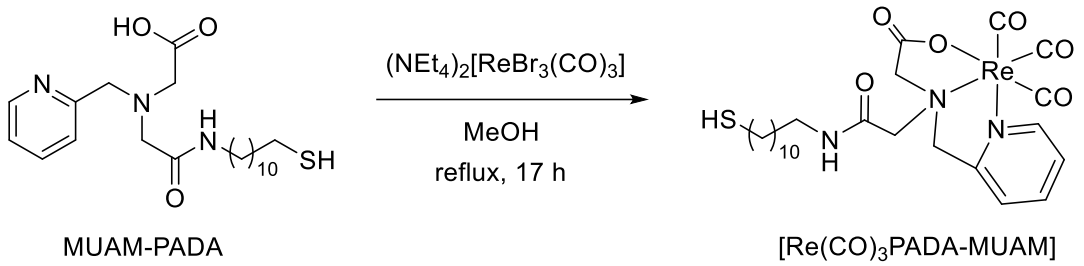

Scheme 42: Synthesis of [Re(CO)$_3$PADA-MUAM].

The purity of the complex was further confirmed using HPLC, only showing one large signal at t_R= 25.73 min, which is clearly distinct from the retention times of the starting materials PADA-MUAM (t_R= 7.37 min) and (NEt$_4$)$_2$[ReBr$_3$(CO)$_3$] (t_R= 14.21 min).

The ^{1}H-NMR spectrum of the [Re(CO)$_3$PADA-MUAM] shows all expected proton resonances including the aromatic protons between 8.75 ppm and 7.57 ppm, which are attributed to the pyridyl unit of PADA. In addition to these proton signals, characteristic resonances in the range of 1.67 ppm to 1.20 ppm exist, which are assigned to the long alkyl chain of the MUAM linker. Furthermore, the ^{1}H-NMR spectrum reveals that the complex formed possesses a stereogenic centre, which causes a splitting of the resonances of the methylene protons (**Figure 69**, **bottom**). This was not observed for the free ligand (**Figure 69**, **top**).

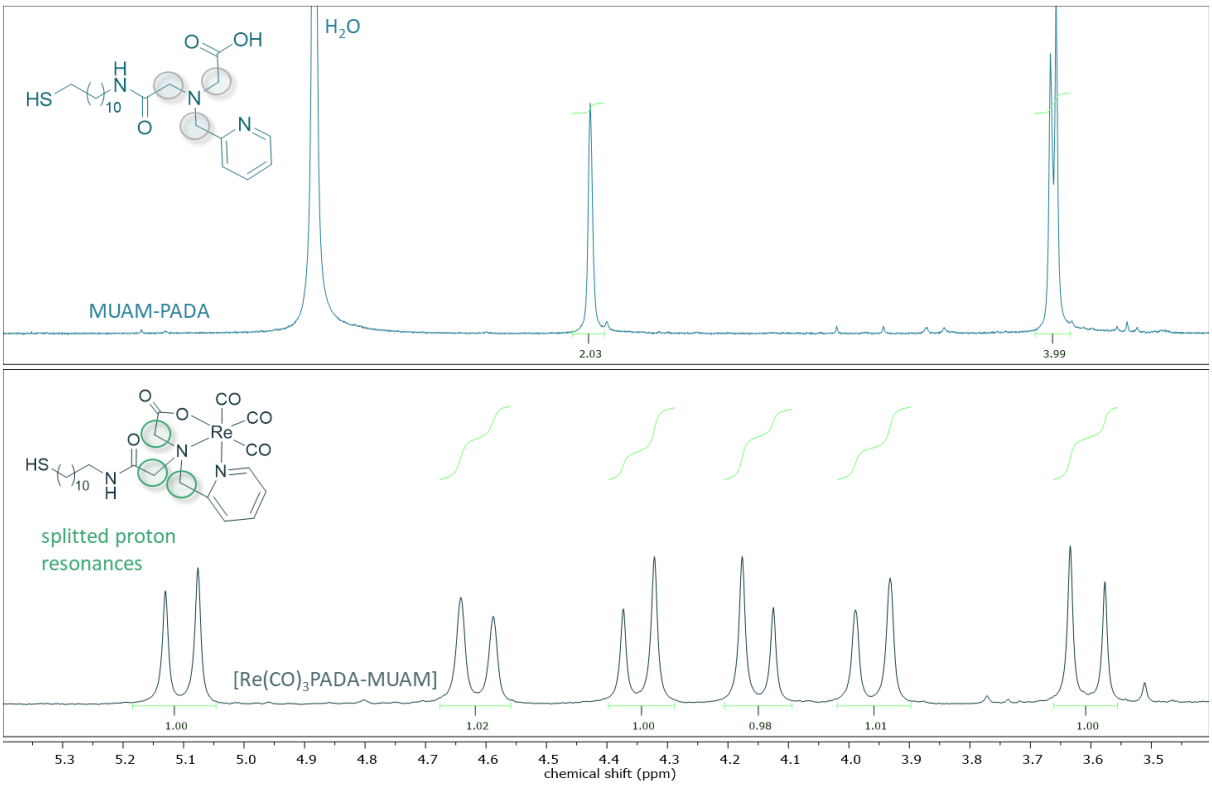

Figure 69: ^{1}H-NMR spectra of the free ligand (**top**) and the complex [Re(CO)$_3$PADA-MUAM] (**bottom**) reveal splitting of the diastereotopic protons.

As highlighted in **Figure 69** (**top**), the ligand PADA-MUAM only reveals three singlet signals between 4.00 ppm and 3.30 ppm, which are assigned to the methylene groups next to the central nitrogen. In contrast, the spectrum of the complex (**Figure 69**, **bottom**) displays their splitting into doublets with extremely large coupling constants up to 16.0 Hz because of the stereogenic centre at the nitrogen atom. The corresponding proton resonances appear now in the region between 5.13 ppm to 3.57 ppm. The splitting pattern, however, is a clear indication of an existing complex. It has been attempted to crystallise the material, but without any success so far.

3.5.4 Surface Functionalisation with a Re-Complex

The complex was further immobilised onto the Au NPs as a proof of principle whether the free thiol moiety is capable for an attachment onto the NP surface. The functionalisation of the Au-Citrate NPs was performed in a ligand exchange reaction according to our published method, as shown in **Scheme 43**.

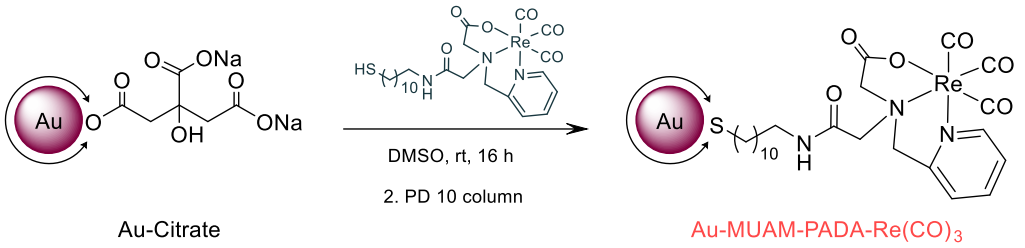

Scheme 43: Functionalisation of Au-Citrate NPs with [Re(CO)$_3$PADA-MUAM].

Au-Citrate NPs were degassed with argon prior to the dropwise addition of [Re(CO)$_3$PADA-MUAM] dissolved in DMSO. A minor quantity of PADA-MUAM in DMSO was also added, in order to obtain a more stable Au NP system. This stabilisation is caused by the electrosteric repulsion of the charged acid moieties of PADA present on the ligand shell. In a further approach, without the addition of the free ligand MUAM-PADA, the Au NPs did not remain stable over time and precipitated quickly.
After the addition of both, complex and ligand, the pH was adjusted to 8 and the reaction mixture was stirred at room temperature under argon atmosphere. Then, it was purified *via* a desalting column PD 10 in order to remove free ligands and unbound species from the functionalised NP system and the stable pink fractions were collected and further analysed.

As displayed in **Figure 70 A**, TEM images reveal that the morphology of the Au NPs has not changed during the functionalisation. Furthermore, spherical monodisperse Au NPs with a size of d_{TEM} = 12.9 ± 0.9 nm were obtained. **Figure 70 B** shows the UV/Vis spectra of Au-MUAM-PADA-Re(CO)$_3$ NPs in comparison to their starting particles Au-Citrate (Ø 13 nm). Both samples reveal a distinct plasmon resonance in the similar range.

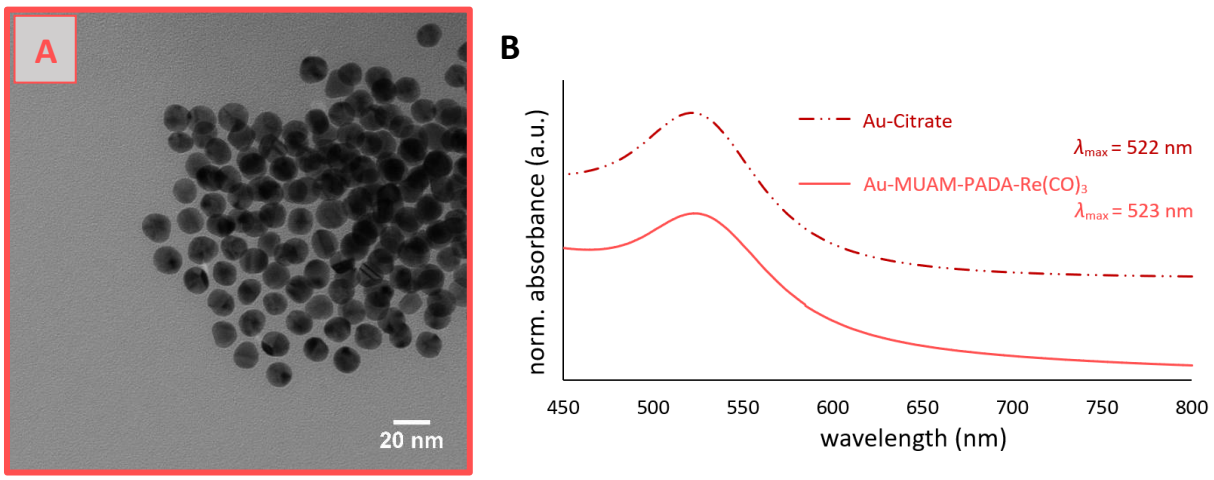

Figure 70: (**A**) TEM image of Au-MUAM-PADA-Re(CO)$_3$ and (**B**) its UV/Vis spectrum in comparison to the starting NPs Au-Citrate.

The organic framework was further analysed using ^{1}H-NMR and IR spectroscopy. The ^{1}H-NMR spectrum of the Au-MUAM-PADA-Re(CO)$_3$ NPs displays all expected proton resonances. The aromatic proton signals in the range of 8.40 ppm and 7.10 ppm are assigned to the pyridyl unit of the complex. Moreover, characteristic resonances between 1.68 ppm and 1.10 ppm are attributed to the long alkyl chain of MUAM.

The plotted IR spectra in **Figure 71** display the spectrum of Au-MUAM-PADA-Re(CO)$_3$ NPs (**bottom**) in comparison to its corresponding starting complex [Re(CO)$_3$PADA-MUAM] (**centre**) as well as the free ligand MUAM-PADA (**top**).

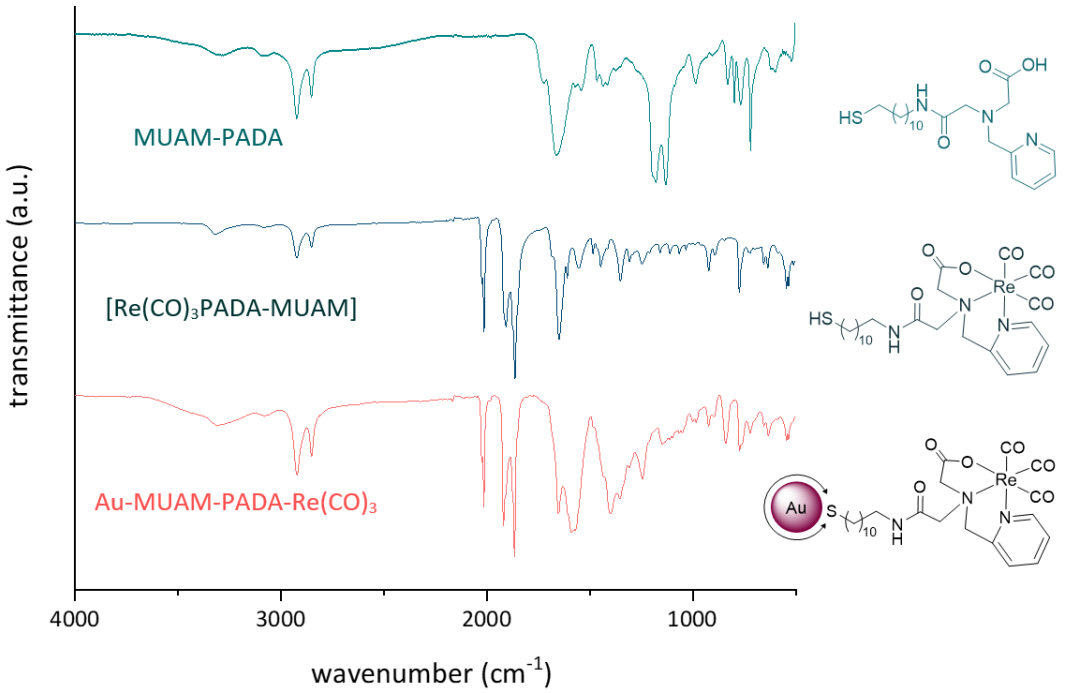

Figure 71: IR spectra of the free ligand MUAM-PADA (**top**), the complex Re(CO)$_3$PADA-MUAM (**centre**) and Au-MUAM-PADA-Re(CO)$_3$ NPs (**bottom**).

The most similarities can be observed in Au-MUAM-PADA-Re(CO)$_3$ NPs (**Figure 71**, **bottom**) and the complex [Re(CO)$_3$PADA-MUAM] (**Figure 71**, **centre**), resulting from the successful immobilisation of the complex onto the Au NPs. Further significant consistencies are found when these are compared with the free ligand (**Figure 71**, **top**), such as strong $\nu_{C=O}$ absorptions around 1650 cm^{-1} and 1570 cm^{-1}, which are assigned to the carboxylic acid and the amide group, respectively. Furthermore, all spectra show a ν_{C-S} band around 620 cm^{-1} as well as ν_{C-H} vibrations around 2900 cm^{-1}, which are attributed to the thiol group and the long alkyl chain of the linker. Most significantly, the spectra of the complex (**Figure 71**, **centre**) as well as the functionalised Au NPs (**Figure 71**, **bottom**) reveal the presence of intense sharp $\nu_{C\equiv O}$ absorptions around 1900 cm^{-1}. These are assigned to the Re(CO)$_3$ moieties, which did not exist in the free ligand. Thus, a successful complexation of the MUAM-PADA as well as the functionalisation of [Re(CO)$_3$PADA-MUAM] onto Au NPs is proven.

Furthermore, EDX measurements were performed using the dried Au NP sample on the TEM grid. The image again shows spherical monodisperse NPs (**Figure 72**). A corresponding EDX quantification was performed on the point 003 highlighted in **Figure 72**, **left**.

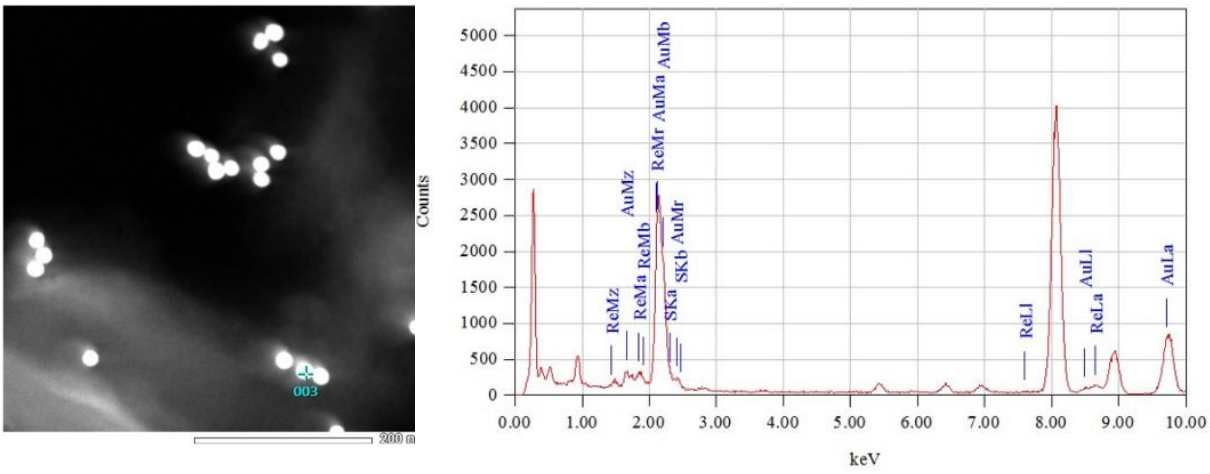

Figure 72: EDX image of Au-MUAM-PADA-Re(CO)$_3$ NPs, (**left**) and EDX analysis at the highlighted spot 003 (**right**).

The analysis (**Figure 72**, **right**) reveals mainly the existence of Au from the Au NPs with 85%. The large signal a 8.00 keV is assigned to Cu and was caused by the copper TEM grid. Quantitative analysis indicates that, in addition to Au, a small percentage of S (9%) and Re (5%) was present (**Table 8**), confirming the successful functionalisation of the Au NPs with the [Re(CO)$_3$PADAMUAM].

Table 8: Thin Film Standardless Quantitative Analysis.

Element	(keV)	Mass %	Counts	Sigma	Atom %
S K	2.307	1.65	1681.43	0.10	9.33
Re M*	1.842	5.41	1735.74	0.41	5.26
Au M (Ref.)	2.120	92.93	27788.40	0.96	85.41
Total		100.00			100.00

3.5.5 Labelling of the Ligands

With ^{99m}Tc being a radioactive isotope (γ-emitter, half-life 6.00 h, 140 keV), all experiments had to be performed in a licensed and appropriately equipped laboratory. Thus, they were carried out at the laboratories of the Alberto group at the University of Zurich. Once the activity of the labelled sample has reached a level below the exemption limit, the material could be transferred to the University of Cologne for post-labelling analyses using TEM, UV/Vis, DLS and IR.

First, the respective ligands were investigated regarding their ability to complex ^{99m}Tc as well as its non-radioactive heavier group 7 homologue Re. Initially, PADA was tested as the chelate parent unit and reacted with ^{99m}Tc. This radioactive isotope was freshly eluted from a generator in the form of $^{99m}TcO_4^-$ and then directly converted to $[^{99m}Tc(OH_2)_3(CO)_3]^+$ using the *Isolink*® kit chemicals sodium boranocarbonate (NaBC), sodium tartrate dihydrate and sodium tetraborate decahydrate as shown in **Scheme 44**.

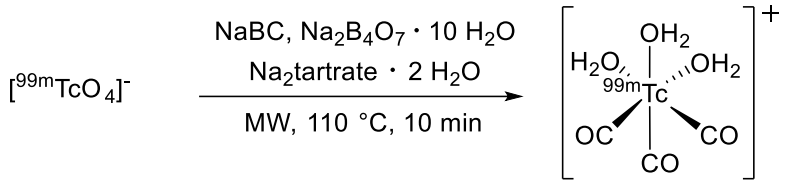

Scheme 44: Synthesis of $[^{99m}Tc(OH_2)_3(CO)_3]^+$ using *Isolink*® kit chemicals.

After the reaction mixture was heated in a microwave at 110 °C for 10 min, unreacted NaBC was quenched with 1 M HCl and the pH was set to 2. Afterwards, the pH was adjusted to 7-8 with 1 M NaOH in order to perform the complexation reactions at a neutral pH. The tricarbonyl complex was analysed *via* HPLC showing a single, distinct signal after 6.1 min with a radiochemical purity (RCP) of 99.4%. $[^{99m}Tc(OH_2)_3(CO)_3]^+$ is an excellent building block, which was first described by Alberto *et al.*[327] Here, the metal ion is octahedrally coordinated. Three carbonyl ligands are strongly bound, but the three aqua ligands can easily be replaced by new ligands and thus the tripodal PADA ligand is very suitable for such a ligand exchange. In order to radiolabel PADA, as shown in **Scheme 45**, the ligand was redissolved in degassed EtOH, $[^{99m}Tc(OH_2)_3(CO)_3]^+$ (pH 8) was added and the colourless reaction mixture was stirred at 80 °C for 30 min.

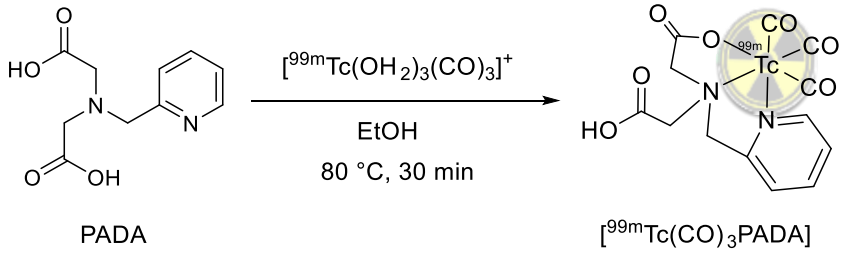

Scheme 45: Synthesis of $[^{99m}Tc(CO)_3PADA]$.

Then, the complex [^{99m}Tc(CO)$_3$PADA] was analysed with HPLC (**Figure 73**, **left**), eluting with a γ signal at 18.42 min and obtained with >99.5% RCP. Since the corresponding Re complex [Re(CO)$_3$PADA] was synthesised as described in **Chapter 3.5.3**, a co-injection was performed to ensure that the present complex with ^{99m}Tc corresponds to the expected one of the Re analogue and can therefore be compared with it. A constant time difference between the signal on the UV/Vis detector and a signal on the γ detector of the HPLC thus confirms the presence of the expected complex.

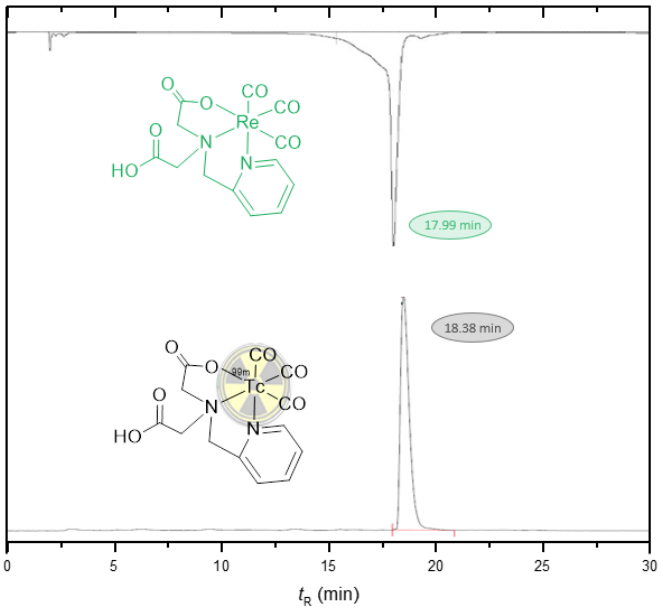

Figure 73: γ HPLC trace of [^{99m}Tc(CO)$_3$PADA] (**bottom**) and the corresponding UV/Vis HPLC trace (with coinjection of [Re(CO)$_3$PADA], **top**).

The coinjection with [Re(CO)$_3$PADA] confirms the existence of [^{99m}Tc(CO)$_3$PADA] in an excellent radio chemical purity. As predicted, the three desired coordination sites bind with the metal ion and the fourth coordination site remains available for possible further attachment. Since the binding behaviour of our chelator unit was determined and conform to the literature,[327] the two synthesised ligands were now each reacted with [^{99m}Tc(OH$_2$)$_3$(CO)$_3$]$^+$. PADA-MUAM was dissolved in degassed H$_2$O and [^{99m}Tc(OH$_2$)$_3$(CO)$_3$]$^+$ (pH 8) was added (**Scheme 46**, **left**).

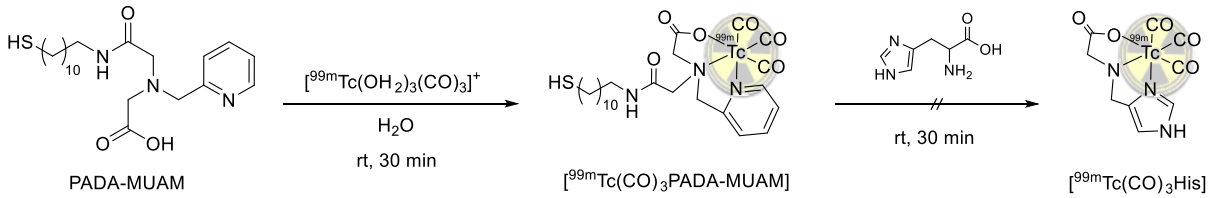

Scheme 46: Synthesis of [^{99m}Tc(CO)$_3$PADA-MUAM] and thereafter stability test with the addition of histidine.

The reaction mixture was stirred at room temperature for 30 min and analysed *via* HPLC showing a signal at 24.42 min with a RCP of 91% (**Figure 74**, **left**). This signal appears to be the desired complex [^{99m}Tc(CO)$_3$PADA-MUAM]. As a side product [^{99m}Tc(CO)$_3$PADA] was found at

18.17 min. This contamination may have occurred during the progress of complex formation, so that a small amount of PADA-MUAM was decomposed during the reaction. However, another reason might be that the parent ligand PADA was not completely removed during the purification of PADA-MUAM before. Nevertheless, this contamination is of no relevance for further attachment to NPs, since PADA-MUAM or [^{99m}Tc(CO)$_3$-PADA-MUAM] are more favoured to attach to the Au NP surface with the thiol unit due to the strong Au-S bond formed.

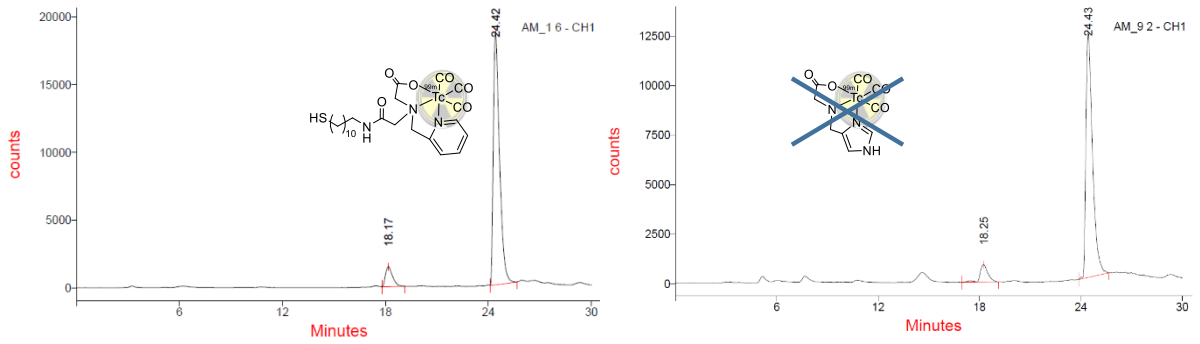

Figure 74: γ HPLC traces of [^{99m}Tc(CO)$_3$PADA-MUAM] (**left**) and [^{99m}Tc(CO)$_3$PADA-MUAM] after the addition of histidine (**right**).

A further step was to investigate the stability of [^{99m}Tc(CO)$_3$PADA-MUAM] with respect to the presence of other competing ligands, which are present in biological systems. For this purpose, histidine, a ubiquitous ligand present in a variety of biological systems, was chosen as a competitive test ligand.[329–332] In this experiment, histidine was dissolved in H_2O and then added to the complex solution in excess. The reaction mixture was stirred at room temperature and monitored by HPLC. No ligand exchange was observed. Instead, [^{99m}Tc(CO)$_3$PADA-MUAM] remained in 92% RCP as displayed in the HPLC trace in **Figure 74** (**right**), suggesting that PADA-MUAM is stable against other strongly coordinating ligands. However, further research should be conducted with ligands, such as cysteine, or directly with biological material, such as cellular or blood plasma or relevant buffer media or sera.

Attempts to synthesise [^{99m}Tc(CO)$_3$PADA-MUAM] at higher temperatures and non-aqueous solvents were not successful. Performing the radiolabelling of PADA-MUAM in MeOH or EtOH led to side products and lower RCPs. Heating during the reaction led also to a decomposition of the ligand and to a variety of side products, and was therefore not further applied.

The strength of MUAM-PADA as a ligand for complexing ^{99m}Tc became even more evident when its concentration was lowered. In previous reactions, 0.4 µmol of the ligand was added, resulting in an overall 0.6 mM solution. Full complexation of ^{99m}Tc with similar RCP could be obtained down to a concentration of 60 µM.

With the knowledge gained in the radiolabelling of PADA-MUAM, the complexation of the short chain ligand Cys-PADA with the radioisotope ^{99m}Tc was performed under mild conditions as well, as shown in **Scheme 47**. The ligand was dissolved in degassed H_2O, [^{99m}Tc(OH$_2$)$_3$(CO)$_3$]$^+$ (pH 7) was added and the reaction mixture was stirred at room temperature.

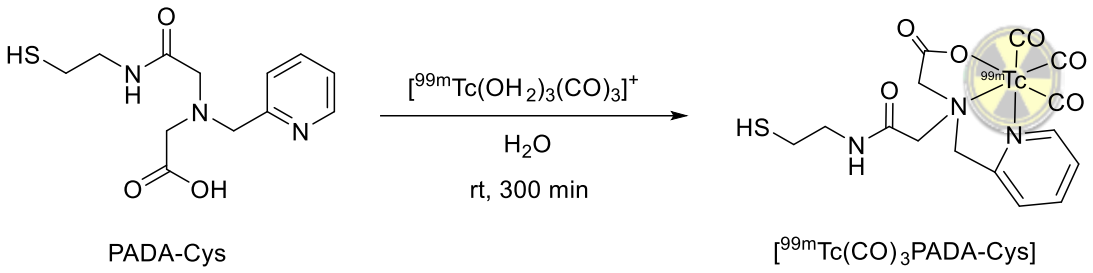

Scheme 47: Synthesis of [^{99m}Tc(CO)$_3$PADA-Cys].

The chronological progress of the reaction was monitored *via* HPLC and the traces are shown in **Figure 75**. After a reaction time of 30 min, the γ HPLC trace (**Figure 75**, **top**) showed a dominant signal at 6.1 min, which can be assigned to the [^{99m}Tc(OH$_2$)$_3$(CO)$_3$]$^+$ still present in the reaction mixture. A second, broader signal with a maximum at t_R = 20.5 min may be attributed to the desired complex [^{99m}Tc(CO)$_3$PADA-Cys]. However, this product is accompanied by side products only with a respective RCP of 23%. Parallel to [^{99m}Tc(CO)$_3$PADA-Cys], a small amount of [^{99m}Tc(CO)$_3$PADA] was present at t_R = 18.0 min, as previously observed with the long chain analogue PADA-MUAM. Furthermore, an additional unknown product existed with a retention time of 19.3 min. Presumably, the nearby thiol unit of the short chain ligand interfered in the complex formation, resulting in side products.

After 100 min of stirring, the γ HPLC trace (**Figure 75**, **centre**) indicated that [^{99m}Tc(OH$_2$)$_3$(CO)$_3$]$^+$ had not been completely consumed since a medium signal at 6.1 min was still present. Nonetheless, the amount of desired [^{99m}Tc(CO)$_3$PADA-Cys] increased to a RCP of 44% (t_R = 20.5 min). As before, additional to the aforementioned and observed by-products, another unknown side product appeared at a slightly longer retention time of 21.2 min.

Full consumption of [^{99m}Tc(OH$_2$)$_3$(CO)$_3$]$^+$ was observed after 300 min (**Figure 75**, **bottom**). All previously mentioned side products persisted, though the desired product formed with a RCP of 76%.

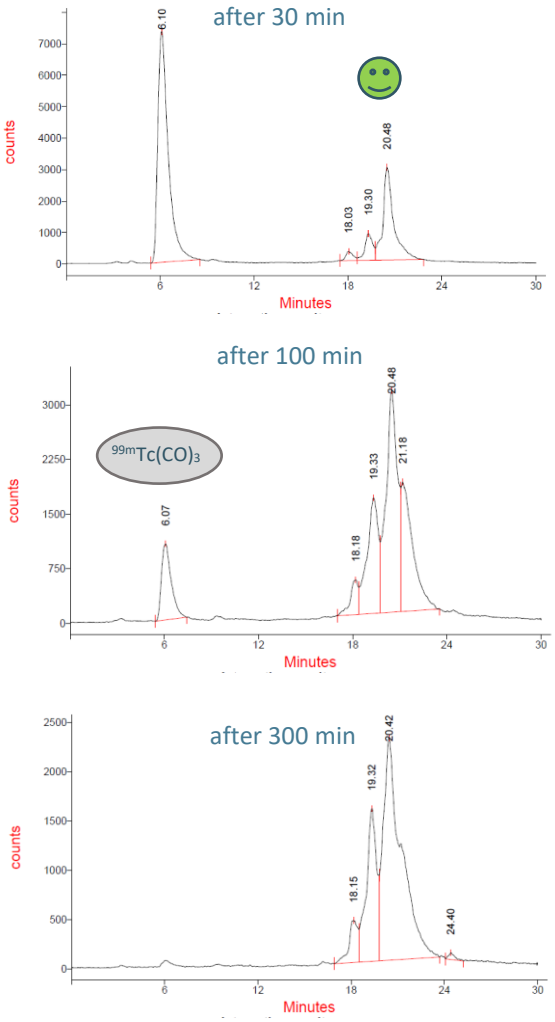

Figure 75: γ HPLC traces of the [^{99m}Tc(CO)$_3$PADA-Cys] approach after 30 min (**top**), 100 min (**centre**) and 300 min (**bottom**).

Because the complexation of Cys-PADA did not lead to a distinctive complex in high yield, another ligand with the thiol unit protected as thioacetate was synthesised. **Scheme 48** shows the two-step synthesis leading to the Ac-Cys-PADA ligand.

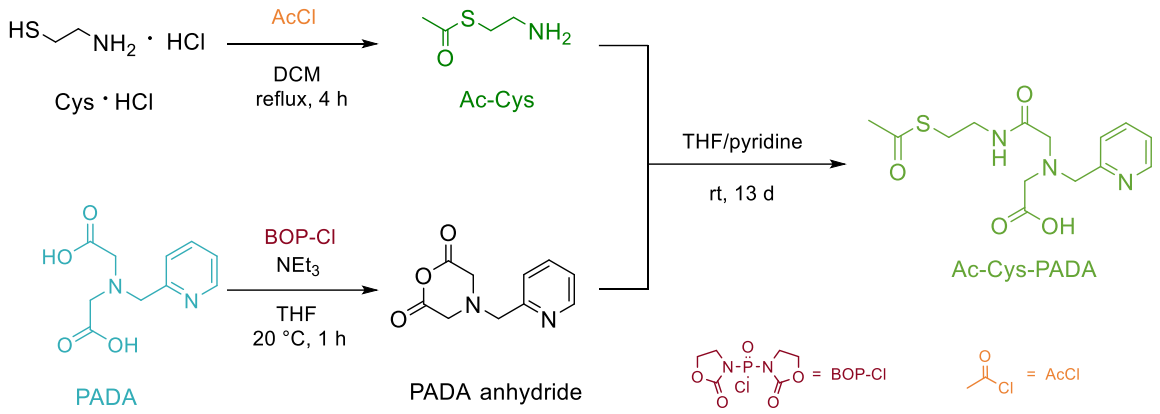

Scheme 48: Two step synthesis of Ac-Cys-PADA *via* Ac-Cys starting from Cys HCl.

First, the protected cysteamine (Ac-Cys) was synthesised with cysteamine hydrochloride and acetyl chloride.[333] The reaction mixture was heated to reflux, and the obtained precipitate was filtered and washed with cold DCM. The colourless solid was further reacted with PADA anhydride, as previously described, and stirred at room temperature until a colour change to a light pale yellow occurred. The product was purified by preparative HPLC to yield a yellow solid.

Ac-Cys-PADA was fully characterised by NMR, IR and ESI-MS. NMR studies showed all predicted proton resonances of the desired ligand and its spectrum differed from the very similar ligand Cys-PADA only in a singlet at 2.33 ppm, which can be assigned to the three protons of the thioacetate protecting group. IR investigations showed close similarities to the previously described chelator ligands, e.g. MUAM-PADA (**Figure 76**, **top**).

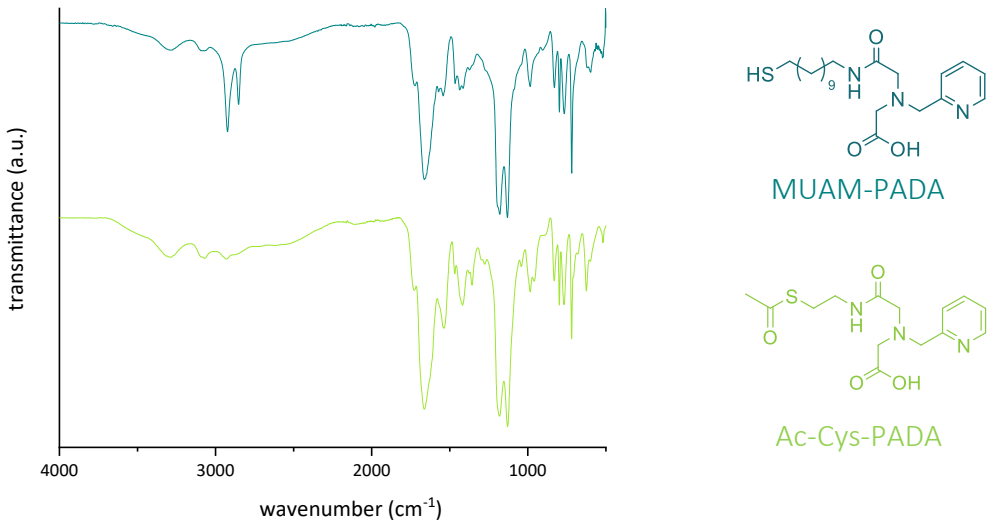

Figure 76: IR spectra of Ac-Cys-PADA (**bottom**) in comparison to MUAM-PADA (**top**).

Likewise, the spectrum of Ac-Cys-PADA (**Figure 76, bottom**) reveals two distinct carbonyl bands at 1720 cm^{-1} and 1655 cm^{-1}, which can be assigned to the acid as well as the amide. Furthermore, the ligand shows a broader resonance ν_{O-H} at 3292 cm^{-1}, which suggests the presence of the free acid. In addition to the unambiguous similarities within the fingerprint area, Ac-Cys-PADA possesses a distinct ν_{C-S} oscillation at 623 cm^{-1}. As mentioned before, a difference in the intensity of ν_{C-H} vibrations appears being significantly smaller for the protected short-chain ligand than for the long chain analogue. Complementary to the IR studies, a molecule ion $[M+H]^+$ of *m/z* 326.2 was found in ESI MS measurements matching the calculated mass of Ac-Cys-PADA.

For the complexation, Ac-Cys-PADA was redissolved in degassed H_2O and $[^{99m}Tc(OH_2)_3(CO)_3]^+$ (pH 8) was added as shown in **Scheme 49**.

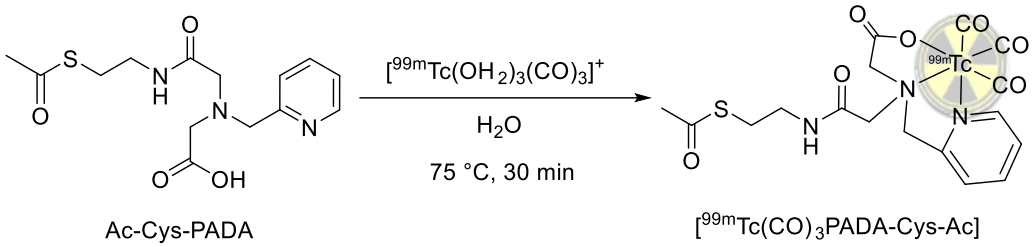

Scheme 49: Synthesis of $[^{99m}Tc(CO)_3PADA-Cys-Ac]$.

The reaction mixture was stirred at 75 °C for 30 min and monitored *via* HPLC. $[^{99m}Tc(CO)_3PADA-Cys-Ac]$ was obtained with a RCP of 83% and displayed a signal at t_R = 19.9 min (**Figure 77, left**). Furthermore, another species is present at t_R = 18.5 min, which can be attributed to the $[^{99m}Tc(CO)_3PADA]$ complex since this signal appeared in different approaches in a retention time range between 18.1 min and 18.5 min.

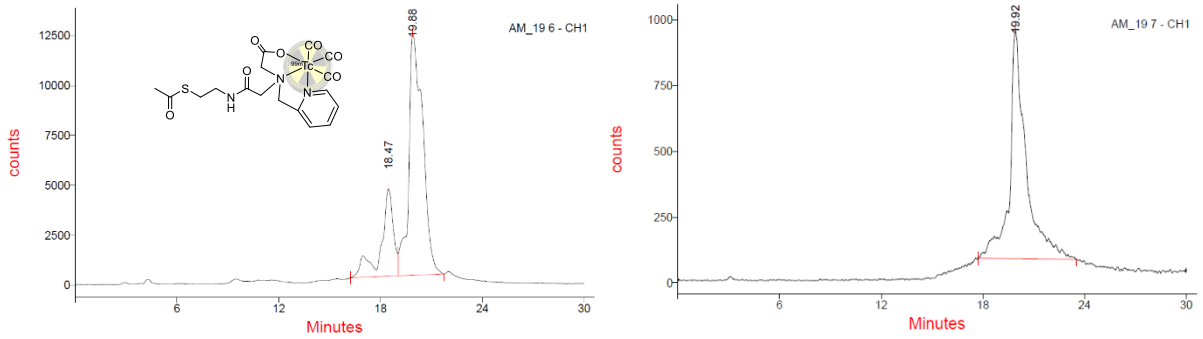

Figure 77: γ HPLC traces of $[^{99m}Tc(CO)_3PADA-Cys-Ac]$ after 90 min (**left**) and semi preparative purified $[^{99m}Tc(CO)_3PADA-Cys-Ac]$ (**right**).

In contrast to previous ligands, the complexation of Ac-Cys-PADA was not only carried out at room temperature. An increase in temperature during the synthesis did not lead to the formation of more undesired side products, as previously described for the complexation with

the long chain MUAM-PADA ligand. During the reaction in H_2O at room temperature, an RCP of 80% was obtained after an incubation for 60 min. When the reaction was carried out at 80 °C, the RCP was 79% after 40 min. However, a synthesis conducted in the microwave at 100 °C or 110 °C led to a large number of by-products and presumably to a decomposition of the ligand. Furthermore, performing the reaction in another solvent such as MeOH resulted primarily in the formation of a side product, which was not found in previous γ HPLC traces and which may presumably be a complex with the esterified ligand.

In conclusion, all synthesised ligands did complex the $[^{99m}Tc\ (CO)_3]^+$ moiety. For the short chain ligand Cys-PADA and the protected species Ac-Cys-PADA, other unknown side products occurred parallel to the desired complex, depending on the procedure (but generally in a lower yield relative to the desired product). The long chain MUAM-PADA ligand showed the most promising results with a high RCP as well as a high potency. Additionally, this complex remained stable in the presence of histidine, thus being of high interest for applications in biological systems.

3.5.6 Radiolabelling of Au NPs

Since the free ligands have been satisfactorily complexed by ^{99m}Tc, this chapter focuses on the interactions between the ^{99m}Tc species and the ligands, once the latter were attached to the Au NP surface. Radiolabelled Au NPs were obtained either *via* labelling of functionalised Au NPs (*pathway 1*). As an alternative, complexation of the bifunctionalised ligand with ^{99m}Tc was performed first and subsequent the functionalisation of the Au NPs with the hot ligand (*pathway 2*).

Radiolabelling procedure and analytical characterisation of the Au NPs

The functionalised NPs were purified *via* a desalting column before the labelling process took place. This ensured that only ligands attached to the NPs were available and present. Afterwards, the dispersion was purged with N_2, $[^{99m}Tc(OH_2)_3(CO)_3]^+$ was added and the pH was adjusted to pH 8-9 to obtain a stable, clear dispersion. The reaction progress was monitored *via* HPLC.

Furthermore, a second purification *via* a desalting columns took place after the actual labelling process. Now, all free ligands and unbound ^{99m}Tc precursors should be removed from the NP dispersion. Thus, only labelled, functionalised Au NPs are eluted in the desired fraction. This purification with desalting columns was repeated after labelling in some cases in order to prove that the ligands are attached firmly to the ligand shell and thus to the NP.

When it comes to the analysis of Au NPs, these cannot be injected into HPLC systems based on a standard reverse phase (RP) column, as they would clog the column and thus damage it. Instead, the NPs were analysed by using a size exclusion chromatography (SEC) column. In this case, separations only occurred with regard to the size of different species. Larger structures (e.g. well shielded stable NPs) interact less with the column matrix than smaller species, for instance free ligand or precursors, which remain longer in the column matrix and are thus detected later.

In order to achieve an optimal separation, the selection of an appropriate eluent was essential. Initially, phosphate buffer solution (PBS) was used to be as close as possible to *in vivo* conditions. We found, however, that no separation of the precursor ($[^{99m}Tc(OH_2)_3(CO)_3]^+$, **Figure 78**, **left**), starting materials ($[^{99m}TcO_4]^-$, **Figure 78**, **centre**) and the functionalised radiolabelled NPs (**Figure 78**, **right**) could be achieved. All eluted at about 11.5 min.

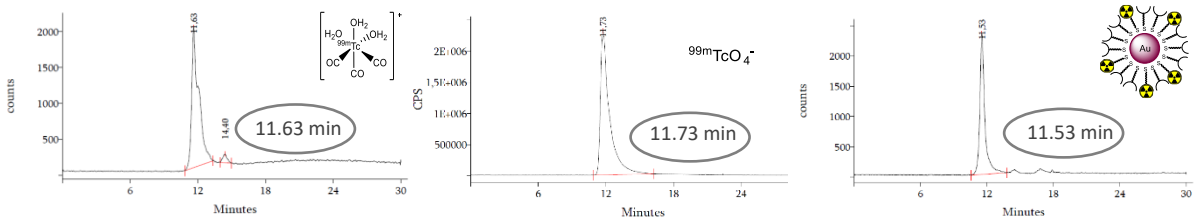

Figure 78: γ SEC HPLC traces of $[^{99m}Tc(OH_2)_3(CO)_3]^+$ (**left**), $[^{99m}TcO_4]^-$ (**centre**) and radiolabelled Au NPs (**right**) with PBS as the eluent.

Research by Liu *et al.*[334] showed that the presence of NaCl or other ions within the eluent potentially leads to NP coagulation and even absorption problems on the SEC column. Therefore, sodium dodecyl sulphate (SDS) in H_2O was chosen as an alternative buffer eluent. **Figure 79** shows the corresponding γ SEC HPLC traces.

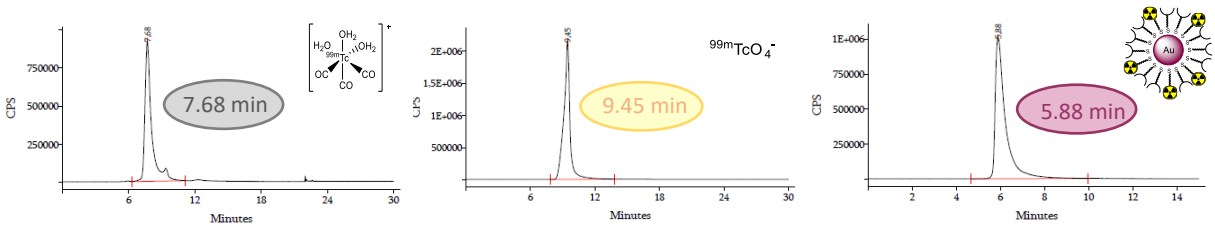

Figure 79: γ SEC HPLC traces of $[^{99m}Tc(OH_2)_3(CO)_3]^+$ (**left**), $[^{99m}TcO_4^-]$(**centre**) and radiolabelled Au NPs (**right**) with 15 mM SDS in H_2O as the eluent.

With these settings, the different components can be separated from each other, since $[^{99m}Tc(OH_2)_3(CO)_3]^+$eluted after 7.7 min (**Figure 79**, **left**) and $[^{99m}TcO_4]^-$ after 9.5 min (**Figure 79, centre**). However, the radiolabelled Au NPs showed a signal after only 5.9 min (**Figure 79, right**) and thus more than one minute earlier compared to the side products. With these settings, the long-chain pre-functionalised Au NPs were initially radiolabelled, as shown in **Scheme 50**.

Radiolabelling of functionalised Au NPs (Au-MUAM-PADA; pathway 1)

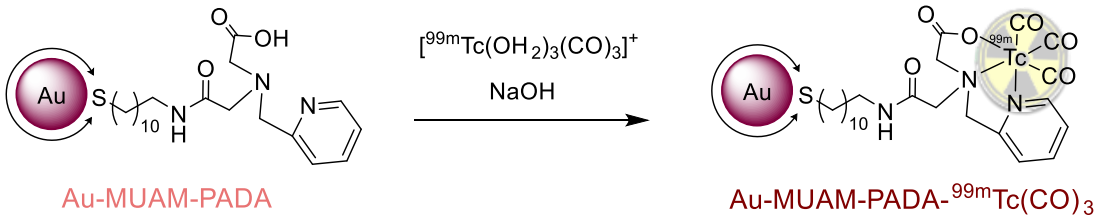

Scheme 50: Radiolabelling of Au-MUAM-PADA NPs with $[^{99m}Tc(OH_2)_3(CO)_3]^+$.

Each NP dispersion was purged with N_2, $[^{99m}Tc(OH_2)_3(CO)_3]^+$ was added and a stable NP dispersion was obtained by adding NaOH. The reaction mixtures were stirred at a respective temperature and the reaction progress was monitored by SEC HPLC. Using the SEC HPLC analysis, the radiolabelled Au-MUAM-PADA-$^{99m}Tc(CO)_3$ NPs were successfully distinguishable from unreacted $[^{99m}Tc(H_2O)_3(CO)_3]^+$ or any remaining $[^{99m}TcO_4]^-$. The yield of radiolabelled NPs was determined by integrating the recorded signals.

In principle, these investigations of reactions processes at different reaction temperatures revealed two general correlations, which can be derived from **Figure 80 A**. The calculated yields of radiolabelled Au NPs (in %) are plotted as a function of time *t* (in min) and show the longer the reaction time, the higher the yield of radiolabelled NPs. Furthermore, the radiolabelling process accelerated at higher temperatures compared to lower temperatures.

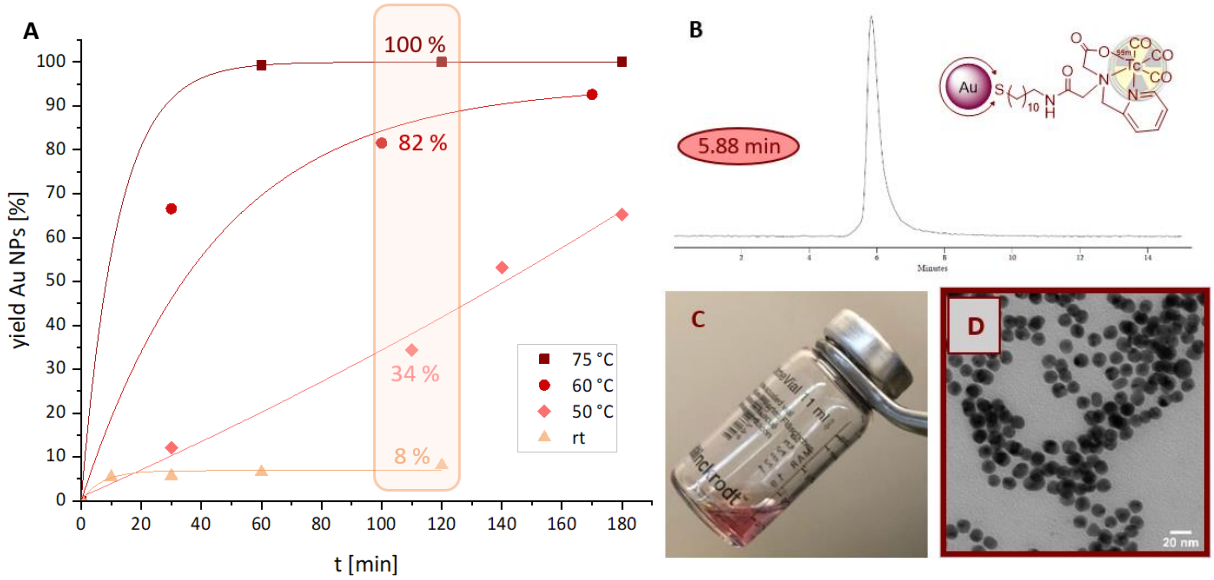

Figure 80: (**A**) SEC γ HPLC yields of radiolabelled Au-MUAM-PADA-$^{99m}Tc(CO)_3$ NPs [%] plotted against time [min]. (**B**) SEC γ HPLC trace before purification indicate the full consumption of $[^{99m}Tc(OH_2)_3(CO)_3]^+$ and furthermore, the complete conversion to radiolabelled Au NPs. (**C**) Picture of a radiolabelled Au-MUAM-PADA-$^{99m}Tc(CO)_3$ NP sample. (**D**) TEM image of Au-MUAM-PADA-$^{99g}Tc(CO)_3$ NPs showing a remained morphology of the Au NPs after being heated to 75 °C during the labelling process.

This trend is particularly noticeable at a reaction time range between 100-120 min (**Figure 80 A, highlighted**). At room temperature, only 8% of the total activity was found to be radiolabelled Au NPs. However, at 50 °C 34% radiolabelled Au NPs were obtained. The yield improved significantly to 82% when the temperature was increased to 60 °C. A complete conversion was achieved at a temperature of 75 °C, even considerably before t = 100 min. Furthermore, all labelling procedures were performed with Au NPs out of the same batch and thus an equal concentration of chelating ligands on the surface.

As displayed in **Figure 80 B** (γ HPLC trace of Au-MUAM-PADA-$^{99m}Tc(CO)_3$ NPs (75 °C), taken after 60 min), only a signal at 5.9 min was observed, corresponding to the radiolabelled Au NPs. Furthermore, **Figure 80 C** shows the NP sample after the heating procedure, without any optical changes and still being a stable pink NP dispersion. Moreover, the TEM image of Au-MUAM-PADA-$^{99g}Tc(CO)_3$ NPs (**Figure 80 D**), which was taken after the radiolabelling, demonstrated evidently that the short term heating of the NPs had no effect on their monodisperse morphology. They still possessed a spherical shape with a size of d_{TEM} = 13.9 ± 1.2 nm.

Even though there was no necessity for the additional removal of $[^{99m}Tc(OH_2)_3(CO)_3]^+$ or $[^{99m}TcO_4]^-$, since the reaction at 75 °C showed a complete conversion of $[^{99m}Tc(OH_2)_3(CO)_3]^+$, this NP dispersion was purified using a PD 10 column in order to obtain and further analyse only the radiolabelled NPs. A pure Au NP fraction with 4.261 MBq was obtained, which corresponds to 77% of the overall activity loaded onto the column.

Since a complete conversion of $[^{99m}Tc(OH_2)_3(CO)_3]^+$ only occurred at high temperatures, all side products were actively removed during the purification at all lower temperature reactions. An approach at room temperature resulted in a yield of radiolabelled Au NPs of 8% after 120 min (**Figure 80 A**, crème coloured graph). Once the mixture was purified after 165 min, various fractions were collected and analysed (**Figure 81 A**).

Fraction 2, which was pink coloured, was found to contain mostly radiolabelled Au NPs (t_R = 5.9 min, **Figure 81 B**, **top**) and possessed an activity of 7.838 MBq, which corresponds to 7.5% of the overall activity loaded on the PD 10 column.

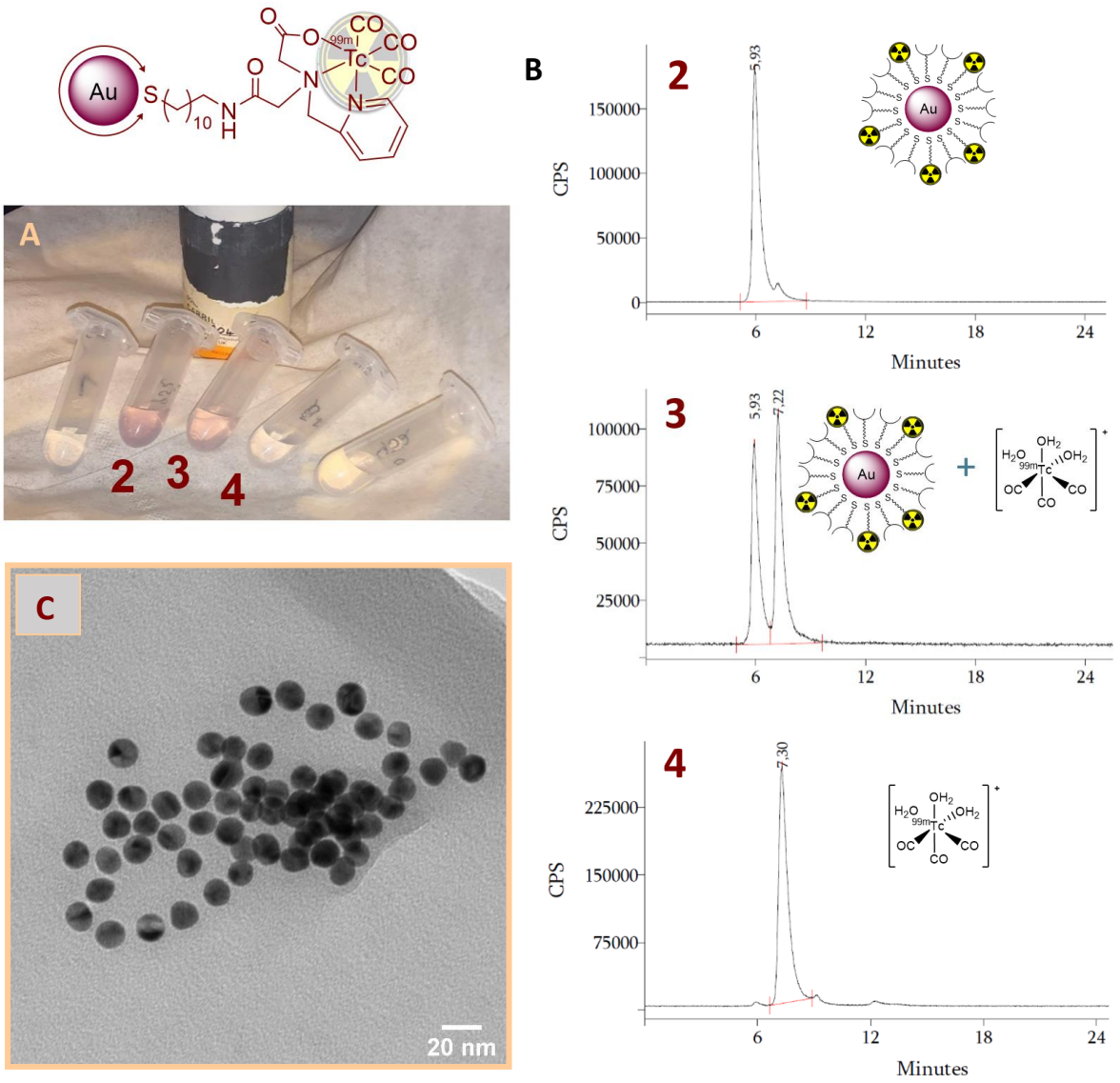

Figure 81: (**A**) Collected fractions of Au-MUAM-PADA-^{99m}Tc(CO)$_3$ NPs (rt, 165 min) after purification *via* PD 10 desalting column, (**B**) their corresponding SEC γ HPLC traces of fractions 2 (**top**), 3 (**centre**) and 4 (**bottom**) and (**C**) TEM image of fraction 2 (Au-MUAM-PADA-^{99g}Tc(CO)$_3$), taken after the radiolabelling process.

The SEC γ HPLC trace (**Figure 81 B**, **centre**) of the slightly pink coloured fraction 3 showed two signals of approximately the same size, which were assigned to the radiolabelled NPs (t_R = 5.9 min) and [^{99m}Tc(OH$_2$)$_3$(CO)$_3$]$^+$ (t_R = 7.2 min). This fraction has 10.52 MBq, thus 17.5% of the total activity on the loaded PD 10 column. The next fraction 4 appeared colourless and was only [^{99m}Tc(OH$_2$)$_3$(CO)$_3$]$^+$ (t_R = 7.3 min) with 19.25 MBq (**Figure 81 B**, **bottom**), being 32.6% of the overall activity. A further 5.672 MBq eluted in later fractions corresponding to both, predominantly [^{99m}Tc(OH$_2$)$_3$(CO)$_3$]$^+$ and [^{99m}TcO$_4$]$^-$. Although only 7.5% yield was obtained during the reaction at room temperature, it was possible to separate the pure radiolabelled Au NP fraction from its side products. Furthermore, the TEM image taken of Au-MUAM-PADA-^{99g}Tc(CO)$_3$ (**Figure 81 C**) showed only monodisperse Au NPs with a size of d_{TEM} = 13.8 ± 1.0 nm and thus confirms that no change in the morphology occurred during the radiolabelling.

Radiolabelling of Au NPs with "hot" labelled biofunctionalised ligand (pathway 2)

An alternative way to synthesise Au-MUAM-PADA-^{99m}Tc(CO)$_3$ NPs included the complexation of MUAM-PADA with [^{99m}Tc(OH$_2$)$_3$(CO)$_3$]$^+$ first, before the Au NPs were functionalised with the "hot ligands" as shown in **Scheme 51**.

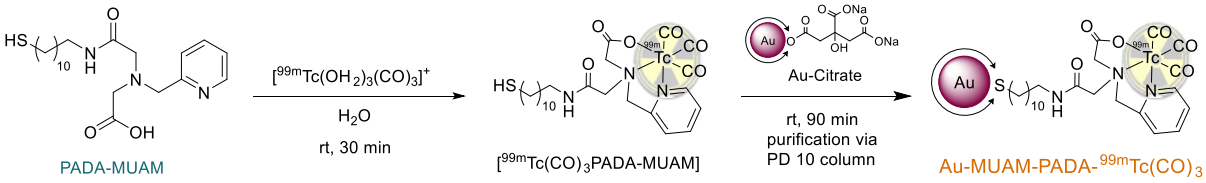

Scheme 51: Consecutive synthetic route towards Au-MUAM-PADA-^{99m}Tc(CO)$_3$ NPs *via* the complexation of PADA-MUAM first (**left**) and the subsequent radiofunctionalisation of Au-Citrate NPs with ^{99m}Tc(CO)$_3$MUAM-PADA in a ligand exchange reaction (**right**).

Here, the Au-Citrate NPs of the desired size were purged with N_2 and freshly prepared ^{99m}Tc(CO)$_3$PADA-MUAM was added. The reaction mixture was stirred at room temperature for 90 min and was purified using a desalting column PD MiniTrap.

A further advantage of a purification *via* a desalting columns remains that only Au NPs with a large and well shielded ligand sphere pass through the column. The starting Au-Citrate NPs, which are just electrostatically stabilised by citrate molecules, strongly interact with the column matrix, thus remained attached to it. Therefore, these were separated from the rapidly eluting radiolabelled functionalised Au NPs. Au-MUAM-PADA-^{99m}Tc(CO)$_3$ NPs (Ø 14 nm) were then analysed by SEC HPLC and showed that only the pure radiolabelled Au NPs were present, which were detected at t_R = 5.88 min by the γ detector (**Figure 82**, **bottom**). These fractions contained 25 MBq and thus 86% of the overall activity loaded onto the column.

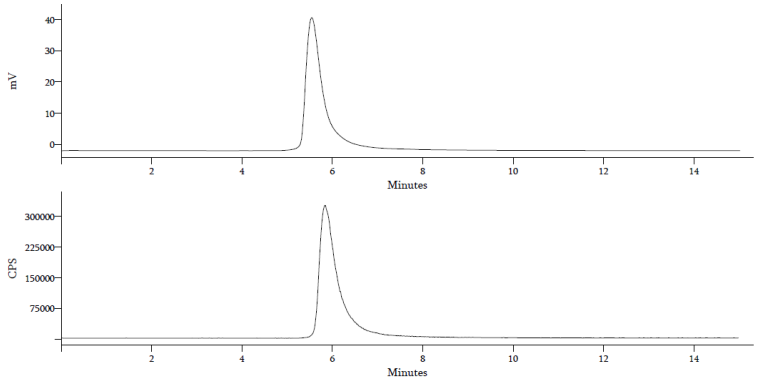

Figure 82: SEC UV HPLC trace (**top**) and SEC γ HPLC trace (**bottom**) of purified Au-MUAM-PADA-^{99m}Tc(CO)$_3$ NPs (Ø 14 nm).

Furthermore, the UV HPLC trace of this sample (**Figure 82**, **top**) showed only one signal, which can be assigned to the Au-MUAM-PADA-^{99m}Tc(CO)$_3$ NPs. The difference in the retention times for each signal in the SEC UV HPLC trace and the SEC γ HPLC trace corresponded exactly to the instrumental set-up between the UV detector and the γ detector. TEM images reveal that purification *via* a desalting column is necessary to obtain high quality material. The NP sample before purification show an apparent contamination of the NP environment (**Figure 83**, **left**). After purification, a clean NP sample freed from impurities was observed (**Figure 83**, **right**). The morphology of the NPs had changed neither through radiofunctionalisation nor by a subsequent purification.

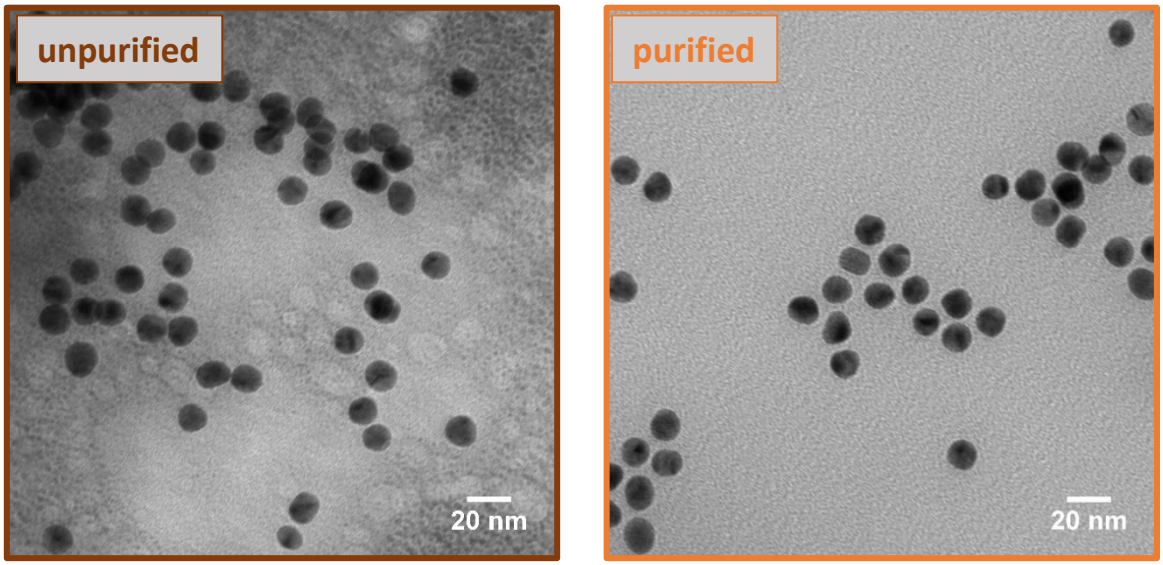

Figure 83: TEM images of Au-MUAM-PADA-^{99g}Tc(CO)$_3$ NPs (Ø 13 nm) taken before purification *via* desalting column, showing a contamination of the NP environment (**left**), and after the purification, revealing a cleaner NP dispersion and still monodisperse spherical NPs with a size of d_{TEM} = 13.9 ± 1.3 nm (**right**).

In another approach Au-Citrate (Ø 12 nm) NPs were used with a slightly higher starting concentration (ca. 16 nM). Furthermore, less of [^{99m}Tc(CO)$_3$PADA-MUAM] was added to the reaction mixture, which was stirred at room temperature for 90 min. In this attempt, we wanted to know whether higher concentrated Au-Citrate NPs can also be sufficiently stabilised by a lower equivalent of radiolabelled complex added. The reaction mixture remained pink and clear, although the pH was not adjusted by the addition of base. Moreover, a bright pink coloured dispersion was eluted during purification on a PD MiniTrap, which possessed with 40.41 MBq a yield of 77.7% of the overall activity loaded onto the column.

In order to determine how stable the NPs were and whether the complex ligand was attached strongly enough to the Au NP surface, the purified pink fraction was purified a second time using PD MiniTrap. The majority of NPs passed through the column and eluted as a pink fraction with 13.34 MBq (**Figure 84 C**, **bottom**). This still corresponds to 57% of the overall activity loaded on the column. However, it appeared that a small amount of NPs remained on the column (**Figure 84 C**, **top**).

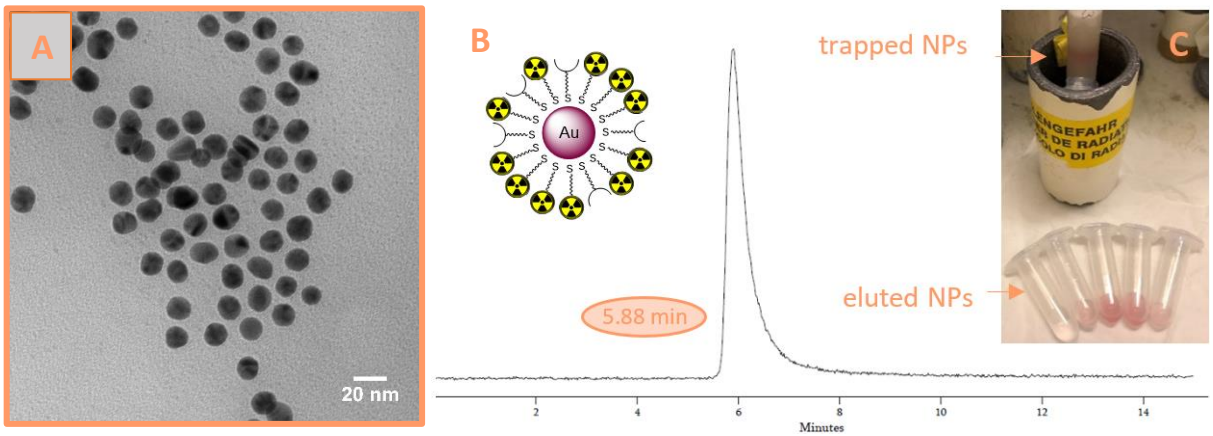

Figure 84: (**A**) TEM image of Au-MUAM-PADA-^{99g}Tc(CO)$_3$ NPs (Ø 12 nm), (**B**) corresponding SEC γ HPLC trace and (**C**) collected fractions of radiolabelled Au NPs after the second purification *via* PD MiniTrap, showing the eluted fractions (**bottom**) as well as the separated unstable Au NPs trapped in the column matrix (**top**).

Nevertheless, the eluted fraction was analysed. It showed a single, distinct signal at 5.9 min corresponding to Au-MUAM-PADA-^{99m}Tc(CO)$_3$ NPs (Ø 12 nm) (**Figure 84 B**). Furthermore, TEM investigations (**Figure 84 A**) revealed that no agglomeration of the NP or changes in their morphology occurred during radiolabelling or purification. Instead, monodisperse near-spherical NP were still present with a size of d_{TEM} = 11.9 ± 1.2 nm.

After the analytical characterisations of the Au NPs for both labelling pathways revealed good results, further characterisations were performed with the inactive NPs since ^{99m}Tc completely decayed. Special attention was paid to the properties of the two Au-MUAM-PADA-^{99g}Tc(CO)$_3$ NP types, which were obtained either by the labelling of functionalised Au NPs (*pathway 1*) or the hot ligand functionalisation (*pathway 2*).

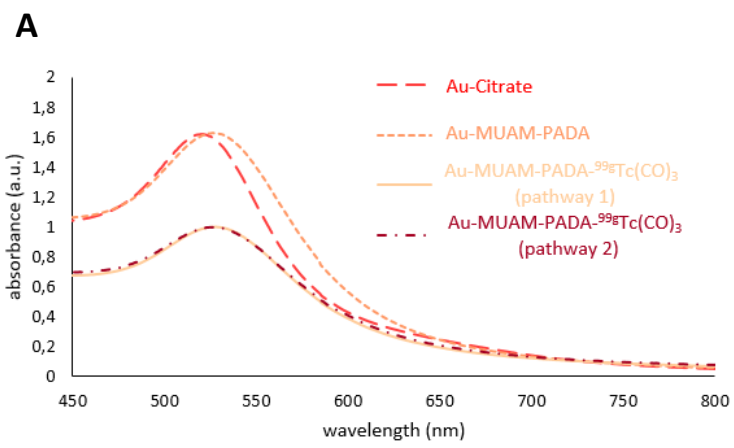

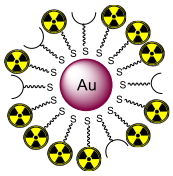

B

	Au-MUAM-PADA-^{99g}Tc(CO)$_3$ (pathway 1)	Au-MUAM-PADA-^{99g}Tc(CO)$_3$ (pathway 2)
d_{TEM}	13.9 ± 1.2 nm	13.9 ± 1.3 nm
λ_{max}	528 nm	527 nm
d_{hydr}	16 ± 3 nm	16 ± 4 nm

Figure 85: (**A**) UV Vis spectra of the starting NPs Au-Citrate and Au-MUAM-PADA as well as the radiolabelled Au-MUAM-PADA-^{99g}Tc(CO)$_3$ NPs synthesised during the radiolabelling of prefunctionalised Au NPs (crème) or in a functionalisation with the hot ligand (dark red), (**B**) corresponding data of the radiolabelled Au-MUAM-PADA-^{99g}Tc(CO)$_3$ NPs revealing highly similar values, although the two NP approaches were obtained using two different reaction pathways.

The UV Vis spectra of the respective starting NPs (Au-Citrate and Au-MUAM-PADA) compared to the respective Au NPs obtained (Au-MUAM-PADA-^{99g}Tc(CO)$_3$) are shown in **Figure 85 A**. First, the uniform plasmon band revealed that all NP samples were stable dispersion in a similar size range. Furthermore, the two curves of the two radiolabelled Au NPs were almost identical, indicating their similarity. The exact data on the radiolabelled NPs are summarised **Figure 85 B.** Here, their determined TEM sizes were identical with d_{TEM} = 13.9 ± 1.2 nm (*pathway 1*) and d_{TEM} = 13.9 ± 1.3 nm (*pathway 2*), respectively. Furthermore, the radiolabelled samples possessed similar λ_{max} = 527 nm or λ_{max} = 528 nm and had similar hydrodynamic radii with d_{hydr} = 16 ± 3 nm or d_{hydr} = 16 ± 4 nm.

IR spectra of the radiolabelled Au NPs compared to Au-MUAM-PADA NPs are displayed in **Figure 86.** Noteworthy to mention is that the IR samples were collected with material from different batches (but the same synthetic pathway) in order to have enough sample material. Therefore, these spectra do not provide information about the individual reaction but about the reaction type.

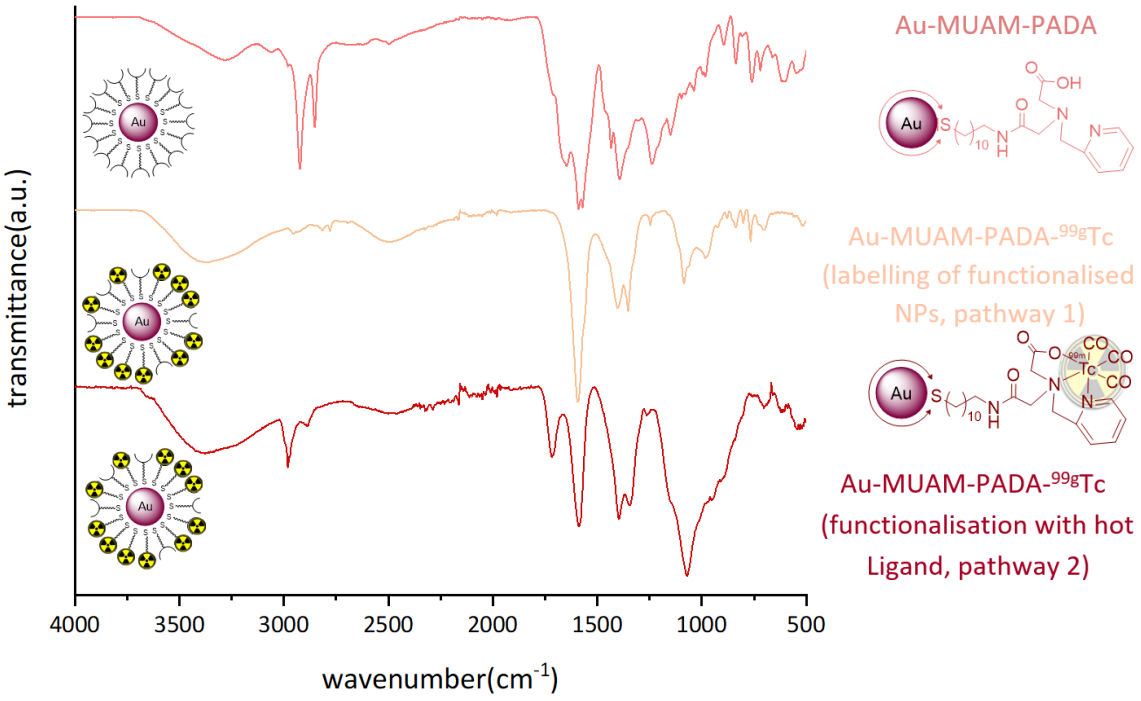

Figure 86: IR spectra of Au-MUAM-PADA NPs (**top**) as a starting dispersion and the radiolabelled Au-MUAM-PADA-^{99g}Tc(CO)$_3$ NPs obtained from *pathway 1* (**centre**) and *pathway 2* (**bottom**).

First, there are distinct similarities between the spectra of the radiolabelled NPs. They only differ in the proportions of the individual bands. The sample from *pathway 2* shows a broad and strong absorption around 1070 cm^{-1}, whereas this is weaker in the sample from *pathway 1*. Even though $\nu_{Tc\equiv N}$ vibrations could be located in this range[335] or $\nu_{Tc=O}$ oscillations around 950 cm^{-1},[336] their appearance seems rather unlikely, since the Tc concentration is very low.

Furthermore, intense $\nu_{C\equiv O}$ absorptions around 2000 cm^{-1} should be observed, indicating distinctly the presence of a tricarbonyl complex. Instead, the new intense band originates most likely from the organic backbone and is located in the range of $\nu_{C\text{-}N}$ or $\nu_{O\text{-}H}$ vibrations.

Moreover, the unambiguous and strong $\nu_{C=O}$ oscillation around 1600 cm^{-1} as well as similar fingerprint area are similar in all spectra. The radiolabelled NPs only differ from the initial Au-MUAM-PADA NPs in the intensity of the $\nu_{C\text{-}H}$ oscillations around 3000 cm^{-1}. These occur significantly stronger in the initial dispersion than in the radiolabelled representatives. In case of the functionalised Au NPs (*pathway 1*), they even appear to be almost completely suppressed. However, all other vibrations indicating the long-chain ligand are present. Both radiolabelled NPs reveal broad $\nu_{O\text{-}H}$ resonances in the region around 3380 cm^{-1}. Furthermore, a visible shoulder in the range around 2400 cm^{-1} indicates the presence of a CO species around the radiolabelled NPs, since the $\nu_{C=O}$ vibrations fall into this range for carbonyl ligands. This suggests that the desired complex is still present.

In summary, both Au NPs approaches showed remarkable similarities in their NP structure and properties as well as their surface functionalisation before and after radiolabelling.

Radiolabelling of functionalised Au NPs (Au-Cys-PADA; pathway 1)

Then, the short-chain functionalised Au NPs (Au-Cys-PADA) were also reacted with ^{99m}Tc. Only *pathway 1* (labelling of functionalised Au NPs) was chosen, as radiolabelling of Cys-PADA did not yield a pure compound and thus was not available for a further and comparable functionalisation of Au-Citrate NPs.

Two peculiarities were identified during the reaction of Au-Cys-PADA NPs with $[^{99m}Tc(OH_2)_3(CO)_3]^+$. First, the preparation of the initial particle dispersion was performed with a desalting column. The majority of the NP passed through the column, but this phase widened enormously, so that the pink-coloured fraction spread over a much larger volume, sometimes even twice as large. Furthermore, the eluate appeared slightly darker (more violet) than before. This indicated that the short-chain NPs were not completely stable directly after purification and therefore had to be stabilised again by adjusting the pH with base.

Furthermore, during the reaction, additional and stronger pH control was required to ensure sufficient stabilisation of the NPs. However, the addition of NEt_3 to the reaction mixture (after addition of $[^{99m}Tc(OH_2)_3(CO)_3]^+$ did not lead to a sufficient stabilisation. Instead, 1M NaOH was added.

As displayed in **Scheme 52**, the reaction mixtures were stirred at different temperatures (either room temperature or 75 °C) for 120 min in order to compare their stabilities during the procedures as well as the radiochemical outcome during these reactions.

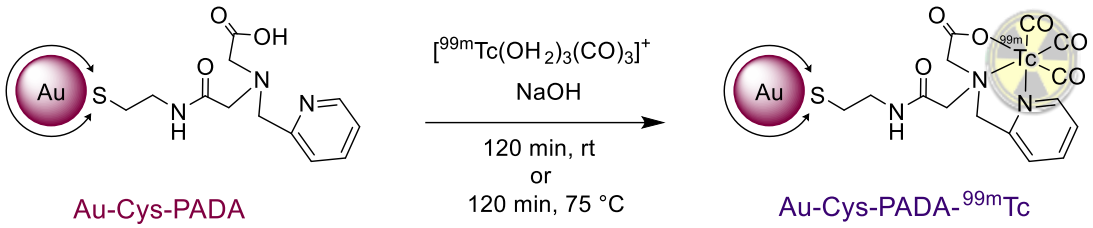

Scheme 52: Radiolabelling of Au-Cys-PADA NPs.

During the purification, the NPs' tendency towards instability was observed in both approaches; again a broadened phase migrated through the column, which eluted in a slightly more violet colour. However, the analysis of the first coloured fraction already showed no distinct separation of pure radiolabelled Au NPs (t_R = 5.9 min, **Figure 87 B**) and unreacted $[^{99m}Tc(OH_2)_3(CO)_3]^+$ (t_R = 7.2 min, **Figure 87 B**). The purification of the NPs stirred at room temperature was performed on the MiniTrap (bed size 2.1 ml, loading volume 0.5 ml Au NPs). In contrast, the approach stirred at 75 °C was purified on a PD 10 column (bed size 8.3 ml, loading volume 0.8 ml Au NPs + 0.7 ml H_2O), which had a larger filling volume and should lead to an easier separation of the $[^{99m}Tc(OH_2)_3(CO)_3]^+$. Even in this setup, $[^{99m}Tc(OH_2)_3(CO)_3]^+$ was not completely removed neither. As the whole process was performed in a lead container, only a selected elution volume (either 0.25 ml or 0.5 ml) was added onto the column, eluted completely, and then the procedure was repeated for the next fraction. Thus, a direct optical monitoring of the elution was not possible.

As the $[^{99m}Tc(OH_2)_3(CO)_3]^+$ was not completely removed from the respective fractions (**Figure 87 B**), the yield related to the overall activity loaded onto the column was also very low for both approaches: at room temperature, only 0.24% conversion was achieved and for the approach at 75 °C, only 1.3%. Moreover, TEM images show that after a reaction at room temperature mainly spherical particles were present (**Figure 87 C**), but that individual ripening processes do occur (marked). At a temperature of 75 °C (**Figure 87 D**), this phenomenon intensifies; here a significant percentage of the NPs began to agglomerate. Ultimately, no stable NP dispersions were obtained.

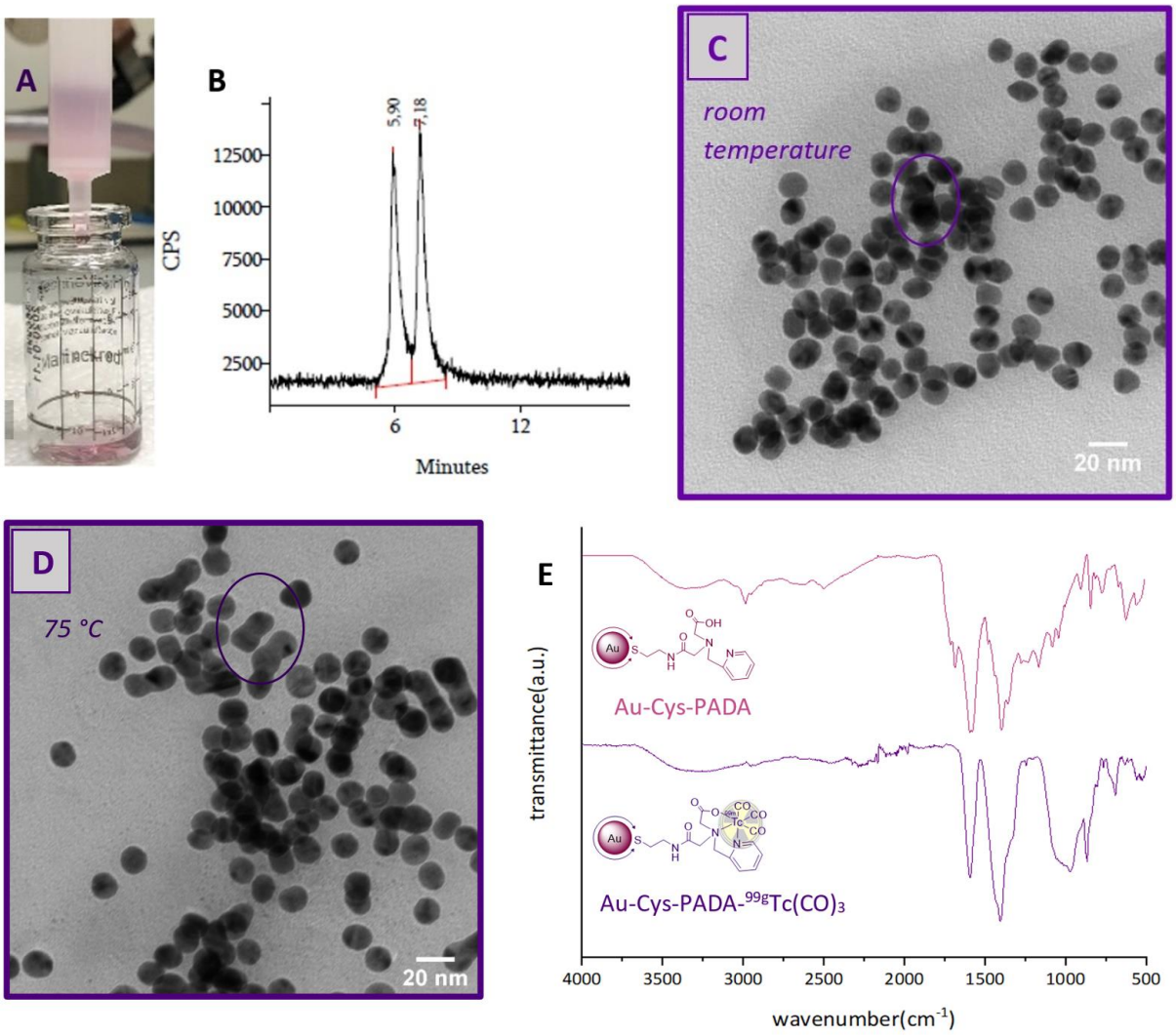

Figure 87: (**A**) Broad violet eluted fraction after purification *via* desalting column, (**B**) SEC γ HPLC trace after purification, TEM images of Au-Cys-PADA-^{99g}Tc(CO)$_3$ NPs after the reaction at room temperature (**C**) and at 75 °C (**D**) and (**E**) IR spectra of mono ligand shell Au-Cys-PADA-^{99m}Tc(CO)$_3$ NPs and in comparison to Au-Cys-PADA NPs.

These results were further supported by a DLS investigation showing d_{hydr} = 272 ± 45 nm, and thus indicated an agglomerated sample.

However, as the IR spectra **Figure 87 E** show, an almost identical surface functionalisation of the NP samples remained present, thus indicating the short-chain ligand Cys-PADA was still attached to the NP surface. Again, only a strong broad band appeared around 1000 cm^{-1}, which was not as intense in the unlabelled Au NP sample.

Nevertheless, the NPs, which were just carrying the short chain ligand Cys-PADA in a mono ligand shell were not satisfactory stabilised during and after a radiolabelling procedure.

Radiolabelling of functionalised Au NPs (mixed ligand shell Au NPs; pathway 1)

In order to compare the radiolabelling behaviour of mono ligand shell NPs with mixed ligand shell NPs, the latter samples were reacted in the following with $[^{99m}Tc(OH_2)_3(CO)_3]^+$. Since they carry another ligand with the biogenic unit atropine in addition to the chelating ligand, they have potential as radiotheragnostics in the future. First, mixed shell Au-MUDA-AT/Cys-PADA NPs were reacted with $[^{99m}Tc(OH_2)_3(CO)_3]^+$ in order to determine whether a more stable NP dispersion was achieved with the additional longer biofunctional ligand. The pink reaction mixture was stirred at room temperature for 120 min, as shown in **Scheme 53**.

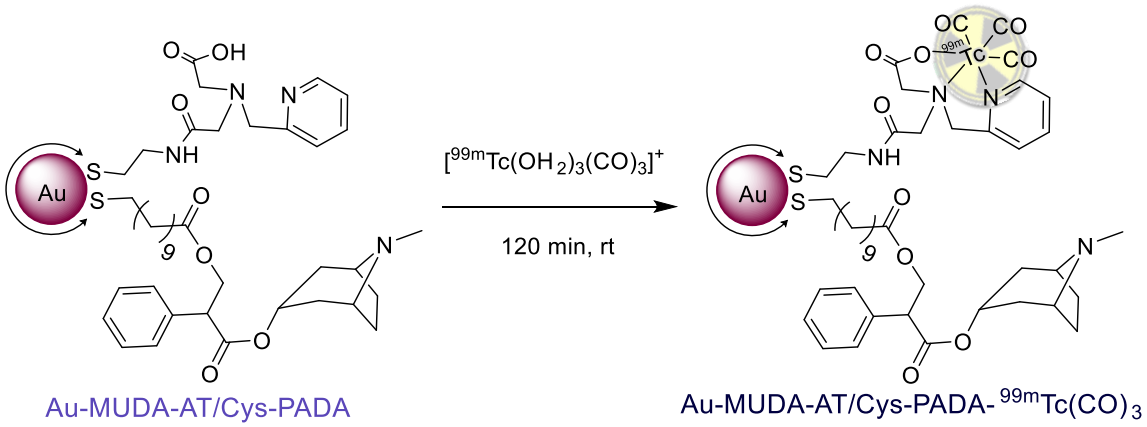

Scheme 53: Radiolabelling of Au-MUDA-AT/Cys-PADA NPs.

A sample of the "crude reaction mixture" was analysed *via* SEC γ HPLC. The chromatogram, which is displayed in **Figure 88 B**, showed predominantly $[^{99m}Tc(OH_2)_3(CO)_3]^+$. Only 0.4% of the total amount of activity eluted after t_R = 5.9 min, which was attributed to the radiolabelled NPs.

Even though the yield was very low, the reaction mixture was purified *via* a desalting column. The coloured fraction eluted later than usual and had a more violet tint (**Figure 88 A**). Analysis *via* SEC γ HPLC showed predominantly a species eluting at t_R = 6.3 min, which can be assigned to the radiolabelled Au NPs (**Figure 88 C**). Furthermore, 12% of the activity within the sample was present as an unknown species, which was detected after 4.9 min. Due to the high dilution of the fraction, UV traces unfortunately did not show any relevant signals from which further insights could have been gained. However, TEM investigations showed that the environment of the NP was contaminated, despite purification *via* the desalting column (**Figure 88 D**). Furthermore, it was observed that several NPs agglomerated (**Figure 88 F**) and occasionally formed NP clusters (highlighted). It may be that the unknown species at t_R = 4.9 min is a form of such a cluster.

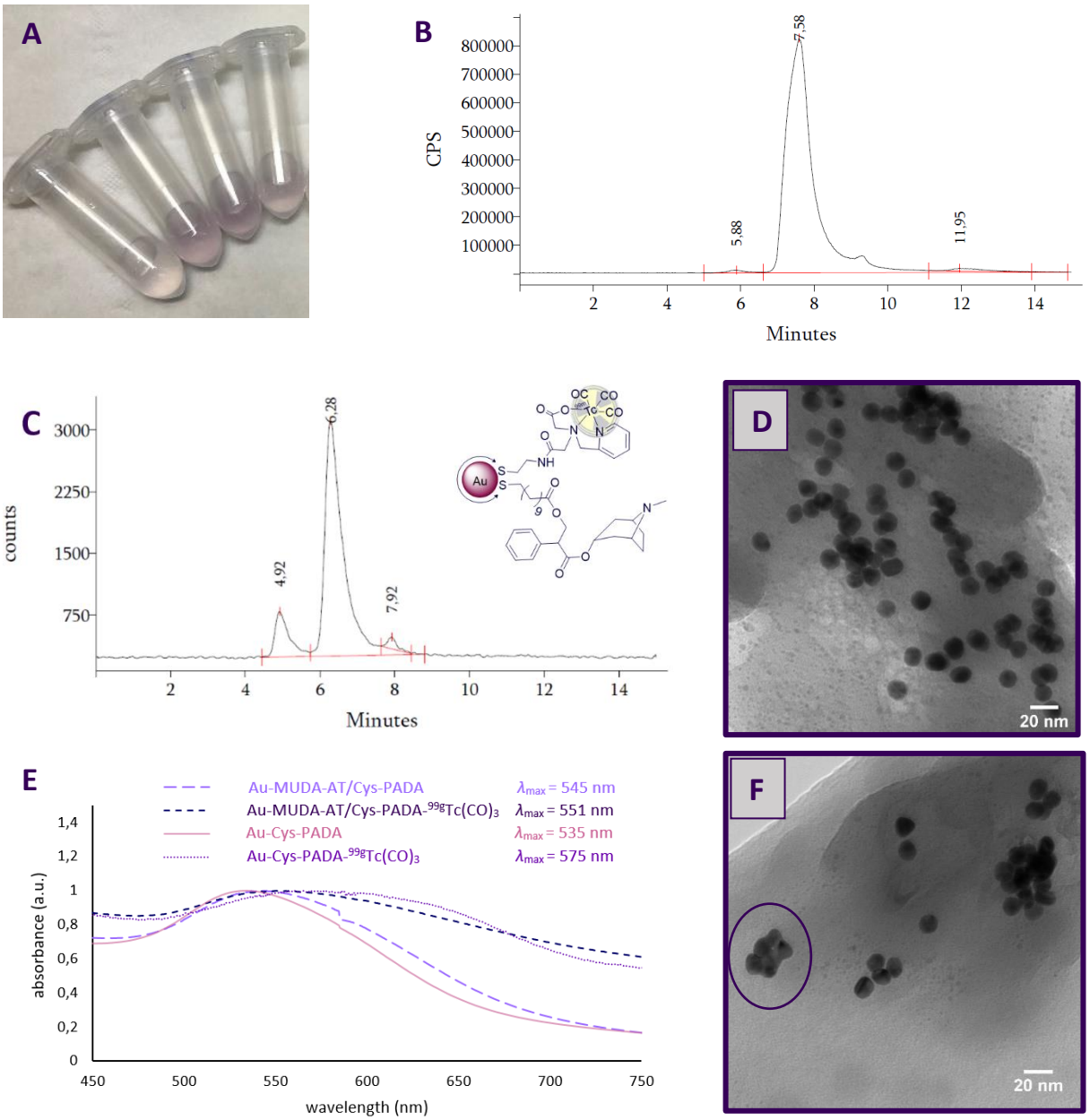

Figure 88: (**A**) Violet eluted fraction after purification *via* desalting column, SEC γ HPLC traces (**B**) before and (**C**) after purification, and (**D**) TEM images of Au-MUDA-AT/Cys-PADA-^{99g}Tc(CO)$_3$ NPs showing contaminated and (**F**) agglomerated NPs and (**E**) UV/Vis spectra of mixed ligand shell NPs Au-MUDA-AT/Cys-PADA and Au-MUDA-AT/Cys-PADA-^{99g}Tc(CO)$_3$ in comparison to mono ligand shell NPs Au-Cys-PADA and Au-Cys-PADA-^{99g}Tc(CO)$_3$.

Even in comparison with Au-Cys-PADA NPs and its corresponding radiolabelled attempt, the UV/Vis spectra (displayed in **Figure 88 E**) show that no stable dispersions were present after the radiolabelling experiments, as far as they carried the short-chain chelate ligand. All plasmon resonances were rather broad and partly showed irregularities. Furthermore, the absorption "maxima" shifted towards higher wavelengths, indicating an agglomeration. In addition to the instability issues of these NPs, the yields of radiolabelled NPs were still very low.

Therefore, the focus of the further progress was set on the long-chain mixed ligand shell Au NPs. Consequently, the labelling of the mixed shell Au NPs was only performed in *pathway 1*, the labelling of the functionalised NPs. First, Au-MUDA-AT/MUAM-PADA NPs were reacted with $[^{99m}Tc(OH_2)_3(CO)_3]^+$ and stirred at room temperature for 120 min (**Scheme 54**).

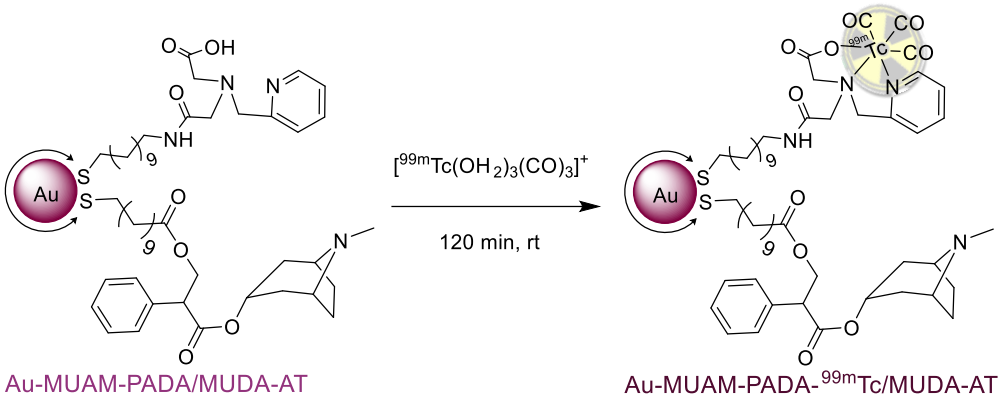

Scheme 54: Radiolabelling of Au-MUDA-AT/MUAM-PADA NPs.

At this point, 89% of the $[^{99m}Tc(OH_2)_3(CO)_3]^+$ had already been consumed (89% signal with t_R = 5.9 min, 11% signal with t_R = 7.4 min, **Figure 90 A**). The NP dispersion was purified using a PD MiniTrap and the collected coloured fractions were analysed. Fractions 3 and 4 were pure radiolabelled Au NPs (t_R = 5.9 min) with 34.53 MBq and thus, a yield of 61% was achieved compared to the overall activity loaded onto the column. Fraction 5, however, was obtained as a mixed fraction containing next to radiolabelled Au NPs also unconsumed $[^{99m}Tc(OH_2)_3(CO)_3]^+$ (t_R = 7.2 min).

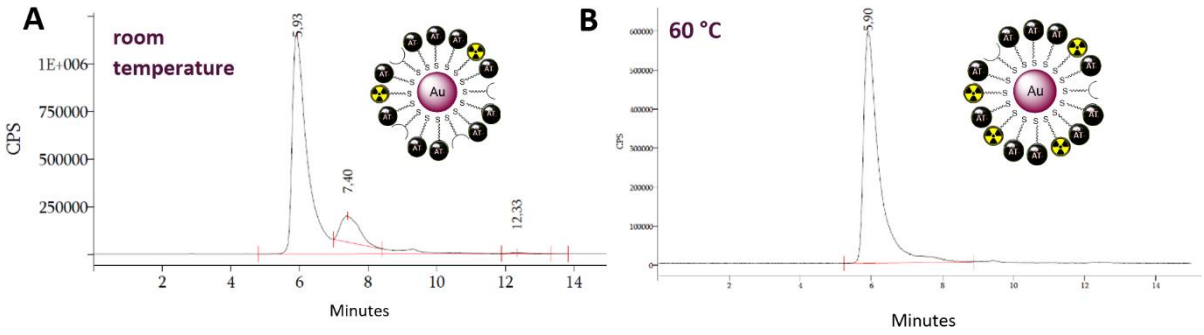

Figure 89: SEC γ HPLC traces of unpurified Au-MUDA-AT/MUAM-PADA-$^{99g}Tc(CO)_3$ NPs stirred at (**A**) room temperature or (**B**) 60 °C.

Since no complete consumption occurred after stirring for 120 min at room temperature, reaction parameters were changed. Now, the reaction mixture was stirred at room temperature for 30 min and further 90 min at 60 °C. Full consumption of $[^{99m}Tc(OH_2)_3(CO)_3]^+$ was observed (**Figure 90 B**).

The UV/Vis spectrum of Au-MUDA-AT/MUAM-PADA-^{99g}Tc(CO)$_3$ NPs (**Figure 90 A**) shows a homogenously formed plasmon resonance with a λ_{max} = 528 nm and thus being very close to the corresponding non-labelled NPs (λ_{max} = 527 nm). TEM investigations (**Figure 90 B**) reveal spherical monodisperse NPs with a size of 11.8 ± 1.3 nm. No visible agglomeration of the Au NPs was observed and further confirmed by a determined d_{hydr} = 15 ± 4 nm. Furthermore, a pink and clear dispersion was present, thus stable radiolabelled Au-MUDA-AT/MUAM-PADA-^{99g}Tc(CO)$_3$ NPs were postulated.

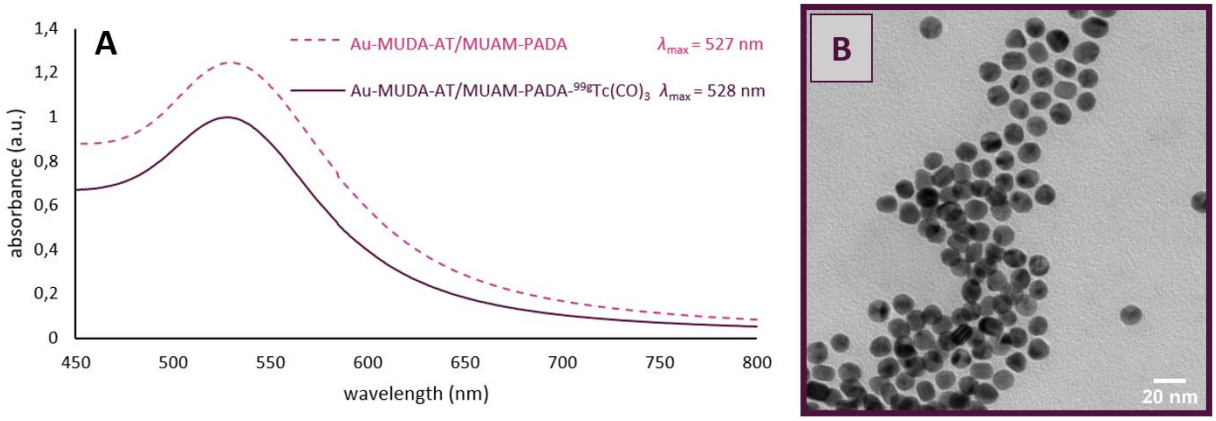

Figure 90: (**A**) UV/Vis spectra of Au-MUDA-AT/MUAM-PADA NPs and Au-MUDA-AT/MUAM-PADA-^{99g}Tc(CO)$_3$ NPs and (**B**) TEM image of Au-MUDA-AT/MUAM-PADA-^{99g}Tc(CO)$_3$ NPs.

For extending these promising results to other biogenic substances, Au-MUDA-ADR/MUAM-PADA NPs – carrying adrenaline as a pharmacologically relevant substance – were reacted with $[^{99m}Tc(OH_2)_3(CO)_3]^+$ (**Scheme 55**).

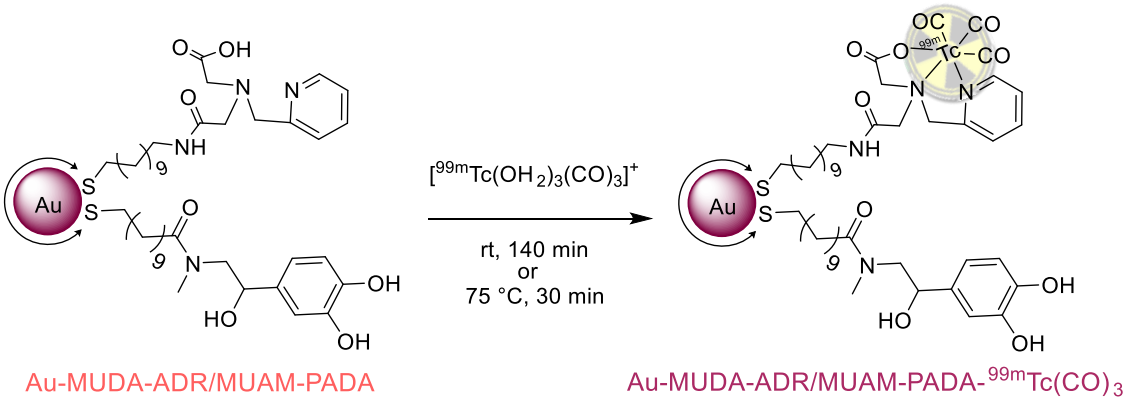

Scheme 55: Radiolabelling of Au-MUDA-ADR/MUAM-PADA NPs.

First, the labelling reaction was performed at room temperature. Over a reaction time of 140 min, the radiolabelling procedure was monitored *via* SEC HPLC and the γ HPLC traces are displayed in **Figure 91**. After 5 min, already 4% of $[^{99m}Tc(OH_2)_3(CO)_3]^+$ (t_R = 7.6 min) was complexed on the Au NPs (**Figure 91 A**). 40% of the overall activity was found on Au-MUDA-ADR/MUAM-PADA-$^{99g}Tc(CO)_3$ NPs (t_R = 5.9 min) after 30 min (**Figure 91 B**).

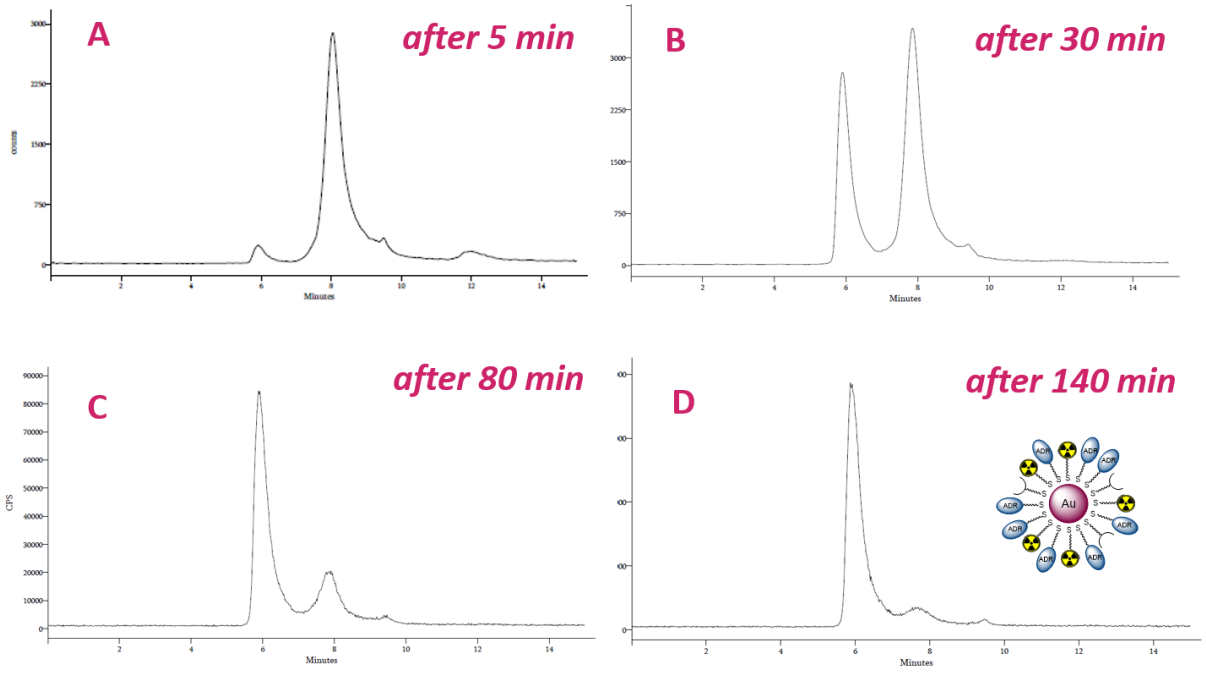

Figure 91: Reaction monitoring during the synthesis of Au-MUDA-ADR/MUAM-PADA-$^{99g}Tc(CO)_3$ NPs *via* HPLC. SEC γ HPLC traces after 5 min (**A**), 30 min (**B**), 80 min (**C**), 140 min (**D**) at room temperature.

Moreover, the yield of radiolabelled Au NPs increased to 80% after 80 min (**Figure 91 C**) and 94% after 140 min (**Figure 91 D**). Subsequently, the Au NP dispersion was purified *via* a desalting column (PD 10) and a pure radiolabelled Au NPs fraction was obtained with 5.612 MBq and thus a yield of 80% compared to the overall activity loaded onto the column. Since no complete consumption of $[^{99m}Tc(OH_2)_3(CO)_3]^+$ was achieved after stirring at room temperature for 140 min, another approach at 75 °C was performed.

Already after 30 min, $[^{99m}Tc(OH_2)_3(CO)_3]^+$ disappeared completely and only a single signal of radiolabelled Au NPs (t_R = 5.9 min) was observed (**Figure 92 A**).

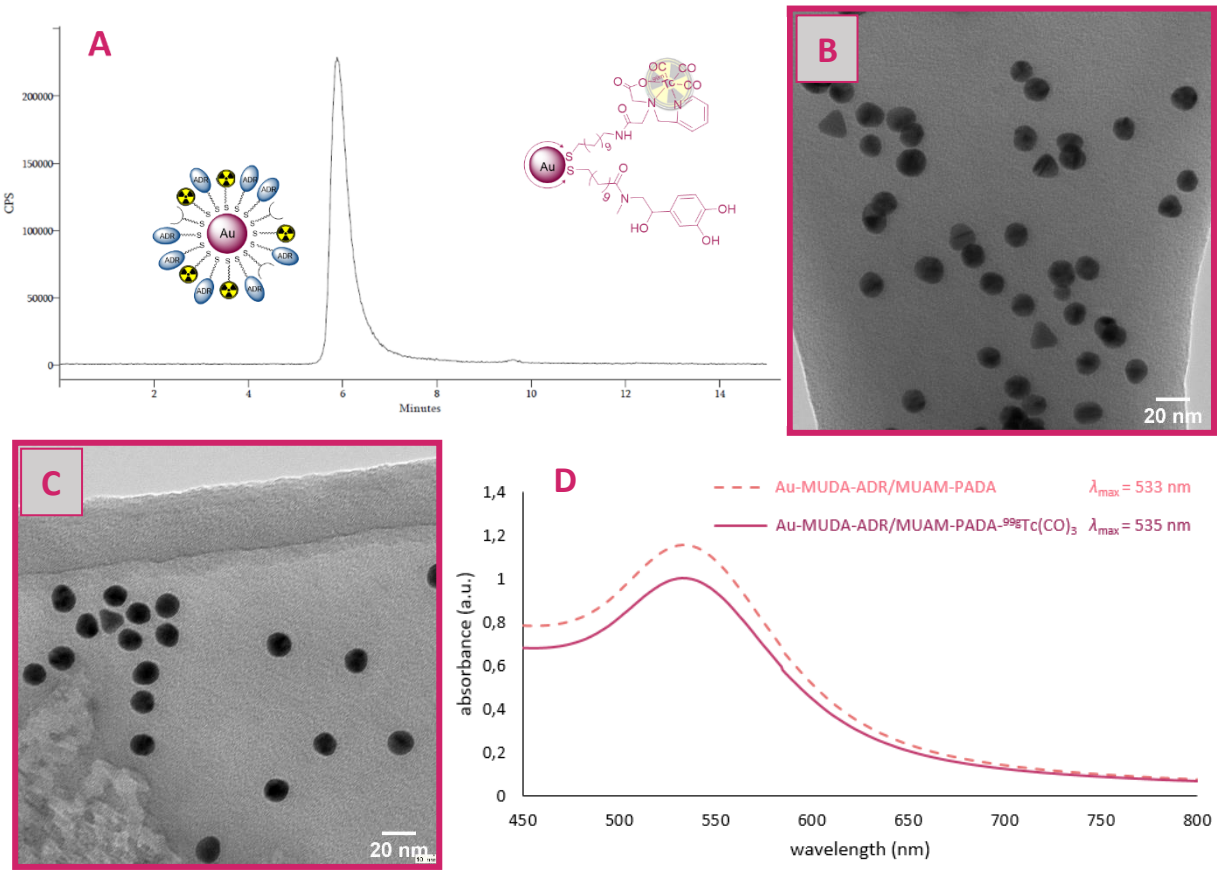

Figure 92: (**A**) SEC γ HPLC trace of unpurified Au-MUDA-ADR/MUAM-PADA-$^{99m}Tc(CO)_3$ NPs after 30 min at 75 °C, (**B**) TEM images of purified Au-MUDA-ADR/MUAM-PADA-$^{99g}Tc(CO)_3$ NPs stirred at room temperature after 140 min or (**C**) 75 °C after 30 min and (**D**) UV/Vis spectra of Au-MUDA-ADR/MUAM-PADA-$^{99g}Tc(CO)_3$ NPs and corresponding Au-MUDA-ADR/MUAM-PADA NPs.

Purification *via* a desalting column was performed and a pink and stable sample of pure radiolabelled Au NPs was obtained with a yield of 78% (7.84 MBq) compared to the total activity loaded onto the column. The clean Au NP fraction was purified a second time with a desalting column, in order to assess the stability of the dispersion. Again, a stable and pink fraction was obtained consisting of pure radiolabelled Au NPs with a yield of 83% (2.13 MBq) compared to the overall activity loaded onto the column. An overall yield of 67% was obtained after the

second purification step, thus showing that the ^{99m}Tc is strongly bond to the Au NPs. Furthermore, TEM investigations reveal that no change in the morphology of the NPs occurred during the labelling procedure. Spherical Au NP with a size of d_{TEM} = 14.0 ± 1.5 nm were obtained during a radiolabelling at room temperature (**Figure 92 B**).

Even the NPs of the approach at 75 °C had a similar monodisperse morphology and thus, no visible agglomeration caused by heating occurred (**Figure 92 C**). UV/Vis measurements revealed that only a small bathochromic shift of the homogenous formed plasmon resonance occurred towards λ_{max} = 535 nm (**Figure 92 D**).

Furthermore, IR investigations were performed and showed that unambiguous similarities of the organic frameworks between the radiolabelled Au-MUDA-ADR/MUAM-PADA-^{99g}Tc(CO)$_3$ NPs as well as the unlabelled corresponding Au-MUDA-ADR/MUAM-PADA NPs exist (**Figure 93**).

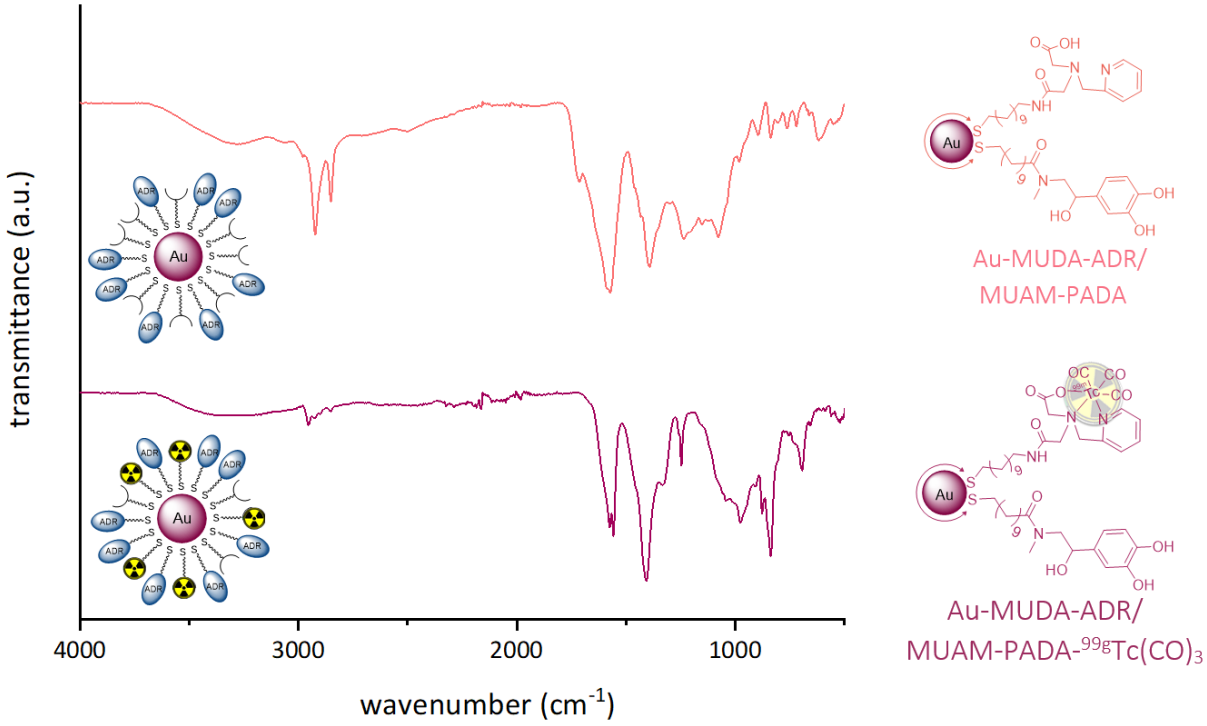

Figure 93: IR spectra of Au-MUDA-ADR/MUAM-PADA-^{99g}Tc(CO)$_3$ NPs (**bottom**) and Au-MUDA-ADR/MUAM-PADA NPs (**top**).

In order to demonstrate that the precursor $[^{99m}Tc(OH_2)_3(CO)_3]^+$ can unambiguously be distinguished from the radiolabelled Au NPs within the SEC HPLC traces, the pure Au NP sample was contaminated with $[^{99m}Tc(OH_2)_3(CO)_3]^+$. However, the HPLC trace shows additional to the Au NPs signal with t_R = 5.9 min, a second strong signal, which was assigned to $[^{99m}Tc(OH_2)_3(CO)_3]^+$.

Radiolabelling of Au-Citrate NPs as a blank test

Finally, a blank test was performed to reveal if the ^{99m}Tc was indeed specifically coordinated to the chelating ligand and not unspecifically bound to the Au NP surface. For this purpose, Au-Citrate NPs were stirred with $[^{99m}Tc(OH_2)_3(CO)_3]^+$ at room temperature (**Scheme 56**).

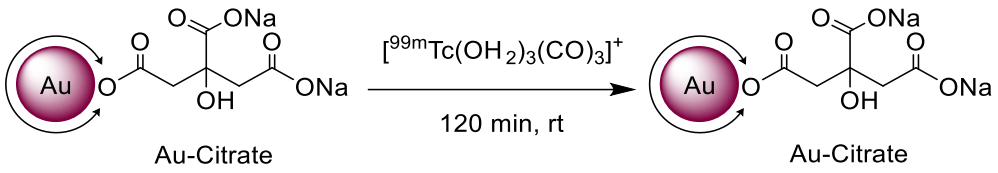

Scheme 56: Blank test with Au-Citrate NPs and $[^{99m}Tc(OH_2)_3(CO)_3]^+$.

However, the HPLC trace did not indicate any presence of radiolabelled Au NPs since no signal at t_R = 5.9 min was detected. Instead only the signal of $[^{99m}Tc(OH_2)_3(CO)_3]^+$ with t_R = 7.7 min was observed (**Figure 94**). Thus, it can be assumed that the ^{99m}Tc can only be complexed in the presence of suitable chelating ligands.

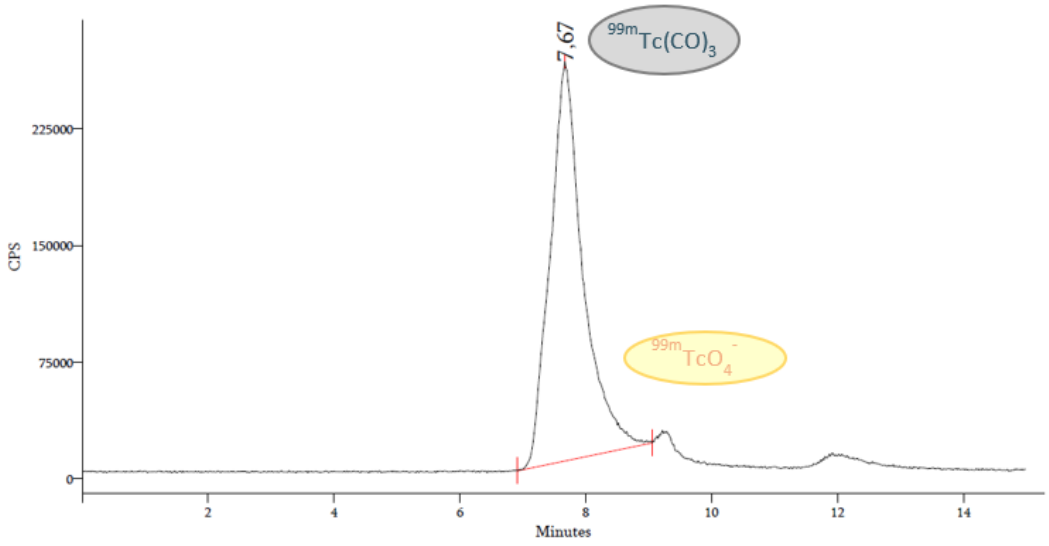

Figure 94: SEC γ HPLC trace of Au-Citrate NPs reacted with $[^{99m}Tc(OH_2)_3(CO)_3]^+$ (blank test).

Nevertheless, further blank tests at different temperatures should be performed in future studies in order to be certain about other reaction conditions.

4 Conclusion and Outlook

In this work, monodisperse, spherical gold nanoparticles (Au NPs) in the size range of 5 nm to 30 nm were successfully synthesised and used as starting particles for further functionalisations (**Figure 95**). Fine-tuning of the sizes can be achieved by varying the gold precursor to stabilising ligand and reducing agent ratio as well as the reaction conditions including solvent volume, temperature and time. As an alternative to Au-Citrate NPs (**Figure 95**, **left**), monodisperse Au NPs have been synthesised in DMSO and subsequently purified and redispersed in H_2O. Various bifunctional thiol linkers show excellent stabilising properties and they offer the possibility to attach various biomolecules to the different functional groups (-COOH, -NH_2) (**Figure 95**, **centre left**, **centre right and right**)).

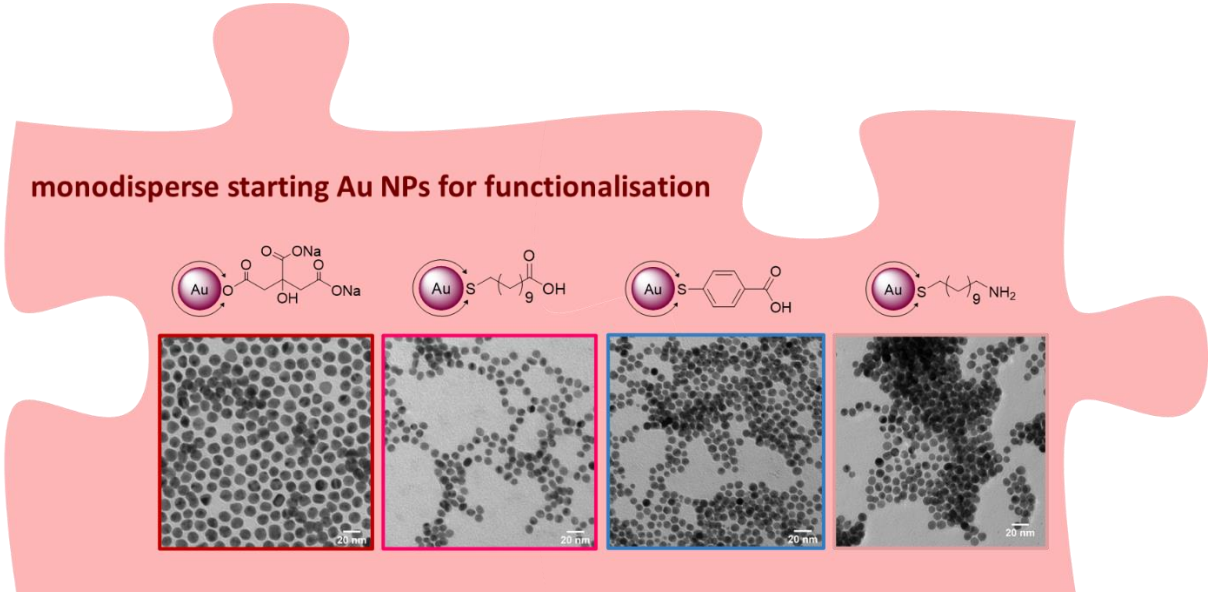

Figure 95: Examples of the synthesised monodisperse Au NPs prepared within this thesis.

Different synthetic routes towards a biofunctionalisation of Au NPs were successfully followed: either a consecutive or a parallel synthetic strategy. The first one includes, after the introduction of a bifunctional thiol linker, a consecutive reaction at the ligand periphery in order to attach the biogenic substance. This route shows good results for carbachol (CCh) functionalised Au NPs (**Figure 96**).

As an alternative, a parallel synthetic route can be employed. First, the complete ligand consisting of biogenic substance and thiol linker is synthesised. Then, it is attached to the Au NPs in a ligand exchange reaction. This strategy was successful for the functionalisation of Au NPs with noradrenaline (NA), adrenaline (ADR) or atropine (AT). Initial attempts with salbutamol (SB) appeared promising (**Figure 96**), since salbutamol functionalised Au NPs were obtained. But further investigations on ligand syntheses and purification should be performed in order to obtain higher yields and pure compounds.

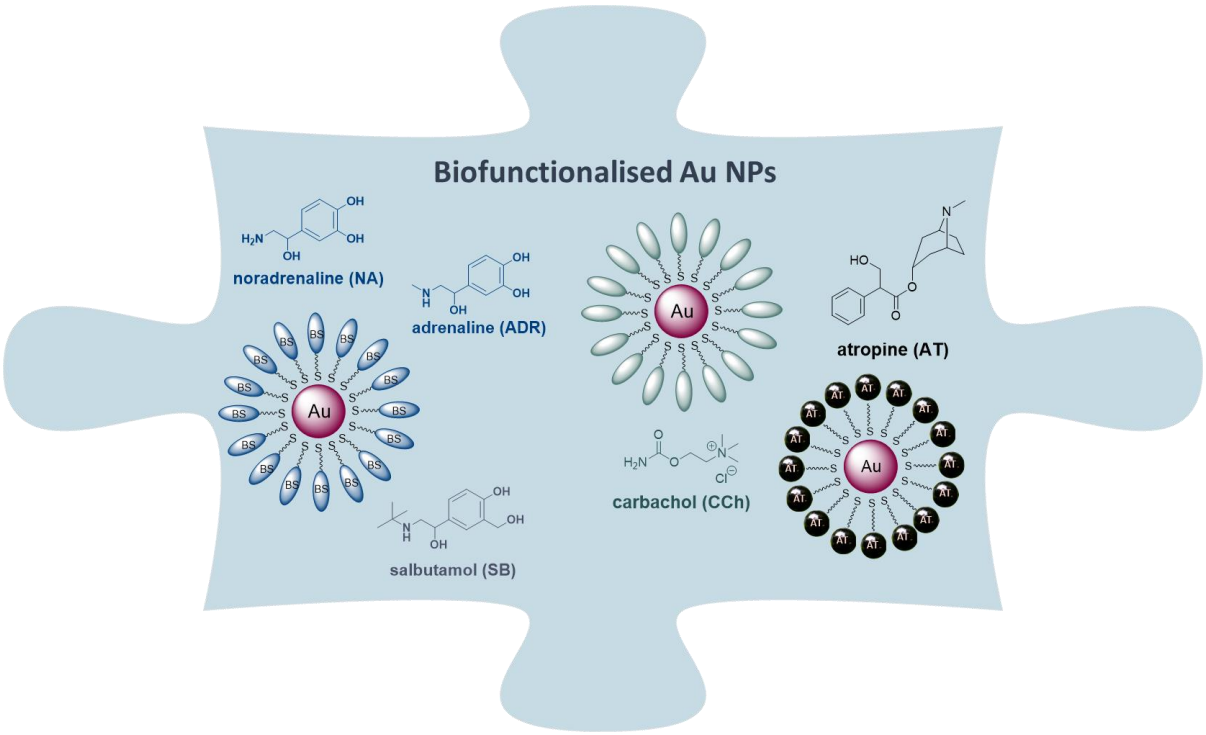

Figure 96: Overview of biogenic substances attached to Au NPs within this thesis.

Furthermore, the biofunctionalised Au NPs were investigated for their receptor activations in different physiological studies, which was always done in comparison to the free ligand. Au-MUDA-CCh NPs with a size of 14 nm show a 10^6-fold potentiation of the induced receptor activation on rat epithelial membranes. Au-MUDA-ADR NPs with a size of 9 nm are biologically active in nanomolar ranges in systems where β_1-adrenergic receptors were involved, such as intestinal secretion or cardiac contractility. Atropine Au NPs with a size of 14 nm were found to cross the epithelial barrier and act as a receptor poison at the basolateral side. Moreover, different Au-MUDA-AT NP samples in the size range between 8 nm to 16 nm were tested in a basolateral application on their blocking effect at M_3 receptors, while Ø 13 nm Au-MUDA-AT NPs showed the strongest blocking effect at the M_3 receptors.

In addition to biofunctionalised Au NPs also biomimetic Au NPs were successfully synthesised. As excellent starting particles, monodisperse amine stabilised Au-MUAM NPs were obtained in different sizes ranging from 5 nm to 17 nm. These were successfully reacted with dihydrocaffeic acid (DHCA) (**Figure 97**, **left**). Au-MUAM-DHCA NP samples mimic the biogenic substance dopamine. These were not tested in biological systems for time restraints but may provide a starting point towards further biomimetic functionalisations and may be applied in further receptor activation studies.

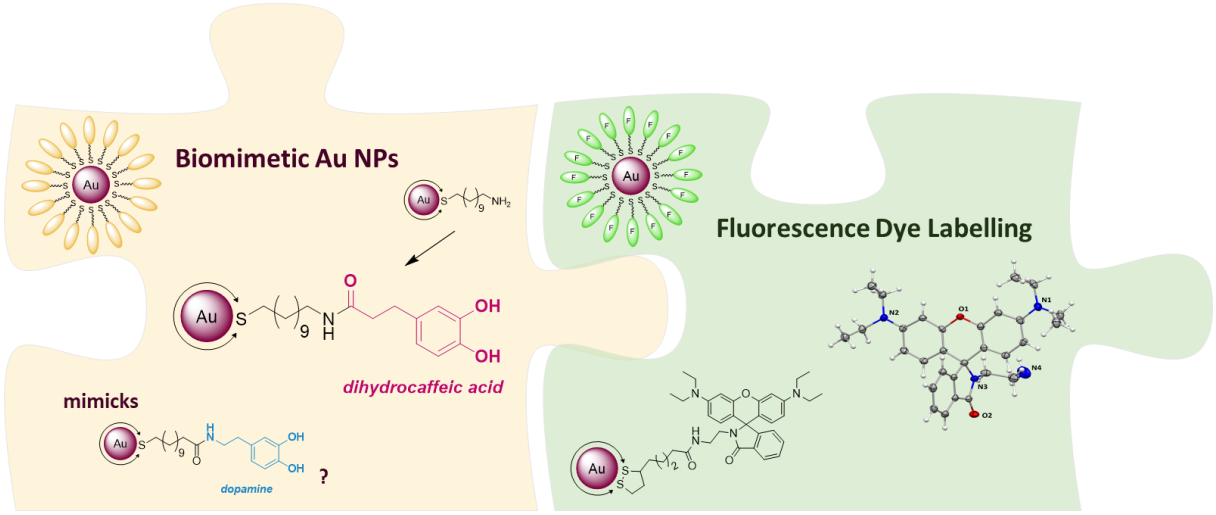

Figure 97: Key elements of the biomimetic Au NPs functionalised with dihydrocaffeic acid (**left**) and the labelling with a fluorescent dye (**right**).

In order to enable further analytical studies, Au NPs were successfully functionalised with a fluorescent dye (**Figure 97**, **right**). Rhodamine B serves as a common fluorescent dye, which can be modified with a thiol linker in order to enable its attachment to the Au NPs. However, the synthesis of a suitable fluorescent dye ligand in fact proves to be rather challenging. Conventional esterification or peptide formation using the coupling reagents *N*-hydroxylsuccinimide (NHS) and diisopropylcarbodiimide (DIC) does not lead to the desired product. Derivatisation of the dye can be achieved through the reaction with diamines, such as ethylenediamine (EN). The crystal structure was confirmed by XRD (**Figure 97**, **right**). Since a free amine moiety is present in the crystallised product, a bifunctional thiol linker can be introduced in the next step using hexafluorophosphate azabenzotriazole tetramethyl uronium (HATU) as a coupling reagent in a novel approach. As a proof of concept, rhodamine B functionalised Au NPs can be synthesised and the successful functionalisation can be confirmed *via* IR spectroscopy. However, the analytics are not fully conclusive, since NMR spectra of the functionalised Au NPs only indicate slightly some of the respective proton resonances. In addition, a quenching effect originating from the Au NPs reduces the overall fluorescence.

In order to synthesise diagnostically more valuable Au NPs, a radiolabelling method was considered and various functionalised Au NPs were labelled with the radionuclide ^{99m}Tc. For this purpose, the tridentate chelator ligand picolylamine diacetic acid (PADA) was synthesised in order to complex the metal ion and further modified with a thiol moiety in order to attach on to the Au NPs. Two new ligands were introduced, which contain either a short cysteamine chain (PADA-Cys) or a long mercaptoundecylamine chain (PADA-MUAM). Several studies on complexes with the non-radioactive group 7 homologue Re show their binding behaviour, and XRD measurements confirm that the metal ion is complexed by the tridentate ligand. Furthermore, a successful immobilisation of [Re(CO)$_3$PADA-MUAM] on to the Au NPs was proven by EDX measurements and reveal the presence of Re around the Au NP core, supporting the successful preparation of Au-MUAM-PADA-Re(CO)$_3$ NPs.

Following these initial studies, radiolabelling of the ligands PADA-Cys and PADA-MUAM with ^{99m}Tc was successfully performed. In the reaction of PADA-MUAM with $[^{99m}Tc(OH_2)_3(CO)_3]^+$, the desired complex can be obtained with a high selectivity and a radiochemical purity (RCP) of 91%. Furthermore, its stability was proven even in the presence of histidine as a biologically relevant competing ligand. The short-chain ligand PADA-Cys and even its corresponding thioacetate protected ligand Ac-Cys-PADA can also be radiolabelled with $[^{99m}Tc(OH_2)_3(CO)_3]^+$ but led to multiple side products and thus resulted in lower radiochemical yields. In addition to the free ligands, Au NPs can also be radiolabelled (**Figure 98**). Two different pathways were followed with equal success. On the one hand, Au NPs which are already functionalised with the chelator can be reacted with $[^{99m}Tc(OH_2)_3(CO)_3]^+$; another possibility consists of immobilising the "fresh" radiolabelled complexes in a ligand exchange reaction on the unfunctionalised Au-Citrate NPs.

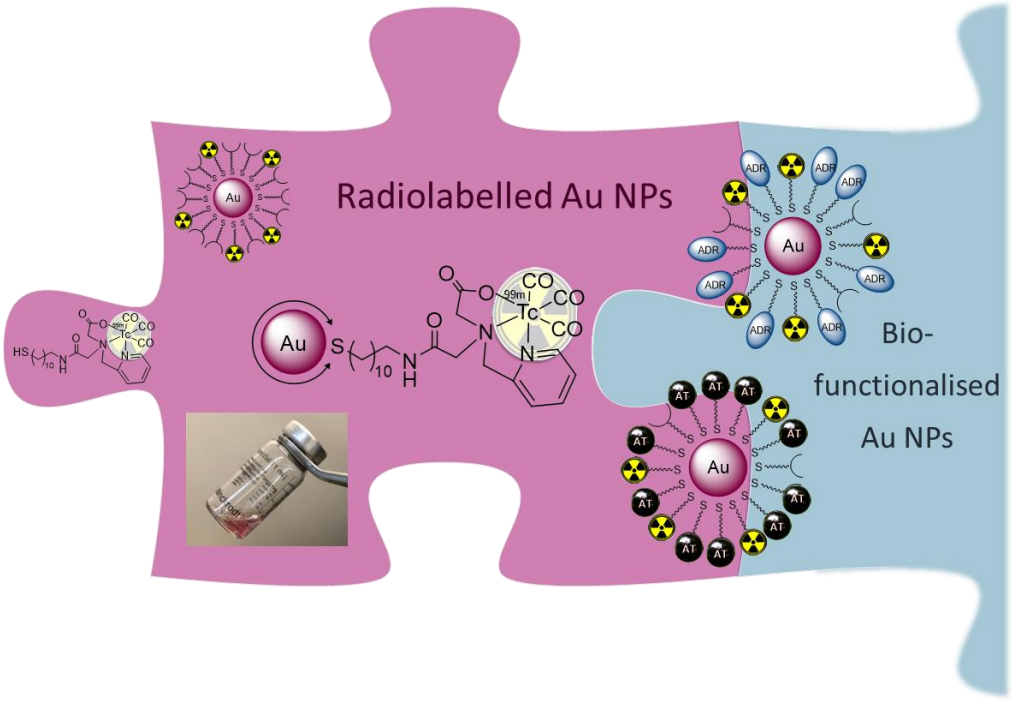

Figure 98: Summary of radiolabelled Au NPs and its linkage to biofunctionalised Au NPs, which allows the preparation of mixed ligand shell Au NPs that are both biofunctionalised and radiolabelled.

Au-MUAM-PADA-^{99m}Tc(CO)$_3$ NPs can be prepared and purified *via* desalting columns in both pathways and in equally high yields. The analytical characterisation of radiolabelled Au NPs can be performed using size exclusion chromatography. Here, the choice of eluent is crucial for an appropriate analysis. In this work, it was found that phosphate buffer solution (PBS) as a prominent biocompatible medium does not lead to a separation of the reaction components in this system. Instead, sodium dodecylsulfate (SDS) in H_2O is used as an alternative buffer resulting in an excellent separation of the radiolabelled Au NPs from the side products of the reaction. In order to cross disciplines, from mono ligand shell NPs into theragnostic drug candidates, biofunctionalised Au NPs were also labelled with ^{99m}Tc. In addition to the chelating

ligand, these carry another ligand with a bioactive unit in a mixed ligand shell. Different Au NPs functionalised with either atropine or adrenaline can be successfully radiolabelled with $[^{99m}Tc(OH_2)_3(CO)_3]^+$. In these reactions, it was found that a temperature increase up to 75 °C led to a higher consumption of $[^{99m}Tc(OH_2)_3(CO)_3]^+$ and thus to a significantly faster radiolabelling of the Au NPs. To further support the integrity of the NPs and their robustness throughout the process, all radiolabelled Au NPs were additionally investigated by TEM, UV/Vis, DLS and IR after decay, revealing an intact functionalisation, shape and uniformity and verifying the presence of stable Au NPs even after radiolabelling.

This thesis presents a broad variety of functionalisations of Au NPs, which may provide further impulses for future studies. Moreover, physiological studies of the synthesised materials should be performed, as they are monodisperse, stable in H_2O at room temperature and may proof vital in the search for other functionalisations. In this context, more efficient ways of attaching salbutamol (SB) can be investigated. The focus should be placed on ligand syntheses, leading to higher yields and pure compounds. Moreover, even terbutaline, which is similar to salbutamol, might be of interest for studies on trachea muscles. In addition, other biogenic substances like tyramine, tyrosine or taurine may be attached to the Au NPs and also tested after successful characterisation. With respect to receptor activation, receptor antagonists could also be immobilised such as propranolol, a non-selective drug from the class of β-blockers. Correspondingly, a non-selective α-blocker may also be employed, such as phentolamine. Moving even further towards medical applications, small drug molecules might be attached on to the Au NPs such as the antiepileptic drug carbamazepine or different kinds of opioids and their effects on biological system may be studied.

Following the successful synthesis of biomimetic Au NPs, their effects on biological systems should be investigated and whether these Au NPs are able to stimulate adrenergic receptors with their functional catechol moiety present on the ligand shell. Once the effects on the biological systems have been investigated, labelling of the Au NPs may be performed in order to enable further examination at the microscopic or macroscopic level. Since the application of fluorescent dyes presented some challenges, their further investigation should be reconsidered. One advantage of applying a fluorescent dye, such as Eosin Y, is the additional analytic opportunity. As this dye contains heavy Br atoms, a quantification of the ligands on the surface of the Au NPs is theoretically feasible by means of EDX. However, any other ligand containing heavy atoms could also be introduced for this kind of analysis.

However, radiolabelling with ^{99m}Tc appears to be the most promising labelling method. The chelator ligand syntheses as well as their complexation and immobilisation on to the Au NPs led to excellent results. In further studies, other chelator ligands, which are able to complex ^{99m}Tc, could also be synthesised. As an example, 2,3-diaminopropionic acid (DAP) is described in the literature as a potent ^{99m}Tc chelator. DAP could be modified in such a way that it can be attached to Au NPs. In addition to the short-lived isotope ^{99m}Tc, similar systems based on the long-lived ^{99g}Tc could be developed in order to investigate whether a successful preparation of ^{99g}Tc labelled multimodal Au NPs is achievable. ^{99g}Tc offers the advantage that the pure

complexes could be investigated in more detail. Crystallisation approaches and further analytics, such as ^{99g}Tc-NMR, would then be possible. However, the first step towards further investigations regarding the already synthesised ^{99m}Tc radiolabelled Au NPs is to perform biodistribution studies on animals. In these *in vivo* experiments, the mixed ligand shell biofunctionalised and radiolabelled Au NPs could be traced and further insights into their behaviour in biological systems could be gained.

5 EXPERIMENTAL SECTION

5.1 CHEMICALS AND MATERIALS

All chemicals were purchased from *Acros Organics*, *Alfa Aesar*, *Carl Roth*, *Fisher Scientific*, *Fluka*, *Merck*, *Santa Cruz Biotechnolgy*, *Sigma Aldrich* or *TCI* and used without further purification. Organic solvents were distilled before use or purchased in an anhydrous state and stored over molecular sieves.

Na[$^{99m}TcO_4$] in 0.9% saline was eluted from a $^{99}Mo/^{99m}Tc$ *UltratechneKow FM* generator purchased from *b. e. imaging AG* (Switzerland).

Chromatographic purifications were performed using *Merck* silica gel 60 (0.040-0.063 mm). Thin layer chromatography (TLC) was performed on *Merck* aluminium-backed plates with silica gel and fluorescent indicator (254 nm). For indicating, UV light (λ = 254 nm/365 nm) was used.

5.2 LABORATORY TECHNIQUES

Reactions were performed under inert conditions (argon atmosphere 99,9999%, *Air Products* at University of Cologne, N_2 at University of Zurich) using standard Schlenk line techniques with oven dried glassware, unless stated differently. Microwave assisted reactions were carried out in a *Biotage Initiator* microwave.

All water-based (nanoparticle) syntheses were performed in demineralised water or *arium* water. All glass vessels were washed with aqua regia and demineralised water prior to use.

5.2.1 DESALTING COLUMN

Nanoparticles were further purified *via* desalting columns. This strategy was used mainly to purify radiolabelled NPs. A desalting column is a gel filtration (exclusion) chromatography column and is predominantly used in protein biology and in DNA extractions.

Their mechanism is based on the separation of chemical (or biological) structures according to their size within the column. Smaller structures can be absorbed within the matrix of the packing material and remain longer on the column. Larger structures, on the other hand, elute faster. Thus, it is possible to separate larger structures, such as functionalised NPs and their ligand shells from the free ligands, smaller side products or the ^{99m}Tc precursor. The quality of a separation strongly depends on the diameter and length of the chosen column.

Desalting columns used in this work included PD 10 (sample volume 1.0-2.5 ml) and PD MiniTrap (sample volume 0.1-0.5 ml) columns filled with *Sephadex*™ (a cross-linked dextran scaffold) as a medium. This gel filtration is considered as a fast alternative to dialysis.

When using desalting columns, the sample is placed on a column saturated with eluent (**Figure 99**, **left**) and eluted with buffer (here H_2O if not stated differently) (**Figure 99**, **centre**). The individual fractions are collected and analysed (**Figure 99**, **right**).

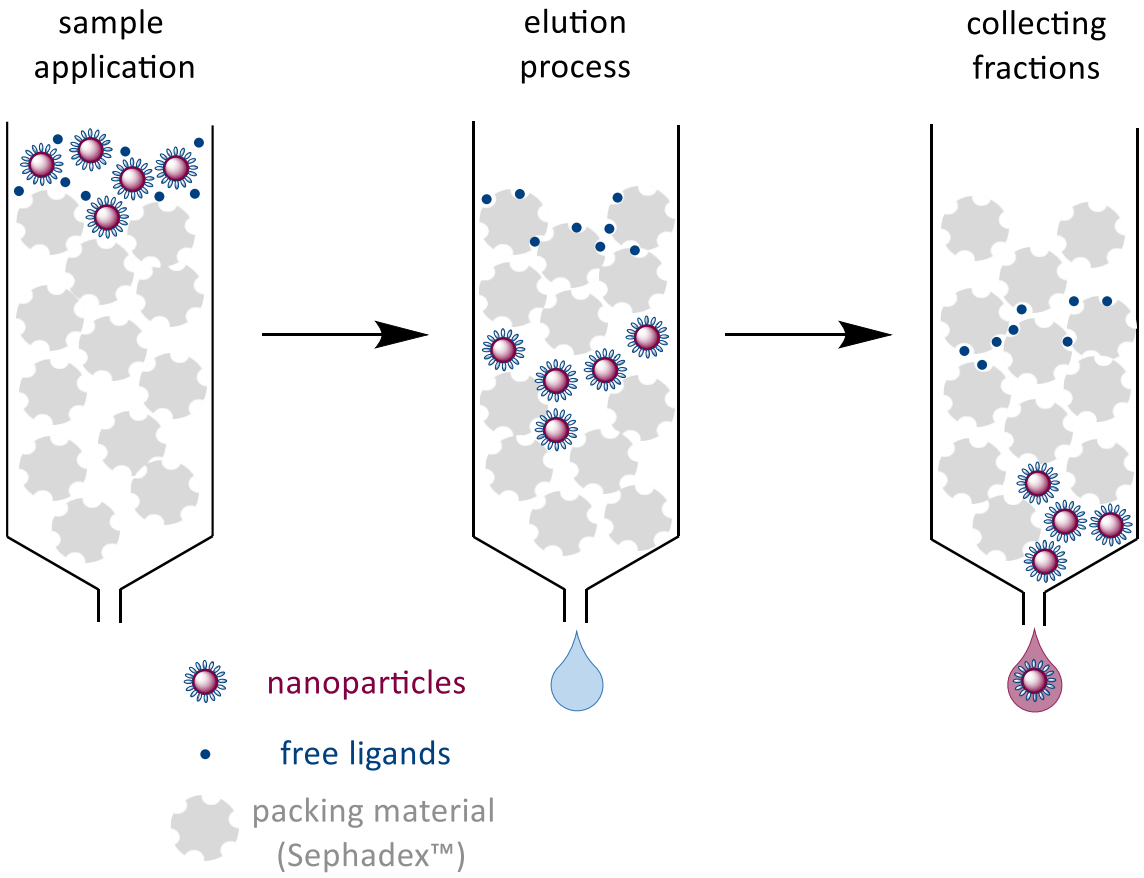

Figure 99: Purification *via* gel filtration chromatography using a desalting column. Preparation steps include the sample application (**left**), the fractional elution process (**centre**) and the collection of different fractions and their analyses (**right**).

5.2.2 Dialysis

Dialysis was used to eliminate an excess of ions, free ligands or side products from the NP dispersion. The NP dispersion is filled into a dialysis membrane, closed with clamps on the ends and immersed in the dialysing solvent (typically demineralised water, DMSO or as stated) for a certain period of time. In this work, membranes of regenerated cellulose "*ZelluTrans*" with different pore sizes ("**m**olecular **w**eight **c**ut **o**ff" (MWCO), e.g.: MWCO 3500, MWCO 6000, MWCO 12000) were used. These were purchased from *Carl Roth GmbH*. The dialysis membrane was immersed in the dialysing solvent for 30 min prior to use. All dialyses were performed at room temperature.

The dialysis process is driven by the chemical concentration gradient and occurs at the surface of the membrane. Small molecules (free ligands, side products, etc.) are transferred from the inner side of the semi-permeable dialysis membrane to the less concentrated solution on the outside. By exchanging the dialysing solvent several times and thus maintaining a high concentration gradient, free ligands and other impurities can be removed while the NPs remain inside the dialysis tube, as shown in Figure 100.

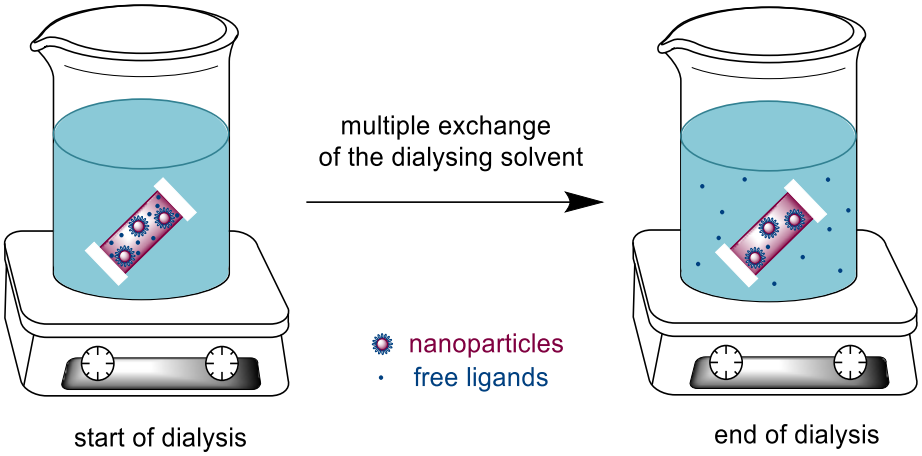

Figure 100: Purification *via* dialysis.

5.3 Analytical Methods

5.3.1 NMR Spectroscopy

^{1}H-NMR and ^{13}C-NMR spectra were recorded on *Bruker Avance 400 MHz (AV 400)*, *Bruker Avance II 300 MHz (AV 300)* and *Bruker Avance II+ 600 MHz (AV II 600)* spectrometers at the Institute of Organic Chemistry, University of Cologne or on *Bruker AV2-400* (400 MHz) or *Bruker AV2-500* (500 MHz), University of Zurich. All measurements were performed at room temperature. Chemical shifts are given in ppm relative to respective solvent peaks or against the internal standards TMS (for non-aqueous solvents) or DSS (for D_2O). ^{1}H-NMR data are reported as follows: chemical shifts (multiplicity [ppm], classification). Multiplicity is recorded as s = singlet, b s = broad singlet, d = doublet, t = triplet, q = quartet, m = multiplet. All spectra were displayed with the software *MestReNova*.[337]

^{1}H-NMR spectra of all Au NP dispersions were recorded. The Au NP dispersion (4-5 ml) was dried *in vacuo* and subsequently dissolved in D_2O in order to prepare the samples. To ensure stable dispersions during the measurements, a base (mainly NEt_3) in D_2O was added. The measured NMR spectra were then compared to the spectra of the initial Au NP dispersions as well as the synthesised ligands. Impurities of D_2O and NEt_3 originate from the sample preparation.

5.3.2 Mass Spectroscopy

The mass spectra were recorded on an ESI mass spectrometer (*micrOTOF*) from *Bruker Daltonics (Bremen, Deutschland)* at the Justus-Liebig University Giessen or on an ESI mass spectrometer of *Agilent Technologies*, model *LC/MSD Vl*, at the research group of Prof. Berkessel at the University of Cologne. UPLC-ESI-MS measurements were performed on a Waters Acquity UPLC System coupled to a *Bruker Daltonics HCT*™ ESI-MS, using an *Acquity UPLC BEH* C18 1.7 µm (2.1 x 50 mm) column, at the University of Zurich. UPLC solvents were formic acid (0.1% in millipore water) (solvent A) and acetonitrile UPLC grade (solvent B). Applied UPLC gradient: 0–0.5 min: 95% A, 5% B; 0.5–4.0 min: linear gradient from 95% A, 5% B to 0% A, 100% B; 4.0–5.0 min: 0% A, 100% B. The flow rate was 0.6 ml min^{-1}. Detection was performed at 250 nm and 480 nm (DAD).

5.3.3 IR Spectroscopy

IR-spectra were recorded on a *Perkin Elmer* FTIR-ATR (*UATR TWO*) at room temperature with a maximum resolution of 1 cm^{-1}. Absorption bands are given in cm^{-1}.

5.3.4 UV/Vis Spectroscopy

UV/Vis measurements were performed with a *UV-1600PC* spectrophotometer from *VWR*.

5.3.5 TEM

The size and shape of the synthesised NPs were determined with TEM images measured on the transmission electron microscope *LEO 912* from *Zeiss*. For sample preparation, Au NP dispersion (10 µl) was placed on a carbon-coated copper grid and dried on air. Determination of the average particle size and standard deviation was achieved by measuring at least 200 individual particles using *Image J Fiji*.[338]

5.3.6 EDX

EDX measurements were performed on a transmission electron microscope *JEOL FS2200* from *JEOL* using the prepared TEM grids.

5.3.7 DLS

The hydrodynamic radius was determined *via* dynamic light scattering measurements on a *NanoZS* from *Malvern.*

5.3.8 Preparative HPLC

Ligands were purified on a *Shimadzu* system (CBM-40 system controller, SPD-40 UV/VIS detector, LC-20AO preparative liquid chromatograph, FCV-200AL prep quaternary valve), using a *Dr. Maisch Reprosil* C18 100-7 (40 × 250 mm) column, at the University of Zurich. HPLC solvents were HPLC grade acetonitrile (with 0.1% trifluoroacetic acid) (solvent A) and water (with 0.1% trifluoroacetic acid) (solvent B). Applied HPLC gradient: 0–3 min: 0% A, 100% B; 3–25 min: 0–100% A, 100–0% B; 25-45 min: 100% A, 0% B. The flow rate was 40 ml min^{-1}. UV/Vis detection was performed between 230 nm and 270 nm.

5.3.9 Analytical HPLC

HPLC analyses of ^{99m}Tc complexes were performed on a *Merck Hitachi Chromaster 5160* pump coupled to a *Merck Hitachi Chromaster 5430* diode array detector and a radio detector, at the University of Zurich. UV/Vis detection was performed at 250 nm. The detection of radioactive ^{99m}Tc complexes was performed with a *Berthold FlowStar LB 514* radio detector equipped with a BGO-X cell. Separations were achieved on a *Macherey-Nagel NUCLEOSIL®*C18 5 µm, 100 Å (250 × 3 mm) column. HPLC solvents were HPLC grade acetonitrile (solvent A) and trifluoroacetic acid (0.1% in Millipore water) (solvent B). Applied HPLC gradient: 0–3 min: 0% A, 100% B; 3–3.1 min: 0–25% A, 100–75% B; 3.1–9 min: 25% A, 75% B; 9–9.1 min: 25–34% A, 75–66% B; 9.1–18 min: 34–100% A, 66–0% B; 18–25 min: 100% A, 0% B; 25–25.1 min: 100–0% A, 0–100% B; 25.1–30 min: 0% A, 100% B. The flow rate was 0.5 ml min^{-1}.

5.3.10 Size Exclusion HPLC

HPLC analyses of ^{99m}Tc radiolabelled NPs were performed on a *Merck Hitachi L7000* system, using a RP-HPLC on a 8 × 300 mm, 200 Å Diol YMC size exclusion column, at the University of Zurich. The system was equipped with the UV-detector L-7400, and the radio-detector *Berthold FlowStar LB513*. The flow rate was 1.0 ml min^{-1} using PBS (pH 6.9) and later on 15% SDS in H_2O as a mobile phase. UV detection was performed at 250 nm.

5.3.11 Elemental Analysis

Elemental analyses for C, H, N and S were acquired by Mr. Dirk Pullem on a *Eurolab EA Elemental Analyzer* at the University of Cologne.

5.3.12 X-ray Crystallographic Analysis

SXRD data of the Re complex was obtained by mounting a suitable single crystal on a *MiTiGen Microloop*™ and attaching this to the goniometer head of an *SC-XRD Bruker D8 Venture*. The

crystal was cooled to 100-120 K by an *Oxford Cryostream* low temperature device.[339] The full data set was recorded and the images processed using *APEX3*.[340] SXRD data of Rhod-EN was obtained at P24.1 beamline of the *PETRA III* facility at the German Electron Synchrotron (DESY) in Hamburg (Germany). Structure solution by direct methods was achieved through the use of *SHELXS* programs,[341] and the structural model refined by full matrix least squares on F2 using *SHELX97*.[342] Molecular graphics were plotted using *Mercury*.[343] Editing of CIFs and construction of tables, bond lengths and angles was achieved using and *PLATON*[344] and *Olex2*.[345]

5.4 Nanoparticle Syntheses

5.4.1 Citrate Coordinated Gold Nanoparticles

5.4.1.1 General Synthetic Procedure

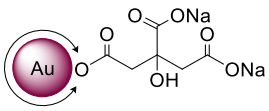

(according to the Turkevich method modified by Mattern *et al.*[4])

$HAuCl_4 \cdot 3\ H_2O$ was dissolved in demineralised H_2O and heated to reflux for 20 min. A solution of trisodium citrate dihydrate in demin. H_2O was added quickly under vigorous stirring. The mixture was heated to 80 °C for 2 h before cooling in an ice bath and filtrated using syringe filtration on a cellulose membrane with 0.2 µm pore size.

Different sizes

Synthesis of Au-Citrate (Ø 11 nm) in H_2O

$HAuCl_4 \cdot 3\ H_2O$ (50 mg, 0.13 mmol, 1.0 eq.) in demin. H_2O (195 ml), trisodium citrate dihydrate (600 mg, 2.04 mmol, 15 eq.) in demin. H_2O (5 ml)
A pink, clear NP dispersion with a particle concentration of 14.6 nM was obtained and stored at 4 °C in the dark.

^{1}H-NMR (600 MHz, D2O): δ/ppm = 2.71-2,69 (m, 2H, CH_2), 2.61-2,58 (m, 2H, CH_2); **IR** (ATR): ν/cm^{-1} = 3425 (ν_{O-H}), 1595 ($\nu_{C=O}$), 1249, 620; **TEM**: d = 11.2 ± 0.9 nm; **UV/Vis**: λ_{max} = 523 nm; **DLS**: d_{hydr} = 13 ± 5 nm.

Synthesis of Au-Citrate (Ø 12 nm) in H_2O

$HAuCl_4 \cdot 3\ H_2O$ (50 mg, 0.13 mmol, 1.0 eq.) in demin. H_2O (195 ml), trisodium citrate dihydrate (400 mg, 1.36 mmol, 10 eq.) in demin. H_2O (5 ml)
A dark red, clear NP dispersion with a particle concentration of 11.9 nM was obtained and stored at 4 °C in the dark.

TEM: d = 12.0 ± 0.8 nm; **UV/Vis**: λ_{max} = 523 nm; **DLS**: d_{hydr} = 12 ± 7 nm.

Synthesis of Au-Citrate (Ø 13 nm) in H_2O

$HAuCl_4 \cdot 3\ H_2O$ (50 mg, 0.13 mmol, 1.0 eq.) in demin. H_2O (195 ml), trisodium citrate dihydrate (254 mg, 0.87 mmol, 6.7 eq.) in demin. H_2O (5 ml)
A dark red, clear NP dispersion with a particle concentration of 9.7 nM was obtained and stored at 4 °C in the dark.

TEM: d = 12.8 ± 1.3 nm; **UV/Vis**: λ_{max} = 522 nm; **DLS**: d_{hydr} = 13 ± 3 nm.

Synthesis of Au-Citrate (Ø 14 nm) in H_2O

$HAuCl_4 \cdot 3\ H_2O$ (50 mg, 0.13 mmol, 1.0 eq.) in demin. H_2O (195 ml), trisodium citrate dihydrate (224 mg, 0.76 mmol, 5.8 eq.) in demin. H_2O (5 ml)
A dark red, clear NP dispersion with a particle concentration of 7.8 nM was obtained and stored at 4 °C in the dark.

TEM: d = 13.8 ± 1.2 nm; **UV/Vis**: λ_{max} = 521 nm; **DLS**: d_{hydr} = 15 ± 3 nm.

Synthesis of Au-Citrate (Ø 16 nm) in H_2O

$HAuCl_4 \cdot 3\ H_2O$ (12.8 mg, 0.03 mmol, 1.0 eq.) in demin. H_2O (47 ml), trisodium citrate dihydrate (38 mg, 0.13 mmol, 4.0 eq.) in demin. H_2O (3 ml)
A dark red, clear NP dispersion with a particle concentration of 5.1 nM was obtained and stored at 4 °C in the dark.

TEM: d = 15.9 ± 1.1 nm; **UV/Vis**: λ_{max} = 521 nm; **DLS**: d_{hydr} = 17 ± 4 nm.

Synthesis of Au-Citrate (Ø 25 nm) in H_2O with a shorter reaction time

(according to the Turkevich method modified by Panigrahi *et al.*[293])

$HAuCl_4 \cdot 3\ H_2O$ (4.9 mg, 12.5 µmol, 1.0 eq.) was dissolved in demin. H_2O (49 ml) and heated to reflux for 20 min. A solution of sodium citrate (8.0 mg, 27.2 µmol, 2.2 eq.) in demin. H_2O (1 ml) was added quickly under vigorous stirring. The reaction mixture was heated to reflux for 30 min before cooling in an ice bath and filtrated (0.2 µm pore size). A red violet, clear NP dispersion with a concentration of 0.5 nM was obtained and stored at 4 °C in the dark.

TEM: d = 24.9 ± 1.2 nm; **UV/Vis**: λ_{max} = 528 nm; **DLS**: d_{hydr} = 46 ± 20 nm.

Synthesis of Au-Citrate (Ø 28 nm) in H_2O with a shorter reaction time

$HAuCl_4 \cdot 3\ H_2O$ (4.9 mg, 12.5 µmol, 1.0 eq.) was dissolved in demin. H_2O (49 ml) and heated to reflux for 20 min. A solution of sodium citrate (6.2 mg, 21.1 µmol, 1.7 eq.) in demin. H_2O (1 ml) was added quickly under vigorous stirring. The reaction mixture was heated to reflux for 30 min before cooling in an ice bath and filtrated (0.2 µm pore size). A red violet, clear NP dispersion with a concentration of 0.4 nM was obtained and stored at 4 °C in the dark.

TEM: d = 28.1 ± 2.4 nm; **UV/Vis**: λ_{max} = 532 nm; **DLS**: d_{hydr} = 43 ± 20 nm.

Different precursors

Synthesis of Au-Citrate (Ø 13.5 nm) in H_2O using $HAuCl_4 \cdot 1\ H_2O$

$HAuCl_4 \cdot 1\ H_2O$ (21.7 mg, 64 µmol, 1.0 eq.) in demin. H_2O (95 ml), trisodium citrate dihydrate (112 mg, 381 µmol, 5.9 eq.) in demin. H_2O (5 ml)
A dark red, clear NP dispersion with a particle concentration of 8.5 nM was obtained and stored at 4 °C in the dark.

TEM: d = 13.48 ± 1.04 nm; **UV/Vis**: λ_{max} = 522 nm; **DLS**: d_{hydr} = 21 ± 8 nm.

Synthesis of Au-Citrate (Ø 14.5 nm) in H_2O using $HAuCl_4 \cdot x\ H_2O$

$HAuCl_4 \cdot x\ H_2O$ (21.7 mg) in demin. H_2O (95 ml), trisodium citrate dihydrate (112 mg, 381 µmol) in demin. H_2O (5 ml)
A dark red, clear NP dispersion with a particle concentration 6.8 nM was obtained and stored at 4 °C in the dark.

TEM: d = 14.47 ± 1.01 nm; **UV/Vis**: λ_{max} = 522 nm; **DLS**: d_{hydr} = 25 ± 12 nm.

Different concentrations

Synthesis of Au-Citrate (Ø 13 nm) in H_2O, higher concentrated (1.5 times)

$HAuCl_4 \cdot 3\ H_2O$ (25 mg, 0.65 mmol, 1.0 eq.) in demin. H_2O (72 ml), trisodium citrate dihydrate (112 mg, 0.38 mmol, 5.8 eq.) in demin. H_2O (3 ml)
A dark red, clear NP dispersion with a particle concentration of 13.7 nM was obtained and stored at 4 °C in the dark.

TEM: d = 12.6 ± 1.1 nm; **UV/Vis**: λ_{max} = 523 nm; **DLS**: d_{hydr} = 15 ± 4 nm.

Synthesis of Au-Citrate (Ø 12 nm) in H_2O, higher concentrated (2.0 times)

$HAuCl_4 \cdot 3\ H_2O$ (25 mg, 0.65 mmol, 1.0 eq.) in demin. H_2O (48 ml), trisodium citrate dihydrate (112 mg, 0.38 mmol, 5.8 eq.) in demin. H_2O (2 ml)
A dark red, clear NP dispersion with a particle concentration of 23.7 nM was obtained and stored at 4 °C in the dark.

TEM: d = 12.0 ± 1.3 nm; **UV/Vis**: λ_{max} = 523 nm; **DLS**: d_{hydr} = 21 ± 5 nm.

Synthesis of Au-Citrate in H_2O, higher concentrated (4.0 times)

$HAuCl_4 \cdot 3\ H_2O$ (25 mg, 0.65 mmol, 1.0 eq.) in demin. H_2O (23 ml), trisodium citrate dihydrate (112 mg, 0.38 mmol, 5.8 eq.) in demin. H_2O (2 ml)
A dark red, clear NP dispersion was obtained at 80 °C but agglomerated when cooled down to room temperature. No further analytical characterisation was performed.

5.4.2 Direct Gold Nanoparticle Syntheses in DMSO

5.4.2.1 General Synthetic Procedure for Mercaptoundecanoic Acid (MUDA) coordinated Gold Nanoparticles in H_2O

(according to the Stucky method modified by Mattern *et al.*[304])

PPh_3AuCl was dissolved in DMSO and a solution of ligand dissolved in DMSO was added. The mixture was heated to 65 °C and a solution of ^{t}Bu-amine borane complex in DMSO/ or solid ^{t}Bu-amine borane complex was added quickly under vigorous stirring. The dark red dispersion was stirred at 65 °C for 3.5 h in the dark and cooled in an ice bath. Subsequently, the particles were precipitated with EtOH (10-14 ml) and centrifuged (45 min, 7000 rpm). The supernatant was discarded, the dark residue was redispersed three times and washed again with EtOH. The obtained dark solid was dried in air and redispersed in H_2O. Diluted NaOH (0.1-0.2 ml) was added to obtain a stable NP dispersion. Then, the dispersion was further purified *via* dialysis against H_2O.

Different sizes

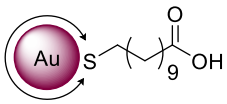

Direct Synthesis of Au-MUDA (Ø 8 nm) in H_2O

PPh_3AuCl (16 mg, 31 µmol, 1.0 eq.) in DMSO (3 ml), MUDA (30 mg, 138 µmol, 4.6 eq.) in DMSO (1 ml), ^{t}Bu-amine borane complex (27 mg, 300 µmol, 10 eq.) in DMSO (1 ml)

The dark solid was redispersed in H_2O (10 ml). Diluted NaOH (2 drops) was added to obtain a stable NP dispersion, which was further purified *via* dialysis against demin. H_2O (in MWCO 12000, 24 h). The violet, clear NP dispersion with a particle concentration of 212 nM was stored at 4 °C in the dark.

^{1}H-NMR (600 MHz, D_2O): δ/ppm = 2.93-2.86 (m, 2 H, CH_2), 2.17 (t, J = 6.6 Hz, 2 H, CH_2), 1.75-1.68 (m, 2 H, CH_2), 1.58-1.50 (m, 2 H, CH_2), 1.45-1.36 (m, 2 H, CH_2), 1.36-1.24 (m, 10 H, CH_2); **IR** (ATR): ν/cm^{-1} = ca. 3300 (ν_{O-H}, H_2O), 2921 (ν_{C-H}), 2846 (ν_{C-H}), 1675, 1555 ($\nu_{C=O}$), 1533, 1443, 1406 (δ_{C-H}), 1293 (ν_{C-O}), 955, 723 (δ_{C-H}); **TEM**: d = 7.9 ± 0.9 nm; **UV/Vis**: λ_{max} = 527 nm; **DLS**: d_{hydr} = 12 ± 3 nm.

Direct Synthesis of Au-MUDA (Ø 9 nm) in H_2O

PPh_3AuCl (16 mg, 31 µmol, 1.0 eq.) in DMSO (3 ml), MUDA (7 mg, 30 µmol, 1.0 eq.) in DMSO (1 ml), ^{t}Bu-amine borane complex (27 mg, 300 µmol, 10 eq.) in DMSO (1 ml)

The dark solid was redispersed in H_2O (10 ml). Diluted NaOH (3 drops) was added to obtain a stable NP dispersion, which was further purified *via* dialysis against demin. H_2O (in MWCO 12000, 24 h). The violet, clear NP dispersion with a particle concentration of 143 nM was stored at 4 °C in the dark.

TEM: d = 9.0 ± 0.9 nm; **UV/Vis**: λ_{max} = 528 nm; **DLS**: d_{hydr} = 14 ± 4 nm.

Direct Synthesis of Au-MUDA (Ø 10 nm) in H_2O

PPh_3AuCl (16 mg, 31 µmol, 1.0 eq.) in DMSO (3 ml), MUDA (5 mg, 20 µmol, 0.7 eq.) in DMSO (1 ml), ^{t}Bu-amine borane complex (2 mg, 20 µmol, 0.7 eq.) in DMSO (1 ml)

The dark solid was redispersed in H_2O (10 ml). Diluted NaOH (3 drops) was added to obtain a stable NP dispersion, which was further purified *via* dialysis against demin. H_2O (in MWCO 12000, 24 h). The violet, clear NP dispersion with a particle concentration of 115 nM was stored at 4 °C in the dark.

TEM: d = 9.7 ± 1.0 nm; **UV/Vis**: λ_{max} = 525 nm; **DLS**: d_{hydr} = 12 ± 3 nm.

Different ligands

5.4.2.2 Syntheses of 4-Mercaptobenzoic Acid (4-MBA) coordinated Gold Nanoparticles

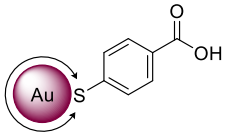

Direct Synthesis of Au-4-MBA (Ø 6 nm) in H_2O

PPh_3AuCl (8 mg, 16.2 µmol, 1.0 eq.) was dissolved in DMSO (2 ml) and a solution of 4-MBA (3 mg, 19.5 µmol, 1.2 eq.) dissolved in DMSO (0.5 ml) was added. The mixture was heated to 60 °C and a solution of ^{t}Bu-amine borane complex (8 mg, 115 µmol, 7.1 eq.) in DMSO (0.5 ml) was added quickly under vigorous stirring. The dark red dispersion was stirred at 60 °C for 1 h and 30 min in the dark and cooled in an ice bath. Then, the particles were precipitated with EtOH and centrifuged (45 min, 8700 rpm). The supernatant was discarded, the dark residue was redispersed three times and washed again with EtOH. The obtained dark solid was dried in air and redispersed in H_2O (5 ml). Afterwards, the NP dispersion was purified *via* dialysis against H_2O (in MWCO 12000, 6 × 1 h). A violet, clear NP dispersion with a concentration of 480 nM was obtained and stored at room temperature in the dark.

TEM: d = 6.0 ± .0.9 nm; **UV/Vis**: λ_{max} = 527 nm; **DLS**: d_{hydr} = 10 ± 2 nm.

Direct Synthesis of Au-4-MBA (Ø 8 nm) in H_2O

PPh_3AuCl (20 mg, 40.5 µmol, 1.0 eq.) was dissolved in DMSO (5 ml) and a solution of 4-MBA (4 mg, 26.0 µmol, 0.6 eq.) dissolved in DMSO (0.5 ml) was added. The mixture was heated to 65 °C and a solution of ^{t}Bu-amine borane complex (24 mg, 276 µmol, 6.8 eq.) in DMSO (0.5 ml) was added quickly under vigorous stirring. The dark red dispersion was stirred at 65 °C for 3 h and 30 min in the dark and cooled in an ice bath. Afterwards, the particles were precipitated with EtOH and centrifuged (45 min, 8700 rpm). The supernatant was discarded, the dark residue was dried in air and redispersed in demin. H_2O (6 ml). Diluted NaOH (2 drops) was added to obtain a red, clear and stable NP dispersion, which was further purified *via* dialysis against H_2O (in MWCO 12000, for 15 h). Au-4MBA NPs were obtained as a red dispersion with a concentration of 425 nM, which was stored at 4 °C in the dark.

TEM: d = 8.0 ± 1.1 nm; **UV/Vis**: λ_{max} = 525 nm; **DLS**: d_{hydr} = 16 ± 4 nm.

Direct Synthesis of Au-4-MBA (Ø 8 nm) in H_2O, solid reducing agent

PPh_3AuCl (20 mg, 40.5 µmol, 1.0 eq.) was dissolved in DMSO (5 ml) and a solution of 4-MBA (4 mg, 26.0 µmol, 0.6 eq.) dissolved in DMSO (1 ml) was added. The mixture was heated to 65 °C and the solid powder ^{t}Bu-amine borane complex (24 mg, 276 µmol, 6.8 eq.) was added quickly under vigorous stirring. The dark red dispersion was stirred at 65 °C for 3 h 30 min in the dark and cooled in an ice bath. Then, the particles were precipitated with CH_3CN and centrifuged (45 min, 7800 rpm). The supernatant was discarded, the dark residue was redispersed three times and washed again with CH_3CN. The obtained dark solid was dried in air, redispersed in H_2O (6 ml) and purified *via* dialysis against H_2O (in MWCO 12000, for 5 × 2 h). A violet, stable NP dispersion with a concentration of 381 nM was obtained and stored at 4 °C in the dark.

TEM: d = 8.3 ± 0.8 nm; **UV/Vis**: λ_{max} = 520 nm; **DLS**: d_{hydr} =11 ± 2nm.

5.5 Biofunctionalised Au NPs

5.5.1 Biofunctionalisation *via* a consecutive route

5.5.1.1 Surface Modification: General Synthetic Procedure of a Ligand Exchange Reaction

(according to a procedure by Mattern *et al.*[4])

The new ligand (mercapto acid, 0.10 mmol) and TMAH (50 µL, 0.55 mmol) were added to Au-Citrate NPs (10 ml) and the reaction mixtures was stirred at room temperature for 16 h. Then, the NP dispersion was purified *via* dialysis against demin. H_2O (in MWCO 12000, 3 × 2 h) and stored at 4 °C in the dark.

Synthesis of Au-MUDA (Ø 14 nm) in H_2O

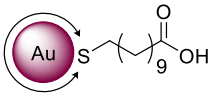

The Au NP dispersion was filtrated using syringe filtration on a cellulose membrane with 0.2 µm pore size. The new ligand MUDA (21 mg, 0.10 mmol) and TMAH (50 µL, 0.55 mmol) were added to Au-Citrate NPs with Ø 14 nm (10 ml) and stirred at room temperature for 16 h. Then, the NP dispersion was purified *via* dialysis against demin. H_2O (in MWCO 12000, 3 × 2 h). A dark red, clear NP dispersion with a particle concentration of 7.3 nM was obtained and stored at 4 °C in the dark.

^{1}H-NMR (600 MHz, D_2O): δ/ppm = 2.76 (t, J = 7.1 Hz,2 H, CH_2), 2.16 (t, J = 7.1 Hz, 2 H, CH_2), 1.73-1.66 (m, 2 H, CH_2), 1.58-1.50 (m, 2 H, CH_2), 1.45-1.38 (m, 2 H, CH_2), 1.37-1.24 (m, 10 H, CH_2); **IR** (ATR): ν/cm^{-1} = 2916 ($\nu_{C\text{-}H}$), 2848 ($\nu_{C\text{-}H}$), 1565 ($\nu_{C=O}$),1411; **TEM**: d = 14,1 ± 1,1 nm; **UV/Vis**: λ_{max} = 522 nm; **DLS**: d_{hydr} = 15 ± 3 nm.

5.5.1.2 Surface Functionalisation: General Procedure of a Reaction at the Ligand Periphery

(according to a procedure by Mattern *et al.*[4])

The Au NP dispersion was filtrated using syringe filtration on a cellulose membrane with 0.2 µm pore size. The coupling reagents EDC and NHS as well as the biogenic substance (amine) were added to the mixture. The pH of the NP dispersion was adjusted with NaOH or HCl to achieve a stable, clear dispersion, which was stirred at room temperature for a certain time in air before purification took place.

Synthesis of Au-MUDA-CCh (Ø 14 nm) in H2O

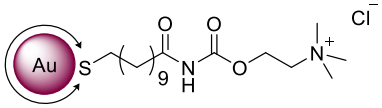

Au-MUDA NPs with Ø 14 nm (10 ml), EDC · HCl (5 mg, 27 µmol), NHS (3 mg, 27 µmol), CCh (4 mg, 22 µmol), NEt_3 (3 drops)

The NP dispersion was purified *via* dialysis against demin. H_2O (in MWCO 12000, 6 × 2 h). A pink, clear NP dispersion with a concentration of 7.6 nM was obtained and stored at 4 °C in the dark.

^{1}H-NMR (600 MHz, D_2O): δ/ppm = 4.54–4.50 (m, 2 H, CH_2), 3.74–3.69 (m, 2 H, CH_2), 3.19 (s, 9 H, CH_3), 2.56–2.34 (m, 4 H, CH_2), 1.94–1.87 (m, 2 H, CH_2), 1.60–1.51 (m, 2 H, CH_2), 1.43–1.25 (m, 12 H, CH_2); **IR** (ATR): ν/cm^{-1} = 3366 ($\nu_{O\text{-}H}$), 3035 ($\nu_{N\text{-}H}$), 2916, 2846 ($\nu_{C\text{-}H}$), 1704 ($\nu_{C=O}$), 1580 ($\delta_{N\text{-}H}$), 1491, 1456 ($\delta_{C\text{-}H}$), 1386 ($\nu_{C\text{-}N}$), 1227, 1073 ($\nu_{C\text{-}O}$), 950, 887, 831, 716 ($\nu_{C\text{-}S}$), 650 ($\delta_{O\text{-}C\text{-}N}$), 606 , 539; **TEM**: d = 13.9 ± 1.4 nm; **UV/Vis**: λ_{max} = 525 nm; **DLS**: d_{hydr} = 17 ± 3 nm, **ζ-potential:** ζ = -56.60 ± 7.50 mV.

Synthesis of Au-MUDA-CCh (Ø 9 nm) in H_2O

Au-MUDA NPs with Ø 9 nm (1 ml) diluted with demin. H_2O (9 ml), EDC · HCl (8 mg, 42 µmol), NHS (5 mg, 44 µmol), CCh (8 mg, 44 µmol), NEt_3 (3 drops)

The NP dispersion was purified *via* dialysis against demin. H_2O (in MWCO 12000, 6 × 2 h). A pink, clear NP dispersion with a concentration of 28.7 nM was obtained and stored at 4 °C in the dark.

^{1}H-NMR (600 MHz, D_2O): δ/ppm = 4.53–4.49 (m, 2 H, CH_2), 3.73–3.69 (m, 2 H, CH_2), 3.20 (s, 9 H, CH_3), 2.37–2.32 (m, 4 H, CH_2), 1.94–1.87 (m, 2 H, CH_2), 1.68–1.61 (m, 2 H, CH_2), 1.36–1.02 (m, 12 H, CH_2); **IR** (ATR): ν/cm^{-1} = 3326 (ν_{O-H}), 3035 (ν_{N-H}), 2978(ν_{C-H}), 1730 ($\nu_{C=O}$), 1648, 1554 (δ_{N-H}), 1435 (δ_{C-H}), 1399 (ν_{C-N}), 1222, 1051 (ν_{C-O}), 927, 835, 800, 698 (ν_{C-S}), 663 (δ_{O-C-N}), 618, 526; **TEM**: d = 9.0 ± 0.9 nm; **UV/Vis**: λ_{max} = 542 nm; **DLS**: d_{hydr} = 25 ± 3 nm.

5.5.2 BIOFUNCTIONALISATION *VIA* PARALLEL ROUTE

5.5.2.1 Ligand Syntheses

Synthesis of MUDA-NA

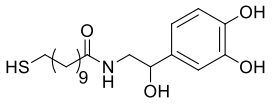

(according to a method of Abed *et al*.[301])

MUDA (52 mg, 0.24 mmol, 1.0 eq.) and NHS (22 mg, 0.19 mmol, 0.8 eq.) were dissolved in anhydrous DMF (4 ml). The coupling reagent DIC (43 µl, 0.28 mmol, 1.2 eq.) was added quickly and the solution was stirred at room temperature for 4 h under argon atmosphere. K_2CO_3 (35 mg, 0.26 mmol, 1.1 eq.) in degassed water (0.5 ml) was added to a solution of NA (75 mg, 0.24 mmol, 1.0 eq.) in anhydrous DMF (0.5 ml), which was then quickly added to the reaction solution and stirred at room temperature for 16 h under argon atmosphere. During the work-up, the reaction mixture was filtered, demin. H_2O (5 ml, pH = 5 [with $NaHSO_4$]) was added and the solution was extracted with EtOAc (3 × 10 ml). The combined organic layers were washed with demin. H_2O (15 ml), dried over Na_2SO_4 and filtered. The solvent was evaporated and the residue was purified *via* column chromatography (EtOAc/$CHCl_3$ 4:1). The product could be obtained as a colourless solid in a moderate yield (57 mg, 67%) and was stored at 4 °C in the dark.

^{1}H-NMR (499 MHz, DMSO-d_6): δ/ppm = 8.88-8.61 (m, 2 H, O*H*), 7.73 (t, *J* = 6.3 Hz,1 H, N*H*), 6.72 (s, 1 H, C*H*), 6.65 (d, *J* = 8.2 Hz, 1 H, C*H*), 6.54 (d, *J* = 8.2 Hz, 1 H, C*H*), 5.20 (s, 1 H, O*H*), 4.41-4.36 (m, 1 H, C*H*), 3.23-3.16 (m, 1 H, S*H*), 2.48-2.43 (m, 2 H, CH_2), 2.04 (t, *J* = 7.4 Hz,2 H, CH_2), 1.56-1.49 (m, 2 H, CH_2), 1.48-1.41 (m, 2 H, CH_2), 1.36-1.29 (m, 2 H, CH_2), 1.28-1.17 (m, 12 H, CH_2); **^{13}C{^{1}H} NMR** (100 MHz, $CDCl_3$): δ/ppm = 173.0, 145.3, 144.6, 135.2, 115.5, 113.8, 71.6, 47.4, 36.3, 34.1, 29.5, 29.4, 29.3, 29.3, 29.2, 29.1, 28.9, 25.7, 24.2; **IR** (ATR): ν/cm^{-1} = 3334 (ν_{N-H}, ν_{O-H}),2969, 2919 (ν_{C-H}), 2846, 1735 ($\nu_{C=O}$), 1608 (δ_{N-H}), 1558 (ν_{C-H} + δ_{C-N-H}), 1455 ($\nu_{C=C}$), 1383 (δ_{C-H}), 1361 (δ_{O-H}), 1242 (δ_{C-N}), 1170 (ν_{C-O}), 866, 795 (δ_{C-H}), 622 (ν_{C-S}); **ESI-MS (*m/z*):** [M-H]$^-$ = 368.20 (calcd: [M-H]$^-$ = 368.53); **Elemental Analysis:** Anal. Calcd for $(C_{19}H_{31}NO_4S)_1(C_7H_{16}N_2O)_{1.5}$: C, 60.48; H, 9.46; N, 9.56; S, 5.47. Found: C, 59.63; H, 10.20; N, 10.85; S, 5.07.

Synthesis of MUDA-ADR

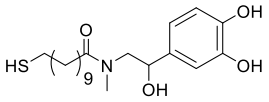

MUDA (131 mg, 0.6 mmol, 1.0 eq.) and NHS (55 mg, 0.48 mmol, 0.8 eq.) were dissolved in anhydrous DMF (4 ml). The coupling reagent DIC (112 µL, 0.72 mmol, 1.2 eq.) was added quickly and the solution was stirred at room temperature for 4 h under argon atmosphere. K_2CO_3 (91 mg, 0.66 mmol, 1.1 eq.) in degassed water (0.5 ml) was added to a solution of ADR (200 mg, 0.6 mmol, 1.0 eq.) in anhydrous DMF (0.5 ml), which was then quickly added to the reaction solution and stirred at room temperature for 16 h under argon atmosphere. During the work-up, the reaction mixture was filtered, demin. H_2O (5 ml, pH = 5 [with $NaHSO_4$]) was added and the solution was extracted with EtOAc (3 × 10 ml). The combined organic layers were washed with demin. H_2O (15 ml), dried over Na_2SO_4 and filtered. The solvent was evaporated and the residue was purified *via* column chromatography (EtOAc/$CHCl_3$ 4:1). The product could be obtained as a colourless solid in a moderate yield (175 mg, 76%) and was stored at 4 °C in the dark.

^{1}H-NMR (499 MHz, DMSO-d_6): *δ*/ppm = 8.83-8.78 (m, 1 H, O*H*), 8.77-8.67 (m, 1 H, O*H*), 6.76-6.72 (m, 1 H, C*H*), 6.69-6.64 (m, 1 H, C*H*), 6.59-6.52 (m, 1 H, C*H*), 5.34-5.11 (m, 1 H, O*H*), 4.58-4.51 (m, 1 H, C*H*), 3.24-3.16 (m, 1 H, S*H*), 2.88-2.78 (m, 3 H, CH_3), 2.48-2.42 (m, 2 H, CH_2), 2.23-2.16 (m, 2 H, CH_2), 1.57-1.44 (m, 4 H, CH_2), 1.36-1.29 (m, 2 H, CH_2), 1.28-1.19 (m, 12 H, CH_2); **^{13}C{^{1}H} NMR** (100 MHz, $CDCl_3$): δ/ppm = 180.3, 119.2, 119.1, 115.5, 115.3, 53.2, 47.2, 37.3, 36.4, 33.4, 33.2, 32.6, 31.5, 30.4, 29.3, 28.7, 28.6, 27.0, 25.3, 24.7; **IR** (ATR): *ν*/cm^{-1} = 3336 (ν_{N-H}, ν_{O-H}),2964, 2925 (ν_{C-H}), 2848, 1735 ($\nu_{C=O}$), 1621 (δ_{N-H}), 1564, 1456 ($\nu_{C=C}$), 1361 (δ_{O-H}), 1240 (δ_{C-N}), 1162 (ν_{C-O}), 617 (ν_{C-S}); **ESI-MS (*m/z*):** [M-H]$^-$ = 368.20 (calcd: [M-H]$^-$ = 368.53); **Elemental Analysis:** Anal. Calcd for $(C_{20}H_{33}NO_4S)_1(C_7H_{16}N_2O)_{1.5}$: C, 61.07; H, 9.58; N, 9.34; S, 5.34. Found: C, 60.31; H, 9.91; N, 10.27; S, 5.53.

Synthesis of MUDA-SB

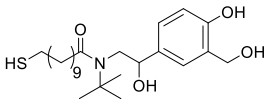

MUDA (57 mg, 0.26 mmol, 1.0 eq.) and NHS (24 mg, 0.21 mmol, 0.8 eq.) were dissolved in anhydrous DMF (4 ml). The coupling reagent DIC (48 µl, 0.31 mmol, 1.2 eq.) was added quickly and the solution was stirred at room temperature for 4 h under argon atmosphere. K_2CO_3 (40 mg, 0.29mmol, 1.1 eq.) in degassed water (0.5 ml) was added to a solution of SB sulfate (150 mg, 0.26 mmol, 1.0 eq.) in anhydrous DMF (0.5 ml), which was then quickly added to the reaction solution and stirred at room temperature for 16 h under argon atmosphere. During the work-up, the reaction mixture was filtered, demin. H_2O (5 ml, pH = 5 [with $NaHSO_4$]) was added and the solution was extracted with EtOAc (3 × 10 ml). The combined organic layers were washed with demin. H_2O (15 ml), dried over Na_2SO_4 and filtered. The solvent was evaporated and the residue was purified *via* column chromatography (EtOAc/$CHCl_3$ 4:1). The product could be obtained as a colourless solid in a modest yield (30 mg, 23%) and was stored at 4 °C in the dark.

^{1}H-NMR (499 MHz, DMSO-d_6): *δ*/ppm = 7.20-7.08 (m, 1 H, C*H*), 7.05-6.81 (m, 1 H, C*H*), 6.74-6.51 (m, 1 H, C*H*), 5.59-5.43 (m, 3 H, O*H*), 4.49-4.41 (m, 1 H, C*H*), 2.87-2.61 (m, 5 H, CH_2, S*H*), 2.40-2.21 (m, 2 H, CH_2), 2.19-2.05 (m, 2 H, CH_2), 1.65-1.41 (m, 4 H, CH_2), 1.39-1.19 (m, 14 H, CH_2), 1.15 (s, 9 H, CH_3); **IR** (ATR): *ν*/cm^{-1} = 3331 (ν_{N-H}, ν_{O-H}), 2964, 2926, 2842 (ν_{C-H}), 1693, 1621 ($\nu_{C=O}$), 1561, 1467 ($\nu_{C=C}$), 1368 (δ_{O-H}), 1245 (δ_{C-N}), 1161 (ν_{C-O}), 1118, 1033 (ν_{C-O}), 1009, 868 (δ_{C-H}), 812 (δ_{C-H}), 764, 616 (ν_{C-S}); **ESI-MS (*m/z*):** [M-H]$^-$ = 438.29 (calcd: [M-H]$^-$ = 439.28)

Synthesis of MUDA-SB

MUDA (121 mg, 0.55 mmol, 1.0 eq.) was dissolved in anhydrous DMF (5 ml) and cooled to 0 °C. NEt_3 (229 µl, 1.65 mmol, 3 eq.) was added and stirred for 5 min. HATU (418 mg, 1.10 mmol, 2.0 eq.) and SB sulfate (160 mg, 0.55 mmol, 1.0 eq.) dissolved in anhydrous DMF (5 ml) were added quickly and the solution was stirred at room temperature for 6 d under argon atmosphere. During the work-up, the colourless precipitate was filtered off, demin. H_2O (10 ml, pH = 5 [with $NaHSO_4$]) was added and the solution was extracted with EtOAc (3 × 10 ml). Afterwards, the aqueous layer was extracted with DCM (3 × 10 ml). The organic layers were separately washed with demin. H_2O (15 ml), dried over Na_2SO_4 and filtered. The solvent was evaporated and a brown solid was obtained and stored at 4 °C in the dark. ESI-MS indicated that no desired product species were present in the residues.

Synthesis of MUDA-AT

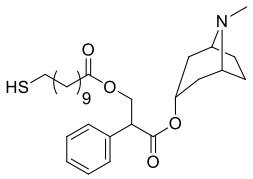

(according to a method by Steglich *et al.*[308])

MUDA (150 mg, 0.69 mmol, 1.0 eq.) was dissolved in anhydrous DCM (10 ml). DMAP (9 mg, 0.07 mmol, 0.1 eq.) was added under argon counter flow and stirred at 0 °C. DIC (150 µL, 0.97 mmol 1.4 eq.) was added quickly and stirred for 5 min at 0 °C. Then, AT (200 mg, 0.69 mmol, 1.0 eq.) was added and stirred for 15 min at 0 °C. Afterwards, the reaction mixture was stirred at room temperature for 16 h under argon atmosphere. During the work-up process, the reaction mixture was filtered and the solvent was evaporated. The residue was redissolved in DCM and washed with diluted HCl (2 × 10 ml) and with saturated $NaHCO_3$ solution (10 ml). The combined organic layers were dried over Na_2SO_4, filtered and the solvent was evaporated. The crude product was purified over a silica plug (eluted with DCM). The product could be obtained as a colourless solid in a good overall yield (283 mg, 84%) and was stored at 4 °C in the dark.

^{1}H-NMR (400 MHz, $CDCl_3$): δ/ppm = 7.30-7.18 (m, 5 H, C*H*), 5.23 (s, 1 H, C*H*), 4.99-4.93 (m, 1 H, C*H*), 4.53 (t, *J* =9.3 Hz, 1 H, C*H*), 4.23 (t, *J* = 6.7 Hz, 1 H, C*H*), 2.60 (t, *J* = 6.7 Hz, 2 H, CH_2), 2.27 (s, 3 H, CH_3), 2.33-2.12 (m, 4 H, CH_2), 1.85-1.67 (m, 4 H, CH_2), 1.63-1.41 (m, 6 H, CH_2), 1.36-1.10 (m, 10 H, CH_2); **^{13}C{^{1}H} NMR** (100 MHz, $CDCl_3$): δ/ppm = 172.2, 169.5, 133.9, 127.9, 127.8, 127.0, 126.6, 66.5, 63.5, 58.6, 50.0, 35.6, 35.2, 33.9, 31.86, 28.6, 28.4, 28.2, 27.8, 27.5, 27.3, 24.9, 24.6; **IR** (ATR): ν/cm^{-1} = 3335, 2921, 2842 (ν_{C-H}), 1730 ($\nu_{C=O}$), 1695 ($\nu_{C=O}$), 1558, 1542 ($\nu_{C=C}$), 1465, 1390, 1360 (δ_{C-H}), 1250 (δ_{C-O}), 1166 (δ_{C-O}), 1029 (ν_{C-N}), 773 (δ_{C-H}), 729 (ν_{C-S}), 700 (δ_{C-H}), 632 (δ_{C-H}); **ESI-MS (*m/z*):** $[M-H]^-$= 488.23 (calcd: $[M-H]^-$ = 488.28); **Elemental Analysis:** Anal. Calcd for MUDA-AT: C, 68.67; H, 8.85; N, 2.86; S, 6.55. Found: C, 58.70; H, 9.40; N, 6.98; S, 5.39.

5.5.2.2 Surface Functionalisation: General Procedure of a Ligand Exchange Reaction (air sensitive)

(according to a procedure by Mattern *et al.*[304])

The Au NP dispersion was filtrated using syringe filtration on a cellulose membrane with 0.2 µm pore size. Then, the NP dispersion was degassed with argon for 45-90 min. The ligand (as a solid or dissolved) was added slowly. The pH of the NP dispersion was adjusted by the addition of acid or base to achieve a stable clear dispersion, which was stirred at room temperature for a certain time under argon before purification took place.

Synthesis of Au-MUDA-NA (Ø 10 nm) in H_2O

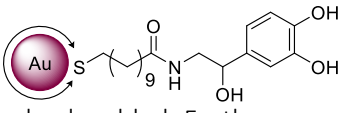

Au-MUDA NPs with Ø 10 nm (2 ml) were diluted in H_2O (7 ml) and purged with argon for 45 min. MUDA-NA (25 mg, 70 µmol) in DMSO (0.3 ml) was slowly added. Furthermore, NEt_3 (0.1 ml) was added to ensure a stable NP dispersion, which was stirred for 16 h at room temperature. Then, the NP dispersion was purified *via* dialysis stepwise against H_2O (in MWCO 12000, 28 h). A pink, clear NP dispersion with a concentration of 35 nM was obtained and stored at 4 °C in the dark.

^{1}H-NMR (400 MHz, D_2O): δ/ppm = 6.77 (s, 1 H, C*H*), 6.72-6.65 (m, 1 H, C*H*), 6.58-6.48 (m, 1 H, C*H*), 4.60-4.51 (m, 1 H, C*H*), 2.58-2.46 (m, 2 H, CH_2), 2.24-2.07 (m, 2 H, CH_2), 1.74-1.65 (m, 2 H, CH_2), 1.58-1.48 (m, 4 H, CH_2), 1.38-1.16 (m, 12 H, CH_2); **IR** (ATR): ν/cm^{-1} =3333 (ν_{O-H}), 2972, 2913 (ν_{C-H}), 2846, 1697 ($\nu_{C=O}$), 1615 (δ_{N-H}), 1571 (ν_{C-H} + $\delta_{C-N-H)}$, 1457 ($\nu_{C=C}$), 1376 (δ_{C-H}), 1360 (δ_{O-H}), 1248 (δ_{C-N}), 1165 (ν_{C-O}), 963, 790 (δ_{C-H}), 625 (ν_{C-S}) ; **TEM**: d = 9.9 ± 0.8 nm; **UV/Vis**: λ_{max} = 528 nm; **DLS**: d_{hydr} = 17 ± 4 nm.

Synthesis of Au-MUDA-ADR (Ø 8 nm) in H_2O

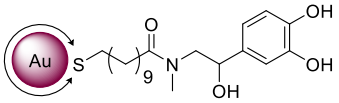

Au-MUDA NPs with Ø 8 nm (5 ml) diluted in demineralised H_2O (5 ml), MUDA-ADR (25 mg, 65 µmol) in DMSO (0.5 ml), NEt_3 (3 drops)

The NP dispersion was stirred at room temperature for 16 h and directly purified *via* dialysis against demineralised H_2O (in MWCO 12000, 6 × 2 h). A violet, clear NP dispersion with a concentration of 157 nM was obtained and stored at 4 °C in the dark.

^{1}H-NMR (600 MHz, D_2O): δ/ppm = 6.81 (s, 1 H, C*H*), 6.77-6.69 (m, 1 H, C*H*), 6.58-6.51 (m, 1 H, C*H*), 4.72-4.66 (m, 1 H, C*H*), 2.92-2.82 (m, 3 H, CH_3), 2.70-2.63 (m, 2 H, CH_2), 2.26-2.10 (m, 2 H, CH_2), 1.58-1.46 (m, 4 H, CH_2), 1.42-1.35 (m, 2 H, CH_2), 1.34-1.20 (m, 12 H, CH_2); **IR** (ATR): ν/cm^{-1} = 3334 (ν_{N-H}, ν_{O-H}), 2921 (ν_{C-H}), 2839, 1691 ($\nu_{C=O}$), 1615 (δ_{N-H}), 1540 (ν_{C-H} + $\delta_{C-N-H)}$, 1457 ($\nu_{C=C}$), 1406 (δ_{C-H}), 1368 (δ_{O-H}), 1255 (δ_{C-N}), 1203 (ν_{C-O}), 1128, 1008, 990, 827, 715 (δ_{C-H}), 648 (ν_{C-S}); **TEM**: d = 8.1 ± 0.6 nm; **UV/Vis**: λ_{max} = 526 nm; **DLS**: d_{hydr} = 17 ± 5 nm.

Synthesis of Au-MUDA-ADR (Ø 9 nm) in H_2O

Au-MUDA NPs with Ø 9 nm (7 ml) diluted in demineralised H_20 (3 ml), MUDA-ADR (15 mg + 10 mg, 65 µmol), NEt_3 (2 drops)

After degassing of the NP dispersion, MUDA-ADR (15 mg in 0.2 ml DMSO) was slowly added and the reaction mixture was stirred at room temperature for 16 h. Further MUDA-ADR (10 mg in 0.2 ml DMSO) was added dropwise and stirred at room temperature for 5 h. Then, the NP dispersion was purified *via* dialysis against demineralised H_2O (in MWCO 12000, 47 h). A pink, clear NP dispersion with a concentration of 191 nM was obtained and stored at 4 °C in the dark.

TEM: d = 8.9 ± 0.8 nm; **UV/Vis**: λ_{max} = 525 nm; **DLS**: d_{hydr} = 13 ± 3 nm.

Synthesis of Au-MUDA-ADR (Ø 10 nm) in H_2O

Au-MUDA NPs with Ø 10 nm (5 ml) diluted in demineralised H_2O (5 ml), MUDA-ADR (30 mg, 78 µmol) in DMSO (0.5 ml), NEt_3 (3 drops)

The NP dispersion was stirred at room temperature for 16 h and directly purified *via* dialysis against demineralised H_2O (in MWCO 12000, 15 × 2 h). A violet, clear NP dispersion with a concentration of 101 nM was obtained and stored at 4 °C in the dark.

TEM: d = 9.9 ± 0.9 nm; **UV/Vis**: λ_{max} = 523 nm; **DLS**: d_{hydr} = 13 ± 5 nm.

Synthesis of Au-MUDA-ADR (Ø 14 nm) in H_2O

Au-Citrate NPs with Ø 14 nm (10 ml), MUDA-ADR (20 mg, 52 µmol) in DMSO (0.5 ml), NEt_3 (2 drops)

The NP dispersion was stirred at room temperature for 16 h and directly purified *via* dialysis against demineralised H_2O (in MWCO 12000, 6 × 2 h). A pink, clear NP dispersion with a concentration of 7.1 nM was obtained and stored at 4 °C in the dark.

TEM: d = 13.9 ± 1.2 nm; **UV/Vis**: λ_{max} = 525 nm; **DLS**: d_{hydr} = 16 ± 5 nm.

Synthesis of Au-MUDA-AT (Ø 8 nm) in H_2O

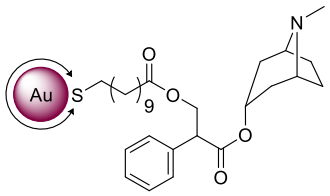

Au-MUDA NPs with Ø 10 nm (3.5 ml) diluted in demin. H_20 (6 ml), MUDA-AT (35 mg, 72 µmol) in DMSO (0.5 ml), NEt_3 (3 drops)

The NP dispersion was purified *via* dialysis against demin. H_2O (in MWCO 12000, 5 × 2 h). A pink, clear NP dispersion with a concentration of 139 nM was obtained and stored at 4 °C in the dark.

^{1}H-NMR (600 MHz, D_2O): δ/ppm = 7.43-7.19 (m, 5 H, C*H*), 5.45 (s, 1 H, C*H*), 4.47-4.30 (m, 1 H, C*H*), 4.00-3.84 (m, 1 H, C*H*), 3.80-3.75 (m, 1 H, C*H*), 3.17-2.89 (m, 2 H, CH_2), 2.56 (s, 3 H, CH_3), 2.46-2.38 (m, 4 H, CH_2), 2.27-1.99 (m, 8 H, CH_2), 1.63-1.49 (m, 6 H, CH_2), 1.42-1.15 (m, 10 H, CH_2); **IR** (ATR): ν/cm^{-1} = 3308 (ν_{O-H}), 2921, 2841 (ν_{C-H}), 1695 ($\nu_{C=O}$), 1646 ($\nu_{C=O}$), 1557 ($\nu_{C=C}$), 1448, 1417 (δ_{C-H}), 1250 (δ_{C-O}), 1184 (δ_{C-O}), 1029 (ν_{C-N}), 813 (δ_{C-H}), 729 (ν_{C-S}), 700 (δ_{C-H}); **TEM**: d = 8.0 ± 0.8 nm; **UV/Vis**: λ_{max} = 530 nm; **DLS**: d_{hydr} = 29 ± 8 nm.

Synthesis of Au-MUDA-AT (Ø 10 nm) in H_2O

Au-MUDA NPs with Ø 10 nm (1 ml) diluted in demin. H_2O (9 ml), MUDA-AT (25 mg, 36 µmol) in DMSO (0.4 ml), NEt_3 (3 drops)

After degassing of the NP dispersion, MUDA-AT (15 mg in 0.2 ml DMSO) was slowly added. To ensure a stable dispersion, NEt_3 (3 drops) was added and the reaction mixture was stirred at room temperature for 45 min. Further MUDA-AT (10 mg in 0.2 ml DMSO) was added dropwise and the mixture was stirred at room temperature for 72 h. Then, the NP dispersion was purified *via* dialysis against demin. H_2O (in MWCO 6000, 6 × 2 h). A pink, clear NP dispersion with a concentration of 19.0 nM was obtained and stored at 4 °C in the dark.

TEM: d = 9.7 ± 0.9 nm; **UV/Vis**: λ_{max} = 530 nm; **DLS**: d_{hydr} = 33 ± 4 nm.

Synthesis of Au-MUDA-AT (Ø 11 nm) in H_2O

Au-Citrate NPs with Ø 11 nm (10 ml), MUDA-AT (25 mg, 36 µmol) in DMSO (0.4 ml), NEt_3 (3 drops)

After degassing of the NP dispersion, MUDA-AT (15 mg in 0.2 ml DMSO) was slowly added. To ensure a stable dispersion NEt_3 (3 drops) was added and the reaction mixture was stirred at room temperature for 45 min. Further MUDA-AT (10 mg in 0.2 ml DMSO) was added dropwise and stirred at room temperature for 72 h. Then NP dispersion was purified *via* dialysis against demin. H_2O (in MWCO 6000, 6 × 2 h). A pink, clear NP dispersion with a concentration of 15.2 nM was obtained and stored at 4 °C in the dark.

TEM: d = 11.2 ± 1.1 nm; **UV/Vis**: λ_{max} = 523 nm; **DLS**: d_{hydr} = 31 ± 5 nm.

Synthesis of Au-MUDA-AT (Ø 12 nm) in H_2O

Au-Citrate NPs with Ø 12 nm (10 ml), MUDA-AT (40 mg, 82 µmol) in DMSO (0.2 ml), diluted NaOH (5 drops)

The NP dispersion was purified *via* dialysis against demin. H_2O (in MWCO 12000, 3 × 2 h). A pink, clear NP dispersion with a concentration of 11 nM was obtained and stored at 4 °C in the dark.

TEM: d = 12.0 ± 1.0 nm; **UV/Vis**: λ_{max} = 529 nm; **DLS**: d_{hydr} = 112 ± 59 nm.

Synthesis of Au-MUDA-AT (Ø 13 nm) in H_2O

Au-Citrate NPs with Ø 13 nm (10 ml), MUDA-AT (30 mg, 61 µmol) in DMSO (0.2 ml), NEt_3 (5 drops)

The NP dispersion was purified *via* dialysis against demin. H_2O (in MWCO 12000, 9 × 2 h). A pink, clear NP dispersion with a concentration of 8.7 nM was obtained and stored at 4 °C in the dark.

TEM: d = 12.9 ± 1.0 nm; **UV/Vis**: λ_{max} = 528 nm; **DLS**: d_{hydr} = 105 ± 42 nm.

Synthesis of Au-MUDA-AT (Ø 14 nm) in H_2O

Au-Citrate NPs with Ø 14 nm (10 ml), MUDA-AT (30 mg, 61 µmol) in DMSO (0.2 ml), NEt_3 (5 drops)

The NP dispersion was purified *via* dialysis against demin. H_2O (in MWCO 6000, 9 × 2 h). A pink, clear NP dispersion with a concentration of 7.5 nM was obtained and stored at 4 °C in the dark.

TEM: d = 14.0 ± 1.0 nm; **UV/Vis**: λ_{max} = 527 nm; **DLS**: d_{hydr} = 31 ± 13 nm.

Synthesis of Au-MUDA-AT (Ø 16 nm) in H_2O

Au-Citrate NPs with Ø 16 nm (10 ml), MUDA-AT (30 mg, 61 µmol) in DMSO (0.5 ml), NEt_3 (3 drops)

The NP dispersion was purified *via* dialysis against demin. H_2O (in MWCO 6000, 5 × 2 h). A pink, clear NP dispersion with a concentration of 3.6 nM was obtained and stored at 4 °C in the dark.

TEM: d = 15.9 ± 1.1 nm; **UV/Vis**: λ_{max} = 528 nm; **DLS**: d_{hydr} = 53 ± 19 nm.

Synthesis of Au-MUDA-SB (Ø 13 nm) in H_2O

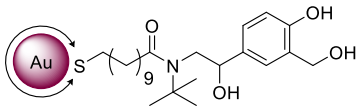

Au-Citrate NPs with Ø 13 nm (10 ml), MUDA-SB (20 mg, 46 µmol) in DMSO (0.2 ml), NEt_3 (2 drops)

The NP dispersion was stirred at room temperature for 16 h and directly purified *via* dialysis against demineralised H_2O (in MWCO 12000, 6 × 2 h). A pink, clear NP dispersion with a concentration of 8.1 nM was obtained and stored at 4 °C in the dark.

IR (ATR): $\tilde{\nu}$/cm^{-1} = 3373 ($\nu_{N\text{-}H}$, $\nu_{O\text{-}H}$), 2981, 2926 ($\nu_{C\text{-}H}$), 2849, 1711 ($\nu_{C=O}$), 1575 ($\nu_{C\text{-}H}$), 1443 ($\nu_{C=C}$), 1381 ($\delta_{O\text{-}H}$), 1225 ($\delta_{C\text{-}N}$), 1198 ($\nu_{C\text{-}O}$), 1081, 1033, 892, 840, 788 ($\delta_{C\text{-}H}$), 618 ($\nu_{C\text{-}S}$), 543 ($\nu_{C\text{-}N}$); **TEM**: d = 13.0 ± 1.0 nm; **UV/Vis**: λ_{max} = 531 nm; **DLS**: d_{hydr} = 18 ± 3 nm.

5.6 Amine stabilised Au NPs and Biomimetic Functionalisation

5.6.1.1 Ligand Synthesis

Preparation of 11-Hydroxyundecylphthalimide

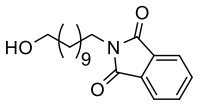

(according to a method by Perez *et al.*[312])

11-Bromoundecanol (4.09 g, 16.28 mmol, 1.0 eq.) was dissolved in anhydr. DMF (70 ml), potassium phthalimide (4.47 g, 24.14 mmol, 1.0 eq.) was added and the reaction mixture was heated to 75 °C for 16 h under argon atmosphere. The clear solution was cooled to room temperature and the colourless precipitate was removed by filtration. The filtrate was evaporated under reduced pressure, the residue was suspended in DCM (40 ml) and washed with demineralised H_2O (3 × 50 ml) and with brine (3 × 50 ml). The organic layer was dried over Na_2SO_4, filtered and the solvent was evaporated. The product could be obtained as a colourless crystalline solid in a very good yield (5.00 g, 15.76 mmol, 97%).

^{1}H-NMR (500 MHz, $CDCl_3$): δ/ppm = 7.84 (dd, *J* = 3.0, 5.5 Hz, 2 H, C*H*), 7.71 (dd, *J* = 3.0, 5.5 Hz, 2 H, C*H*), 3.67 (t, *J* = 7.3 Hz, 2H, CH_2N), 3.60 (t, *J* = 6.8 Hz, 2 H, CH_2O), 1.72-1.62 (m, 2 H, CH_2), 1.56 (q, 2 H, CH_2), 1.41-1.22 (m, 16 H, CH_2); **^{13}C{^{1}H} NMR** (125 MHz, $CDCl_3$): δ/ppm = 168.5, 133.9, 132.2, 123.2, 63.0, 38.1, 32.8, 30.9, 29.5, 29.4, 29.1, 28.6, 26.8, 25.7 ; **IR** (ATR): ν/cm^{-1} = 3548, 3498 (ν_{O-H}), 2919, 2848 (ν_{C-H}), 1770 (δ_{C-H}), 1702 ($\nu_{C=O}$), 1459 (δ_{O-H}), 1398 (δ_{C-H}), 1061 (ν_{N-H}), 718 (δ_{C-H}), 627, 527; **ESI-MS (*m/z*):** $[M+Na]^+$ = 340.19 (calcd: $[M+Na]^+$ = 340.20); **Elemental Analysis:** Anal. Calcd for $C_{19}H_{27}NO_3$: C, 71.89; H 8.57; N, 4.41. Found: C, 72.04; H, 8.66; N, 4.02.

Synthesis of 11-Bromoundecylphthalimide

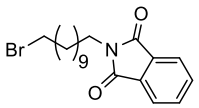

(according to a procedure by Jarboe *et al.*[313])

2-(11-Hydroxy-undecyl)-isoindole-1,3-dione (1.77 g, 5.58 mmol, 1 eq.) and tetrabromomethane (1.86 g, 5.61 mmol, 1.01 eq.) were dissolved in dry DCM (50 ml). Triphenylphosphine (1.65 g, 6.29 mmol, 1.13 eq.) was added under vigorous stirring and the reaction mixture was stirred at room temperature for 2 h under argon atmosphere. The solution was reduced *in vacuo* before Et_2O was added. The precipitate was filtered off and the concentrated filtrate was purified *via* column chromatography (eluted with hexane : ethyl acetate, 10:1; Rf = 0.36). The pure product could be obtained as a colourless solid in a good yield (1.67 g, 4.41 mmol, 70%).

^{1}H-NMR (500 MHz, $CDCl_3$): δ/ppm = 7.83 (dd, *J* = 2.8, 5.5 Hz, 2 H, C*H*), 7.70 (dd, *J* = 2.8, 5.5 Hz, 2 H, C*H*), 3.66 (t, *J* = 7.3 Hz, 2 H, CH_2N), 3.39 (t, *J* = 6.8 Hz, 2 H, CH_2Br), 1.83 (q, 2 H, CH_2), 1.65 (q, 2 H, CH_2), 1.40 (q, 2 H, CH_2), 1.36-1.21 (m, 12 H, CH_2); **^{13}C{^{1}H} NMR** (125 MHz, $CDCl_3$): δ/ppm = 168.5, 134.0, 132.1, 123.2, 38.1, 34.2, 33.6, 29.5, 28.6, 28.3, 26.9; **IR** (ATR): ν/cm^{-1} = 2919, 2845 (ν_{C-H}), 1770 (δ_{C-H}), 1697 ($\nu_{C=O}$), 1466, 1398 (δ_{C-H}), 1053 (ν_{N-H}), 866 ($\delta_{C=C}$), 722 (δ_{C-H}), 639 (ν_{C-Br}), 627, 524; **ESI-MS (*m/z*):** $[M+Na]^+$ = 404.0 (calcd: $[M+Na]^+$ = 404.1); **Elemental Analysis:** Anal. Calcd for $C_{19}H_{26}NOo_2Br$: C, 60.00; H 6.89; N, 3.68. Found: C, 60.22; H, 7.01; N, 3.29.

Synthesis of 1-[11-(N-phthalimido)]undecyl thioacetate

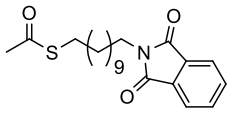

(according to a procedure by Wang *et al.*[315])

11-Bromoundecylphthalimide (0.61 g, 1.63 mmol, 1 eq.) was dissolved in anhydrous THF (20 ml) before potassium thioacetate (0.30 g, 2.62 mmol, 1.48 eq.) was added. The reaction mixture was heated to reflux for 24 h under argon atmosphere. After cooling down, demineralised H_2O (50 ml) was added and the mixture was stirred for 1 h. The product was extracted with EtOAc (5 × 30 ml). The combined organic layers were dried over Na_2SO_4, filtered and the solvent was removed *in vacuo*. The pure product was obtained as a brown solid in a very good yield (0.61 g, 1.63 mmol, 92%).

^{1}H-NMR (300 MHz, $CDCl_3$): *δ*/ppm = 7.83 (dd, *J* = 2.8, 5.5 Hz, 2 H, C*H*), 7.70 (dd, *J* = 2.8, 5.5 Hz, 2 H, C*H*), 3.67 (t, *J* = 7.3 Hz, 2 H, CH_2N), 2.85 (t, *J* = 7.4 Hz, 2 H, CH_2S), 2.31 (s, 3 H, CH_3), 1.66 (q, 2 H, CH_2), 1.54 (q, 2 H, CH_2), 1.41-1.15 (m, 14 H, CH_2); **^{13}C{^{1}H} NMR** (75 MHz, $CDCl_3$): δ/ppm = 196.1, 168.5, 134.0, 132.1, 123.2, 38.1, 30.6, 29.5, 29.4, 29.1, 28.8, 28.6, 26.8; **IR** (ATR): *ν*/cm^{-1} = 2916, 2850 ($\nu_{C\text{-}H}$), 1770 ($\delta_{C\text{-}H}$), 1681 ($\nu_{C=O}$), 1395 ($\delta_{C\text{-}H}$), 1105, 1046 ($\nu_{N\text{-}H}$), 961, 878 ($\delta_{C=C}$), 716 ($\delta_{C\text{-}H}$), 624 ($\nu_{C\text{-}S}$), 535; **ESI-MS (*m/z*):** $[M+H]^+$ = 376.1 (calcd: $[M+H]^+$ = 376.2); **Elemental Analysis:** Anal. Calcd for $C_{21}H_{29}NO_3S$: C, 67.17; H 7.78; N, 3.73; S, 8.54. Found: C, 67.18; H, 2.61; N, 2.50; S, 9.10.

Synthesis of 11-Mercaptoundecylamine (MUAM)

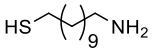

(according to a method described by Wang *et al.*[315])

1-[11-(N-phthalimido)]undecyl thioacetate (0.89 g, 2.36 mmol, 1 eq.) was dissolved in dry EtOH (90 ml) and cooled to 0 °C. Hydrazine hydrate (0.45 g, 0.44 ml, 9.00 mmol, 4 eq.) was added slowly and the reaction mixture was heated to 85 °C for 24 h. After cooling down, the reaction mixture was adjusted to pH 1 and extracted with DCM (3 × 50 ml). Now the pH was adjusted to 13, and it was further extracted with DCM (5 × 50 ml). The combined organic phase was dried over Na_2SO_4, filtered and the solvent was removed *in vacuo*. The pure product could be obtained as a slightly brown solid in a good yield (0.36 g, 1.77 mmol, 75%) and was stored at 4 °C in the dark.

^{1}H-NMR (600 MHz, $CDCl_3$): *δ*/ppm = 5.94 (s, 3 H, NH_2, S*H*), 2.51 (t, *J* = 7.2 Hz, 2 H, CH_2S), 1.68 (m, 2 H, CH_2) 1.59 (q, 2 H, CH_2), 1.47-1.12 (m, 18 H, CH_2); **^{13}C{^{1}H} NMR** (125 MHz, $CDCl_3$): δ/ppm = 40.6, 40.2, 29.5, 34.0, 29.5, 29.4, 29.1, 29.0, 28.3, 26.6, 24.6; **IR** (ATR): *ν*/cm^{-1} = 3367, 3194 ($\nu_{N\text{-}H}$), 2916, 2845 ($\nu_{C\text{-}H}$), 2550($\nu_{S\text{-}H}$), 1657, 1513 ($\delta_{N\text{-}H}$), 1143 ($\nu_{C\text{-}N}$), 624 ($\nu_{C\text{-}S}$); **ESI-MS (*m/z*):** $[M+H]^+$ = 204.2 (calcd: $[M+H]^+$ = 204.2); **Elemental Analysis:** Anal. Calcd for $C_{11}H_{25}NS$: C, 64.96; H 12.39; N, 6.89; S, 15.76. Found: C, 44.16; H, 8.32; N, 6.10; S, 11.10.

5.6.1.2 Nanoparticle Syntheses

Direct Synthesis of Au-Cys (Ø 46 nm)

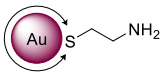

(according to a method described by Lee *et al*.[309])

$HAuCl_4 \cdot 3\ H_2O$ (8.3 mg, 21 µmol, 1.0 eq.) was dissolved in H_2O (14 ml) and CA · HCl (3.6 mg, 32 µmol, 1.5 eq.) was added and stirred at room temperature in the dark for 20 min. 0.001 M $NaBH_4$ solution (375 µl, 0.38 µmol, 0.18 eq.) was added quickly under vigorous stirring and the reaction mixture was stirred at room temperature in the dark for 16 h. Then, the violet NP dispersion was purified *via* dialysis against H_2O (in MWCO 12000, for 3 × 2 h). A dark violet NP dispersion was obtained and stored at 4 °C in the dark, but was not stable over time.

TEM: d = 46.5 ± 3.4 nm

Syntheses of 4-Aminothiophenol (ATP) coordinated Gold Nanoparticles

Direct Synthesis of Au-ATP (Ø 8 nm)

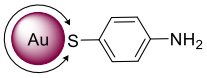

PPh_3AuCl (9 mg, 18 µmol, 1.0 eq.) was dissolved in DMSO (4 ml) and a solution of ATP (1.3 mg, 11 µmol, 0.6 eq.) dissolved in DMSO (0.5 ml) was added. The mixture was heated to 60 °C and a solution of ^{t}Bu-amine borane complex (14 mg, 160 µmol, 8.9 eq.) in DMSO (0.5 ml) was added quickly under vigorous stirring. The dark red dispersion was stirred at 60 °C for 1 h in the dark and cooled in an ice bath. Then, the NP dispersion was purified *via* dialysis stepwise against H_2O (in MWCO 12000, for 36 h). A pink violet, stable NP dispersion with a concentration of 238 nM was obtained and stored at 4 °C in the dark.

^{1}H-NMR (600 MHz, **DMSO-d$_6$**): δ/ppm = 7.55 (d, J = 9.0 Hz, 2 H, C*H*), 7.23 (d, J = 9.0 Hz, 2 H, C*H*); **IR** (ATR): ν/cm^{-1} = 3450, 3329 ($\nu_{N\text{-}H}$), 2980, 2889, 3329 ($\nu_{C\text{-}H}$; DMSO), 1973 ($\delta_{C\text{-}H}$), 1581 ($\delta_{N\text{-}H}$), 1463, 1392, 1303 ($\nu_{C\text{-}N}$), 1206, 1147, 1073 ($\nu_{S=O}$; DMSO), 825 ($\delta_{C\text{-}H}$), 689, 565 ($\nu_{C\text{-}S}$), 547; **TEM**: d = 7.9 ± 0.8 nm; **UV/Vis**: λ_{max} = 537 nm; **DLS**: d_{hydr} = 45 ± 8 nm.

Direct Synthesis of Au-ATP (Ø 6 nm)

PPh_3AuCl (12 mg, 24 µmol, 1.0 eq.) was dissolved in DMSO (3.5 ml) and a solution of ATP (3 mg, 24 µmol, 1.0 eq.) dissolved in DMSO (0.5 ml) was added. The mixture was heated to 60 °C and a solution of ^{t}Bu-amine borane complex (20 mg, 230 µmol, 9.6 eq.) in DMSO (1.0 ml) was added quickly under vigorous stirring. The dark red dispersion was stirred at 60 °C for 1 h in the dark and cooled in an ice bath. Then, NP dispersion was purified *via* dialysis against DMSO (in MWCO 12000, for 3 × 2 h) and afterwards stepwise against H_2O (in MWCO 12000, for 3 × 2 h). A violet, stable NP dispersion with a concentration of 570 nM was obtained and stored at 4 °C in the dark.

TEM: d = 5.8 ± 0.8 nm; **UV/Vis**: λ_{max} = 538 nm; **DLS**: d_{hydr} = 100 ± 15 nm.

Syntheses of Mercaptoundecylamine (MUAM) coordinated Gold Nanoparticles

Direct Synthesis of Au-MUAM (Ø 11 nm)

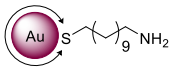

PPh_3AuCl (9 mg, 18 µmol, 1.0 eq.) was dissolved in DMSO (2 ml) and a solution of MUAM (4 mg, 20 µmol, 1.1 eq.) dissolved in DMSO (0.5 ml) was added. The mixture was heated to 60 °C and a solution of ^{t}Bu-amine borane complex (15 mg, 173 µmol, 9.6 eq.) in DMSO (0.5 ml) was added quickly under vigorous stirring. The dark red dispersion was stirred at 60 °C for 1 h in the dark and cooled in an ice bath. Then, the particles were precipitated with CH_3CN and centrifuged (1 h, 7000 rpm). The supernatant was discarded and the dark residue was redispersed in H_2O (5 ml). Semi concentrated HCl (1 drop) was added to obtain a violet, clear and stable NP dispersion, which was purified *via* dialysis against H_2O (in MWCO 12000, for 2 × 2.5 h). A violet, stable NP dispersion with a concentration of 95 nM was obtained and stored at 4 °C in the dark.

^{1}H-NMR (600 MHz, **D_2O**): δ/ppm = 4.41 (m, 2 H, NH_2), 2.98 (m, 2 H, CH_2N), 2.52 (m, 2 H, CH_2S), 1.68 -1.54 (m, 4 H, CH_2), 1.43-1.16 (m, 14 H, CH_2); **IR** (ATR): ν/cm^{-1} = 3391 ($\nu_{N\text{-}H}$), 2919, 2836 ($\nu_{C\text{-}H}$), 1723 ($\delta_{N\text{-}H}$), 1487 ($\delta_{C\text{-}H}$), 1223, 1117 ($\nu_{C\text{-}N}$), 1041 ($\nu_{C\text{-}N}$), 606 ($\nu_{C\text{-}S}$); **TEM**: d = 10.7 ± 1.3 nm; **UV/Vis**: λ_{max} = 538 nm; **DLS**: d_{hydr} = 40 ± 19 nm.

Direct Synthesis of Au-MUAM (Ø 12 nm), solid reducing agent

PPh_3AuCl (10 mg, 20 µmol, 1.0 eq.) was dissolved in DMSO (2.5 ml) and a solution of MUAM (3 mg, 15 µmol, 0.8 eq.) dissolved in DMSO (0.5 ml) was added. The mixture was heated to 60 °C and the solid powder ^{t}Bu-amine borane complex (17 mg, 196 µmol, 9.8 eq.) was added quickly under vigorous stirring. The dark red dispersion was stirred at 60 °C for 1 h in the dark and cooled in an ice bath. Then, the NP dispersion was purified *via* dialysis stepwise against H_2O (in MWCO 12000, for 2 × 2.5 h). A violet, stable NP dispersion with a concentration of 135 nM was obtained and stored at 4 °C in the dark.

TEM: d = 11.7 ± 1.7 nm; **UV/Vis**: λ_{max} = 534 nm; **DLS**: d_{hydr} = 21 ± 5 nm.

Direct Synthesis of Au-MUAM (Ø 8 nm), solid reducing agent at 55 °C

PPh_3AuCl (10 mg, 20 µmol, 1.0 eq.) was dissolved in DMSO (2.5 ml) and a solution of MUAM (3 mg, 15 µmol, 0.8 eq.) dissolved in DMSO (0.5 ml) was added. The mixture was heated to 55 °C and the solid powder ^{t}Bu-amine borane complex (17 mg, 196 µmol, 9.8 eq.) was added quickly under vigorous stirring. The dark red dispersion was stirred at 55 °C for 1 h in the dark and cooled in an ice bath. Then, NP dispersion was centrifuged after adding of CH_3CN (30 min, 7000 rpm) and redispersed in H_2O (5 ml). The violet dispersion was further purified *via* dialysis against H_2O (in MWCO 6000, for 6 × 2 h). A violet, stable NP dispersion with a concentration of 255 nM was obtained and stored at 4 °C in the dark.

TEM: d = 8.0 ± 0.9 nm; **UV/Vis**: λ_{max} = 532 nm; **DLS**: d_{hydr} = 25 ± 8 nm.

Direct Synthesis of Au-MUAM (Ø 6 nm), at 55 °C

PPh_3AuCl (10 mg, 20 µmol, 1.0 eq.) was dissolved in DMSO (2.5 ml) and a solution of MUAM (3 mg, 15 µmol, 0.8 eq.) dissolved in DMSO (0.2 ml) was added. The mixture was heated to 55 °C and ^{t}Bu-amine borane complex (17 mg, 196 µmol, 9.8 eq.) dissolved in DMSO (0.3 ml) was added quickly under vigorous stirring. The dark red dispersion was stirred at 55 °C for 1 h in the dark and cooled in an ice bath. Then, the NP dispersion was centrifuged after adding of CH_3CN (30 min, 7000 rpm) and redispersed in H_2O (5 ml). The violet dispersion was further purified *via* dialysis against H_2O (in MWCO 6000, for 6 × 2 h). A violet, stable NP dispersion with a concentration of 522 nM was obtained and stored at 4 °C in the dark.

TEM: d = 6.3 ± 0.7 nm; **UV/Vis**: λ_{max} = 525 nm; **DLS**: d_{hydr} = 19 ± 4 nm.

Direct Synthesis of Au-MUAM (Ø 8 nm)

PPh_3AuCl (10 mg, 20 µmol, 1.0 eq.) was dissolved in DMSO (2 ml) and a solution of MUAM (10 mg, 20 µmol, 2.5 eq.) dissolved in DMSO (0.5 ml) was added. The mixture was heated to 60 °C and a solution of ^{t}Bu-amine borane complex (15 mg, 173 µmol, 8.6 eq.) in DMSO (0.5 ml) was added quickly under vigorous stirring. 4 drops of diluted HCl was added and the dark red dispersion was stirred at 40 °C for 2 h in the dark and cooled in an ice bath. Then, the particles were precipitated with CH_3CN and centrifuged (30 min, 8000 rpm). The supernatant was discarded, the dark residue was washed with CH_3CN 3 times (8000 rpm, 30 min) before it was redispersed in H_2O (5 ml). Semi concentrated HCl (1 drop) was added to obtain a violet, clear and stable NP dispersion, which was purified *via* dialysis against H_2O (in MWCO 12000, for 2 × 2.5 h). A violet, stable NP dispersion with a concentration of 196 nM was obtained and stored at 4 °C in the dark.

TEM: d = 7.8 ± 0.9 nm; **UV/Vis**: λ_{max} = 524 nm; **DLS**: d_{hydr} = 47 ± 16 nm.

Direct Synthesis of Au-MUAM (Ø 5 nm)

PPh_3AuCl (12 mg, 45 µmol, 1.0 eq.) was dissolved in DMSO (3.5 ml) and a solution of MUAM (10 mg, 49 µmol, 1.3 eq.) dissolved in DMSO (0.5 ml) was added. The mixture was heated to 45 °C and ^{t}Bu-amine borane complex (20 mg, 230 µmol, 5.1 eq.) dissolved in DMSO (1 ml) was added quickly under vigorous stirring. The dark red dispersion was stirred at 45 °C for 80 min in the dark and cooled in an ice bath. Then, NP dispersion was precipitated with CH_3CN: H_2O (2:1) and purified *via* centrifugation (3 times, 7000 rpm, 30 min). The residue was redispersed in H_2O (5 ml). Semi concentrated HCl (1 drop) was added to obtain a violet, clear and stable NP dispersion with a concentration of 697 nM which was stored at 4 °C in the dark.

TEM: d = 5.0 ± 0.7 nm; **UV/Vis**: λ_{max} = 524 nm; **DLS**: d_{hydr} = 64 ± 1 nm; **ζ potential:** ζ = -29.67 ± 1.16 mV.

Direct Synthesis of Au-MUAM (Ø 17 nm)

PPh_3AuCl (10 mg, 20 µmol, 1.0 eq.) was dissolved in DMSO (2 ml) and a solution of MUAM (4 mg, 20 µmol, 1.0 eq.) dissolved in DMSO (0.5 ml) was added. The mixture was heated to 60 °C and a solution of ^{t}Bu-amine borane complex (17 mg, 195 µmol, 9.8 eq.) in DMSO (0.5 ml) was added quickly under vigorous stirring. 4 drops of diluted HCl were added and the dark red dispersion was stirred at 60 °C for 1 h in the dark and cooled in an ice bath. Then, the particles were precipitated with CH_3CN and centrifuged (30 min, 8000 rpm). The supernatant was discarded, the dark residue was redispersed in H_2O and washed with EtOH three times (30 min, 8000 rpm). The residue was redispersed in in H_2O (6 ml). The pH was adjusted to 2 with semi concentrated HCl to obtain a violet, clear and stable NP dispersion which was purified *via* dialysis against H_2O (in MWCO 6000, for 5 × 2 h). A violet, stable NP dispersion with a concentration of 23 nM was obtained and stored at 4 °C in the dark.

TEM: d = 16.8 ± 1.4 nm; **UV/Vis**: λ_{max} = 537 nm; **DLS**: d_{hydr} = 38 ± 19 nm.

Synthesis of Au-MUAM (Ø 13 nm) in H_2O in a Ligand Exchange Reaction

(according to a procedure by Mattern *et al.*[4])

The Au-Citrate NP dispersion with Ø 13 nm (10 ml) was filtrated using syringe filtration on a cellulose membrane with 0.2 µm pore size. MUAM (7 mg, 34 µmol) was dissolved in 0.01 M HCl (0.2 ml) and added to the Au-Citrate NPs dispersion. Semi concentrated HCl (2 drops) was added and the reaction mixture was stirred at room temperature for 3 h. Then, MUAM (7 mg, 34 µmol) dissolved in 0.01 M HCl (0.2 ml) was added a second time and the reaction mixture was stirred at room temperature for 16 h. Subsequently, the Au NP dispersion was purified *via* dialysis against demineralised H_2O (in MWCO 12000, 6 × 2 h). A violet, clear NP dispersion with a particle concentration of 7.4 nM was obtained and stored at 4 °C in the dark.

^{1}H-NMR (600 MHz, D_2O): δ/ppm = 4.41 (m, 2 H, NH_2), 2.98 (m, 2 H, CH_2N), 2.52 (m, 2 H, CH_2S), 1.68 -1.54 (m, 4 H, CH_2), 1.43-1.16 (m, 14 H, CH_2); **IR** (ATR): ν/cm^{-1} = 3421, 3217 (ν_{N-H}), 2921, 2842 (ν_{C-H}), 1708, 1513 (δ_{N-H}), 1232, 1176, 1126 (ν_{C-N}), 981, 598 (ν_{C-S}) ; **TEM**: d = 13.2 ± 1.1 nm; **UV/Vis**: λ_{max} = 530/523 nm; **DLS**: d_{hydr} = 20 ± 4 nm.

5.6.1.3 Surface Functionalisation: General Synthetic Procedure of a Reaction at the Ligand Periphery (air sensitive)

The coupling reagents EDC and NHS, as well as the biogenic substance (amine) and the base (NEt_3), were dissolved in degassed H_2O and stirred for 0.5 h – 2 h at room temperature under argon atmosphere. In the meantime, the Au NP dispersion of the preferred size was filtrated using syringe filtration on a cellulose membrane with 0.2 µm pore size. Then, the NP dispersion was degassed with argon for 45 min. The ligand solution was slowly added to the NP dispersion and was stirred at room temperature for a certain time under argon before purification took place.

Synthesis of Au-MUAM-DHCA (Ø 13 nm) in H_2O

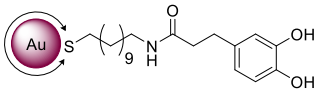

Au-MUAM NPs with Ø 13 nm (6 ml), DHCA (8 mg, 44 µmol), EDC (10 mg, 52 µmol), NHS (5 mg, 43 µmol), triethyl amine (NEt_3) in D_2O (1 drop)

EDC, NHS and NEt_3 were dissolved in degassed H_2O (0.5 ml). Dihydrocaffeic acid (DHCA) in DMSO (0.2 ml) was added and the mixture was stirred for 2 h at room temperature under argon atmosphere. Au-MUAM NPs with Ø 13 nm were degassed with argon for 45 min. The ligand solution was slowly added dropwise to the NP dispersion and was stirred at room temperature for 16 h under argon. Then, the NP dispersion was purified *via* dialysis against demineralised H_2O (in MWCO 6000, 3 × 2 h). A violet, clear NP dispersion with a concentration of 191 nM was obtained and stored at 4 °C in the dark.

^{1}H-NMR (600 MHz, D_2O): δ/ppm = 6.59 (d, J = 4.1 Hz, 1 H, C*H*), 6.55 (s, 1 H, C*H*), 6.39 (d, J = 4.1 Hz, 1 H, C*H*), 3.07-2.99 (m, 3 H, CH_2, N*H*), 2.39-2.16 (m, 6 H, CH_2), 1.61–1.02 (m, 18 H, CH_2); **IR** (ATR): ν/cm^{-1} = 3359 ($\nu_{N\text{-}H;}$ $\nu_{O\text{-}H}$), 2987 ($\nu_{O\text{-}H}$), 2921, 2842 ($\nu_{C\text{-}H}$), 2030 ($\delta_{C\text{-}H}$), 1782 ($\nu_{C=O}$), 1708, 1628 ($\delta_{N\text{-}H}$), 1560 ($\delta_{O\text{-}H}$), 1454 ($\delta_{C\text{-}H}$), 1392, 1289, 1209 ($\nu_{C\text{-}O}$), 1073 ($\nu_{C\text{-}N}$), 807, 716 ($\delta_{C\text{-}H}$), 640 ($\nu_{C\text{-}S}$); **TEM**: d = 12.98 ± 1.1 nm; **UV/Vis**: λ_{max} = 556 nm; **DLS**: d_{hydr} = 198 ± 65 nm.

Synthesis of Au-MUAM-DHCA (Ø 8 nm) in H_2O

Au-MUAM NPs with Ø 8 nm (0.75 ml) diluted in demineralised H_2O (7.75 ml), DHCA (8 mg, 44 µmol), EDC (10 mg, 52 µmol), NHS (5 mg, 43 µmol), triethyl amine (NEt_3) in D_2O (1 drop)

EDC, NHS, NEt_3 were dissolved in degassed H_2O (0.5 ml), DHCA in DMSO (0.2 ml) was added and the mixture was stirred for 2 h at room temperature under argon atmosphere. Au-MUAM NPs with Ø 8 nm were degassed with argon for 45 min. The ligand solution was slowly added dropwise to the NP dispersion and was stirred at room temperature for 16 h under argon. Then, the NP dispersion was purified *via* dialysis against demineralised H_2O (in MWCO 6000, 3 × 2 h). A pink, clear NP dispersion with a concentration of 191 nM was obtained and stored at 4 °C in the dark.

TEM: d = 8.2 ± 0.9 nm; **UV/Vis**: λ_{max} = 550 nm; **DLS**: d_{hydr} = 164 ± 39 nm.

Synthesis of Au-MUAM-DHCA (Ø 5 nm) in H_2O

Au-MUAM NPs with Ø 5 nm (0.75 ml) diluted in demineralised H_2O (7.75 ml), DHCA (8 mg, 44 µmol), EDC (10 mg, 52 µmol), NHS (5 mg, 43 µmol)

EDC and NHS were dissolved in degassed H_2O (1ml), DHCA in DMSO (0.2 ml) was added and the mixture was stirred for 1 h at room temperature under argon atmosphere. Au-MUAM NPs with Ø 8 nm were degassed with argon for 45 min. The NP dispersion was added to the ligand solution and was stirred at room temperature for 16 h under argon. Then, the NP dispersion was purified *via* dialysis against demineralised H_2O (in MWCO 6000, 2 × 3 h). A violet, clear NP dispersion with a concentration of 191 nM was obtained and stored at 4 °C in the dark.

TEM: d = 5.0 ± 0.8 nm; **UV/Vis**: λ_{max} = 545 nm; **DLS**: d_{hydr} = 101 ± 27 nm; **ζ potential:** ζ = -48.07 ± 1.99 mV.

5.7 Fluorescent Dye Functionalised Au NPs

5.7.1 Ligand Syntheses

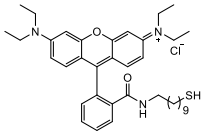

Synthesis of Rhod-MUAM

Rhod (100 mg, 0.21 mmol, 1.0 eq.) was dissolved anhydrous DMF (2 ml) and cooled to 0 °C. NEt_3 (87 µl, 0.63 mmol, 3.0 eq.) and HATU (160 mg, 0.42 mmol, 2.0 eq.) were added and stirred for 5 min at 0 °C. MUAM (43 mg, 0.21 mmol, 1.0 eq.) dissolved in anhydrous DMF (2 ml) was added slowly dropwise and the dark violet reaction mixture was stirred under argon atmosphere at room temperature for 12 d. The reaction mixture was quenched with demineralised H_2O (3 ml) and diluted HCl (15 ml) was added before extraction with EtOAc (3 × 15 ml) as well as with DCM (3 × 15 ml). The different organic layers were washed with demin. H_2O twice separately, dried over Na_2SO_4, filtered and the solvents were evaporated. However, ESI-MS spectra did not reveal a mass peak of the desired product in any fraction.

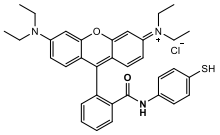

Synthesis of Rhod-ATP

(according to a method of Abed *et al.*[301])

Rhod (100 mg, 0.20 mmol, 1.0 eq.) and NHS (18 mg, 0.16 mmol, 0.8 eq.) were dissolved anhydrous pyridine (5 ml). DIC (39 µL, 0.24 mmol, 1.2 eq.) was added to the purple solution and the reaction mixture was stirred at room temperature for 4 h. K_2CO_3 (30 mg, 0.22mmol, 1.1 eq.) in degassed water (0.5 ml) was added to a solution of ATP (25 mg, 0.20 mmol, 1.0 eq.) in anhydrous DMF (0.5 ml), which was then quickly added to the reaction solution and stirred at room temperature for 40 h under argon atmosphere in the dark. However, ESI-MS spectra did not reveal a mass peak of the desired product.

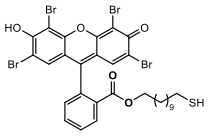

Synthesis of Eosin-MUDOL

(according to a method by Steglich *et al.*[308])

Eosin Y (138 mg, 0.20 mmol, 1.0 eq.) was dissolved in anhydrous DCM (5 ml). DMAP (73 mg, 0.60 mmol, 3.0 eq.) and mercaptoundecanol (MUDOL, 41 mg, 0.20 mmol, 1.0 eq.) dissolved in anhydrous DCM (5 ml) were added under argon counter flow and stirred at -5 °C. DIC (34 µL, 0.22 mmol 1.1 eq.) was added quickly and stirred for 5 min at 0 °C. Afterwards, the reaction mixture was stirred at room temperature for 18 h under argon atmosphere. During the work-up process, the solvent was evaporated to obtain a dark purple solid. The ESI-MS spectra revealed a mass peak of the desired product, so the crude material was purified *via* flash column chromatography (DCM/MeOH 60:1). However, pure product was not isolated.

ESI-MS (*m/z*): $[M+H]^+$= 832.86 (calcd: $[M+H]^+$ = 832.83).

Synthesis of Eosin-Cys

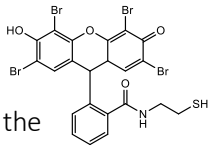

Eosin Y (138 mg, 0.20 mmol, 1.0 eq.) and NHS (19 mg, 0.17 mmol, 0.8 eq.) were dissolved anhydrous MeCN (5 ml). DIC (39 µL, 0.24 mmol, 1.2 eq.) was added to the purple solution and the reaction mixture was heated to reflux for 4 h. K_2CO_3 (152 mg, 1.10mmol, 5.2 eq.) in degassed water (3 ml) was added to a solution of cysteamine hydrochloride (24 mg, 0.21 mmol, 1.0 eq.) in anhydrous DMF (3 ml), which was then quickly added to the reaction solution and stirred at 60 °C for 19 h under argon atmosphere. The solvent was evaporated and a red, sticky solid was obtained. However, ESI-MS spectra did not reveal a mass peak of the desired product.

Synthesis of Rhod-EN

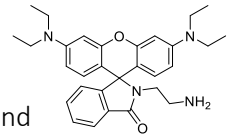

Rhodamine B (430 mg, 0.89 mmol, 1.0 eq.) was dissolved anhydrous EtOH (8 ml) and heated to 90 °C. In the meantime, ethylenediamine (80 µL, 1.16 mmol, 1.3 eq.) was diluted in anhydrous EtOH (2 ml) and added to the reaction mixture slowly dropwise under vigorous stirring. The reaction mixture was heated to reflux for 16 h under argon atmosphere. The solvent was removed *in vacuo*. The residue was colourless with slightly orange spots and was dissolved in EtOAc (15 ml). Demin. H_2O (20 ml) was added and extracted with EtOAc (3 × 15 ml). The combined organic layers were washed with demin. H_2O twice, dried over Na_2SO_4, filtered and the solvent was evaporated. The pure product was obtained as a colourless (some parts slightly pink, orange) crystalline solid in a very good yield (370 mg, 85%) and stored at 4 °C in the dark. The product was crystallised *via* slow diffusion of *n*-pentane into a deuterated chloroform solution to yield colourless crystals.

^{1}H-NMR (499 MHz, $CDCl_3$): δ/ppm = 7.96-7.88 (m, 1 H, C*H*), 7.51-7.42 (m, 2 H, C*H*), 7.15-7.07 (m, 1 H, C*H*), 6.58 (d, *J* = 9.0 Hz, 2 H, C*H*), 6.46 (s, 1 H, C*H*), 6.45 (s, 1 H, C*H*), 6.35 (dd, *J* = 9.0 Hz, 2.7 Hz, 2 H, C*H*), 3.35 (q, *J* = 7.1, 14.2 Hz 8 H, CH_2,), 3.21 (t, *J* = 6.6 Hz, 2 H, CH_2), 2.44 (t, *J* = 6.6 Hz, 2 H, CH_2), 1.44-1.24 (m, 2 H, NH_2), 1.18 (t, *J* = 7.1 Hz, 12 H, CH_3); **^{13}C{^{1}H} NMR** (125 MHz, $CDCl_3$): δ/ppm = 156.2, 154.7, 153.3, 148.8, 132.4, 128.7, 128.0, 123.8, 122.8, 108.2, 105.6, 97.7, 64.4, 44.3, 43.8, 40.8, 12.6; **IR** (ATR): ν/cm^{-1} = 3320 (ν_{N-H}), 2971, 2921, 2866 (ν_{C-H}), 1678 ($\nu_{C=O}$), 1613 ($\nu_{C=C}$), 1542, 1514 (δ_{N-H}), 1353 (ν_{C-N}), 1265, 1218 (ν_{C-N}), 1118 (ν_{C-O}), 1076, 1019, 820 (δ_{C-H}), 789 ($\delta_{C=C}$), 768 (δ_{C-H}), 704 ($\delta_{C=C}$), 576, 539; **ESI-MS (*m/z*):** $[M+H]^+$ = 485.31 (calcd: $[M+H]^+$ = 485.29); **Elemental Analysis:** Anal. Calcd for $C_{30}H_{36}N_4O_2$: C, 74.35; H 7.49; N, 11.56. Found: C, 73.26; H, 7.50; N, 11.01.

Synthesis of Rhod-DAH

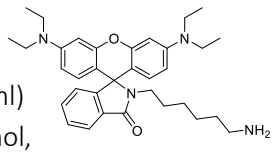

Rhodamine B (400 mg, 0.84 mmol, 1.0 eq.) was dissolved anhydrous EtOH (8 ml) and heated to 90 °C. In the meantime, diaminohexane (DAH) (126 mg, 1.08 mmol, 1.3 eq.) was dissolved in anhydrous EtOH (2 ml) and added to the reaction mixture slowly dropwise under vigorous stirring. The reaction mixture was heated to reflux for 3 d under argon atmosphere. The solvent was removed under reduced pressure. The residue was colourless with slightly orange spots and was dissolved in EtOAc (15 ml). Demin. H_2O (20 ml) was added and extracted with EtOAc (3 × 20 ml). The combined organic layers were washed with demin. H_2O (5 × 50 ml), dried over Na_2SO_4, filtered and the solvent was evaporated. The pure product was obtained as a colourless (sometimes slightly pink, orange) crystalline solid in a very good yield (382 mg, 84%) and stored at 4 °C in the dark.

^{1}H-NMR (499 MHz, $CDCl_3$): δ/ppm = 8.03-7.99 (m, 1 H, C*H*), 7.69-7.55 (m, 2 H, C*H*), 7.23 (d, *J* = 7.1 Hz, 1 H, C*H*), 6.45 (d, *J* = 8.8 Hz, 2 H, C*H*), 6.40 (s, 1 H, C*H*), 6.39 (s, 1 H, C*H*), 6.29 (dd, *J* = 8.8 Hz, 2.5 Hz, 2 H, C*H*), 3.37 (q, *J* = 8.8 Hz, 2.5 Hz, 8 H, CH_2), 3.35-3.25 (m, 2 H, CH_2), 1.69 (b.s, 2 H, NH_2), 1.28 (t, 4 H, CH_2), 1.23-1.05

(m, 16 H, C*H*$_3$, C*H*$_2$); **^{13}C{^{1}H} NMR** (125 MHz, $CDCl_3$): δ/ppm = 153.4, 153.1, 149.5, 134.3, 129.1, 128.9, 124.8, 124.2, 108.0, 106.0, 97.6, 60.4, 44.5, 12.5; **IR** (ATR): ν/cm^{-1} =3392, 2973, 2921, 2866 (ν_{C-H}), 1749 ($\nu_{C=O}$), 1688 ($\nu_{C=O}$), 1604 ($\nu_{C=C}$), 1539, 1519(δ_{N-H}), 1428 (δ_{C-H}), 1325 (ν_{C-N}), 1212 (ν_{C-N}), 1102 (ν_{C-O}), 1011, 851(δ_{C-H}), 813 ($\delta_{C=C}$), 760 (δ_{C-H}), 699 ($\delta_{C=C}$), 665, 580, 535; **ESI-MS (*m/z*):** $[M+H]^+$ = 541.35 (calcd: $[M+H]^+$ = 541.35); **Elemental Analysis:** Anal. Calcd for $C_{34}H_{44}N_4O_2$: C, 75.52; H 8.20; N, 10.36. Found: C, 74.91; H, 7.22; N, 6.93.

Synthesis of Rhod-EN-LA

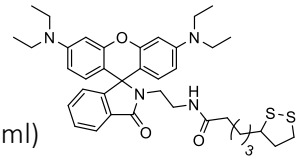

Lipoic acid (LA) (44 mg, 0.21 mmol, 1.2 eq.) was dissolved anhydrous DMF (2 ml) and cooled to 0 °C. NEt_3 (84 µl, 0.61 mmol, 3.4 eq.) and HATU (152 mg, 0.40 mmol, 2.2 eq.) were added. Rhod-EN (90 mg, 0.18 mmol, 1 eq.) dissolved in anhydrous DMF (2 ml) was added slowly dropwise and the dark violet reaction mixture was stirred under argon atmosphere at room temperature for 48 h. The reaction mixture was quenched with demineralised H_2O (3 ml) and diluted HCl (15 ml) was added before extraction with EtOAc (3 × 15 ml). The combined organic layers were washed with demin. H_2O twice, dried over Na_2SO_4, filtered and the solvent was evaporated. Then it was extracted again with DCM (15 ml). The product was obtained as a pink residue in a moderate yield (52 mg, 77 µmol, 42%) and stored at 4 °C in the dark. However, traces of Rhod remained within the residue.

^{1}H-NMR (499 MHz, $CDCl_3$): δ/ppm = 7.92-7.86 (m, 1 H, C*H*), 7.47-7.42 (m, 2 H, C*H*), 7.10-7.04 (m, 1 H, C*H*), 6.90-6.82 (m, 1 H, C*H*), 6.45-6.39 (m, 2 H, C*H*), 6.38-6.35 (m, 2 H, C*H*), 6.29-6.24 (m, 2 H, C*H*), 3.58-3.50 (m, 1 H, N*H*), 3.38-3.31 (q, 8 H, C*H*$_2$, *J* = 6.6 Hz), 3.18-3.07 (m, 2 H, C*H*$_2$), 3.06-3.00 (m, 2 H, C*H*$_2$), 2.50-2.24 (m, 3 H, C*H*$_2$), 1.98-1.81 (m, 3 H, C*H*$_2$), 1.73-1.55 (m, 5 H, C*H*$_2$), 1.52-1.23 (m, 2 H, C*H*$_2$), 1.16 (t, 12 H, C*H*$_3$, *J* = 6.6 Hz); **^{13}C{^{1}H} NMR** (125 MHz, $CDCl_3$): δ/ppm = 172.6, 169.7, 153.3, 149.0, 132.4, 128.5, 128.0, 123.8, 122.4, 108.0, 104.6, 97.7, 56.0, 55.5, 44.4, 40.8, 40.3, 39.5, 36.6, 34.7, 28.7, 25.2, 12.4; **IR** (ATR): ν/cm^{-1} = 3398 (ν_{N-H}), 2917, 2846 (ν_{C-H}), 1720 ($\nu_{C=O}$), 1641 ($\nu_{C=O}$), 1585 (δ_{N-H}), 1457, 1415 (δ_{C-H}), 1330 (ν_{C-N}), 1274, 1240 (ν_{C-N}), 1179, 1128 (ν_{C-O}), 1066, 1009, 920, 840 (δ_{H-C-S}), 680 (ν_{C-S}), 548 (ν_{S-S}); **ESI-MS (*m/z*):** $[M+Na]^+$ = 695.31 (calcd: $[M+Na]^+$ = 695.31); **Elemental Analysis:** Anal. Calcd for $C_{38}H_{48}N_4O_3S_2$: C, 67.82; H 7.19; N, 8.33; S 9.53. Found: C, 62.46; H, 7.31; N, 8.72; S 8.45.

5.7.2 Surface Functionalisation

Synthesis of Au-LA-EN-Rhod (Ø 13 nm) in H_2O

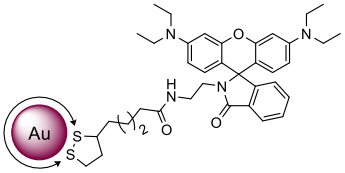

Au-Citrate NP Ø 13 nm dispersion (10 ml) was purged with argon for 45 min. Rhod-EN-LA (25 mg, 37 µmol) in DMSO (0.3 ml) was slowly added. Furthermore, NEt_3 (0.1 ml) was added to ensure a stable NP dispersion, which was stirred for 16 h at room temperature. The Au NPs were precipitated with EtOH and centrifuged (30 min, 7000 rpm). The supernatant was discarded, the residue was redispersed three times and washed again with EtOH. The supernatant was discarded and the residue was redispersed in H_2O (10 ml). The clear Au NP dispersion was further purified *via* dialysis against H_2O (in MWCO 6000, for 3 × 2 h). A violet, clear NP dispersion with a concentration of 15 nM was obtained and stored at 4 °C in the dark.

IR (ATR): ν/cm^{-1} = 2918, 2846 (ν_{C-H}), 1678 ($\nu_{C=O}$), 1586 (δ_{N-H}), 1514, 1400 (δ_{C-H}), 1344 (ν_{C-N}), 1264, 1217 (ν_{C-N}), 1175, 1108 (ν_{C-O}), 1066, 835 (δ_{H-C-S}), 746 (δ_{N-H}), 681 (ν_{C-S}), 563 (ν_{S-S}); **TEM**: *d* = 12.9 ± 0.9 nm; **UV/Vis**: λ_{max} = 534 nm; **DLS**: d_{hydr} = 75 ± 16 nm.

5.8 Multifunctional Au NPs Labelled with ^{99m}Tc

5.8.1 Precursor Syntheses

Synthesis of [ReBr(CO)$_5$]

$Re(CO)_{10}$ (4.90 g, 7.51 mmol, 1.0 eq.) was dissolved in dry DCM (147 ml) and cooled to 0 °C. Bromine (0.42 ml, 8.20 mmol, 1.1 eq.) was diluted in dry DCM (25 ml) and added dropwise to the Re solution over a time period of 30 min. In the meantime, the clear solution turned orange over yellow and a colourless precipitate formed. The reaction mixture was then further stirred at room temperature for 2 h under nitrogen atmosphere and filtered. The colourless residue was dried *in vacuo*. The filtrate was reduced *in vacuo* (colour intensified) to ¼ of its original volume. The reaction mixture was stirred at room temperature for 16 h under N_2 atmosphere before the colourless precipitate was filtered off again and dried *in vacuo*. $ReBr(CO)_5$ could be obtained as a colourless powder in a good yield (5.24 g, 84%).

IR (ATR): ν/cm^{-1} = 2149, 2078, 2061, 2021, 1956 ($\nu_{C\equiv O}$), 1078, 1038, 1003, 937, 906, 575 ($\nu_{Re\text{-}Br}$); **Elemental Analysis:** Anal. Calcd for C_5O_5ReBr: C, 14.79. Found: C, 14.59.

Synthesis of (NEt$_4$)$_2$[ReBr$_3$(CO)$_3$]

NEt_4Br (5.25 g, 25.0 mmol, 2.03 eq.) was dried *in vacuo* before use and suspended in degassed diglyme (130 ml) in a three necked flask (250 ml) and heated to 85 °C for 20 min. $ReBr(CO)_5$ (5.00 g, 12.31 mmol, 1.0 eq.) was added and stirred at 115 °C for 19 h under N_2 atmosphere. A yellow solution with colourless precipitate was cooled in an ice bath, filtered and the crude product was washed with cold Et_2O (3 × 5 ml), suspended in cold EtOH (45 ml), filtered and washed with cold EtOH (3 × 5 ml). The product was dried in vacuo and could be obtained as a colourless solid in a good yield (7,08 g, 73%).

IR (ATR): ν/cm^{-1} = 2988 ($\nu_{C\text{-}H}$), 1993 ($\nu_{C\equiv O}$), 1845, 1459, 1402, 1180, 1028 ($\nu_{N\text{-}C}$), 1002, 798, 650 ($\nu_{Re\text{-}Br}$); **Elemental Analysis:** Anal. Calcd for $C_{11}H_{40}N_2O_3ReBr_3$: C, 29.62; H, 5.23; N, 3.64. Found: C, 29.49; H, 5.18; N, 2.49.

Synthesis of 2-Picolylamine-*N*,*N*-diacetic acid (PADA)

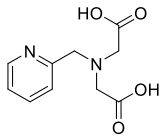

(according to a method described by Shepherd *et al.*[323])

Bromoacetic acid (11.76 g, 106 mmol, 2 eq.) was dissolved in demin. H_2O (13 ml) and cooled to 0 °C. 2-Picolylamine (5.74 g, 53 mmol, 1 eq.) in demin. H_2O (6 ml) was added dropwise and the reaction mixture was stirred at 0 °C for 10 min. An 8 M NaOH solution (212 mmol, 4 eq.) was added slowly under vigorous stirring. The strongly orange reaction mixture was stirred at 0 °C for 15 min and at room temperature for 16 h. The pH of the dark red brown solution was adjusted to 4 with semi concentrated HCl (15 ml) and was reduced *in vacuo*. Brown residue with crystalline solid was filtered and washed with MeOH. EtOH (120 ml) was added to the brown filtrate and left to crystallise at – 18 °C for 2 d. A formed yellow precipitate was filtered and recrystallised in EtOH/H_2O (3:1), filtered again and dried *in vacuo*. The product was obtained as a colourless crystalline solid in a good yield (5.87 g, 26 mmol, 49%).

^{1}H-NMR (400 MHz, DMSO-d$_6$): δ/ppm = 8.47 (d, 1 H, C*H*), 7.75 (t, *J* = 7.8 Hz, 1 H, C*H*), 7.40 (d, *J* = 7.8 Hz, 1 H, C*H*), 7.25 (t, *J* = 7.8 Hz, 1 H, C*H*), 3.90 (s, 2 H, CH_2), 3.35 (s, 4 H, CH_2); **^{13}C{^{1}H} NMR** (100 MHz, DMSO-d$_6$): δ/ppm = 174.8,

159.3, 149.0, 137.0, 122.5, 59.5, 59.3; **IR** (ATR): ν/cm^{-1} = 3401 (ν_{O-H}), 3017 (ν_{C-H}), 1743($\nu_{C=C}$), 1620 ($\nu_{C=O}$), 1439 (δ_{C-H}), 1390 (δ_{C-O}), 1342(ν_{C-O}), 901 (δ_{O-H}), 773 (δ_{C-H}), 526 (ν_{C-N}); **ESI-MS (*m/z*):** [M-H]$^-$ = 223.0 (calcd: [M-H]$^-$ = 223.1); **Elemental Analysis:** Anal. Calcd for $C_{10}H_{12}N_2O_4$: C, 53.57; H, 5.39; N, 12.49. Found: C, 43.77; H, 5.23; N, 6.10; S, 10.24.

Synthesis of S-Thioacetyl-cysteamine (Ac-Cys)

(modified version of Frost *et al.*[333])

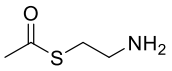

Cysteamine hydrochloride (500 mg, 4.40 mmol, 1 eq.) was dissolved in anhydr. DCM (24 ml). Acetyl chloride 1 M in DCM (13.2 ml, 13.2 mmol, 3 eq.) was slowly added under vigorous stirring. The yellow solution with solid was heated to reflux for 4.5 h and was further stirred at room temperature for 16 h under N_2 atmosphere. The precipitate was filtered, washed with cold DCM (5 × 3 ml each) and dried *in vacuo*. The product was obtained as colourless solid in a good yield (372 mg, 3.12 mmol, 71%).

^{1}H-NMR (400 MHz, MeOH-d$_4$): δ/ppm = 3.32-3.29 (m, 2 H, CH_2), 3.19-3.09 (m, 4 H, CH_2 and NH_2), 2.38 (s, 3 H, CH_3); **^{13}C{^{1}H} NMR** (100 MHz, MeOH-d$_4$): δ/ppm = 195.1, 39.3, 29.0, 25.7; **IR** (ATR): ν/cm^{-1} = 3293 (ν_{N-H}), 2868 (ν_{C-H}), 1995, 1682($\nu_{C=O}$), 1523 (δ_{C-H}), 1373, 1254, 1139(δ_{C-N}), 1108, 967, 893 (δ_{C-H}), , 681, 623 (ν_{C-S}), 531 (ν_{C-N}); **ESI-MS (*m/z*):** [M+H]$^+$ = 120.1 (calcd: [M+H]$^+$ = 120.1); **Elemental Analysis:** Anal. Calcd for C_4H_9NOS: C, 40.31; H, 7.61; N, 11.75; S, 26.90. Found: C, 28.49; H, 6.21; N, 9.73; S, 18.74.

5.8.2 Ligand Syntheses

Synthesis of MUAM-PADA

(modified version of Chiotellis *et al*.[324])

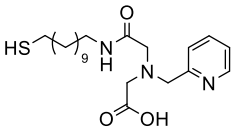

PADA (180 mg, 0.80 mmol, 1 eq.) and BOP-Cl (200 mg, 0.80 mmol, 1 eq.) were dissolved in anhydr. THF (8 ml) and NEt_3 (326 µl, 2.35 mmol, 3 eq.) was added. The reaction mixture was stirred at 20 °C for 1 h under argon atmosphere. The orange solution with a colourless precipitate was filtered using a Schlenk filter. Anhydr. THF (10 ml) was added to the orange solution and cooled to 0 °C. MUAM (210 mg, 1.03 mmol, 1.3 eq.) was suspended in anhydr. pyridine (3 ml) and anhydr. THF (2 ml) and slowly added to the orange solution. The reaction mixture was stirred at room temperature under argon atmosphere for 7 d. The light yellow solution was evaporated to yield a yellow gel, which was further dissolved in DCM (10 ml) and arium® H_2O (ca. 15 ml) was added. Gas evolution occurred. The organic layer was washed with H_2O (10 ml, pH 8 with NaOH). The combined aqueous layers were extracted with DCM (3 × 15 ml each). The combined organic phase was washed with H_2O (15 ml, pH 7), dried over Na_2SO_4, filtered and evaporated. The product was obtained as a yellow gel in a moderate yield (101 mg, 0.25 mmol, 31%).

^{1}H-NMR (400 MHz, MeOH-d$_4$): δ/ppm = 8.79 (d, J = 7.0 Hz 1 H, CH), 8.39 (t, J = 7.1 Hz, 1 H, CH), 7.91-7.81 (m, 2 H, CH) 4.39 (s, 2 H, CH_2), 3.65 (s, 2 H, CH_2,; 3.64 (s, 2 H, CH_2), 3.26-3.17 (m, 2 H. CH_2), 2.51-2.54 (m, 2 H, NH and SH) 1.62-1.54 (m, 2 H, CH_2), 1.53-1.45 (m, 2H, CH_2), 1.43-1.35 (m, 2 H, CH_2), 1.34-1.26 (m, 14 H CH_2); **^{13}C{^{1}H} NMR** (100 MHz, MeOH-d$_4$): δ/ppm = 172.4, 171.3, 155.2, 144.9, 141.5, 125.5, 125.1, 57.1, 56.2, 54.9, 39.1, 28.3, 33.8, 29.2, 29.0, 28.9, 28.8, 28.0, 26.6, 23.5; **IR** (ATR): ν/cm^{-1} = 3300 (ν_{O-H}), 3075 (ν_{N-H}), 2916, 2846 (ν_{C-H}), 1730 ($\nu_{C=C}$), 1659 ($\nu_{C=O}$), 1540 ($\nu_{C=O}$), 1426 (δ_{C-H}), 1184 (δ_{C-N}), 1135, 980, 773 (δ_{C-H}), 720 (δ_{N-H}), 601 (ν_{C-S}), 521 (ν_{C-N}); **ESI-MS (*m/z*):** [M-H]$^-$ = 408.2 (calcd: [M-H]$^-$ = 408.2); **Elemental Analysis:** Anal. Calcd for $C_{21}H_{35}N_3O_3S$: C, 61.58; H, 8.61; N, 10.26; S, 7.83. Found: C, 60.36; H, 7.61; N, 8.50; S, 4.02.

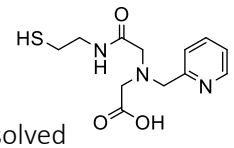

Synthesis of Cys-PADA

PADA (300 mg, 1.34 mmol, 1 eq.) and BOP-Cl (339 mg, 1.34 mmol, 1 eq.) were dissolved in anhydr. THF (8 ml) and NEt_3 (555 µl, 4.12 mmol, 3 eq.) was added. The reaction mixture was stirred at 20 °C for 1 h under argon atmosphere. The orange solution with a colourless precipitate was filtered using a Schlenk filter. The orange clear filtrate was cooled to 0 °C. Cysteamine (Cys)(134 mg, 1.73 mmol, 1.3 eq.) was dissolved in anhydr. DCM (15 ml) and slowly added to the orange solution. The reaction mixture was stirred at room temperature under argon atmosphere for 5 d. The light yellow solution was evaporated to yield a slightly yellow gel, which was further dissolved in DCM (10 ml) and arium® H_2O (ca. 10 ml) was added. The aqueous layer was washed with DCM (3 × 10 ml). Then the pH of the aqueous layer was adjusted to 7 (by adding dil. NaOH), washed with EtOAc (3 × 15 ml each) and the solvent was evaporated and dried *in vacuo*. The product was obtained as a yellow solid in a good yield (280 mg, 0.99 mmol, 77%).

^{1}H-NMR (400 MHz, MeOH-d_4): *δ*/ppm = 8.87-8 81 (m, 1 H, C*H*), 8.57-8.48 (m, 1 H, C*H*), 7.91-7.81 (m, 2 H, C*H*) 4.48 (d, 2 H, CH_2), 3.76-3.64 (m, 4 H, CH_2), 3.53 (t, *J* = 6.7 Hz 2 H, CH_2), 3.41-3.29 (m, 2 H, N*H* and S*H*), 2.85 (t, *J* = 6.7 Hz, 2 H, CH_2); **^{13}C{^{1}H} NMR** (100 MHz, MeOH-d_4): δ/ppm = 171.8, 171.3, 154.9, 146.1, 140.9, 126.1, 125.6, 57.2, 55.8, 55.0, 38.1, 36.9; **IR** (ATR): $\tilde{\nu}$/cm^{-1} = 3256 (ν_{O-H}), 3053 (ν_{N-H}), 2921 (ν_{C-H}), 1743 ($\nu_{C=C}$), 1638 ($\nu_{C=O}$), 1540 ($\nu_{C=O}$), 1439 (δ_{C-H}), 1390 (δ_{C-O}), 1219(δ_{C-N}), 1078, 985, 901 (δ_{O-H}), 769 (δ_{C-H}), 592 (ν_{C-S}), 523 (ν_{C-N}); **ESI-MS (*m/z*):** [M-H]$^-$ = 282.0 (calcd: [M-H]$^-$ = 282.1); **Elemental Analysis:** Anal. Calcd for $C_{12}H_{17}N_3O_3S$: C, 51.05; H, 5.71; N, 14.88; S, 11.36. Found: , 39.65; H, 6.13; N, 10.67; S, 7.87.

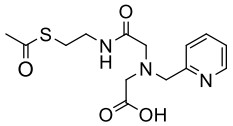

Synthesis of Ac-Cys-PADA

PADA (300 mg, 1.34 mmol, 1 eq.) and BOP-Cl (340 mg, 1.34 mmol, 1 eq.) were dissolved in anhydr. THF (8 ml) and NEt_3 (555 µl, 4.12 mmol, 3 eq.) was added. The reaction mixture was stirred at 20 °C for 1 h under argon atmosphere. The orange solution with a colourless precipitate was filtered using a Schlenk filter. Ac-Cys (207 mg, 1.74 mmol, 1.3 eq.) was dissolved in anhydr. pyridine (1 ml) and anhydr. THF (12 ml) and slowly added to the orange solution. The reaction mixture was stirred at room temperature under argon atmosphere for 13 d. The light yellow solution was filtered and the solvent was evaporated to yield a slightly yellow gel, which was further dissolved in DCM (5 ml) and arium® H_2O (ca. 10 ml) was added. The DCM layer was extracted with arium H_2O (3 × 10 ml). Then the aqueous layer was extracted with EtOAc (6 × 10 ml each). The combined EtOAc phases were dried over Na_2SO_4, filtered and the solvent was evaporated and dried *in vacuo*. The product was obtained as a yellow solid in a poor yield (88 mg, 0.27 mmol, 21%). And it was further purified *via* prep. HPLC to obtain a yellow solid in a rather good yield (60 mg, 0.19 mmol, 14%).

^{1}H-NMR (400 MHz, MeOH-d_4): *δ*/ppm 8.76 (d, *J* = 6.7 Hz, 1 H, C*H*), 8.54 (t, *J* = 6.7 Hz, 1 H, C*H*), 8.03-7.93 (m, 2 H, C*H*), 4.39 (s, 2 H, CH_2), 3.69 (s, 2 H, CH_2), 3.56 (s, 2 H, CH_2), 3.50 (t, *J* = 6.7 Hz, 1 H, N*H*), 3.40 (t, *J* = 6.7 Hz, 2 H, CH_2), 3.02 (t, *J* = 6.7 Hz 2 H, CH_2), 2.89-2.80 (m, 1 H, O*H*), 2.33 (s, 3 H, CH_3); **^{13}C{^{1}H} NMR** (100 MHz, MeOH-d_4): δ/ppm = 200.2, 174.4, 172.7, 153.2, 146.8, 140.7, 126.5, 126.0, 57.3, 55.7, 55.3, 38.3, 29.8, 28.5; **IR** (ATR): $\tilde{\nu}$/cm^{-1} = 3293 (ν_{O-H}), 3083 (ν_{N-H}), 2936 (ν_{C-H}), 1720 ($\nu_{C=C}$), 1655 ($\nu_{C=O}$), 1537 ($\nu_{C=O}$), 1420 (δ_{C-H}), 1349 (δ_{C-O}), 1188 (δ_{C-N}), 1128, 981, 951 (δ_{O-H}), 826 (δ_{C-H}), 798, 764, 710, 623 (ν_{C-S}), 525 (ν_{C-N}); **ESI-MS (*m/z*):** [M+H]$^+$ = 326.2 (calcd: [M+H]$^+$ = 326.2); **Elemental Analysis:** Anal. Calcd for $C_{14}H_{19}N_3O_4S$: C, 51.68; H, 5.89; N, 12.91; S, 9.85. Found: 56.50; H, 6.58; N, 12.67; S, 11.16.

5.8.2.1 Surface Functionalisation: General Synthetic Procedure of a Ligand Exchange Reaction

(according to a procedure by Mattern *et al.*[304])

The Au NP dispersion was filtrated using syringe filtration on a cellulose membrane with 0.2 µm pore size. Then, the NP dispersion was degassed with argon for 45 min. The dissolved ligand was added dropwise. The pH of the NP dispersion was adjusted by the addition of acid or base to achieve a stable clear dispersion, which was stirred at room temperature for a certain time under argon atmosphere before purification took place.

Synthesis of Au-MUAM-PADA (Ø 14 nm) in H_2O

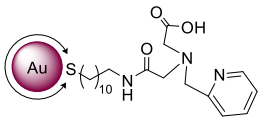

Au-Citrate NPs with Ø 14 nm (10 ml), MUAM-PADA (17 mg, 42 µmol) in DMSO (0.2 ml), NEt_3 (2 drops)

The NP dispersion was stirred at room temperature for 16 h and directly purified *via* dialysis against demin. H_2O (in MWCO 6000, 4 × 2 h). A pink, clear NP dispersion with a concentration of 8.0 nM was obtained and stored at 4 °C in the dark.

^{1}H-NMR (600 MHz, D_2O): δ/ppm = 8.52-8.41 (m, 1 H, C*H*), 7.82-7.70 (m, 1 H, C*H*), 7.52-7.41 (m, 1 H, C*H*), 7.25-7.14 (m, 1 H, C*H*), 4.19-3.97 (m, 2 H, CH_2), 3.59-3.31 (m, 2 H, CH_2), 3.15-2.95(m, 2 H. CH_2), 1.80-1.59 (m, 2 H, CH_2), 1.48-1.04 (m, 18 H, CH_2); **IR** (ATR): ν/cm^{-1} = 3283 (ν_{O-H}), 3057 (ν_{N-H}), 2925, 2841 (ν_{C-H}), 1655 ($\nu_{C=O}$), 1571 ($\nu_{C=O}$), 1395 (δ_{C-O}), 1232 (δ_{C-N}), 1148, 1135, 990 (δ_{O-H}), 760 (δ_{C-H}), 720 (δ_{N-H}), 614 (ν_{C-S}), 535 (ν_{C-N}); **TEM**: d = 14.0 ± 0.9 nm; **UV/Vis**: λ_{max} = 527 nm; **DLS**: d_{hydr} = 19 ± 4 nm.

Synthesis of Au-Cys-PADA (Ø 14 nm) in H_2O

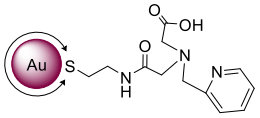

Au-Citrate NPs with Ø 14 nm (10 ml), Cys-PADA (15 mg, 53 µmol) in DMSO (0.2 ml), NEt_3 (2 drops)

The NP dispersion was stirred at room temperature for 72 h and directly purified *via* dialysis against demin. H_2O (in MWCO 6000, 4 × 2 h). A pink, clear NP dispersion with a concentration of 7.0 nM was obtained and stored at 4 °C in the dark.

^{1}H-NMR (600 MHz, D_2O): δ/ppm = 8.56 (d, J = 6.1 Hz, 1 H, C*H*), 8.04 (t, J = 6.1 Hz, 1 H, C*H*), 7.66 (d, J = 6.1 Hz, 1 H, C*H*), 7.54 (t, J = 6.0 Hz, 1 H, C*H*), 4.12 (s, 2 H, CH_2), 3.51 (s, 2 H, CH_2), 3.48-3.40 (m, 5 H, CH_2 and N*H*); 2.77 (t, J = 6.2 Hz, 2 H, CH_2); **IR** (ATR): ν/cm^{-1} =3343 (ν_{O-H}), 3059(ν_{N-H}), 2975 (ν_{C-H}), 1712 ($\nu_{C=C}$), 1678 ($\nu_{C=O}$), 1581 ($\nu_{C=O}$), 1394 (δ_{C-O}), 1162 (ν_{C-O}), 1077 (δ_{C-N}), 895 (δ_{O-H}), 828, 765 (δ_{C-H}), 618 (ν_{C-S}), 544 (ν_{C-N}); **TEM**: d = 13.9 ± 1.1 nm; **UV/Vis**: λ_{max} = 522 nm; **DLS**: d_{hydr} = 19 ± 6 nm.

Synthesis of mixed shell Au-MUDA-AT/MUAM-PADA (Ø 12 nm) in H_2O

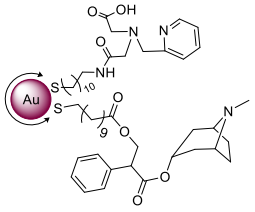

Au-Citrate NPs with Ø 12 nm (10 ml), MUDA-AT (10 mg, 24 µmol) in DMSO (0.2 ml) and MUAM-PADA (8 mg, 16 µmol) in DMSO (0.5 ml) were added simultaneously under vigorous stirring, NEt_3 (2 drops)

The NP dispersion was stirred at room temperature for 16 h and directly purified *via* dialysis against demin. H_2O (in MWCO 6000, 4 × 2 h). A pink, clear NP dispersion with a concentration of 9.5 nM was obtained and stored at 4 °C in the dark.

^{1}H-NMR (600 MHz, D_2O): δ/ppm = 8.51-8.40 (m, 1 H, C*H*), 7.82-7.77 (m, 1 H, C*H*), 7.72-7.61 (m, 1 H, C*H*), 7.52-7.08 (m, 6 H, C*H*), 4.97-4.81 (m, 2 H, C*H*), 3.97-3.76 (m, 4 H, CH_2), 3.57-3.18 (m, 2 H, CH_2), 2.78-2.67 (m, 2 H, CH_2), 2.64-2.59 (m, 2 H, CH_2), 2.33- 2.23 (s, 3 H, CH_3), 2.03-2.01 (m, 4 H, CH_2), 1.64-1.41 (m ,12 H, C*H*2), 1.36-1.29 (m, 6 H, CH_2), 1.28-1.18 (m, 34/28 H, CH_2); **IR** (ATR): ν/cm^{-1} = 2982 (ν_{N-H}), 2916, 2854 (ν_{C-H}), 1712 ($\nu_{C=O}$), 1580 (ν_{C-0}), 1390 (δ_{C-0}), 1232, 1073 (δ_{C-N}), 1033, 897, 835 (δ_{C-H}), 663 (ν_{C-S}) 610, 549 (ν_{C-N}); **TEM**: d = 12.0 ± 1.0 nm; **UV/Vis**: λ_{max} = 528 nm; **DLS**: d_{hydr} = 20 ± 6 nm.

Synthesis of mixed shell Au-MUDA-ADR/MUAM-PADA (Ø 14 nm) in H_2O

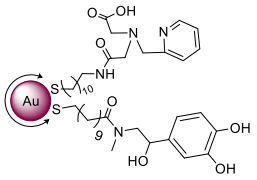

Au-Citrate NPs with Ø 14 nm (10 ml), MUDA-ADR (15 mg, 39 µmol) in DMSO (0.30 ml) and MUAM-PADA (8 mg, 20 µmol) in DMSO (0.30 ml), NEt_3 (2 drops)

After degassing of the NP dispersion, MUDA-ADR (10 mg in 0.2 ml DMSO) and MUAM-PADA (5 mg in 0.2 ml DMSO) were slowly added simultaneously. To ensure a stable dispersion NEt_3 was added and the reaction mixture was stirred at room temperature for 3 h. Further MUDA-ADR (5 mg in 0.1 ml DMSO) and MUAM-PADA (3 mg in 0.1 ml DMSO) were simultaneously added dropwise and stirred at room temperature for 16 h. Then, the NP dispersion was purified *via* dialysis against demin. H_2O (in MWCO 6000, 6 × 2 h). A pink, clear NP dispersion with a concentration of 8.0 nM was obtained and stored at 4 °C in the dark.

^{1}H-NMR (400 MHz, $CDCl_3$): δ/ppm = 7.30-7.18 (m, 5 H, C*H*), 5.23 (s, 1 H, C*H*), 4.99-4.93 (m, 1 H, C*H*), 4.53 (t, *J*=9.3 Hz, 1 H, C*H*), 4.23 (t, *J*=6.7 Hz, 1 H, C*H*), 2.60 (t, *J*=6.7 Hz, 2 H, CH_2), 2.27 (s, 3 H, CH_3), 2.33-2.12 (m, 4 H, CH_2), 1.85-1.67 (m, 4 H, CH_2), 1.63-1.41 (m, 6 H, CH_2), 1.36-1.10 (m, 10 H, CH_2); **IR** (ATR): ν/cm^{-1} = 3287 (ν_{O-H}), 2925, 2850 (ν_{C-H}), 1725 ($\nu_{C=O}$), 1575 (ν_{C-O}), 1395 (δ_{C-O}), 1241, 1147; 1077 (δ_{C-N}), 971 (δ_{O-H}), 892, 843 (δ_{C-H}), 764, 720, 654 (ν_{C-S}), 618, 530 (ν_{C-N}); **TEM**: d = 13.9 ± 1.2 nm; **UV/Vis**: λ_{max} = 532/533 nm; **DLS**: d_{hydr} = 20 ± 6 nm.

Synthesis of Au-MUDA-AT/Cys-PADA (Ø 14 nm) in H_2O

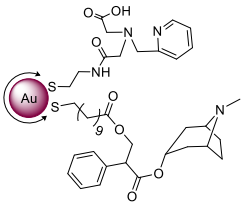

Au-Citrate NPs with Ø 14 nm (10 ml), MUDA-AT (7 mg, 14 µmol) in DMSO (0.2 ml) and Cys-PADA (7 mg, 25 µmol) in DMSO (0.2 ml) were added simultaneously under vigorous stirring, NEt_3 (3 drops)

The NP dispersion was stirred at room temperature for 16 h and directly purified *via* dialysis against demin. H_2O (in MWCO 6000, 4 × 2 h). A pink, clear NP dispersion with a concentration of 7.1 nM was obtained and stored at 4 °C in the dark.

^{1}H-NMR (600 MHz, D_2O): δ/ppm = 8.40-8.37 (m, 1 H, C*H*), 8.35-8.32 (m, 1 H, CH), 7.81-7.77 (m, 1 H, C*H*), 7.74-7.69 (m, 1 H, C*H*), 7.53-7.19 (m, 5 H, C*H*), 4.97 (s, 1 H, C*H*), 4.39-4.35 (m, 2 H, C*H*), 3.91-3.86 (m, 1 H, C*H*), 3.82-3.74 (m, 2 H, CH_2), 3.40-3.28 (m, 2 H, CH_2), 3.26-3.16 (m, 5 H, CH_2 and N*H*), 3.02-2.98 (m, 2 H, CH_2),2.69-2.60 (m, 4 H, CH_2), 2.08-2.00 (m, 2 H, CH_2), 1.88 (s, 3 H, CH_3), 1.51-1.37 (m, 2 H, CH_2), 1.36-1.11 (m, 10 H, CH_2); **IR** (ATR): ν/cm^{-1} = 2992 (ν_{N-H}), 2921, 2850 (ν_{C-H}), 1704 ($\nu_{C=O}$), 1575 (ν_{C-0}), 1386 (δ_{C-0}), 1231, 1073 (δ_{C-N}), 1033, 896, 835 (δ_{C-H}), 720, 658 (ν_{C-S}) 610, 539 (ν_{C-N}); **TEM**: d = 13.8 ± 1.1 nm; **UV/Vis**: λ_{max} = 545 nm; **DLS**: d_{hydr} = 29 ± 11 nm.

5.8.3 Re-Complexes of the Ligands

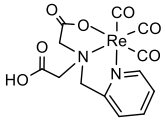

Synthesis of [Re(CO)$_3$PADA]

$(NEt_4)_2[ReBr_3(CO)_3]$ (77 mg, 0.1 mmol, 1 eq.) was dissolved in purged MeOH (10 ml). PADA (22 mg, 0.1 mmol, 1 eq.) dissolved in purged MeOH (2 ml) was added under vigorous stirring and the mixture was heated to 65 °C for 3.5 h under N_2 atmosphere. The solvent was reduced to half of the volume *in vacuo* and the flask was stored at 4 °C for 72 h. Colourless crystals were obtained after 3 d, which were filtered off and dried. The pure product was obtained in a moderate yield (25 mg, 49 µmol, 49%).

^{1}H-NMR (400 MHz, MeOH-d_5): δ/ppm = 8.81 (d, *J* = 5.9 Hz, 1 H, C*H*), 8.10 (t, *J* = 7.3 Hz, 1 H, C*H*), 7.75 (d, *J* = 7.4 Hz, 1 H, C*H*), 7.55 (t, *J* = 5.9 Hz, 1 H, C*H*), 5.25 (d, *J* = 15.5 Hz, 1 H, CH_2), 4.65 (d, *J* = 15.4 Hz, 1 H, CH_2), 4.59 (d, *J* = 16.5 Hz, 1 H, CH_2), 4.40 (d, *J* = 16.5 Hz, 1 H, CH_2), 4.08 (d, *J* = 17.6 Hz, 1 H, CH_2), 3.86 (d, *J* = 17.5 Hz, 1 H, CH_2); **^{13}C{^{1}H} NMR** (100 MHz, DMSO-d_6): δ/ppm = 197.7, 197.5, 197.3, 179.4, 170.4, 160.1, 152.3, 141.0 126.3, 124.5, 68.3, 68.0, 62.1; **IR** (ATR): ν/cm^{-1} 3442 (ν_{O-H}), 2975 (ν_{C-H}), 2021, 1921($\nu_{C\equiv O}$), 1879, 1716, 1616 ($\nu_{C=O}$), 1483, 1445 (δ_{C-H}), 1383 (δ_{C-O}), 1303 (ν_{C-O}), 1197, 1103 (ν_{Re-N}), 996, 914 (ν_{Re-O}), 866 (δ_{O-H}), 768 (δ_{C-H}), 626; **Elemental Analysis:** Anal. Calcd for $C_{14}H_{14}N_2O_7Re$: C, 33.07; H, 2.78; N, 5.51. Found: C, 33.10; H, 5.04; N, 5.41.

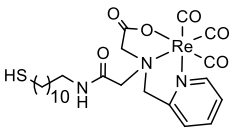

Synthesis of [Re(CO)$_3$PADA-MUAM]

$(NEt_4)_2[ReBr_3(CO)_3]$ (188 mg, 0.24 mmol, 1 eq.) was dissolved in purged MeOH (20 ml). PADA-MUAM (100 mg, 0.24 mmol, 1 eq.) dissolved in purged MeOH (4 ml) was added under vigorous stirring and the mixture was heated to reflux for 19 h under argon atmosphere. The solvent was removed *in vacuo* when the solution cooled down to room temperature and was purified *via* column chromatography ($CHCl_3$: MeOH; 10:2). The pure product was obtained as a brown solid in a rather low yield (51 mg, 0.08 mmol, 33%).

^{1}H-NMR (300 MHz, DMSO-d_6): δ/ppm = 8.75 (d, *J* = 6.5 Hz, 1 H, C*H*), 8.28 (t, *J* = 5.3 Hz, 1 H, N*H*), 8.13 (d, *J* = 7.3 Hz, 1 H, C*H*), 7.81 (d, *J* = 7.3 Hz, 1 H, C*H*), 7.57 (d, *J* = 6.6 Hz, 1 H, C*H*), 5.10 (d, *J* = 16.0 Hz, 1 H, CH_2), 4.61 (d, *J* = 15.5 Hz, 1 H, CH_2), 4.34 (d, *J* = 15.5 Hz, 1 H, CH_2), 4.15 (d, *J* = 16.0 Hz, 1 H, CH_2), 3.96 (d, *J* = 16.0 Hz, 1 H, CH_2), 3.60 (d, *J* = 16.0 Hz, 1 H, CH_2), 3.10 (q, *J* = 8.8 Hz, 2 H, CH_2), 2.68 (t, *J* = 8.2 Hz, 2 H, CH_2), 1.67-1.53 (m, 2 H, CH_2), 1.51-1.39 (m, 2 H, CH_2), 1.38-1.20 (m, 14 H CH_2); **^{13}C{^{1}H} NMR** (75 MHz, DMSO-d_6): δ/ppm = 197.7, 179.3, 167.5, 160.1, 152.3, 140.9, 126.3, 124.5, 69.3, 68.8, 62.4, 39.9, 38.3, 29.4, 29.4, 29.4, 29.3, 29.2, 29.1, 29.0, 28.2, 26.9; **IR** (ATR): ν/cm^{-1} = 3313 (ν_{O-H}), 3087 (ν_{N-H}), 2921, 2846 (ν_{C-H}), 2008, 1914 ($\nu_{C\equiv O}$), 1857, 1645 ($\nu_{C=O}$), 1551 ($\nu_{C=O}$), 1448 (δ_{C-H}), 1349, 1250, 1156 (δ_{C-N}), 1113, 1061 (ν_{Re-N}), 925 (ν_{Re-O}), 774 (δ_{C-H}), 638 (ν_{C-S}), 539 (ν_{C-N}); **Elemental Analysis:** Anal. Calcd for $C_{25}H_{37}N_3O_6ReS$: C, 42.47; H, 5.05; N, 6.19; S, 4.72. Found: C, 38.44; H, 4.13; N, 5.84; S, 3.85.

5.8.4 Surface Functionalisation with a Re-Complex

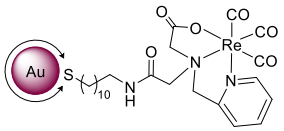

Synthesis of Au-MUAM-PADA-Re(CO)$_3$

Au-Citrate NPs with Ø 13 nm (5 ml) were filtrated using syringe filtration on a cellulose membrane with 0.2 µm pore size. Then, the NP dispersion was degassed with argon for 45 min. The complex [Re(CO)$_3$PADA-MUAM] (5 mg, 7 µmol) dissolved in DMSO (0.2 ml) and the ligand PADA-MUAM (1 mg, 2 µmol) dissolved in DMSO (0.2 ml) were slowly added dropwise. The pH of the reaction mixture was

adjusted by the addition of dil. NaOH (2 drops) in order to achieve a stable clear dispersion, which was stirred at room temperature for 17 h under argon atmosphere. The reaction mixture was purified *via* desalting column PD 10 and the stable pink coloured fractions were collected and stored at 4 °C in the dark.

^{1}H-NMR (600 MHz, D_2O): δ/ppm = 8.40-8.36 (m, 1 H, C*H*), 7.72-7.63 (m, 1 H, C*H*), 7.54-7.45 (m, 1 H, C*H*), 7.20-7.10 (m, 1 H, C*H*), 3.87-3.82 (m, 2 H, CH_2), 3.35-3.31 (m, 2 H, CH_2), 3.17-3.09 (m, 2 H, CH_2), 2.63-2.58 (m, 2 H, CH_2), 1.68-1.56 (m, 2 H, CH_2), 1.42-1.32 (m, 2 H, CH_2), 1.23-1.10 (m, 14 H CH_2); **IR** (ATR): ν/cm^{-1} = 3308 (ν_{O-H}), 3072 (ν_{N-H}), 2921, 2846 (ν_{C-H}), 2017, 1918 ($\nu_{C\equiv O}$), 1862, 1655 ($\nu_{C=O}$), 1584 ($\nu_{C=O}$), 1396 (δ_{C-H}), 1349, 1240, 1151 (δ_{C-N}), 1052 (ν_{Re-N}), 981, 920 (ν_{Re-O}), 835, 770 (δ_{C-H}), 713 (δ_{N-H}), 618 (ν_{C-S}), 534 (ν_{C-N}); **TEM**: d = 12.9 ± 0.9 nm; **UV/Vis**: λ_{max} = 523 nm; **DLS**: d_{hydr} = 15 ± 3 nm.

5.8.5 Labelling of the Ligands

Synthesis of $[^{99m}Tc(OH_2)_3(CO)_3]^+$

A microwave vial (0.5 – 2 ml) was charged with the Isolink kit chemicals sodium boranocarbonate NaBC (4 mg, 38 µmol), sodium tartrate dihydrate (7 mg, 30 µmol) and sodium tetraborate decahydrate (7 mg, 18 µmol). The vial was sealed, purged with N_2 for 20 min and $[^{99m}TcO_4]^-$ eluate (2 ml) from a commercial generator was added. Afterwards, the solution was heated in the microwave to 110 °C for 10 min. Unreacted NaBC was quenched with 1 M HCl to a pH of 2. Then, then pH of the solution was adjusted to 7 or 8 with 1 M NaOH.

5.8.5.1 General Procedure of ^{99m}Tc Radiolabelling

A vial was charged with the ligand dissolved in MeOH, sealed and purged with N_2 into dryness. The residue was redissolved in a certain volume degassed EtOH or degassed H_2O and freshly prepared $[^{99m}Tc(OH_2)_3(CO)_3]^+$ solution was added. The reaction mixture was stirred for a certain time and was monitored *via* HPLC.

Labelling of PADA with $[^{99m}Tc(OH_2)_3(CO)_3]^+$

A vial was charged with a 2 mM MeOH solution of PADA (0.2 ml, 0.4 µmol), sealed and purged with N_2 into dryness. Then, the residue was redissolved in degassed EtOH (0.2 ml) and freshly prepared $[^{99m}Tc(OH_2)_3(CO)_3]^+$ solution (0.4 ml, pH 8) was added. The reaction mixture was stirred at 80 °C for 30 min and analysed *via* HPLC. The complex $[^{99m}Tc(CO)_3PADA]$ was obtained in >99.5% RCP.

Labelling of MUAM-PADA with $[^{99m}Tc(OH_2)_3(CO)_3]^+$

A vial was charged with a 2 mM MeOH solution of MUAM-PADA (0.2 ml, 0.4 µmol), sealed and purged with N_2 into dryness. Then, the residue was redissolved in degassed H_2O (0.2 ml) and freshly prepared $[^{99m}Tc(OH_2)_3(CO)_3]^+$ solution (0.4 ml, pH 8) was added. The reaction mixture was stirred at room temperature for 30 min and analysed *via* HPLC. The complex $[^{99m}Tc(CO)_3PADA\text{-}MUAM]$ was obtained in 91.9% RCP.

Stability test of [^{99m}Tc(CO)$_3$PADA-MUAM] in the presence of Histidine

The reaction mixture of [^{99m}Tc(CO)$_3$PADA-MUAM] was incubated with histidine (0.5 mg, 0.5 µmol) in degassed H_2O (0.1 ml), stirred at room temperature and monitored *via* HPLC analysis. The complex [^{99m}Tc(CO)$_3$PADA-MUAM] remained in 92% RCP.

Labelling of Cys-PADA with [^{99m}Tc(OH$_2$)$_3$(CO)$_3$]$^+$

A vial was charged with a 2 mM MeOH solution of Cys-PADA (0.2 ml, 0.4 µmol), sealed and purged with N_2 into dryness. Then, the residue was redissolved in degassed H_2O (0.2 ml) and freshly prepared [[^{99m}Tc(OH$_2$)$_3$(CO)$_3$]$^+$ solution (0.4 ml, pH 7) was added. The reaction mixture was stirred at room temperature and monitored *via* HPLC analysis. The complex [^{99m}Tc(CO)$_3$PADA-Cys] was obtained in 76% RCP after 300 min.

Labelling of Ac-Cys-PADA with [^{99m}Tc(OH$_2$)$_3$(CO)$_3$]$^+$

A vial was charged with a 2 mM MeOH solution of Ac-Cys-PADA (0.2 ml, 0.4 µmol), sealed and purged with N_2 into dryness. Then, the residue was redissolved in degassed H_2O (0.2 ml) and 1 drop degassed DMF and freshly prepared [^{99m}Tc(OH$_2$)$_3$(CO)$_3$]$^+$ solution (0.4 ml, pH 8) was added. The reaction mixture was stirred at 75 °C for 30 min and monitored *via* HPLC analysis. The complex [^{99m}Tc(CO)$_3$PADA-Cys-Ac] was obtained in 82.6% RCP after 90 min.

5.8.6 Radiolabelling of Au NPs

5.8.6.1 General Procedure of ^{99m}Tc Radiolabelling of functionalised Au NPs

The Au NP dispersion was purified *via* a desalting column (PD MiniTrap). Then, the NP dispersion was purged with N_2 (for 30-45 min). [^{99m}Tc(OH$_2$)$_3$(CO)$_3$]$^+$ was added. The pH of the NP dispersion was adjusted by the addition of base to achieve a stable, clear dispersion. The complexation was monitored *via* SEC HPLC. After [^{99m}Tc(OH$_2$)$_3$(CO)$_3$]$^+$ was consumed or no further change was observed, purification *via* desalting columns (PD 10 or PD mini) took place before the collected pink fractions were further analysed *via* (size exclusion) SEC HPLC.

^{99m}Tc Radiolabelling of Au-MUAM-PADA (Ø 14 nm)

Au-MUAM-PADA NP dispersion with Ø 14 nm (0.5 ml) was purged with N_2. [^{99m}Tc(OH$_2$)$_3$(CO)$_3$]$^+$ (0.5 ml, (a)/(b)/(c) pH 7 or (d) pH 8) was added together with 2 drops NaOH (1 M) in order to achieve a stable pink dispersion. The reaction mixture was stirred at (**a**) room temperature for 165 min, (**b**) 50 °C for 180 min (**c**) 60 °C for 170 min or (**d**) 75 °C for 60 min and subsequently purified *via* a desalting column (PD10 ((**a**) and (**c**)) or PD MiniTrap (**b**) and (**c**)). The pink coloured fractions were collected and further analysed *via* size exclusion HPLC. Furthermore, the activities of the collected fractions were measured with a dose calibrator. Fractions 2 & 3 contained pure labelled functionalised Au NPs.

IR (ATR): ν/cm^{-1} = 3375 (ν_{O-H}), 3087 (ν_{N-H}), 2925, 2823 (ν_{C-H}), 1712 ($\nu_{C=O}$), 1590 (ν_{C-O}), 1390 (δ_{C-O}), 1071 (δ_{C-N}), 971 (δ_{O-H}), 601 (ν_{C-S}), 522 (ν_{C-N}); **TEM**: d = 13.9 ± 1.2 nm; **UV/Vis**: λ_{max} = 528 nm; **DLS**: d_{hydr} = 16 ± 3 nm.

^{99m}Tc Radiolabelling of Au-Cys-PADA (Ø 14 nm)

Au-Cys-PADA NP dispersion with Ø 14 nm (0.5 ml) was purged with N_2. $[^{99m}Tc(OH_2)_3(CO)_3]^+$ (0.5 ml, pH 7) was added together with 1 drop NaOH (1 M) in order to achieve a stable pink dispersion. The reaction mixture was stirred at room temperature for 120 min and subsequently purified *via* a desalting column (PD MiniTrap). The pink coloured fractions were collected and further analysed *via* size exclusion HPLC. Furthermore, the activities of the collected fractions were measured with a dose calibrator. Fractions 2 & 3 contained pure labelled functionalised Au NPs.

IR (ATR): ν/cm^{-1} = 3303 (ν_{O-H}), 2952 (ν_{C-H}), 1598 (ν_{C-O}), 1399 (δ_{C-O}), 976 (δ_{O-H}), 866, 694 (δ_{C-H}/ν_{C-S}), 548 (ν_{C-N}); **TEM**: d = 15.3 ± 4.7 nm; **UV/Vis**: λ_{max} = 575 nm; **DLS**: d_{hydr} = 272 ± 45 nm.

^{99m}Tc Radiolabelling of mixed shell Au-MUDA-AT/MUAM-PADA (Ø 12 nm)

Au-MUDA-AT/MUAM-PADA NP dispersion with Ø 12 nm (0.5 ml) was purged with N_2. $[^{99m}Tc(OH_2)_3(CO)_3]^+$ (0.5 ml, (pH 7) was added together with 2 drops NaOH (1 M) in order to achieve a stable pink dispersion. The reaction mixture was stirred (**a**) for 90 min at room temperature, (**b**) for 30 min at room temperature and 90 min at 60 °C and subsequently purified *via* a desalting column (PD MiniTrap). The pink coloured fractions were collected and further analysed *via* size exclusion HPLC. Furthermore, the activities of the collected fractions were measured with a dose calibrator.

TEM: d = 11.8 ± 1.3 nm; **UV/Vis**: λ_{max} = 528 nm; **DLS**: d_{hydr} = 15 ± 4 nm.

^{99m}Tc Radiolabelling of mixed shell Au-MUDA-ADR/MUAM-PADA (Ø 14 nm)

Au-MUDA-ADR/MUAM-PADA NP dispersion with Ø 14 nm (0.5 ml) was purged with N_2. $[^{99m}Tc(OH_2)_3(CO)_3]^+$ (pH 8) was added together with 1 drop NaOH (1 M) in order to achieve a stable pink dispersion. The reaction mixture was stirred (**a**) at room temperature for 140 min or (**b**) at 75 °C for 30 min and subsequently purified *via* a desalting column (PD10). The pink coloured fractions were collected and further analysed *via* size exclusion HPLC. Furthermore, the activities of the collected fractions were measured with a dose calibrator. Additionally, the collected and analysed pink fractions were used for a second purification step with a new desalting column. Again, the pink coloured fractions were collected and analysed *via* size exclusion HPLC. Furthermore, the activities of the collected fractions were measured with a dose calibrator. All fractions contained pure labelled functionalised Au NPs.

IR (ATR): ν/cm^{-1} = 2952 (ν_{C-H}), 1576 ($\nu_{C=O}$), 1554 (ν_{C-O}), 1330 (δ_{C-O}), 1245, 1042 (δ_{C-N}), 971 (δ_{O-H}), 875, 840 (δ_{C-H}), 693 (ν_{C-S}), 517 (ν_{C-N}); **TEM**: d = 14.0 ± 1.5 nm; **UV/Vis**: λ_{max} = 535 nm; **DLS**: d_{hydr} = 35 ± 13 nm.

^{99m}Tc Radiolabelling of mixed shell Au-MUDA-AT/Cys-PADA (Ø 14 nm)

Au-MUDA-AT/Cys-PADA NP dispersion with Ø 14 nm (0.5 ml) was purged with N_2. $[^{99m}Tc(OH_2)_3(CO)_3]^+$ (0.5 ml, pH 7) was added together with 2 drops NaOH (1 M) in order to achieve a stable dispersion. The reaction mixture was stirred at room temperature for 260 min and subsequently purified *via* a desalting column (PD MiniTrap). The violet coloured fractions were collected and further analysed *via* size exclusion HPLC.

TEM: d = 14.0 ± 1.6 nm; **UV/Vis**: λ_{max} = 551 nm; **DLS**: d_{hydr} = 243 ± 38 nm.

^{99m}Tc Radiolabelling of Au-Citrate (blind study)

Au-Citrate NP dispersion with Ø 14 nm (0.5 ml) was filtrated using syringe filtration on a cellulose membrane with 0.2 µm pore size and was purged with N_2. $[^{99m}Tc(OH_2)_3(CO)_3]^+$ (0.5 ml, pH 7) was added together with 2 drops NaOH (1 M) in order to achieve a stable darker dispersion. The reaction mixture was stirred at room temperature for 60 min and subsequently analysed *via* size exclusion HPLC.

5.8.6.2 General Procedure of a Hot Ligand Exchange

The Au-Citrate NP dispersion was filtrated using syringe filtration on a cellulose membrane with 0.2 µm pore size. Then, the NP dispersion was purged with N_2 (for 30-45 min). [$^{99m}Tc(CO)_3$MUAM-PADA] was added. The pH of the NP dispersion was adjusted by the addition of base to achieve a stable clear dispersion and the reaction mixture was stirred for a certain time. Purification was performed *via* desalting columns (PD 10 or PD mini) before the collected pink fractions were further analysed *via* size exclusion HPLC.

Hot ligand labelling of Au-Citrate (Ø 14 nm) with ^{99m}Tc-MUAM-PADA

Au-Citrate NP dispersion with Ø 14 nm (0.5 ml) was purged with N_2. [$^{99m}Tc(CO)_3$MUAM-PADA] (ca. 0.5 ml, pH 8) was added. The pink reaction mixture was stirred at room temperature for 90 min and subsequently purified *via* a desalting column (PD MiniTrap). The pink coloured fractions were collected and analysed *via* size exclusion HPLC. Furthermore, the activities of the collected fractions were measured with a dose calibrator. All fractions contained pure radiolabelled functionalised Au NPs with a yield of 86% of the overall activity loaded on the column.

IR (ATR): ν/cm^{-1} = 3384 (ν_{O-H}), 2925, 2823 (ν_{C-H}), 1718 ($\nu_{C=O}$), 1594 (ν_{C-O}), 1396 (δ_{C-O}), 1340, 1065 (δ_{C-N}), 960 (δ_{O-H}), 614 (ν_{C-S}), 533 (ν_{C-N}); **TEM**: d = 13.9 ± 1.3 nm; **UV/Vis**: λ_{max} = 526 nm; **DLS**: d_{hydr} = 16 ± 4 nm.

Hot ligand labelling of Au-Citrate (Ø 12 nm) with ^{99m}Tc-MUAM-PADA

Au-Citrate NP dispersion with Ø 12 nm (0.5 ml) was purged with N_2. [$^{99m}Tc(CO)_3$MUAM-PADA] (0.3 ml, pH 7) was added. The pink reaction mixture was stirred at room temperature for 90 min and subsequently purified *via* a desalting column (PD MiniTrap). The pink coloured fractions were collected and analysed *via* size exclusion HPLC. Additionally, these fractions were used for a second purification step with a new desalting column. Again, the pink coloured fractions were collected and analysed *via* size exclusion HPLC. Furthermore, the activities of the collected fractions were measured with a dose calibrator. All fractions contained pure labelled functionalised Au NPs.

TEM: d = 11.9 ± 1.2 nm; **UV/Vis**: λ_{max} = 528 nm; **DLS**: d_{hydr} = 12 ± 3 nm.

5.9 Studies on the Functionality of the Synthesised Nanoparticles

Experiments on the functionality of the NPs were performed at the Institute of Veterinary Physiology and Biochemistry at the Justus Liebig University Giessen by Rebecca Claßen as part of her PhD thesis.

Depending on the type of NPs, they were tested in isometric contraction measurements on their (relaxing or contracting) effect on a smooth trachea muscle of a rat or they were studied in Ussing Chamber experiments to investigate their receptor activation on rat Jejunal epithelial membranes.

5.9.1 Isometric Contraction Measurements

The synthesised Au NPs were tested in isometric contraction measurements on their receptor effects. An isometric contraction is a static contraction without a change in the length of the muscle. Instead, the force with which the muscle pulls at the force transducer is measured. In this way it is possible to detect muscle contractions or relaxations. The measurements were performed in an organ bath, shown Figure 101. In this setup, the interaction between the parasympathetic (contraction by the acetylcholine derivative carbachol) and the sympathetic (relaxation by norepinephrine or epinephrine) nervous system can be investigated.

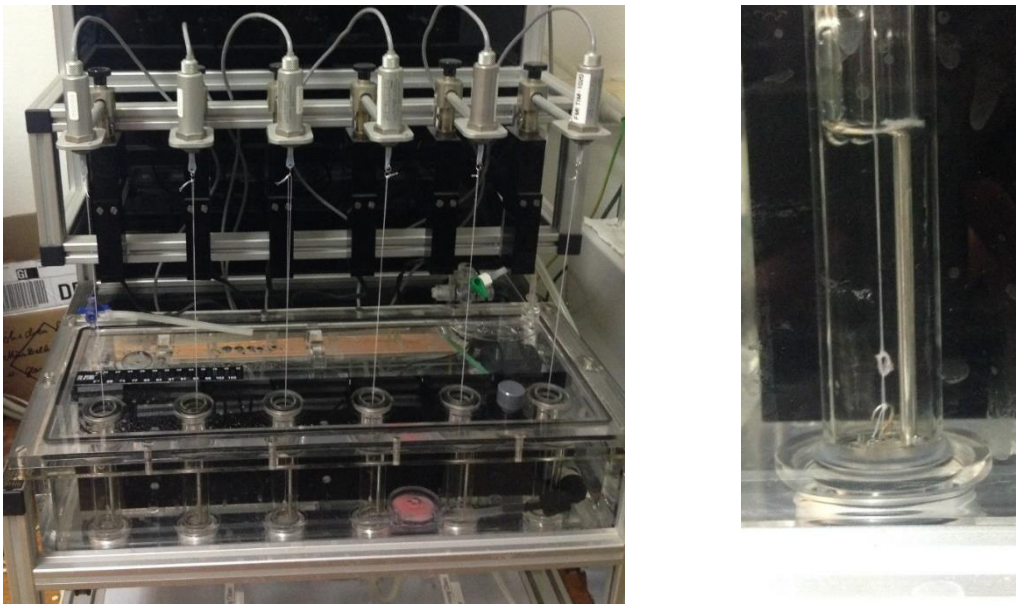

Figure 101: Set of organ baths (**left**) with rat trachea muscle restrained in the middle (**right**).

5.9.1.1 Setup of a Muscle Bath and Procedure of a Measurement

A muscle bath consists of a chamber which is filled with 10 ml Parsons buffer solution **Figure 102** (**left**). This chamber is surrounded by a temperature-controlled water bath. A gas mixture of 5% CO_2/ 95% O_2 flows through the buffer solution *via* an opening at the bottom of the chamber. The tissue is restrained in the middle between the bottom of the chamber and the force transducer. A contraction or relaxation is detected by the force transducer, transformed into voltage, amplified, displayed and analysed on the computer (**Figure 102** (**right**).[346] The experiments were performed on smooth muscle tissue of a rat trachea.

solution	composition [in mmol·L^{-1}]
Parsons buffer solution	107 NaCl; 25 $NaHCO_3$; 12.2 Glucose; 4.5 KCl; 1.8 Na_2HPO_4; 1.25 $CaCl_2$; 1 $MgSO_4$; 0.2 NaH_2PO_4. brought to pH = 7.4 with addition of NaOH/HCl

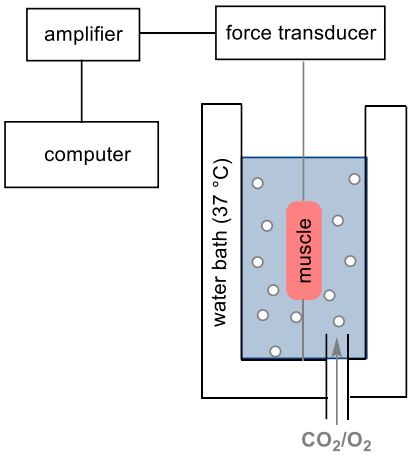

Figure 102: Composition of Parsons buffer solution (**left**) and schematic set up of a muscle bath (**right**).

After preparation of the tissue, it was clamped in the chamber which was filled with warm and gas-flowing Parsons buffer solution. The force transducer was adjusted electrically, and the voltage was calibrated to a value of 1 g. In a period of approx. 10 min an equilibrium was adjusted. Prior to the addition of the substances to be tested, carbachol (10 µM) was added as a stable acetylcholine derivative to trigger a pre-contraction of the rat trachea and to create a stable standard of the tissue. Subsequently, the substances (NPs) were added and the resulting relaxation or contraction was measured.[316]

Animals

Female and male Wistar rats with a body mass of 200 – 250 g were used. The animals were bred and housed at the Institute for Veterinary Physiology and Biochemistry of the Justus Liebig University Giessen at an ambient temperature of 22.5 °C and air humidity of 50 – 55% on a 12 h : 12 h light-dark cycle with free access to water and food until the time of the experiment. Experiments were approved by the animal welfare officer of the Justus Liebig University (administrative number 577_M) and performed according to the German and European animal welfare law.

Tissue preparation

Animals were anaesthetised in a cage filled with air (20% O_2) by pure CO_2 (flow rate 20% of the cage volume/min) and killed by a cervical dislocation and heart cut after opening the chest cavity. By using thin tweezers and scissors, trachea rings about 0.5 cm in size were isolated and kept refrigerated in Parsons buffer solution at 0 °C until use.

5.9.2 Ussing Chamber Experiments

Receptor activities and the ability of a substance to stimulate receptors can be investigated in Ussing Chamber setups. Here, jejunal epithelium of a rat's intestines was used and restrained in the middle of the chamber. A short circuit current (I_{sc}) was measured to detect the receptor activities after the addition of an agent of interest. In a standard Ussing Chamber setup, the substance of interest is added on the same side on which the receptors to be investigated are located. A stimulation of the receptors would be displayed in an increase of the measured I_{sc}. Measuring an increase in I_{sc} is equivalent to a strong Ca^{2+} or a respective cAMP-dependent Cl^- secretion, which is a direct result from the stimulation of the receptors with the agent of interest.

5.9.2.1 Setup of an Ussing Chamber and Procedure of a Measurement

As shown in **Figure 103**, an Ussing Chamber consists of two half chambers, which are separated in the middle by the tissue to be investigated. In this work, epithelial tissue from the rats jejunum was used. The half chambers are filled with Parsons buffer solution (pH 7.4) and incubated at 37 °C. The solution is gassed with carbogen (5% CO_2 in 95% O_2, v/v) *via* an opening at the bottom of each half chamber. Throughout the entire experiment, the tissue was short-circuited by a computer-controlled voltage-clamp device (**Figure 103**).

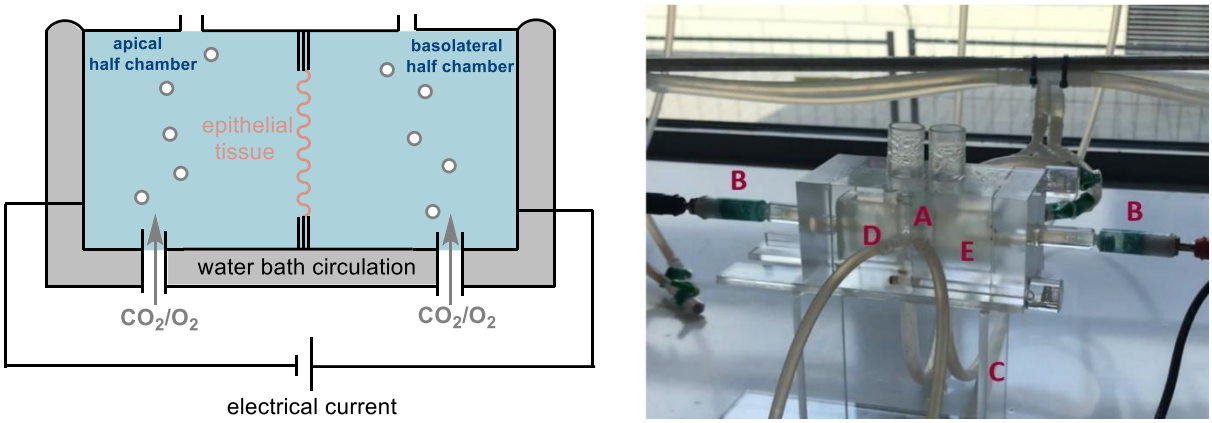

Figure 103: Schematic illustration of an Ussing Chamber (**left**) and actual laboratory setup (**right**) consisting of an intestinal/epithelial tissue preparation (**A**), Ag-AgCl electrodes (**B**), O_2/CO_2 supply (**C**), an apical compartment (half chamber, **D**) and a basolateral compartment (half chamber, **E**).

The prepared tissue was fixed in the Ussing Chamber and incubated in gas-flowing Parsons buffer solution at 37 °C. The substance of interest was basolaterally added. The tissue was incubated for a certain time before carbachol (CCh) as a M_3 receptor agonist was added on the basolateral side to attempt a stimulation of the receptors. At the end of an experiment, the secretagogue forskolin (Forsk.) was inserted to test the tissue viability by inducing a strong increase of the measured I_{sc}.

Animals

Female and male Wistar rats with a body mass of 200 – 250 g were used. The animals were bred and housed at the Institute for Veterinary Physiology and Biochemistry of the Justus Liebig University Giessen at an ambient temperature of 22.5 °C and air humidity of 50 – 55% on a 12 h : 12 h light-dark cycle with free access to water and food until the time of the experiment. Experiments were approved by the named animal welfare officer of the Justus Liebig University (administrative number 577_M) and performed according to the German and European animal welfare law.

Tissue preparation

Animals were killed by stunning followed by exsanguination. The serosa and tunica muscularis were stripped away by hand to obtain a mucosa-submucosa preparation of the proximal colon. Briefly, the colon was placed on a small plastic rod with a diameter of 5 mm. A circular incision was made near the anal end with a blunt scalpel, and the serosa together with the tunica muscularis were gently removed in a proximal direction. Two segments of the proximal colon of each rat were prepared. In the case of the jejunum, unstripped preparations were used.

6 REFERENCES

1 N. Taniguchi, On the Basic Concept of Nanotechnology, Tokyo, 1974.

2 M. S. Ermolin, P. S. Fedotov, N. A. Malik and V. K. Karandashev, *Chemosphere*, 2018, **200**, 16–22.

3 N. Tepe and M. Bau, *Sci. Total Environ.*, 2014, **488-489**, 243–251.

4 A. Mattern, F. Machka, M. S. Wickleder, O. S. Ilyaskina, M. Bünemann, M. Diener and E. Pouokam, *Org. Biomol. Chem.*, 2018, **16**, 6680–6687.

5 C. Rohner, I. Tavernaro, L. Chen, P. J. Klar and S. Schlecht, *Phys. Chem. Chem. Phys.*, 2015, **17**, 5932–5941.

6 A. Borowik, R. Banasiuk, N. Derewonko, M. Rychlowski, M. Krychowiak-Masnicka, D. Wyrzykowski, M. Ziabka, A. Woziwodzka, A. Krolicka and J. Piosik, *Sci. Rep.*, 2019, **9**, 4987.

7 G. D. M. R. Dabera, M. Walker, A. M. Sanchez, H. J. Pereira, R. Beanland and R. A. Hatton, *Nat. Commun.*, 2017, **8**, 1894.

8 B. Kumanek, G. Stando, P. Stando, K. Matuszek, K. Z. Milowska, M. Krzywiecki, M. Gryglas-Borysiewicz, Z. Ogorzałek, M. C. Payne, D. MacFarlane and D. Janas, *Sci. Rep.*, 2021, **11**, 8649.

9 K. R. Wierzbinski, T. Szymanski, N. Rozwadowska, J. D. Rybka, A. Zimna, T. Zalewski, K. Nowicka-Bauer, A. Malcher, M. Nowaczyk, M. Krupinski, M. Fiedorowicz, P. Bogorodzki, P. Grieb, M. Giersig and M. K. Kurpisz, *Sci. Rep.*, 2018, **8**, 3682.

10 I. Tavernaro, C. Cavelius, H. Peuschel and A. Kraegeloh, *Beilstein J. Nanotechnol.*, 2017, **8**, 1283–1296.

11 A. S. Schulze, I. Tavernaro, F. Machka, O. Dakischew, K. S. Lips and M. S. Wickleder, *J. Nanopart. Res.*, 2017, **19**, 475401.

12 A. Creamer, C. S. Wood, P. D. Howes, A. Casey, S. Cong, A. V. Marsh, R. Godin, J. Panidi, T. D. Anthopoulos, C. H. Burgess, T. Wu, Z. Fei, I. Hamilton, M. A. McLachlan, M. M. Stevens and M. Heeney, *Nat. Commun.*, 2018, **9**, 3237.

13 S. Karimi and H. Namazi, *New J. Chem.*, 2021, **45**, 6397–6405.

14 T. Repenko, A. Rix, S. Ludwanowski, D. Go, F. Kiessling, W. Lederle and A. J. C. Kuehne, *Nat. Commun.*, 2017, **8**, 470.

15 N. Bono, C. Pennetta, M. C. Bellucci, A. Sganappa, C. Malloggi, G. Tedeschi, G. Candiani and A. Volonterio, *ACS Omega*, 2019, **4**, 6796–6807.

16 Z. Hua, A. Pitto-Barry, Y. Kang, N. Kirby, T. R. Wilks and R. K. O'Reilly, *Polym. Chem.*, 2016, **7**, 4254–4262.

17 G. Arias-Alpizar, L. Kong, R. C. Vlieg, A. Rabe, P. Papadopoulou, M. S. Meijer, S. Bonnet, S. Vogel, J. van Noort, A. Kros and F. Campbell, *Nat. Commun.*, 2020, **11**, 3638.

18 W. Deng, W. Chen, S. Clement, A. Guller, Z. Zhao, A. Engel and E. M. Goldys, *Nat. Commun.*, 2018, **9**, 2713.

19 A. R. Salgarella, A. Zahoranová, P. Šrámková, M. Majerčíková, E. Pavlova, R. Luxenhofer, J. Kronek, I. Lacík and L. Ricotti, *Sci. Rep.*, 2018, **8**, 9893.

20 X. Wang, Y. Feng, J. Fu, C. Wu, B. He, H. Zhang, X. Wang, W. Dai, Y. Sun and Q. Zhang, *AAPS PharmSciTech*, 2019, **20**, 316.

21 M. L. Brader, S. J. Williams, J. M. Banks, W. H. Hui, Z. H. Zhou and L. Jin, *Biophys. J.*, 2021, **120**, 1–5.

22 M. J. Mulligan, K. E. Lyke, N. Kitchin, J. Absalon, A. Gurtman, S. Lockhart, K. Neuzil, V. Raabe, R. Bailey, K. A. Swanson, P. Li, K. Koury, W. Kalina, D. Cooper, C. Fontes-Garfias, P.-Y. Shi, Ö. Türeci, K. R. Tompkins, E. E. Walsh, R. Frenck, A. R. Falsey, P. R. Dormitzer, W. C. Gruber, U. Şahin and K. U. Jansen, *Nature*, 2020, **586**, 589–593.

23 K. Pabortsava and R. S. Lampitt, *Nat. Commun.*, 2020, **11**, 4073.

24 K. Möller and T. Bein, *Chem. Mater.*, 2019, **31**, 4364–4378.

25 R. Wei, Z. Cai, B. W. Ren, A. Li, H. Lin, K. Zhang, H. Chen, H. Shan, H. Ai and J. Gao, *Chem. Mater.*, 2018, **30**, 7950–7961.

26 L. Shmakova, S. Malavin, N. Iakovenko, T. Vishnivetskaya, D. Shain, M. Plewka and E. Rivkina, *Curr. Biol.*, 2021, **31**, R712-R713.

27 C. Ricci and G. Melone, *Hydrobiologia*, 2000, **418**, 73–80.

28 V. H. Grassian, *J. Phys. Chem. C*, 2008, **112**, 18303–18313.

29 B. Molleman and T. Hiemstra, *Phys. Chem. Chem. Phys.*, 2018, **20**, 20575–20587.

30 P. Schlexer, A. B. Andersen, B. Sebok, I. Chorkendorff, J. Schiøtz and T. W. Hansen, *Part. Part. Syst. Charact.*, 2019, **36**, 1800480.

31 J. L. Huang, Z. Li, H. H. Duan, Z. Y. Cheng, Y. D. Li, J. Zhu and R. Yu, *J. Am. Chem. Soc.*, 2017, **139**, 575–578.

32 B. Molleman and T. Hiemstra, *Environ. Sci.: Nano*, 2017, **4**, 1314–1327.

33 B. Molleman and T. Hiemstra, *Langmuir*, 2015, **31**, 13361–13372.

34 S. Xiong, S. George, Z. Ji, S. Lin, H. Yu, R. Damoiseaux, B. France, K. W. Ng and S. C. J. Loo, *Arch. Toxicol.*, 2013, **87**, 99–109.

35 L. An, Di Zhang, L. Zhang and G. Feng, *Nanoscale*, 2019, **11**, 9563–9573.

36 T. Hiemstra, *Environ. Sci.: Nano*, 2018, **5**, 752–764.

37 Z.-Q. Zhang and S.-C. Song, *Biomaterials*, 2016, **106**, 13–23.

38 A. Mashhadi Malekzadeh, A. Ramazani, S. J. Tabatabaei Rezaei and H. Niknejad, *J. Colloid Interface Sci.*, 2017, **490**, 64–73.

39 R. Lin, Y. Li, T. MacDonald, H. Wu, J. Provenzale, X. Peng, J. Huang, L. Wang, A. Y. Wang, J. Yang and H. Mao, *Colloids Surf., B*, 2017, **150**, 261–270.

40 H. Zeng, L. Zhai, T. Qiao, Y. Yu, J. Zhang and D. Li, *Sci. Rep.*, 2020, **10**, 9335.

41 G. Guisbiers, *Adv. Phys.: X*, 2019, **4**, 1668299.

42 L. D. Geoffrion and G. Guisbiers, *J. Phys. Chem. Solids*, 2020, **140**, 109320.

43 A. Campos, N. Troc, E. Cottancin, M. Pellarin, H.-C. Weissker, J. Lermé, M. Kociak and M. Hillenkamp, *Nat. Phys.*, 2019, **15**, 275–280.

44 K. Kolwas and A. Derkachova, *Nanomaterials*, 2020, **10**, 1411.

45 H. de Puig, J. O. Tam, C.-W. Yen, L. Gehrke and K. Hamad-Schifferli, *J. Phys. Chem. C Nanomater. Interfaces*, 2015, **119**, 17408–17415.

46 A. Kohut, L. P. Villy, A. Kéri, Á. Bélteki, D. Megyeri, B. Hopp, G. Galbács and Z. Geretovszky, *Sci. Rep.*, 2021, **11**, 5117.

47 R. Jin and T. Higaki, *Commun. Chem.*, 2021, **4**, 10346.

48 A. Sohrabi Kashani, A. Piekny and M. Packirisamy, *Microsyst. Nanoeng.*, 2020, **6**, 110.

49 G. A. Monti, G. A. Fernández, N. M. Correa, R. D. Falcone, F. Moyano and G. F. Silbestri, *R. Soc. Open Sci.*, 2017, **4**, 170481.

50 M. J. MacLeod and J. A. Johnson, *J. Am. Chem. Soc.*, 2015, **137**, 7974–7977.

51 U. Kostiv, Z. Farka, M. J. Mickert, H. H. Gorris, N. Velychkivska, O. Pop-Georgievski, M. Pastucha, E. Odstrčilíková, P. Skládal and D. Horák, *Biomacromolecules*, 2020, **21**, 4502–4513.

52 E. A. Egorova, M. M. J. van Rijt, N. Sommerdijk, G. S. Gooris, J. A. Bouwstra, A. L. Boyle and A. Kros, *ACS Nano*, 2020, **14**, 5874–5886.

53 P. Priyananda, H. Sabouri, N. Jain and B. S. Hawkett, *Langmuir*, 2018, **34**, 3068–3075.

54 G. M. D. M. Rúbio, B. K. Keppler, J. M. Chin and M. R. Reithofer, *Chem. Eur. J.*, 2020, **26**, 15859–15862.

55 L. Staiger, T. Kratky, S. Günther, O. Tomanek, R. Zbořil, R. W. Fischer, R. A. Fischer and M. Cokoja, *ChemCatChem*, 2021, **13**, 227–234.

56 G. Fritz, V. Schädler, N. Willenbacher and N. J. Wagner, *Langmuir*, 2002, **18**, 6381–6390.

57 D. Selli and C. Di Valentin, *J. Phys. Chem. C Nanomater. Interfaces*, 2016, **120**, 29190–29201.

58 S. Schöttler, G. Becker, S. Winzen, T. Steinbach, K. Mohr, K. Landfester, V. Mailänder and F. R. Wurm, *Nat. Nanotechnol.*, 2016, **11**, 372–377.

59 E. Steiert, J. Ewald, A. Wagner, U. A. Hellmich, H. Frey and P. R. Wich, *Polym. Chem.*, 2020, **11**, 551–559.

60 X. Li, L. Liu, S. Li, Y. Wan, J.-X. Chen, S. Tian, Z. Huang, Y.-F. Xiao, X. Cui, C. Xiang, Q. Tan, X.-H. Zhang, W. Guo, X.-J. Liang and C.-S. Lee, *ACS Nano*, 2019, **13**, 12901–12911.

61 Q. Xu, L. M. Ensign, N. J. Boylan, A. Schön, X. Gong, J.-C. Yang, N. W. Lamb, S. Cai, T. Yu, E. Freire and J. Hanes, *ACS Nano*, 2015, **9**, 9217–9227.

62 G. Vilé, N. Almora-Barrios, S. Mitchell, N. López and J. Pérez-Ramírez, *Chem. Eur. J.*, 2014, **20**, 5926–5937.

63 R. Coppage, J. M. Slocik, B. D. Briggs, A. I. Frenkel, H. Heinz, R. R. Naik and M. R. Knecht, *J. Am. Chem. Soc.*, 2011, **133**, 12346–12349.

64 A. Mandl, S. L. Filbrun and J. D. Driskell, *Bioconjugate Chem.*, 2017, **28**, 38–42.

65 D. Fleischmann, S. Maslanka Figueroa and A. Goepferich, *ACS Appl. Bio Mater.*, 2021, **4**, 640–650.

66 M. Felber, M. Bauwens, J. M. Mateos, S. Imstepf, F. M. Mottaghy and R. Alberto, *Chem. Eur. J.*, 2015, **21**, 6090–6099.

67 S. Garbujo, E. Galbiati, L. Salvioni, M. Mazzucchelli, G. Frascotti, X. Sun, S. Megahed, N. Feliu, D. Prosperi, W. J. Parak and M. Colombo, *Chem. Commun.*, 2020, **56**, 11398–11401.

68 X. Huang, J. Z. Williams, R. Chang, Z. Li, C. E. Burnett, R. Hernandez-Lopez, I. Setiady, E. Gai, D. M. Patterson, W. Yu, K. T. Roybal, W. A. Lim and T. A. Desai, *Nat. Nanotechnol.*, 2021, **16**, 214–223.

69 S. Sun, S. Yang, H. L. Xin, D. Nykypanchuk, M. Liu, H. Zhang and O. Gang, *Nat. Commun.*, 2020, **11**, 2279.

70 K. K. Sandhu, C. M. McIntosh, J. M. Simard, S. W. Smith and V. M. Rotello, *Bioconjugate Chem.*, 2002, **13**, 3–6.

71 Y. Jiang, S. Huo, T. Mizuhara, R. Das, Y.-W. Lee, S. Hou, D. F. Moyano, B. Duncan, X.-J. Liang and V. M. Rotello, *ACS Nano*, 2015, **9**, 9986–9993.

72 T. Osaka, T. Nakanishi, S. Shanmugam, S. Takahama and H. Zhang, *Colloids Surf., B*, 2009, **71**, 325–330.

73 V. K. LaMer and R. H. Dinegar, *J. Am. Chem. Soc.*, 1950, **72**, 4847–4854.

74 R. Xing, F. Xu, S. Liu and J. Niu, *Mater. Lett.*, 2014, **134**, 71–74.

75 J. Knossalla, P. Paciok, D. Göhl, D. Jalalpoor, E. Pizzutilo, A. M. Mingers, M. Heggen, R. E. Dunin-Borkowski, K. J. J. Mayrhofer, F. Schüth and M. Ledendecker, *J. Am. Chem. Soc.*, 2018, **140**, 15684–15689.

76 Z. Chen, J. W. Chang, C. Balasanthiran, S. T. Milner and R. M. Rioux, *J. Am. Chem. Soc.*, 2019, **141**, 4328–4337.

77 J.-H. Lee, K. J. Gibson, G. Chen and Y. Weizmann, *Nat. Commun.*, 2015, **6**, 7571.

78 M. R. K. Ali, B. Snyder and M. A. El-Sayed, *Langmuir*, 2012, **28**, 9807–9815.

79 K. I. Requejo, A. V. Liopo and E. R. Zubarev, *Langmuir*, 2020, **36**, 3758–3769.

80 A. G. Butterfield, C. R. McCormick, J. M. Veglak and R. E. Schaak, *J. Am. Chem. Soc.*, 2021, **143**, 7915–7919.

81 S. Zhou, J. Li, K. D. Gilroy, J. Tao, C. Zhu, X. Yang, X. Sun and Y. Xia, *ACS Nano*, 2016, **10**, 9861–9870.

82 A. Ruditskiy and Y. Xia, *J. Am. Chem. Soc.*, 2016, **138**, 3161–3167.

83 Z. Chen, T. Balankura, K. A. Fichthorn and R. M. Rioux, *ACS Nano*, 2019, **13**, 1849–1860.

84 A. J. Biacchi and R. E. Schaak, *ACS Nano*, 2011, **5**, 8089–8099.

85 X. Zhang, P. Li, Á. Barreda, Y. Gutiérrez, F. González, F. Moreno, H. O. Everitt and J. Liu, *Nanoscale Horiz.*, 2016, **1**, 75–80.

86 C. G. Khoury and T. Vo-Dinh, *J. Phys. Chem. C Nanomater. Interfaces*, 2008, **112**, 18849–18859.

87 X. Cao, C. Shi, W. Lu, H. Zhao, M. Wang, W. Tong, J. Dong, X. Han and W. Qian, *J. Nanosci. Nanotechnol.*, 2015, **15**, 4829–4836.

88 A. Tomitaka, H. Arami, A. Ahmadivand, N. Pala, A. J. McGoron, Y. Takemura, M. Febo and M. Nair, *Sci. Rep.*, 2020, **10**, 10115.

89 F. Liebig, R. Henning, R. M. Sarhan, C. Prietzel, C. N. Z. Schmitt, M. Bargheer and J. Koetz, *RSC Adv.*, 2019, **9**, 23633–23641.

90 Y. Xiong, J. M. McLellan, J. Chen, Y. Yin, Z.-Y. Li and Y. Xia, *J. Am. Chem. Soc.*, 2005, **127**, 17118–17127.

91 Y. Huang, A. R. Ferhan, Y. Gao, A. Dandapat and D.-H. Kim, *Nanoscale*, 2014, **6**, 6496–6500.

92 K. Nambara, K. Niikura, H. Mitomo, T. Ninomiya, C. Takeuchi, J. Wei, Y. Matsuo and K. Ijiro, *Langmuir*, 2016, **32**, 12559–12567.

93 C. Carnovale, G. Bryant, R. Shukla and V. Bansal, *ACS Omega*, 2019, **4**, 242–256.

94 J. Yue, T. J. Feliciano, W. Li, A. Lee and T. W. Odom, *Bioconjugate Chem.*, 2017, **28**, 1791–1800.

95 G. B. Kauffman, *Gold Bull.*, 1985, **18**, 31–44.

96 J. v. Liebig, *Familiar Letters on Chemistry*, Walton & Maberly, London, 1859, p. 42.

97 W. Pagel, *Paracelsus an Introduction to Philosophical Medicine in the Era of the Renaissance*, Karger, Basel, 2nd edn., 1982.

98 J. Kunckels, *Nuetzliche Observationes oder Anmerkungen von Auro und Argento potabili*, G. Schultzens, Hamburg, 1676, p. 117.

99 E. A. Hauser, *J. Chem. Educ.*, 1952, **29**, 456–458.

100 L. B. Hunt, *Gold Bull.*, 1976, **9**, 134–139.

101 M. Faraday, *Philos. Trans. R. Soc. London*, 1857, **147**, 145–181.

102 P. D. Jadzinsky, G. Calero, C. J. Ackerson, D. A. Bushnell and R. D. Kornberg, *Science*, 2007, **318**, 430–433.

103 M. W. Heaven, A. Dass, P. S. White, K. M. Holt and R. W. Murray, *J. Am. Chem. Soc.*, 2008, **130**, 3754–3755.

104 N. Yan, N. Xia, L. Liao, M. Zhu, F. Jin, R. Jin and Z. Wu, *Sci. Adv.*, 2018, **4**, 7259.

105 T. Lahtinen, E. Hulkko, K. Sokołowska, T.-R. Tero, V. Saarnio, J. Lindgren, M. Pettersson, H. Häkkinen and L. Lehtovaara, *Nanoscale*, 2016, **8**, 18665–18674.

106 M. Haruta, N. Yamada, T. Kobayashi and S. Iijima, *J. Catal.*, 1989, **115**, 301–309.

107 L. Prati, A. Villa, A. Jouve, A. Beck, C. Evangelisti and A. Savara, *Faraday Discuss.*, 2018, **208**, 395–407.

108 G. Bond and D. Thompson, *Gold Bull.*, 2009, **42**, 247–259.

109 G. Bond and P. A. Sermon, *Gold Bull.*, 1973, **6**, 102–105.

110 P. D. Giorgi, N. Elizarov and S. Antoniotti, *ChemCatChem*, 2017, **9**, 1830–1836.

111 G. Hajisalem, M. S. Nezami and R. Gordon, *Nano Lett.*, 2017, **17**, 2940–2944.

112 Y. Zhao, Y. Huang, H. Zhu, Q. Zhu and Y. Xia, *J. Am. Chem. Soc.*, 2016, **138**, 16645–16654.

113 D. Huang, F. Liao, S. Molesa, D. Redinger and V. Subramanian, *J. Electrochem. Soc.*, 2003, **150**, G412.

114 T. Teranishi, *C. R. Chim.*, 2003, **6**, 979–987.

115 I. de Lázaro and D. J. Mooney, *Nat. Mater.*, 2020, **19**, 486–487.

116 A. Nel, E. Ruoslahti and H. Meng, *ACS Nano*, 2017, **11**, 9567–9569.

117 X. Wang, S. Gao, Z. Qin, R. Tian, G. Wang, X. Zhang, L. Zhu and X. Chen, *ACS Appl. Mater. Interfaces*, 2018, **10**, 15140–15149.

118 J. Wang, Y. Zhang, N. Jin, C. Mao and M. Yang, *ACS Appl. Mater. Interfaces*, 2019, **11**, 11136–11143.

119 P. K. Jain, K. S. Lee, I. H. El-Sayed and M. A. El-Sayed, *J. Phys. Chem. B*, 2006, **110**, 7238–7248.

120 J. Nam, S. Son, L. J. Ochyl, R. Kuai, A. Schwendeman and J. J. Moon, *Nat. Commun.*, 2018, **9**, 1074.

121 A.-W. Zhang, W.-H. Guo, Y.-F. Qi, J.-Z. Wang, X.-X. Ma and D.-X. Yu, *Nanoscale Res. Lett.*, 2016, **11**, 279.

122 A. S. Schwartz-Duval, C. J. Konopka, P. Moitra, E. A. Daza, I. Srivastava, E. V. Johnson, T. L. Kampert, S. Fayn, A. Haran, L. W. Dobrucki and D. Pan, *Nat. Commun.*, 2020, **11**, 4530.

123 Y. Cheng, J. D. Meyers, A.-M. Broome, M. E. Kenney, J. P. Basilion and C. Burda, *J. Am. Chem. Soc.*, 2011, **133**, 2583–2591.

124 S. Kolemen, T. Ozdemir, D. Lee, G. M. Kim, T. Karatas, J. Yoon and E. U. Akkaya, *Angew. Chem., Int. Ed.*, 2016, **55**, 3606–3610.

125 P. García Calavia, M. J. Marín, I. Chambrier, M. J. Cook and D. A. Russell, *Photochem. Photobiol. Sci.*, 2018, **17**, 281–289.

126 Z. R. Goddard, A. M. Beekman, M. M. D. Cominetti, M. A. O'Connell, I. Chambrier, M. J. Cook, M. J. Marín, D. A. Russell and M. Searcey, *RSC Med. Chem.*, 2020, **12**, 288–292.

127 W. Sun, L. Luo, Y. Feng, Y. Cai, Y. Zhuang, R.-J. Xie, X. Chen and H. Chen, *Angew. Chem., Int. Ed.*, 2020, **59**, 9914–9921.

128 Y. Cheng, A. C Samia, J. D. Meyers, I. Panagopoulos, B. Fei and C. Burda, *J. Am. Chem. Soc.*, 2008, **130**, 10643–10647.

129 M. Camerin, M. Moreno, M. J. Marín, C. L. Schofield, I. Chambrier, M. J. Cook, O. Coppellotti, G. Jori and D. A. Russell, *Photochem. Photobiol. Sci.*, 2016, **15**, 618–625.

130 J. Lin, S. Wang, P. Huang, Z. Wang, S. Chen, G. Niu, W. Li, J. He, D. Cui, G. Lu, X. Chen and Z. Nie, *ACS Nano*, 2013, **7**, 5320–5329.

131 X. Wei, H. Chen, H. P. Tham, N. Zhang, P. Xing, G. Zhang and Y. Zhao, *ACS Appl. Nano Mater.*, 2018, **1**, 3663–3672.

132 J. F. Hainfeld, F. A. Dilmanian, D. N. Slatkin and H. M. Smilowitz, *J. Pharm. Pharmacol.*, 2008, **60**, 977–985.

133 K. T. Butterworth, J. R. Nicol, M. Ghita, S. Rosa, P. Chaudhary, C. K. McGarry, H. O. McCarthy, G. Jimenez-Sanchez, R. Bazzi, S. Roux, O. Tillement, J. A. Coulter and K. M. Prise, *Nanomedicine*, 2016, **11**, 2035–2047.

134 L. Bennie, S. A. Belhout, S. J. Quinn and J. A. Coulter, *ACS Appl. Nano Mater.*, 2020, **3**, 3157–3162.

135 K. Bromma, L. Cicon, W. Beckham and D. B. Chithrani, *Sci. Rep.*, 2020, **10**, 12096.

136 A. V. Verkhovtsev, A. V. Korol and A. V. Solov'yov, *J. Phys. Chem. C*, 2015, **119**, 11000–11013.

137 J. F. Hainfeld, S. M. Ridwan, F. Y. Stanishevskiy and H. M. Smilowitz, *Sci. Rep.*, 2020, **10**, 15627.

138 J. F. Hainfeld, H. M. Smilowitz, M. J. O'Connor, F. A. Dilmanian and D. N. Slatkin, *Nanomedicine*, 2013, **8**, 1601–1609.

139 X.-D. Zhang, Di Wu, X. Shen, J. Chen, Y.-M. Sun, P.-X. Liu and X.-J. Liang, *Biomaterials*, 2012, **33**, 6408–6419.

140 X.-D. Zhang, J. Chen, Z. Luo, Di Wu, X. Shen, S.-S. Song, Y.-M. Sun, P.-X. Liu, J. Zhao, S. Huo, S. Fan, F. Fan, X.-J. Liang and J. Xie, *Adv. Healthcare Mater.*, 2014, **3**, 133–141.

141 S. Lv, Y. Wu, K. Cai, H. He, Y. Li, M. Lan, X. Chen, J. Cheng and L. Yin, *J. Am. Chem. Soc.*, 2018, **140**, 1235–1238.

142 M. U. Farooq, V. Novosad, E. A. Rozhkova, H. Wali, A. Ali, A. A. Fateh, P. B. Neogi, A. Neogi and Z. Wang, *Sci. Rep.*, 2018, **8**, 2907.

143 Y. Wang, J. E. Q. Quinsaat, T. Ono, M. Maeki, M. Tokeshi, T. Isono, K. Tajima, T. Satoh, S.-I. Sato, Y. Miura and T. Yamamoto, *Nat. Commun.*, 2020, **11**, 6089.

144 R. Chowdhury, H. Ilyas, A. Ghosh, H. Ali, A. Ghorai, A. Midya, N. R. Jana, S. Das and A. Bhunia, *Nanoscale*, 2017, **9**, 14074–14093.

145 W. Ma, A. Saccardo, D. Roccatano, D. Aboagye-Mensah, M. Alkaseem, M. Jewkes, F. Di Nezza, M. Baron, M. Soloviev and E. Ferrari, *Nat. Commun.*, 2018, **9**, 1489.

146 R. Khandelia, A. Jaiswal, S. S. Ghosh and A. Chattopadhyay, *J. Mater. Chem. B*, 2014, **2**, 6472–6477.

147 F. Gasiorek, E. Pouokam, M. Diener, S. Schlecht and M. S. Wickleder, *Org. Biomol. Chem.*, 2015, **13**, 9984–9992.

148 R. Kozlowski, A. Ragupathi and R. B. Dyer, *Bioconjugate Chem.*, 2018, **29**, 2691–2700.

149 T. Robson, D. S. H. Shah, A. S. Solovyova and J. H. Lakey, *ACS Applied Nano Materials*, 2018, **1**, 3590–3599.

150 Q. Dai, C. Walkey and W. C. W. Chan, *Angew. Chem., Int. Ed.*, 2014, **53**, 5093–5096.

151 S. Tenzer, D. Docter, J. Kuharev, A. Musyanovych, V. Fetz, R. Hecht, F. Schlenk, D. Fischer, K. Kiouptsi, C. Reinhardt, K. Landfester, H. Schild, M. Maskos, S. K. Knauer and R. H. Stauber, *Nat. Nanotechnol.*, 2013, **8**, 772–781.

152 K. P. Chan, S.-H. Chao and J. C. Y. Kah, *Bioconjugate Chem.*, 2019, **30**, 920–930.

153 L. Mocan, C. Matea, F. A. Tabaran, O. Mosteanu, T. Pop, C. Puia, L. Agoston-Coldea, G. Zaharie, T. Mocan, A. D. Buzoianu and C. Iancu, *Biomaterials*, 2017, **119**, 33–42.

154 R. Marega, L. Karmani, L. Flamant, P. G. Nageswaran, V. Valembois, B. Masereel, O. Feron, T. V. Borght, S. Lucas, C. Michiels, B. Gallez and D. Bonifazi, *J. Mater. Chem.*, 2012, **22**, 21305.

155 R. T. Busch, F. Karim, J. Weis, Y. Sun, C. Zhao and E. S. Vasquez, *ACS Omega*, 2019, **4**, 15269–15279.

156 A. J. Di Pasqua, R. E. Mishler, Y.-L. Ship, J. C. Dabrowiak and T. Asefa, *Mater. Lett.*, 2009, **63**, 1876–1879.

157 N. A. Byzova, I. V. Safenkova, E. S. Slutskaya, A. V. Zherdev and B. B. Dzantiev, *Bioconjugate Chem.*, 2017, **28**, 2737–2746.

158 R. Rojanathanes, A. Sereemaspun, N. Pimpha, V. Buasorn, P. Ekawong and V. Wiwanitkit, *Taiwan J. Obstet. Gynecol.*, 2008, **47**, 296–299.

159 A. L. Tomás, M. P. de Almeida, F. Cardoso, M. Pinto, E. Pereira, R. Franco and O. Matos, *Front. Microbiol.*, 2019, **10**, 2917.

160 Y. Shen and G. Shen, *ACS Omega*, 2019, **4**, 5083–5087.

161 N. Mustafaoglu, T. Kiziltepe and B. Bilgicer, *Nanoscale*, 2017, **9**, 8684–8694.

162 N. Nagatani, R. Tanaka, T. Yuhi, T. Endo, K. Kerman, Y. Takamura and E. Tamiya, *Sci. Technol. Adv. Mater.*, 2006, **7**, 270–275.

163 H. de Puig, I. Bosch, M. Carré-Camps and K. Hamad-Schifferli, *Bioconjugate Chem.*, 2017, **28**, 230–238.

164 C. Huang, T. Wen, F.-J. Shi, X.-Y. Zeng and Y.-J. Jiao, *ACS Omega*, 2020, **5**, 12550–12556.

165 A. V. Ramsey, A. J. Bischoff and M. B. Francis, *J. Am. Chem. Soc.*, 2021, **143**, 7342–7350.

166 J. Conde, A. Ambrosone, V. Sanz, Y. Hernandez, V. Marchesano, F. Tian, H. Child, C. C. Berry, M. R. Ibarra, P. V. Baptista, C. Tortiglione and J. M. de La Fuente, *ACS Nano*, 2012, **6**, 8316–8324.

167 M.-E. Kyriazi, D. Giust, A. H. El-Sagheer, P. M. Lackie, O. L. Muskens, T. Brown and A. G. Kanaras, *ACS Nano*, 2018, **12**, 3333–3340.

168 D. A. Giljohann, D. S. Seferos, A. E. Prigodich, P. C. Patel and C. A. Mirkin, *J. Am. Chem. Soc.*, 2009, **131**, 2072–2073.

169 J.-H. Kim, H. H. Jang, S.-M. Ryou, S. Kim, J. Bae, K. Lee and M. S. Han, *Chem. Commun.*, 2010, **46**, 4151–4153.

170 H.-C. Huang, S. Barua, D. B. Kay and K. Rege, *ACS Nano*, 2009, **3**, 2941–2952.

171 S. Guo, Y. Huang, Q. Jiang, Y. Sun, L. Deng, Z. Liang, Q. Du, J. Xing, Y. Zhao, P. C. Wang, A. Dong and X.-J. Liang, *ACS Nano*, 2010, **4**, 5505–5511.

172 S. Zhao, F. Caruso, L. Dähne, G. Decher, B. G. de Geest, J. Fan, N. Feliu, Y. Gogotsi, P. T. Hammond, M. C. Hersam, A. Khademhosseini, N. Kotov, S. Leporatti, Y. Li, F. Lisdat, L. M. Liz-Marzán, S. Moya, P. Mulvaney, A. L. Rogach, S. Roy, D. G. Shchukin, A. G. Skirtach, M. M. Stevens, G. B. Sukhorukov, P. S. Weiss, Z. Yue, D. Zhu and W. J. Parak, *ACS Nano*, 2019, **13**, 6151–6169.

173 R. Shahbazi, G. Sghia-Hughes, J. L. Reid, S. Kubek, K. G. Haworth, O. Humbert, H.-P. Kiem and J. E. Adair, *Nat. Mater.*, 2019, **18**, 1124–1132.

174 S. K. Lee, M. S. Han, S. Asokan and C.-H. Tung, *Small*, 2011, **7**, 364–370.

175 T. Mizuhara, K. Saha, D. F. Moyano, C. S. Kim, B. Yan, Y.-K. Kim and V. M. Rotello, *Angew. Chem., Int. Ed.*, 2015, **54**, 6567–6570.

176 X. Li, S. M. Robinson, A. Gupta, K. Saha, Z. Jiang, D. F. Moyano, A. Sahar, M. A. Riley and V. M. Rotello, *ACS Nano*, 2014, **8**, 10682–10686.

177 E. C. Dreaden, S. C. Mwakwari, Q. H. Sodji, A. K. Oyelere and M. A. El-Sayed, *Bioconjugate Chem.*, 2009, **20**, 2247–2253.

178 S. D. Brown, P. Nativo, J.-A. Smith, D. Stirling, P. R. Edwards, B. Venugopal, D. J. Flint, J. A. Plumb, D. Graham and N. J. Wheate, *J. Am. Chem. Soc.*, 2010, **132**, 4678–4684.

179 Y. Du, L. Xia, A. Jo, R. M. Davis, P. Bissel, M. F. Ehrich and D. G. I. Kingston, *Bioconjugate Chem.*, 2018, **29**, 420–430.

180 S. S. Agasti, A. Chompoosor, C.-C. You, P. Ghosh, C. K. Kim and V. M. Rotello, *J. Am. Chem. Soc.*, 2009, **131**, 5728–5729.

181 X. Wang, X. Cai, J. Hu, N. Shao, F. Wang, Q. Zhang, J. Xiao and Y. Cheng, *J. Am. Chem. Soc.*, 2013, **135**, 9805–9810.

182 S. A. R. Kazmi, M. Z. Qureshi, S. Ali and J.-F. Masson, *Langmuir*, 2019, **35**, 16266–16274.

183 J. Mosquera, M. Henriksen-Lacey, I. García, M. Martínez-Calvo, J. Rodríguez, J. L. Mascareñas and L. M. Liz-Marzán, *J. Am. Chem. Soc.*, 2018, **140**, 4469–4472.

184 Y. Zhao, Y. Tian, Y. Cui, W. Liu, W. Ma and X. Jiang, *J. Am. Chem. Soc.*, 2010, **132**, 12349–12356.

185 X. Yang, J. Yang, Le Wang, B. Ran, Y. Jia, L. Zhang, G. Yang, H. Shao and X. Jiang, *ACS Nano*, 2017, **11**, 5737–5745.

186 J. Bresee, C. M. Bond, R. J. Worthington, C. A. Smith, J. C. Gifford, C. A. Simpson, C. J. Carter, G. Wang, J. Hartman, N. A. Osbaugh, R. K. Shoemaker, C. Melander and D. L. Feldheim, *J. Am. Chem. Soc.*, 2014, **136**, 5295–5300.

187 Le Wang, M. Natan, W. Zheng, W. Zheng, S. Liu, G. Jacobi, I. Perelshtein, A. Gedanken, E. Banin and X. Jiang, *Nanoscale Adv.*, 2020, **2**, 2293–2302.

188 Y.-F. Lee, F.-H. Nan, M.-J. Chen, H.-Y. Wu, C.-W. Ho, Y.-Y. Chen and C.-C. Huang, *Anal. Methods*, 2012, **4**, 1709.

189 K. Vaid, J. Dhiman, N. Sarawagi and V. Kumar, *Langmuir*, 2020, **36**, 12319–12326.

190 K. P. Lisha, Anshup and T. Pradeep, *Gold Bull.*, 2009, **42**, 144–152.

191 I. Ojea-Jiménez, X. López, J. Arbiol and V. Puntes, *ACS Nano*, 2012, **6**, 2253–2260.

192 G. Chen, J. Hai, H. Wang, W. Liu, F. Chen and B. Wang, *Nanoscale*, 2017, **9**, 3315–3321.

193 M. Gou, X. Qu, W. Zhu, M. Xiang, J. Yang, K. Zhang, Y. Wei and S. Chen, *Nat. Commun.*, 2014, **5**, 3774.

194 T. P. Fato, D.-W. Li, L.-J. Zhao, K. Qiu and Y.-T. Long, *ACS Omega*, 2019, **4**, 7543–7549.

195 Z. Pang, C.-M. J. Hu, R. H. Fang, B. T. Luk, W. Gao, F. Wang, E. Chuluun, P. Angsantikul, S. Thamphiwatana, W. Lu, X. Jiang and L. Zhang, *ACS Nano*, 2015, **9**, 6450–6458.

196 Y. Dou, Y. Guo, X. Li, X. Li, S. Wang, L. Wang, G. Lv, X. Zhang, H. Wang, X. Gong and J. Chang, *ACS Nano*, 2016, **10**, 2536–2548.

197 Y. C. Dong, M. Hajfathalian, P. S. N. Maidment, J. C. Hsu, P. C. Naha, S. Si-Mohamed, M. Breuilly, J. Kim, P. Chhour, P. Douek, H. I. Litt and D. P. Cormode, *Sci. Rep.*, 2019, **9**, 14912.

198 P. Chhour, J. Kim, B. Benardo, A. Tovar, S. Mian, H. I. Litt, V. A. Ferrari and D. P. Cormode, *Bioconjugate Chem.*, 2017, **28**, 260–269.

199 J. F. Hainfeld, D. N. Slatkin, T. M. Focella and H. M. Smilowitz, *Br. J. Radiol. Suppl.*, 2006, **79**, 248–253.

200 G. Jiménez Sánchez, P. Maury, L. Stefancikova, O. Campion, G. Laurent, A. Chateau, F. Bouraleh Hoch, F. Boschetti, F. Denat, S. Pinel, J. Devy, E. Porcel, S. Lacombe, R. Bazzi and S. Roux, *Int. J. Mol. Sci.*, 2019, **20**, 4618.

201 J. Zhang, C. Li, X. Zhang, S. Huo, S. Jin, F.-F. An, X. Wang, X. Xue, C. I. Okeke, G. Duan, F. Guo, X. Zhang, J. Hao, P. C. Wang, J. Zhang and X.-J. Liang, *Biomaterials*, 2015, **42**, 103–111.

202 L. Jing, X. Liang, Z. Deng, S. Feng, X. Li, M. Huang, C. Li and Z. Dai, *Biomaterials*, 2014, **35**, 5814–5821.

203 P. van Nguyen, W. Qian, Y. Li, B. Liu, M. Aaberg, J. Henry, W. Zhang, X. Wang and Y. M. Paulus, *Nat. Commun.*, 2021, **12**, 34.

204 S. Mallidi, T. Larson, J. Tam, P. P. Joshi, A. Karpiouk, K. Sokolov and S. Emelianov, *Nano Lett.*, 2009, **9**, 2825–2831.

205 T. Kim, Q. Zhang, J. Li, L. Zhang and J. V. Jokerst, *ACS Nano*, 2018, **12**, 5615–5625.

206 K. C. L. Black, W. J. Akers, G. Sudlow, B. Xu, R. Laforest and S. Achilefu, *Nanoscale*, 2015, **7**, 440–444.

207 Y. Zhao, D. Sultan, L. Detering, S. Cho, G. Sun, R. Pierce, K. L. Wooley and Y. Liu, *Angew. Chem., Int. Ed.*, 2014, **53**, 156–159.

208 A. F. Frellsen, A. E. Hansen, R. I. Jølck, P. J. Kempen, G. W. Severin, P. H. Rasmussen, A. Kjær, A. T. I. Jensen and T. L. Andresen, *ACS Nano*, 2016, **10**, 9887–9898.

209 Y. Zhao, L. Detering, D. Sultan, M. L. Cooper, M. You, S. Cho, S. L. Meier, H. Luehmann, G. Sun, M. Rettig, F. Dehdashti, K. L. Wooley, J. F. DiPersio and Y. Liu, *ACS Nano*, 2016, **10**, 5959–5970.

210 A. Y. Al-Yasiri, M. Khoobchandani, C. S. Cutler, L. Watkinson, T. Carmack, C. J. Smith, M. Kuchuk, S. K. Loyalka, A. B. Lugão and K. V. Katti, *Dalton Trans.*, 2017, **46**, 14561–14571.

211 R. Chakravarty, S. Chakraborty, A. Guleria, R. Shukla, C. Kumar, K. V. Vimalnath Nair, H. D. Sarma, A. K. Tyagi and A. Dash, *Ind. Eng. Chem. Res.*, 2018, **57**, 14337–14346.

212 Y. Zhao, B. Pang, H. Luehmann, L. Detering, X. Yang, D. Sultan, S. Harpstrite, V. Sharma, C. S. Cutler, Y. Xia and Y. Liu, *Adv. Healthcare Mater.*, 2016, **5**, 928–935.

213 X. Li, Z. Xiong, X. Xu, Y. Luo, C. Peng, M. Shen and X. Shi, *ACS Appl. Mater. Interfaces*, 2016, **8**, 19883–19891.

214 Ł. Dziawer, A. Majkowska-Pilip, D. Gaweł, M. Godlewska, M. Pruszyński, J. Jastrzębski, B. Wąs and A. Bilewicz, *Nanomaterials*, 2019, **9**, 632.

215 F. Silva, A. Zambre, M. P. C. Campello, L. Gano, I. Santos, A. M. Ferraria, M. J. Ferreira, A. Singh, A. Upendran, A. Paulo and R. Kannan, *Bioconjugate Chem.*, 2016, **27**, 1153–1164.

216 M. Pretze, A. Hien, M. Rädle, R. Schirrmacher, C. Wängler and B. Wängler, *Bioconjugate Chem.*, 2018, **29**, 1525–1533.

217 D. J. Kwekkeboom, W. W. de Herder, B. L. Kam, C. H. van Eijck, M. van Essen, P. P. Kooij, R. A. Feelders, M. O. van Aken and E. P. Krenning, *J. Clin. Oncol.*, 2008, **26**, 2124–2130.

218 F. Novruzov, J. A. Aliyev, Z. Jaunmuktane, J. B. Bomanji and I. Kayani, *Clin. Nucl. Med.*, 2015, **40**, 47–49.

219 W. J. Lees, A. Spaltenstein, J. E. Kingery-Wood and G. M. Whitesides, *J. Med. Chem.*, 1994, **37**, 3419–3433.

220 J. Huskens, *Curr. Opin. Chem. Biol.*, 2006, **10**, 537–543.

221 A. F. Smeijers, K. Pieterse, P. A. J. Hilbers and A. J. Markvoort, *Macromolecules*, 2019, **52**, 2778–2788.

222 M. Mammen, S.-K. Choi and G. M. Whitesides, *Angew. Chem., Int. Ed.*, 1998, **37**, 2754–2794.

223 P. I. Kitov and D. R. Bundle, *J. Am. Chem. Soc.*, 2003, **125**, 16271–16284.

224 C. S. Mahon and D. A. Fulton, *Nat. Chem.*, 2014, **6**, 665–672.

225 P. H. Ehrlich, *J. Theor. Biol.*, 1979, **81**, 123–127.

226 Y.-Y. Chien, M.-D. Jan, A. K. Adak, H.-C. Tzeng, Y.-P. Lin, Y.-J. Chen, K.-T. Wang, C.-T. Chen, C.-C. Chen and C.-C. Lin, *ChemBioChem*, 2008, **9**, 1100–1109.

227 J. Wang, J. Min, S. A. Eghtesadi, R. S. Kane and A. Chilkoti, *ACS Nano*, 2020, **14**, 372–383.

228 L. L. Kiessling, J. E. Gestwicki and L. E. Strong, *Angew. Chem. Int. Ed.*, 2006, **45**, 2348–2368.

229 A. Joshi, S. Kate, V. Poon, D. Mondal, M. B. Boggara, A. Saraph, J. T. Martin, R. McAlpine, R. Day, A. E. Garcia, J. Mogridge and R. S. Kane, *Biomacromolecules*, 2011, **12**, 791–796.

230 S. Liese and R. R. Netz, *ACS Nano*, 2018, **12**, 4140–4147.

231 E. Moradi, D. Vllasaliu, M. Garnett, F. Falcone and S. Stolnik, *RSC Adv.*, 2012, **2**, 3025.

232 S. Barua, J.-W. Yoo, P. Kolhar, A. Wakankar, Y. R. Gokarn and S. Mitragotri, *Proc. Natl. Acad. Sci. U. S. A.*, 2013, **110**, 3270–3275.

233 D. Di Iorio, M. L. Verheijden, E. van der Vries, P. Jonkheijm and J. Huskens, *ACS Nano*, 2019, **13**, 3413–3423.

234 J. Wang, S. Tian, R. A. Petros, M. E. Napier and J. M. Desimone, *J. Am. Chem. Soc.*, 2010, **132**, 11306–11313.

235 B. Jennifer, V. Berg, M. Modak, A. Puck, M. Seyerl-Jiresch, S. Künig, G. J. Zlabinger, P. Steinberger, J. Chou, R. S. Geha, L. Öhler, A. Yachie, H. Choe, M. Kraller, H. Stockinger and J. Stöckl, *Commun. Biol.*, 2020, **3**, 621.

236 M.-C. Bowman, T. E. Ballard, C. J. Ackerson, D. L. Feldheim, D. M. Margolis and C. Melander, *J. Am. Chem. Soc.*, 2008, **130**, 6896–6897.

237 A. Rosemary Bastian, A. Nangarlia, L. D. Bailey, A. Holmes, R. V. Kalyana Sundaram, C. Ang, D. R. M. Moreira, K. Freedman, C. Duffy, M. Contarino, C. Abrams, M. Root and I. Chaiken, *J. Biol. Chem.*, 2015, **290**, 529–543.

238 R. Frederiksson, M. C. Lagerström, L.-G. Lundin and H. B. Schiöth, *Mol. Pharmacol.*, 2003, **63**, 1256–1272.

239 S. Basith, M. Cui, S. J. Y. Macalino, J. Park, N. A. B. Clavio, S. Kang and S. Choi, *Front. Pharmacol.*, 2018, **9**, 128.

240 A. P. Davenport, C. C. G. Scully, C. de Graaf, A. J. H. Brown and J. J. Maguire, *Nat. Rev. Drug Discovery*, 2020, **19**, 389–413.

241 J. B. Soriano, A. A. Abajobir, K. H. Abate, S. F. Abera, A. Agrawal, M. B. Ahmed, A. N. Aichour, I. Aichour, M. T. E. Aichour, K. Alam, N. Alam, J. M. Alkaabi, F. Al-Maskari, N. Alvis-Guzman, A. Amberbir, Y. A. Amoako, M. G. Ansha, J. M. Antó, H. Asayesh, T. M. Atey, E. F. G. A. Avokpaho, A. Barac, S. Basu, N. Bedi, I. M. Bensenor, A. Berhane, A. S. Beyene, Z. A. Bhutta, S. Biryukov, D. J. Boneya, M. Brauer, D. O. Carpenter, D. Casey, D. J. Christopher, L. Dandona, R. Dandona, S. D. Dharmaratne, H. P. Do, F. Fischer, T. T. Gebrehiwot, A. Geleto, A. G. Ghoshal, R. F. Gillum, I. A. M. Ginawi, V. Gupta, S. I. Hay, M. T. Hedayati, N. Horita, H. D. Hosgood, M. B. Jakovljevic, S. L. James, J. B. Jonas, A. Kasaeian, Y. S. Khader, I. A. Khalil, E. A. Khan, Y.-H. Khang, J. Khubchandani, L. D. Knibbs, S. Kosen, P. A. Koul, G. A. Kumar, C. T. Leshargie, X. Liang, H. M. A. El Razek, A. Majeed, D. C. Malta, T. Manhertz, N. Marquez, A. Mehari, G. A. Mensah, T. R. Miller, K. A. Mohammad, K. E. Mohammed, S. Mohammed, A. H. Mokdad, M. Naghavi, C. T. Nguyen, G. Nguyen, Q. Le Nguyen, T. H. Nguyen, D. N. A. Ningrum, V. M. Nong, J. I. Obi, Y. E. Odeyemi, F. A. Ogbo, E. Oren, M. PA, E.-K. Park, G. C. Patton, K. Paulson, M. Qorbani, R. Quansah, A. Rafay, M. H. U. Rahman, R. K. Rai, S. Rawaf, N. Reinig, S. Safiri, R. Sarmiento-Suarez, B. Sartorius, M. Savic, M. Sawhney, M. Shigematsu, M. Smith, F. Tadese, G. D. Thurston, R. Topor-Madry, B. X. Tran, K. N. Ukwaja, J. F. M. van Boven, V. V. Vlassov, S. E. Vollset, X. Wan, A. Werdecker, S. W. Hanson, Y. Yano, H. H. Yimam, N. Yonemoto, C. Yu, Z. Zaidi, M. El Sayed Zaki, A. D. Lopez, C. J. L. Murray and T. Vos, *Lancet Respir. Med.*, 2017, **5**, 691–706.

242 R. A. Panettieri, T. Pera, S. B. Liggett, J. L. Benovic and R. B. Penn, *Curr. Opin. Pharmacol.*, 2018, **40**, 120–125.

243 S. Eyerich, M. Metz, A. Bossios and K. Eyerich, *Allergy*, 2020, **75**, 546–560.

244 M. Lommatzsch, R. Buhl and S. Korn, *Dtsch. Ärztebl. Int.*, 2020, **117**, 434–444.

245 G. R. Kelman, K. N. V. Palmer and M. R. Cross, *Nature*, 1969, **221**, 1251.

246 K. Kainuma, T. Kobayashi, C. N. D'Alessandro-Gabazza, M. Toda, T. Yasuma, K. Nishihama, H. Fujimoto, Y. Kuwabara, K. Hosoki, M. Nagao, T. Fujisawa and E. C. Gabazza, *Respir. Res.*, 2017, **18**, 79.

247 K. Wang, Y. Feng, S. Li, W. Li, X. Chen, R. Yi, H. Zhang and Z. Hong, *J. Biomed. Nanotechnol.*, 2018, **14**, 1806–1815.

248 W. Wang, R. Zhu, Q. Xie, A. Li, Y. Xiao, K. Li, H. Liu, D. Cui, Y. Chen and S. Wang, *Int. J. Nanomed.*, 2012, **7**, 3667–3677.

249 R. Halwani, A. Sultana Shaik, E. Ratemi, S. Afzal, R. Kenana, S. Al-Muhsen and A. Al Faraj, *Exp. Mol. Med.*, 2016, **48**, e262.

250 A. J. Omlor, D. D. Le, J. Schlicker, M. Hannig, R. Ewen, S. Heck, C. Herr, A. Kraegeloh, C. Hein, R. Kautenburger, G. Kickelbick, R. Bals, J. Nguyen and Q. T. Dinh, *Small*, 2017, **13**, 1603070.

251 E. Barreto, M. F. Serra, R. V. Dos Santos, C. E. A. Dos Santos, J. Hickmann, A. C. Cotias, C. R. R. Pão, S. G. Trindade, V. Schimidt, C. Giacomelli, V. F. Carvalho, P. M. Rodrigues E Silva, R. S. B. Cordeiro and M. A. Martins, *J. Biomed. Nanotechnol.*, 2015, **11**, 1038–1050.

252 C. A. Smith, C. A. Simpson, G. Kim, C. J. Carter and D. L. Feldheim, *ACS Nano*, 2013, **7**, 3991–3996.

253 M. Yao, L. He, D. J. McClements and H. Xiao, *J. Agric. Food Chem.*, 2015, **63**, 8044–8049.

254 J. Li, R. Cha, X. Zhao, H. Guo, H. Luo, M. Wang, F. Zhou and X. Jiang, *ACS Nano*, 2019, **13**, 5002–5014.

255 E. P. Weledji, *Acute Med. Surg.*, 2020, **7**, e573.

256 T. O. Vilz, B. Stoffels, C. Strassburg, H. H. Schild and J. C. Kalff, *Dtsch. Ärztebl. Int.*, 2017, **114**, 508–518.

257 P. Lim, O. J. Morris, G. Nolan, S. Moore, B. Draganic and S. R. Smith, *Ann. Surg.*, 2013, **257**, 1016–1024.

258 S. Marwah, S. Singla and P. Tinna, *Saudi J. Gastroenterol.*, 2012, **18**, 111–117.

259 F. M. Ledari, S. Barat and M. A. Delavar, *Bosn. J. Basic Med. Sci.*, 2012, **12**, 265–268.

260 V. Short, G. Herbert, R. Perry, S. J. Lewis, C. Atkinson, A. R. Ness, C. Penfold and S. Thomas, in *The Cochrane Collaboration*, 2014, pp. 1–10.

261 G. Schultheiss, B. Hennig, W. Schunack, G. Prinz and M. Diener, *Eur. J. Pharmacol.*, 2006, **546**, 161–170.

262 M. Eisenhut, *J. Inflammation*, 2006, **3**, 5.

263 M.-C. Saada, J.-L. Montero, D. Vullo, A. Scozzafava, J.-Y. Winum and C. T. Supuran, *J. Med. Chem.*, 2011, **54**, 1170–1177.

264 A. Parveen, V. B. Malashetty, B. Mantripragada, M. S. Yalagatti, V. Abbaraju and R. Deshpande, *Saudi J. Biol. Sci.*, 2017, **24**, 1925–1932.

265 F. Campbell, F. L. Bos, S. Sieber, G. Arias-Alpizar, B. E. Koch, J. Huwyler, A. Kros and J. Bussmann, *ACS Nano*, 2018, **12**, 2138–2150.

266 S. Hirn, M. Semmler-Behnke, C. Schleh, A. Wenk, J. Lipka, M. Schäffler, S. Takenaka, W. Möller, G. Schmid, U. Simon and W. G. Kreyling, *Eur. J. Pharm. Biopharm.*, 2011, **77**, 407–416.

267 S. G. Elci, Y. Jiang, B. Yan, S. T. Kim, K. Saha, D. F. Moyano, G. Yesilbag Tonga, L. C. Jackson, V. M. Rotello and R. W. Vachet, *ACS Nano*, 2016, **10**, 5536–5542.

268 A. P. Walczak, P. J. M. Hendriksen, R. A. Woutersen, M. van der Zande, A. K. Undas, R. Helsdingen, H. H. J. van den Berg, I. M. C. M. Rietjens and H. Bouwmeester, *J. Nanopart. Res.*, 2015, **17**, 231.

269 A.-L. Bailly, F. Correard, A. Popov, G. Tselikov, F. Chaspoul, R. Appay, A. Al-Kattan, A. V. Kabashin, D. Braguer and M.-A. Esteve, *Sci. Rep.*, 2019, **9**, 12890.

270 S. K. Balasubramanian, J. Jittiwat, J. Manikandan, C.-N. Ong, L. E. Yu and W.-Y. Ong, *Biomaterials*, 2010, **31**, 2034–2042.

271 Stefan Wilhelm, Anthony J. Tavares, Qin Dai, Seiichi Ohta, Julie Audet, Harold F. Dvorak and Warren C. W. Chan, *Nat. Rev. Mater.*, 2016, **1**, 1–12.

272 E. Blanco, H. Shen and M. Ferrari, *Nat. Biotechnol.*, 2015, **33**, 941–951.

273 S. Schwartz, *Nanomedicine*, 2017, **12**, 271–274.

274 E. Durantie, D. Vanhecke, L. Rodriguez-Lorenzo, F. Delhaes, S. Balog, D. Septiadi, J. Bourquin, A. Petri-Fink and B. Rothen-Rutishauser, *Part. Fibre Toxicol.*, 2017, **14**, 49.

275 G. Bachler, S. Losert, Y. Umehara, N. von Goetz, L. Rodriguez-Lorenzo, A. Petri-Fink, B. Rothen-Rutishauser and K. Hungerbuehler, *Part. Fibre Toxicol.*, 2015, **12**, 18.

276 E. Dulkeith, M. Ringler, T. A. Klar, J. Feldmann, A. Muñoz Javier and W. J. Parak, *Nano Lett.*, 2005, **5**, 585–589.

277 H. Y. Lee, H. Son, J. M. Lim, J. Oh, D. Kang, W. S. Han and J. H. Jung, *Analyst*, 2010, **135**, 2022–2027.

278 A. Treibs and F. H. Kreuzer, *Justus Liebigs Ann. Chem.*, 1968, **718**, 208–223.

279 C. Alric, J. Taleb, G. Le Duc, C. Mandon, C. Billotey, A. Le Meur-Herland, T. Brochard, F. Vocanson, M. Janier, P. Perriat, S. Roux and O. Tillement, *J. Am. Chem. Soc.*, 2008, **130**, 5908–5915.

280 M. Durand, E. Lelievre, A. Chateau, A. Berquand, G. Laurent, P. Carl, S. Roux, L. Chazee, R. Bazzi, F. Eghiaian, J. Jubreaux, P. Ronde, M. Barberi-Heyob, P. Chastagner, J. Devy and S. Pinel, *Nanoscale*, 2021, **13**, 9236–9251.

281 C. Alric, I. Miladi, D. Kryza, J. Taleb, F. Lux, R. Bazzi, C. Billotey, M. Janier, P. Perriat, S. Roux and O. Tillement, *Nanoscale*, 2013, **5**, 5930–5939.

282 I. Miladi, C. Alric, S. Dufort, P. Mowat, A. Dutour, C. Mandon, G. Laurent, E. Bräuer-Krisch, N. Herath, J.-L. Coll, M. Dutreix, F. Lux, R. Bazzi, C. Billotey, M. Janier, P. Perriat, G. Le Duc, S. Roux and O. Tillement, *Small*, 2014, **10**, 1116-1124.

283 M. Bartholomä, J. Valliant, K. P. Maresca, J. Babich and J. Zubieta, *Chem. Commun.*, 2009, **5**, 493–512.

284 J. C. Stendahl and A. J. Sinusas, *J. Nucl. Med.*, 2015, **56**, 1637–1641.

285 M. Varani, F. Galli, S. Auletta and A. Signore, *Clin. Transl. Imaging*, 2018, **6**, 271–292.

286 C. M. R. Oda, R. S. Fernandes, S. C. de Araújo Lopes, M. C. de Oliveira, V. N. Cardoso, D. M. Santos, A. M. de Castro Pimenta, A. Malachias, R. Paniago, D. M. Townsend, P. M. Colletti, D. Rubello, R. J. Alves, A. L. B. de Barros and E. A. Leite, *Biomedicine & Pharmacotherapy*, 2017, **89**, 268–275.

287 B. E. Ocampo-García, F. d. M. Ramírez, G. Ferro-Flores, L. M. de León-Rodríguez, C. L. Santos-Cuevas, E. Morales-Avila, C. A. de Murphy, M. Pedraza-López, L. A. Medina and M. A. Camacho-López, *Nuclear Medicine and Biology*, 2011, **38**, 1–11.

288 N. Jiménez-Mancilla, G. Ferro-Flores, C. Santos-Cuevas, B. Ocampo-García, M. Luna-Gutiérrez, E. Azorín-Vega, K. Isaac-Olivé, M. Camacho-López and E. Torres-García, *J. Labelled Compd. Radiopharm.*, 2013, **56**, 663–671.

289 M. Felber and R. Alberto, *Nanoscale*, 2015, **7**, 6653–6660.

290 G. Frens, *Nat. Phys. Sci.*, 1973, **241**, 20–22.

291 N. Zheng, J. Fan and G. D. Stucky, *J. Am. Chem. Soc.*, 2006, **128**, 6550–6551.

292 J. Piella, N. G. Bastús and V. Puntes, *Chem. Mater.*, 2016, **28**, 1066–1075.

293 S. Panigrahi, S. Basu, S. Praharaj, S. Pande, S. Jana, A. Pal, S. K. Ghosh and T. Pal, *J. Phys. Chem. C*, 2007, **111**, 4596–4605.

294 H. Al-Johani, E. Abou-Hamad, A. Jedidi, C. M. Widdifield, J. Viger-Gravel, S. S. Sangaru, D. Gajan, D. H. Anjum, S. Ould-Chikh, M. N. Hedhili, A. Gurinov, M. J. Kelly, M. El Eter, L. Cavallo, L. Emsley and J.-M. Basset, *Nat. Chem.*, 2017, **9**, 890–895.

295 S. K. Balasubramanian, L. Yang, L.-Y. L. Yung, C.-N. Ong, W.-Y. Ong and L. E. Yu, *Biomaterials*, 2010, **31**, 9023–9030.

296 N. E. A. Reeler, K. A. Lerstrup, W. Somerville, J. Speder, S. V. Petersen, B. W. Laursen, M. Arenz, X. Qiu, T. Vosch and K. Nørgaard, *Sci. Rep.*, 2015, **5**, 15273.

297 G. P. Maier, C. M. Bernt and A. Butler, *Biomater. Sci.*, 2018, **6**, 332–339.

298 E. A. Pillar, R. C. Camm and M. I. Guzman, *Environ. Sci. Technol.*, 2014, **48**, 14352–14360.

299 R. Riessen, O. Tschritter, U. Janssens and M. Haap, *Med. Klin. Intensivmed. Notfmed.*, 2016, **111**, 37–46.

300 M. Johnson, *Paediatr. Respir. Rev.*, 2001, **2**, 57–62.

301 O. Abed, M. Wanunu, A. Vaskevich, R. Arad-Yellin, A. Shanzer and I. Rubinstein, *Chem. Mater.*, 2006, **18**, 1247–1260.

302 D. G. Brown and J. Boström, *J. Med. Chem.*, 2016, **59**, 4443–4458.

303 E. Oh, K. Susumu, J. B. Blanco-Canosa, I. L. Medintz, P. E. Dawson and H. Mattoussi, *Small*, 2010, **6**, 1273–1278.

304 A. Mattern, R. Claßen, A. Wolf, E. Pouokam, K.-D. Schlüter, M. S. Wickleder and M. Diener, *Nanoscale Adv.*, 2021, submitted.

305 G. Stene-Larsen, J. A. Ask, K. B. Helle and R. Fin, *Am. J. Cardiol.*, 1986, **57**, F7-F10.

306 B. January, A. Seibold, C. Allal, B. S. Whaley, B. J. Knoll, R. H. Moore, B. F. Dickey, R. Barber and R. B. Clark, *Br. J. Pharmacol.*, 1998, **123**, 701–711.

307 W. O. Foye, T. L. Lemke and D. A. Williams, eds., *Foye's principles of medicinal chemistry*, Wolters Kluwer Health/Lippincott Williams & Wilkins, Philadelphia, 7th edn., 2013, p. 1317.

308 B. Neises and W. Steglich, *Angew. Chem.*, 1978, **90**, 556–557.

309 S. H. Lee, K. H. Bae, S. H. Kim, K. R. Lee and T. G. Park, *Int. J. Pharm.*, 2008, **364**, 94–101.

310 S. Gabriel, *Ber. Dtsch. Chem. Ges.*, 1887, **20**, 2224–2236.

311 R. Appel, *Angew. Chem. Int. Ed. Engl.*, 1975, **14**, 801–811.

312 E. M. Pérez, D. T. F. Dryden, D. A. Leigh, G. Teobaldi and F. Zerbetto, *J. Am. Chem. Soc.*, 2004, **126**, 12210–12211.

313 S. G. Jarboe, M. S. Terrazas and P. Beak, *The Journal of organic chemistry*, 2008, **73**, 9627–9632.

314 O. Mitsunobu and M. Yamada, *Bull. Chem. Soc. Jpn.*, 1967, **40**, 2380–2382.

315 X. Wang, X. Zhao, W. Dong, X. Zhang, Y. Xiang, Q. Huang and H. Chen, *J. Mater. Chem. A*, 2019, **7**, 16277–16284.

316 A. Mattern, Masterthesis, Justus Liebig University, 2017.

317 J. Bucevičius, G. Kostiuk, R. Gerasimaitė, T. Gilat and G. Lukinavičius, *Chemical science*, 2020, **11**, 7313–7323.

318 J. Gong, C. Liu, X. Jiao, S. He, L. Zhao and X. Zeng, *RSC Adv.*, 2020, **10**, 38038–38044.

319 W. Chi, Q. Qi, R. Lee, Z. Xu and X. Liu, *J. Phys. Chem. C*, 2020, **124**, 3793–3801.

320 K. Umezawa, M. Yoshida, M. Kamiya, T. Yamasoba and Y. Urano, *Nat. Chem.*, 2017, **9**, 279–286.

321 S.-N. Uno, M. Kamiya, A. Morozumi and Y. Urano, *Chem. Commun.*, 2017, **54**, 102–105.

322 C. J. Eling, T. W. Price, A. R. L. Marshall, F. Narda Viscomi, P. Robinson, G. Firth, A. M. Adawi, J.-S. G. Bouillard and G. J. Stasiuk, *ChemPlusChem*, 2017, **82**, 674–680.

323 R. E. Shepherd, M. A. Sweetland and D. E. Junker, *J. Inorg. Chem.*, 1997, **65**, 1–14.

324 A. Chiotellis, C. Tsoukalas, M. Pelecanou, I. Pirmettis and M. Papadopoulos, *Radiochim. Acta*, 2011, **99**, 307–315.

325 R. Alberto, A. Egli, U. Abram, K. Hegetschweiler, V. Gramlich and P. A. Schubiger, *J. Chem. Soc., Dalton Trans.*, 1994, 2815–2820.

326 S. P. Schmidt, W. C. Trogler and F. Basolo, in *Inorganic Syntheses*, 1985, 44 ff.

327 R. Alberto, R. Schibli, A. Egli, A. P. Schubiger, U. Abram and T. A. Kaden, *J. Am. Chem. Soc.*, 1998, **120**, 7987–7988.

328 N. Marti, B. Spingler, F. Breher and R. Schibli, *Inorg. Chem.*, 2005, **44**, 6082–6091.

329 F. Gan, R. Liu, F. Wang and P. G. Schultz, *J. Am. Chem. Soc.*, 2018, **140**, 3829–3832.

330 R. J. Sundberg and R. B. Martin, *Chem. Rev.*, 1974, **74**, 471–517.

331 R. C. Dunbar, J. Martens, G. Berden and J. Oomens, *J. Phys. Chem. A*, 2018, **122**, 5589–5596.

332 D. Brasili, J. Watly, E. Simonovsky, R. Guerrini, N. A. Barbosa, R. Wieczorek, M. Remelli, H. Kozlowski and Y. Miller, *Dalton Trans.*, 2016, **45**, 5629–5639.

333 L. Frost, P. Suryadevara, S. J. Cannell, P. W. Groundwater, P. A. Hambleton and R. J. Anderson, *Eur. J. Med. Chem.*, 2016, **109**, 206–215.

334 F.-K. Liu and G.-T. Wei, *Chromatographia*, 2004, **59**, 115–119.

335 J. Baldas, in *Technetium and Rhenium Their Chemistry and Its Applications*, ed. K. Yoshihara and T. Omori, Springer, Berlin, Heidelberg, 1996, pp. 37–76.

336 R. Alberto, in *Mc Cleverty, Meer (Hg.) Eds.; Comprehensive Coordination Chemistry II*, Elsevier Science, Amsterdam, 2003, 127–271.

337 Mestrelab Research SL, *MestReNova*, v. 6.0.2-5474, 2009.

338 J. Schindelin, I. Arganda-Carreras, E. Frise, V. Kaynig, M. Longair, T. Pietzsch, S. Preibisch, C. Rueden, S. Saalfeld, B. Schmid, J.-Y. Tinevez, D. J. White, V. Hartenstein, K. Eliceiri, P. Tomancak and A. Cardona, *Nat. Methods*, 2012, **9**, 676–682.

339 J. Cosier and A. M. Glazer, *J. Appl. Crystallogr.*, 1986, **19**, 105–107.

340 Bruker, *APEX3*, Bruker AXS Inc., Madison, Wisconsin, USA, 2018.

341 G. M. Sheldrick, *Acta Crystallogr. A*, 2008, **64**, 112–122.

342 G. M. Sheldrick and T. R. Schneider, in *Macromolecular Crystallography Part B*, Elsevier, 1997, pp. 319–343.

343 C. F. Macrae, I. J. Bruno, J. A. Chisholm, P. R. Edgington, P. McCabe, E. Pidcock, L. Rodriguez-Monge, R. Taylor, J. van de Streek and P. A. Wood, *J. Appl. Crystallogr.*, 2008, **41**, 466–470.

344 A. L. Spek, *J. Appl. Crystallogr.*, 2003, **36**, 7–13.

345 O. V. Dolomanov, L. J. Bourhis, R. J. Gildea, J. A. K. Howard and H. Puschmann, *J. Appl. Crystallogr.*, 2009, **42**, 339–341.

346 L. K. Würner, Dissertation, Justus Liebig University, 2013.

7 APPENDIX

TEM images

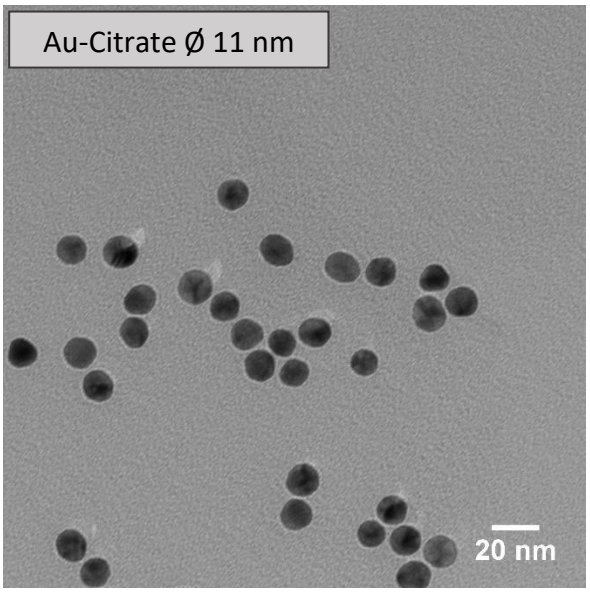

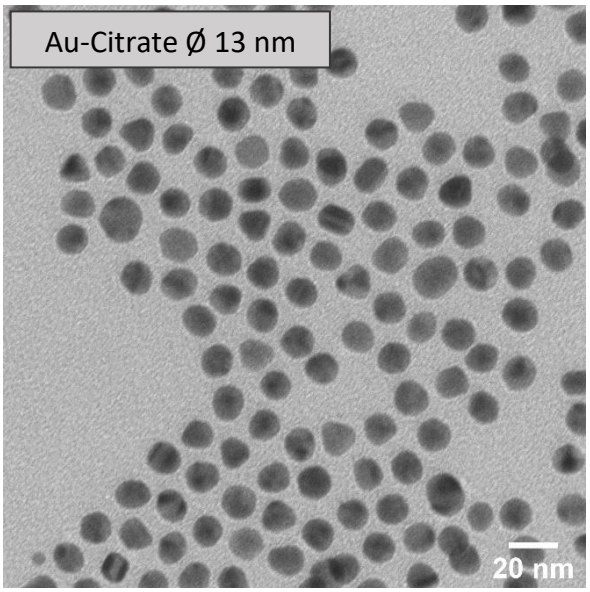

NMR spectra

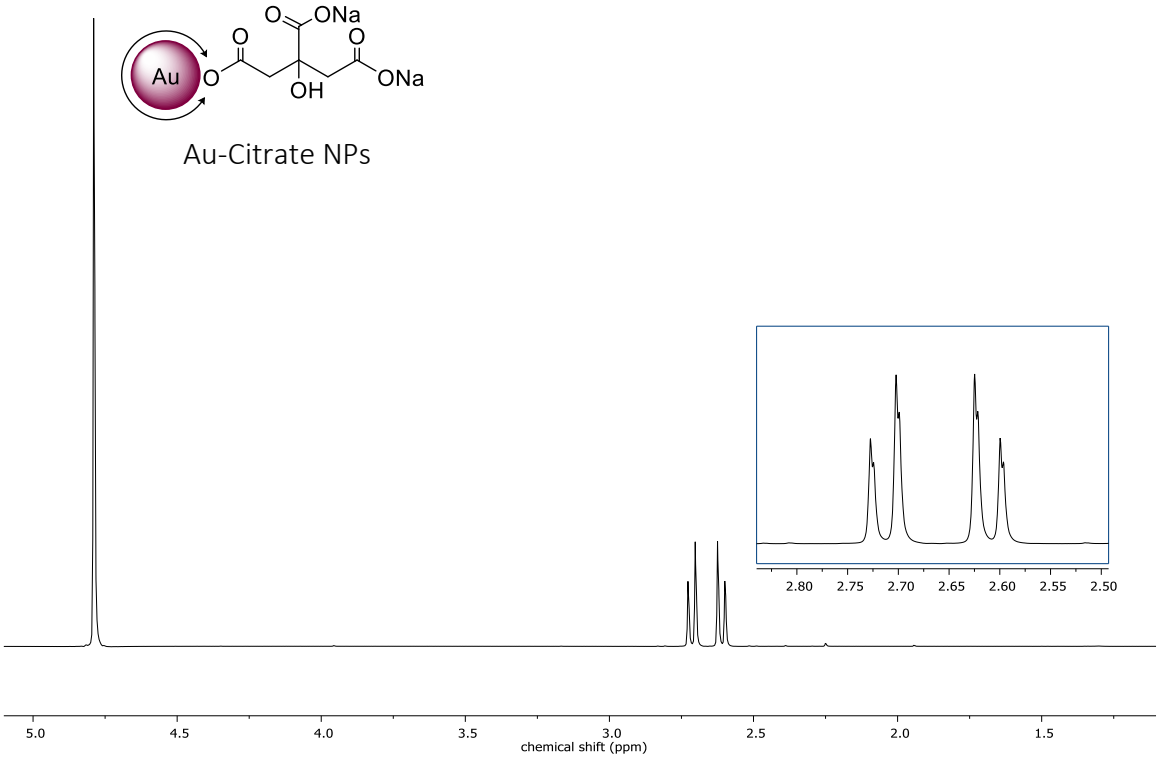

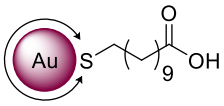

Au-MUDA NPs

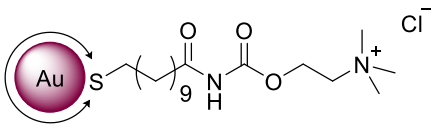

Au-MUDA-CCh NPs

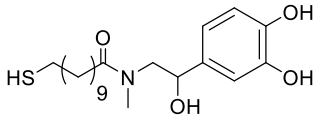

MUDA-ADR

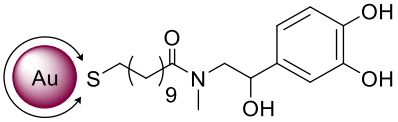

Au-MUDA-ADR NPs

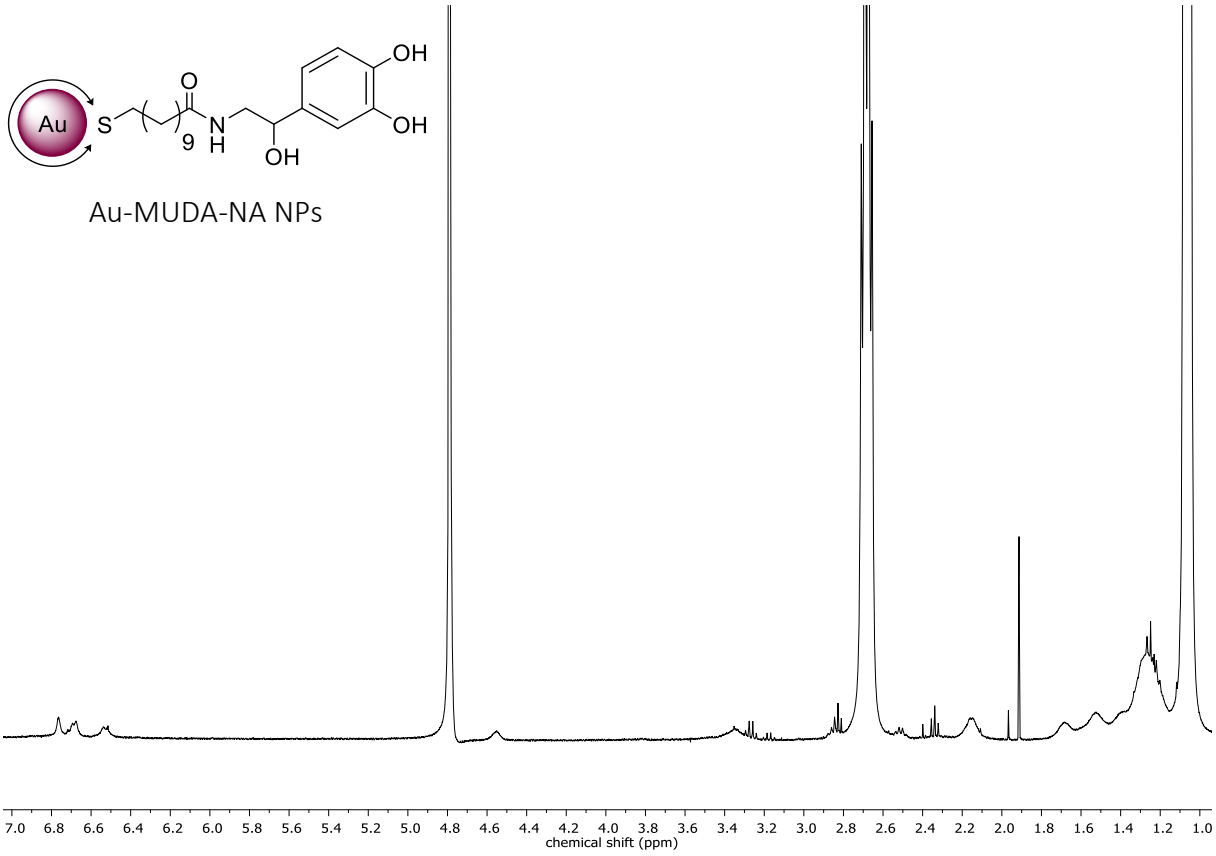

Au-MUDA-NA NPs

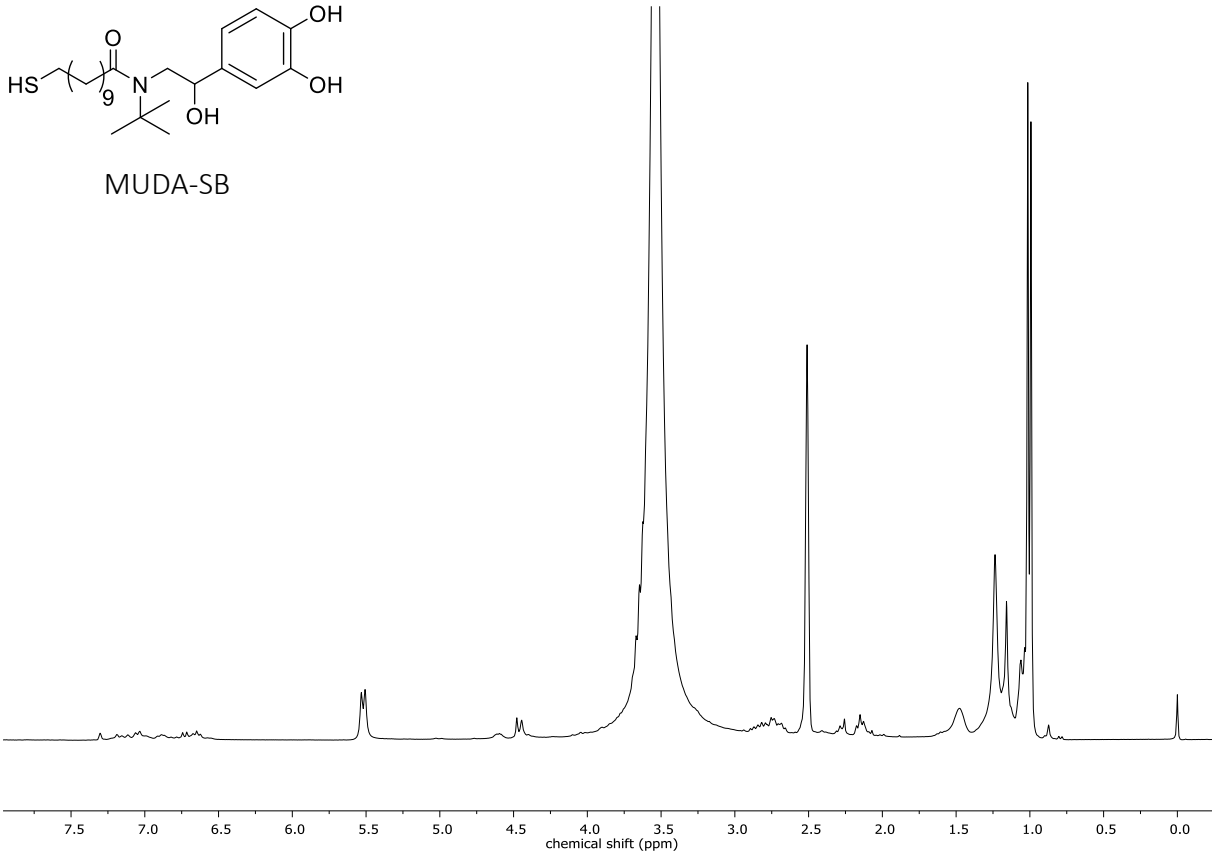

MUDA-SB

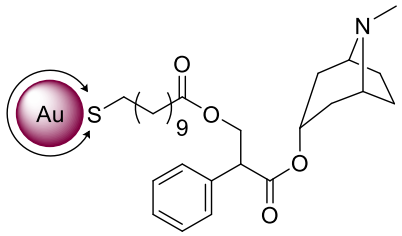

Au-MUDA-AT NPs

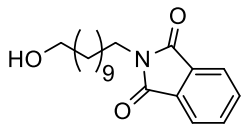

HUPh

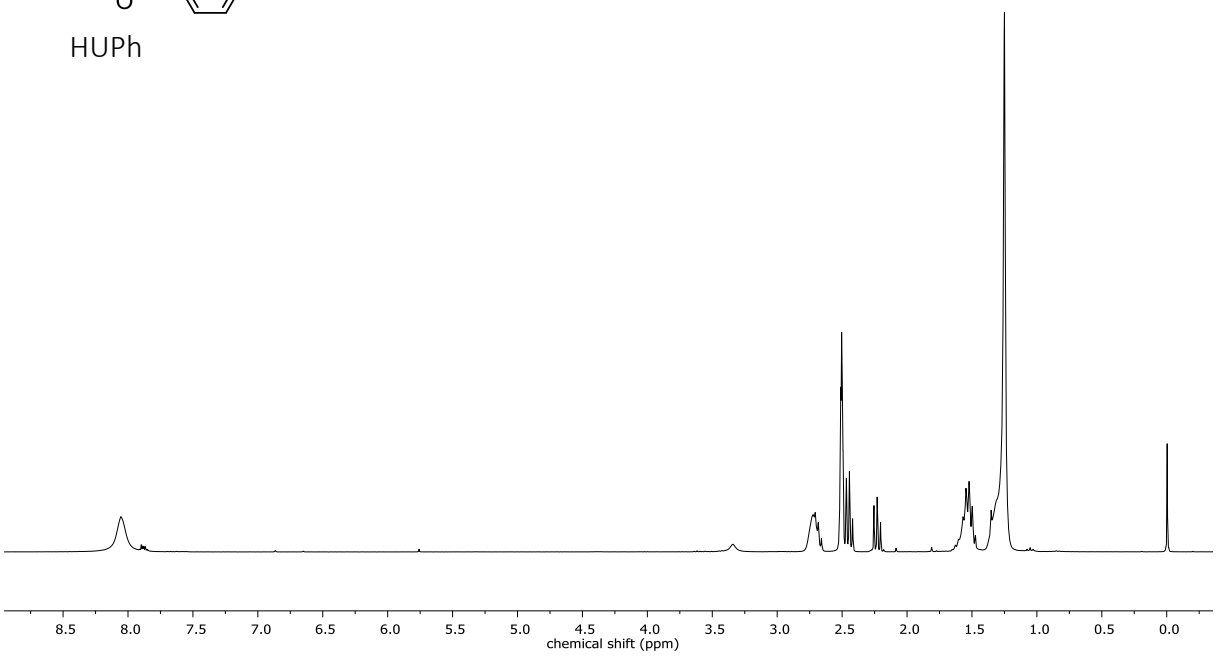

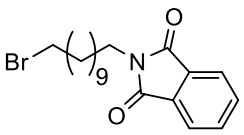

BrUPh

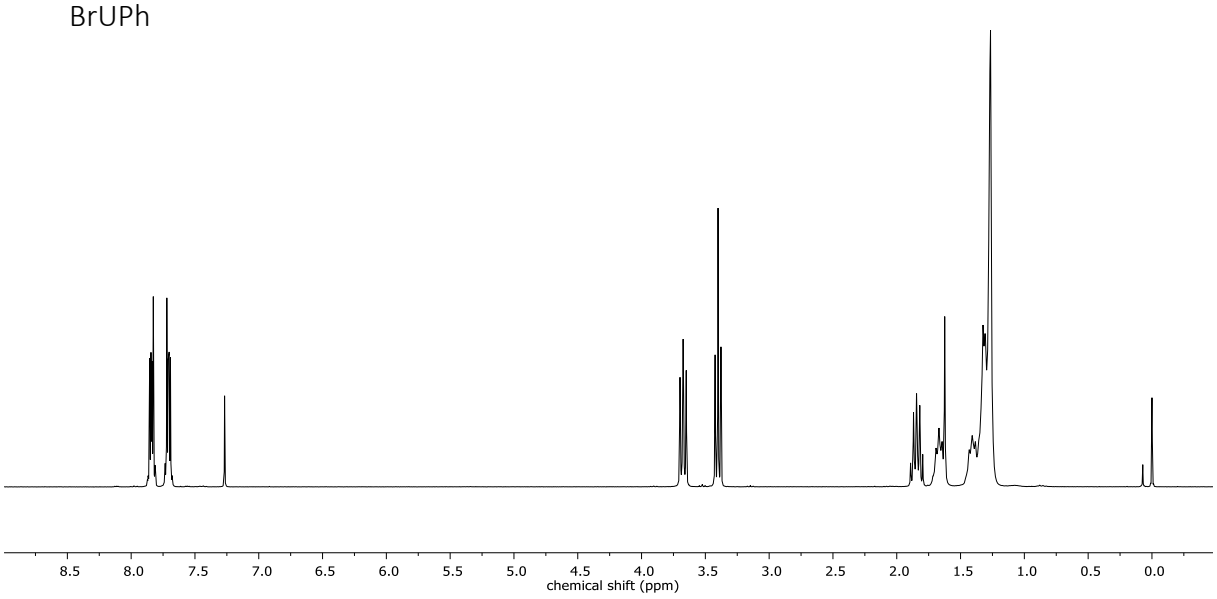

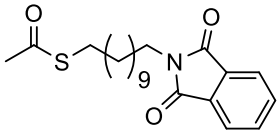

AcSUPh

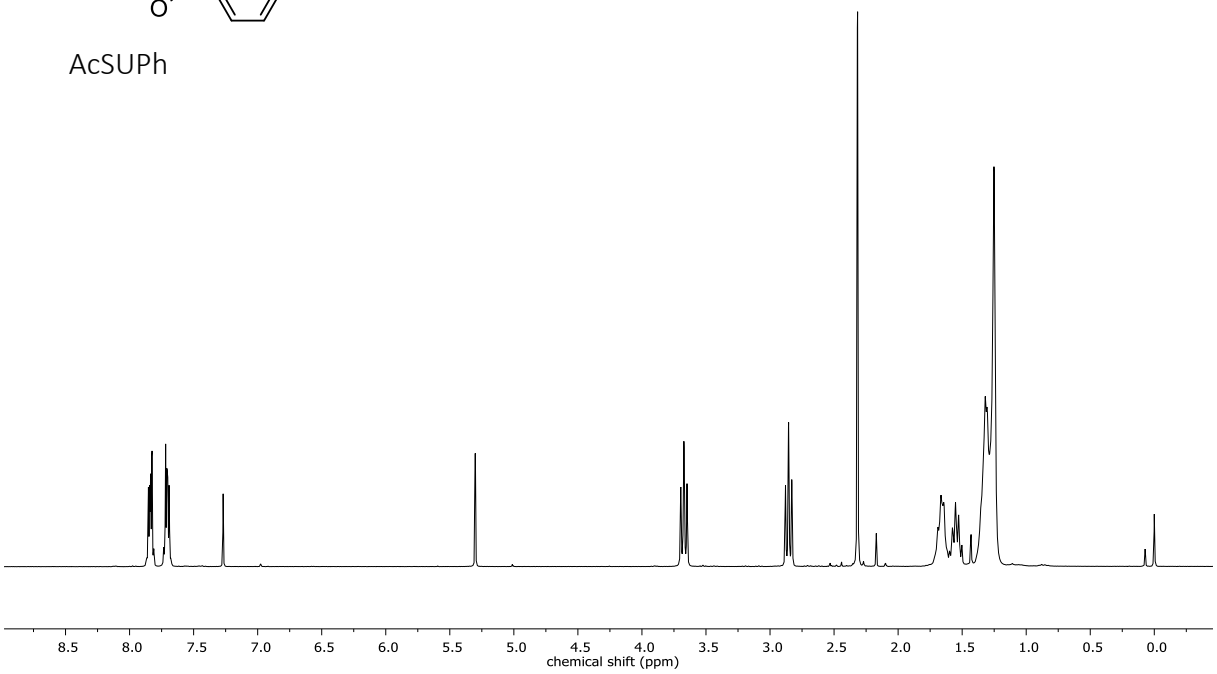

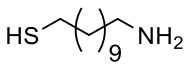

MUAM

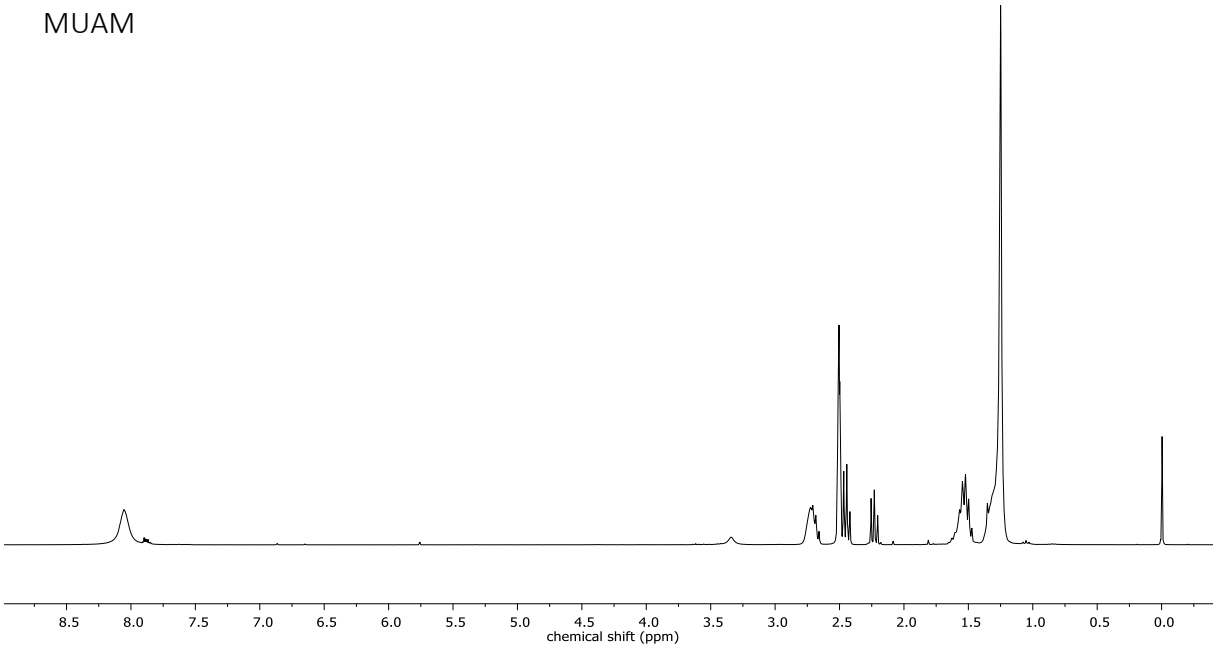

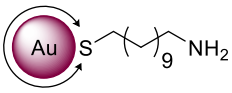

Au-MUAM NPs

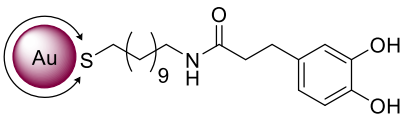

Au-MUAM-DHCA NPs

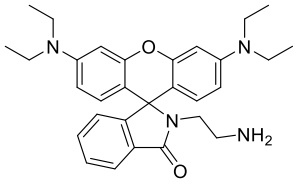

Rhod-EN

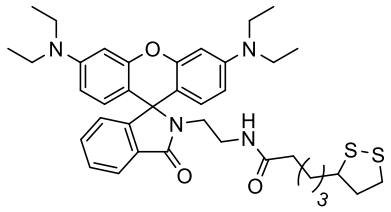

Rhod-EN-LA

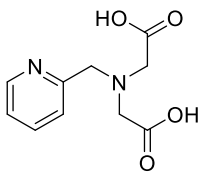

PADA

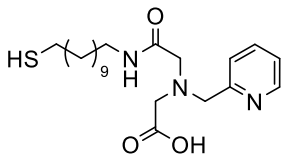

MUAM-PADA

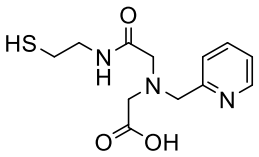

Cys-PADA

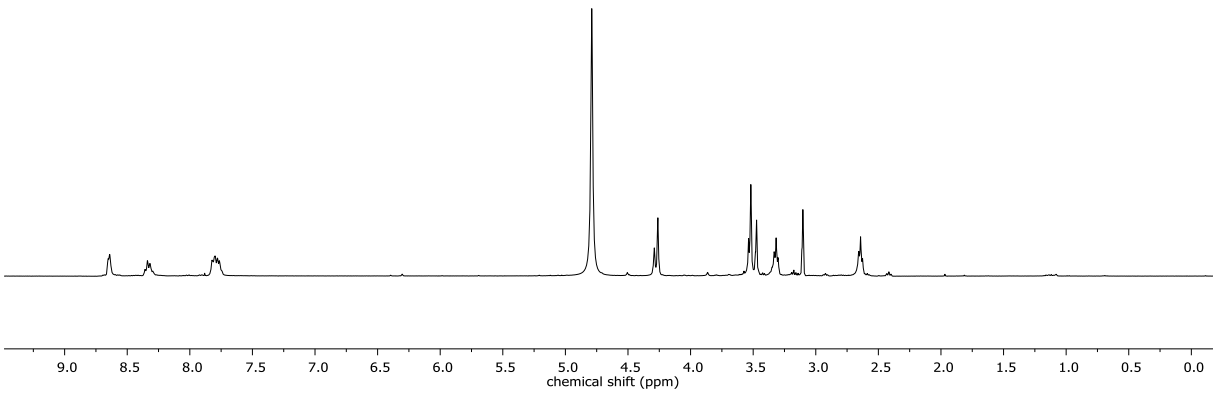

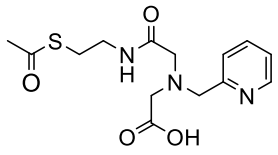

Ac-Cys-PADA

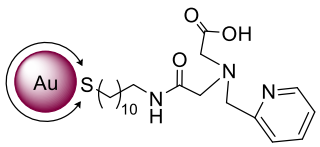

Au-MUAM-PADA

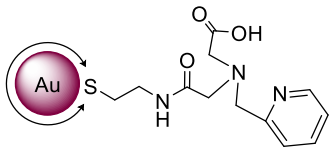

Au-Cys-PADA

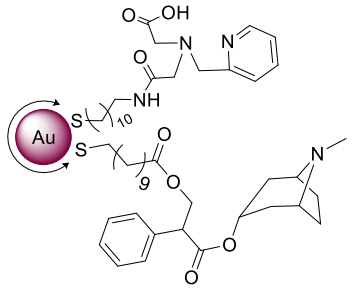

Au-MUDA-AT/ MUAM-PADA

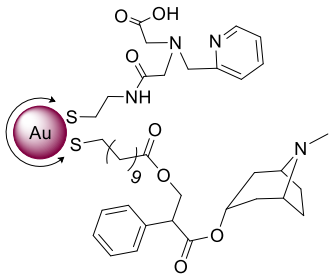

Au-MUDA-AT/Cys-PADA

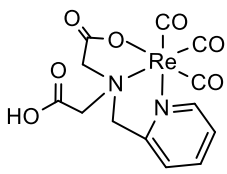

$Re(CO)_3PADA$

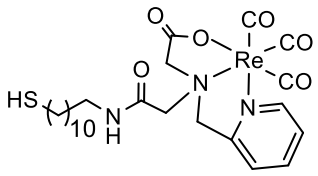

$Re(CO)_3PADA\text{-}MUAM$

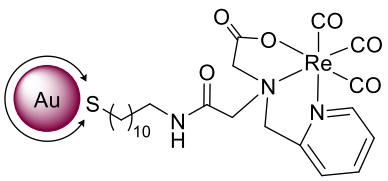

$Au\text{-}MUAM\text{-}PADA\text{-}Re(CO)_3$

XRD Data

Table 9: Crystal data and structure refinement for v1_run1_2 (Rhod-EN).

Identification code	v1_run1_2
Empirical formula	$C_{30}H_{36}N_4O_2$
Formula weight	484.63
Temperature/K	120
Crystal system	triclinic
Space group	P-1
a/Å	11.097(2)
b/Å	11.539(2)
c/Å	12.280(3)
α/°	80.45(3)
β/°	63.33(3)
γ/°	64.82(3)
Volume/Å^3	1270.9(6)
Z	2
ρ_{calc} g/cm^3	1.266
μ/mm^{-1}	0.080
F(000)	520.0
Crystal size/mm^3	0.04 × 0.04 × 0.04
Radiation	MoKα (λ = 0.71073)
2Θ range for data collection/°	3.714 to 51.354
Index ranges	-13 ≤ h ≤ 13, -14 ≤ k ≤ 14, -14 ≤ l ≤ 14
Reflections collected	24297
Independent reflections	4666 [R_{int} = 0.0846, R_{sigma} = 0.0576]
Data/restraints/parameters	4666/0/470
Goodness-of-fit on F^2	1.087
Final R indexes [I>=2σ (I)]	R_1 = 0.0595, wR_2 = 0.1356
Final R indexes [all data]	R_1 = 0.0881, wR_2 = 0.1503
Largest diff. peak/hole / e Å^{-3}	0.42/-0.33

Table 10: Crystal data and structure refinement for mo_AM400_full070 ($Re(CO)_3PADA$).

Identification code	mo_AM400_full070
Empirical formula	$C_{13}H_{11}N_2O_7Re$
Formula weight	493.44
Temperature/K	100.0
Crystal system	monoclinic
Space group	$P2_1/c$
a/Å	7.6084(3)
b/Å	24.1148(11)
c/Å	7.7772(3)
α/°	90
β/°	91.146(2)
γ/°	90
Volume/Å^3	1426.64(10)
Z	4
ρ_{calc} g/cm^3	2.297
μ/mm^{-1}	8.558
F(000)	936.0
Crystal size/mm^3	0.403 × 0.234 × 0.232
Radiation	MoKα (λ = 0.71073)
2Θ range for data collection/°	5.356 to 61.004
Index ranges	-10 ≤ h ≤ 10, -34 ≤ k ≤ 34, -11 ≤ l ≤ 11
Reflections collected	70718
Independent reflections	4341 [R_{int} = 0.0527, R_{sigma} = 0.0190]
Data/restraints/parameters	4341/0/209
Goodness-of-fit on F^2	1.171
Final R indexes [I>=2σ (I)]	R_1 = 0.0207, wR_2 = 0.0480
Final R indexes [all data]	R_1 = 0.0218, wR_2 = 0.0484
Largest diff. peak/hole / e Å^{-3}	1.42/-1.85

7.1 List of Figures

7.2 List of Schemes

7.3 List of Tables

8 Publications

8.1 Full Papers

- A. Mattern, F. Machka, M. S. Wickleder, O. S. Ilyaskina, M. Bünemann, M. Diener and E. Pouokam, Potentiation of the activation of cholinergic receptors by multivalent presentation of ligands supported on gold nanoparticles, *Organic & Biomolecular Chemistry*, 2018, **16**, 6680–6687.

- A. Mattern, R. Claßen, A. Wolf, E. Pouokam, K.-D. Schlüter, M. S. Wickleder and M. Diener, Multivalent Stimulation of β_1-, but not β_2-Receptors by Adrenaline Functionalised Gold Nanoparticles, *Nanoscale Advances*, 2021, submitted.

- A. Mattern, R. Claßen, E. Pouokam, M. S. Wickleder and M. Diener, Atropine Functionalised Gold Nanoparticles Passing Through Epithelial Barrier, in preparation.

8.2 Oral Presentations

- *„Nanos in a Nutshell- Exploring Hot ^{99m}Tc Labelled Gold Nanoparticles"*, Virtual Workshop on Radiochemistry and Imaging Science, Online, 19. February 2021

- *„Where are they going? – Evidence of Atropine Functionalised Gold Nanoparticles Passing Through Epithelial Barrier"*, Nanoscience Days 2019, Jyvaskyla (Finland), 8.-9. October 2019

- *„Where are they going? – Evidence of Atropine Functionalised Gold Nanoparticles Passing Through Epithelial Barrier"*, GDCh Wissenschaftsforum, Aachen (Germany), 15.-18. September 2019

- *„Gold Nanoparticles with Biogenic Substances – A New Way to Treat Asthma?"* GW4 NanoMedicine Workshop, Exeter (UK), 16. July 2019

- *„Synthesis and Functionalisation of Gold Nanoparticles with Biogenic Substances"* 7th EuCheMS Chemistry Congress, Liverpool (UK), 26.-30. August 2018

- *„Synthesis and Functionalisation of Gold Nanoparticles with Biogenic Amines"* 6th International Symposium on Metallomics, Vienna (Austria), 14.-17. August 2017

8.3 Poster Presentations

- *„Where are they going? – Evidence of Atropine Functionalised Gold Nanoparticles Passing Through Epithelial Barrier"*, GDCh Wissenschaftsforum, Aachen (Germany), 15.-18. September 2019

- *„Gold Nanoparticles with Biogenic Substances – A New Way to Treat Asthma?"* GW4 NanoMedicine Workshop, Exeter (UK), 16. July 2019

- *„A New Way to Treat Asthma? – Synthesis and Functionalisation of Gold Nanoparticles with Biogenic Substances"* 2nd CGSC PhD Symposium, Cologne (Germany), 09. April 2019

- *„Systematic Studies on Synthesis and Functionalisation of Gold Nanoparticles with Biogenic Substances"* 19. Vortragstagung für Anorganische Chemie der Fachgruppen Wöhler-Vereinigung und Festkörperchemie und Materialforschung, Regensburg (Germany), 24.-28. September 2018

9 ERKLÄRUNG ZUR DISSERTATION

Hiermit versichere ich an Eides statt, dass ich die vorliegende Dissertation selbstständig und ohne die Benutzung anderer als der angegebenen Hilfsmittel und Literatur angefertigt habe. Alle Stellen, die wörtlich oder sinngemäß aus veröffentlichten und nicht veröffentlichten Wortlaut oder dem Sinn nach entnommen wurden, sind als solche kenntlich gemacht. Ich versichere an Eides statt, dass diese Dissertation noch keiner anderen Fakultät oder Universität zur Prüfung vorgelegen hat; dass sie – abgesehen von unten angegebenen Teilpublikationen und eingebundenen Artikeln und Manuskripten – noch nicht veröffentlicht worden ist sowie, dass ich eine Veröffentlichung der Dissertation vor Abschluss der Promotion nicht ohne Genehmigung des Promotionsausschusses vornehmen werde. Die Bestimmungen dieser Ordnung sind mir bekannt. Darüber hinaus erkläre ich hiermit, dass ich die Ordnung zur Sicherung guter wissenschaftlicher Praxis und zum Umgang mit wissenschaftlichem Fehlverhalten der Universität zu Köln gelesen und sie bei der Durchführung der Dissertation zugrundeliegenden Arbeiten und der schriftlich verfassten Dissertation beachtet habe und verpflichte mich hiermit, die dort genannten Vorgaben bei allen wissenschaftlichen Tätigkeiten zu beachten und umzusetzen. Ich versichere, dass die eingereichte elektronische Fassung der eingereichten Druckfassung vollständig entspricht.

_____ _____

Köln, 19.08.2021 Annabelle Mattern